Plasmonic Waveguide Lithography for Patterning Nanostructures with High Aspect-Ratio and Large-Area Uniformity

by

Xi Chen

A dissertation submitted in partial fulfillment
of the requirements for the degree of
Doctor of Philosophy
(Applied Physics)
in the University of Michigan
2018

Doctoral Committee:

Professor L. Jay Guo, Chair
Professor Julie Biteen
Professor Roy Clarke
Professor Cagliyan Kurdak
Professor Ted Norris

Xi Chen

sxichen@umich.edu

ORCID iD: 0000-0002-3451-7310

© Xi Chen 2018

ACKNOWLEDGEMENTS

First and foremost, I wish to express my sincere gratitude to my advisor, Prof. L. Jay Guo, for his patient guidance and mentorship throughout my Ph.D. study and for suggesting various topics of research. I also appreciate his continuing optimism and his ability to always highlight the positive. He has always been willing to give me great freedom to explore new ideas, and offer plenty of opportunities for both internal and external collaborations. This work would not have been possible without his unfailing inspiration and immense knowledge. His instructions and continuous encouragement kept me motivated and will also remain so in the future. I would also like to thank my committee members, Prof. Julie Biteen, Prof. Roy Clarke, Prof. Cagliyan Kurdak, and Prof. Ted Norris, for their guidance and serving on my committee. Their insightful comments and encouragement motivated me to improve this work from various perspectives.

I am also grateful to many current and former group members, for their discussion and help throughout my study. I would like to thank my mentors and collaborators, Dr. Fan Yang, Dr. Cheng Zhang, Dr. Gaofeng Liang, Dr. Jing Zhou, Sung Ho Lee, Qiaochu Li, Darwin Cordovilla, Dr. Long Chen, Dr. Joong Hwan Bahng, Chengang Ji, Qingyu Cui, Sangeon Lee and Zeyu Lei, *etc*., without whose help I cannot complete these projects. Particularly, I'd like to acknowledge the collaborations with Dr. Fan Yang and Dr. Cheng Zhang on the lithography experiments, Dr. Gaofeng Liang on the roughness analyses, Dr. Jing Zhou on the enhanced Mie scattering and thermal radiation of hyperbolic metamaterials, Sung Ho Lee on the development of the plasmonic roller system, Dr. Long Chen and Zeyu Lei on the enhanced photoluminescence. In addition, my thanks must go the technical support of the Lurie Nanofabrication Facility (LNF), especially the

following staff members for their continuous assistance: Matt Oonk, Shawn Wright, Dr. Vishva Ray, Brian Armstrong, David Sebastian, Dr. Pilar Herrera-Fierro, Robert Hower, Kevin Owen, Steven Sostrom, Dr. Sandrine Martin and Dr. Nadine Wang *etc*.

I would like to acknowledge the financial support from Samsung Advanced Institute of Technology, National Science Foundation (NSF) and Center for Photonic and Multiscale Nanomaterials (CPHOM). It has been an amazing and rewarding experience to study and at the University of Michigan, especially in Applied Physics program and Electrical Engineering and Computer Science (EECS) department. This is a place full of unending inspirations and unbounded resources.

Last but not least, I would like to express my deepest gratitude to my husband Lin, for his love and patience, and for proof-reading this dissertation. My deepest appreciations also go to my family and my friends, especially my parents, for their unconditional love and support throughout this program and my life. Their company gives me the confidence to try anything and the fortitude to see it though.

TABLE OF CONTENTS

ACKNOWLEDGEMENTS ii

LIST OF TABLES x

LIST OF FIGURES xi

ABSTRACT xvi

CHAPTER 1 Principle of Plasmonic Lithography 1

1.1 Introduction to lithography and resolution limit 1

1.2 Plasmonic lithography 5

1.2.1 Superlens system 9

1.2.2 HMM system 11

1.3 Dissertation overview 13

CHAPTER 2 Waveguide Lithography Utilizing Single High-k Mode 15

2.1 Spatial frequency selection 15

2.2 Waveguide lithography 18

2.2.1 Design of waveguide lithography 18

2.2.2 Waveguide mode analyses 22

2.3 Fabrication and experimental setup 24

2.3.1 Nanofabrication of mask and substrate 24

2.3.2 Exposure system 25
2.4 Results and discussions 27
2.4.1 Experimental conditions 27
2.4.2 Partially polarized light 29
2.4.3 Double exposure 30
2.4.4 Applications 30
2.5 Other cases 33
2.5.1 Effects of film roughness 33
2.5.2 Waveguide lithography at 365 nm and 436 nm 34
2.5.3 Extremely small patterns using 193 nm and 248 nm light 35
2.5.4 Using high-index dielectrics for lithography 36
2.5.5 Comparison with direct contact lithography 37
2.6 Plasmonic roller system 38
2.6.1 Design principle of plasmonic roller system 39
2.6.2 Fabrication of the flexible mask and experimental setup 40
2.6.3 Stress on the roller system 42
2.6.4 Results and discussions 44
2.7 Summary 45
CHAPTER 3 Interference Lithography Based on ENZ HMM 47
3.1 Lithography system using HMM 47

3.1.1 ENZ HMM lithography system using Al 49

3.1.2 ENZ HMM lithography system using Ag 51

3.2 Principle of ENZ HMM 53

3.2.1 Surface wave 53

3.2.2 Waveguide modes 55

3.2.3 Type I and II ENZ HMM 60

3.2.4 Direction of the light propagation 62

3.2.5 Mode coupling in the HMM 66

3.2.6 Loss of the ENZ waveguide mode 67

3.3 Lithography design using ENZ HMM 68

3.4 Experiment and discussion 72

3.5 Analyses of the design 75

3.5.1 Optical constants 75

3.5.2 Parameter sweeping 75

3.5.3 Discussion on experimental conditions 76

3.5.4 Effects of film roughness 77

3.5.5 Lithography systems at a wavelength of 365 nm 78

3.5.6 Small patterns made by light wavelength of 248 nm and 193 nm 79

3.5.7 2-D patterns using circularly polarized light 80

3.5.8 Micron-scale photomasks 81

3.5.9 DUV Lithography system using photonic crystal 82
3.6 Analyses of natural HMM 84
3.6.1 Introduction to natural hyperbolic material 84
3.6.2 Optical properties of h-BN 84
3.6.3 Waveguide modes of other regimes 88
3.6.4 TE modes 90
3.7 Summary 92
CHAPTER 4 Roughness Analyses of Plasmonic Lithography Systems 93
4.1 Introduction to roughness 93
4.2 The roughness of the films and validation of the simulation 94
4.2.1 Comparison of the rough surfaces in measurement and simulation 94
4.2.2. Calculation method of the line edge roughness 96
4.3 The comparison between the superlens and HMM 96
4.3.1 Performance of the superlens system 97
4.3.2 Performance of the HMM system 99
4.3.3 Comparison of the electric field components 103
4.3.4 Waveguide lithography using frequency selection principle 106
4.3.5 Effect of rough surface on SP excitation 107
4.3.6 Fourier transform of 2D field distribution 109
4.4 Other systems and result 109

4.4.1 Impact of isolated defects on the mask 109
4.4.2 Effect of rough mask in plasmonic lithography 110
4.4.3 Different functions of metal films at different wavelengths 111
4.5 Summary 113
CHAPTER 5 Applications and Other Plasmonic Works 115
5.1 Photonic spin Hall effect 115
5.1.1 Mie scattering of dielectric particles 115
5.1.2 Introduction to photonic spin Hall effects 117
5.1.3 Circularly polarized dipole 118
5.1.4 Reflection phase from a reflective material 119
5.1.5 Near field scattering of a dipole on HMM 122
5.1.6 Scattering by different polarizations 125
5.2.7 Chiral absorption 128
5.2 Lidar design 130
5.2.1 Magnetic resonance for efficient size detection 130
5.2.2 Introduction to Lidar system in self-driving cars 132
5.2.3 Far field scattering of dielectric particles 132
5.2.4 Size, angular, material and polarization dependence 135
5.2.5 Particles dispersed in glass 138
5.3 Si nanowires in optical applications 140

5.3.1 Metal assisted chemical etching to fabricate Si NW 140

5.3.2 Si NW array as surface enhanced IR sensor 141

5.3.3 Si NW array as color panel 145

5.4 Functional devices using plasmonic materials.. 147

5.4.1 Efficient thermal-light inter-conversions based on HMM....................................... 147

5.4.2 Plasmonic lasing using dye molecules and 2D materials 149

5.5 Summary 151

CHAPTER 6 Conclusions and Future Work 153

REFERENCES 157

LIST OF TABLES

Table 1 The parameters which affect the results in ENZ lithography. 76

Table 2 The parameters in the h-BN permittivity model. 85

LIST OF FIGURES

Figure 1 Schematic of a typical lithography system. 2

Figure 2 Schematic of a subwavelength grating. 4

Figure 3 Typical plasmonic lithography/imaging systems and their results. 6

Figure 4 Previous experimental results using different techniques. 9

Figure 5 Illustration of SPP and subwavelength grating. 10

Figure 6 Principle of a HMM system 12

Figure 7 OTF of Ag and Al films. 17

Figure 8 Schematics of the design in a Cartesian coordinate. 18

Figure 9 Spatial frequency selection principle for waveguide lithography. 20

Figure 10 Simulations of the electric field distribution for 100 nm PR. 21

Figure 11 Mode analyses of the plasmonic lithoraphy system. 23

Figure 12 Fabrication process flow of masks on transparent glass substrate. 25

Figure 13 Exposure setup of the plasmonic lithography system. 26

Figure 14 SEM images of 100 nm thickness PR. 27

Figure 15 SEM images of the 200 nm thick patterned PR. 28

Figure 16 Experiment for partially polarized light. 29

Figure 17 Experimenatal 2D patterns by double exposure. 30

Figure 18 SEM images of 100 nm thick patterned photoresist after double exposure. 31

Figure 19 Applications of the pattern as an anti-reflective film. 32

Figure 20 Roughness of 15 nm Al films. 33

Figure 21 Simulated electric field distribution in xy plane. 34

Figure 22 Field patterns at other wavelengths. 35

Figure 23 Simulated electric field distribution for extremely small patterns. 36

Figure 24 Lithography system using dielectrics. 37

Figure 25 Field distribution of direct contact lithography for the PR with 250 nm thickness. 38

Figure 26 Schematic of plasmonic roller system. 39

Figure 27 Fabrication of the flexible Al photomask. 40

Figure 28 Optical setup of the roller system in the lab. 41

Figure 29 Stress analyses and photoelasticity of the PR film. 43

Figure 30 Experimental results made by the plasmonic roller system. 45

Figure 31 Different HMMs and their applications in lithography systems. 49

Figure 32 ENZ lithography design based on Ag. 52

Figure 33 Schematic for the symmetric slab waveguide. 54

Figure 34 Field sketches at the top and the bottom interface of the waveguide. 57

Figure 35 Comparison among different methods of the HMM. 61

Figure 36 Light propagation in different types of HMMs. 64

Figure 37 WG mode as a function of $kx/k0$ and thickness of the ENZ core. 66

Figure 38 Coupled mode analyses of ENZ HMM. 67

Figure 39 Loss of the waveguide mode. 68

Figure 40 Surface wave in a waveguide made of ENZ HMM. 70

Figure 41 Lithography design using ENZ HMM. 72

Figure 42 Fabrication process flow of ENZ mask and substrate. 73

Figure 43 The SEM of the patterns made by the Al/Al_2O_3 ENZ HMM. 74

Figure 44 SEM images of the patterns on the PR. 77

Figure 45 Normalized $E2$ distribution for roughness. 78

Figure 46 ENZ design at 365 nm based on Al. 79

Figure 47 ENZ systems at other wavelengths. 80

Figure 48 2-D simulation using circuarly polarized light. 81

Figure 49 ENZ HMM lithography using micron-scale photomasks. 82

Figure 50 193 nm lithography using photonic crytals. 83

Figure 51 Dispersion of h-BN as a function of wavelength. 85

Figure 52 Excitation of the surface wave in h-BN. 86

Figure 53 Waveguide modes anlyses at a wavelength of 6.3 μm 87

Figure 54 Magnetic field distribution at 6.3 μm. 88

Figure 55 Waveguide mode analyses at different wavelentgths. 89

Figure 56 Waveguide mode at 10 μm. 89

Figure 57 Modes for a slab with a thickness of 0.5 μm at a wavelength of 12.3 um. 90

Figure 58 Wavaguide mode at a wavelength of 12.3 μm. 91

Figure 59 Waveguide mode at 12.3 μm. 92

Figure 60 Image and simulation of the rough surfaces. 95

Figure 61 Performance of superlens lithography system. 98

Figure 62 Performance of HMM lithography system. 100

Figure 63 LER and electric field intensity variation of the patterns in the PR film. 102

Figure 64 Electric field distribution to analyze the mode. 104

Figure 65 Roughness performance of the waveguide lithography system. 106

Figure 66 Performance of isolated particle on the mask. 110

Figure 67 Effect of rough mask. 111

Figure 68 Superlens using Al at 193 nm. 112

Figure 69 Roughness of plasmonic lithography with an Al film-based superlens. 113

Figure 70 The ED and MD of a Si particle with radius of 50 nm. 116

Figure 71 Several ways of excitation of rotated electromagnetic field. 119

Figure 72 The reflection amplitude and phase of a HMM. 121

Figure 73 Resonant cone of HMM and circularly polarized dipole. 123

Figure 74 Electromagnetic field for a Si particle siting on HMM with 466 nm light. 124

Figure 75 Anglar dependent scattering of TE polarized light. 125

Figure 76 Anglar dependent scattering of TM polarized light. 126

Figure 77 Anglar dependent scattering of diagonal polarized light. 127

Figure 78 Anglar dependent scattering of circularly polarized light. 127

Figure 79 Absorption of a Ag helix particle. 128

Figure 80 Demonstration of the particle sizing 130

Figure 81 BCS and FCS of particles wirh different size and angle. 133

Figure 82 The resonance of electrical dipole and magnetic dipole. 134

Figure 83 BCS and FCS of particles wirh different size and angle. 135

Figure 84 SiO_2 particles coated with different materials. 136

Figure 85 For light with incident angle of 60°. 137

Figure 86 Different light polarizations. 138

Figure 87 Scattering of SiO_2 particle in glass. 139

Figure 88 Light scattering of TiO_2 particle in glass. 140

Figure 89 Schematic of the formation of Si NW by MacEtching. 141

Figure 90 Optical property of Si NW. 142

Figure 91 The simulation of Si NW with thickness 10 μm on Si substrate. 143

Figure 92 SEM images of Si nanowires with different conditions. 144

Figure 93 Simulation of the effective modes in Si NW covered by Au layer. 145

Figure 94 Reflective microscope bright field images of various Si NW forests. 146

Figure 95 Reflection spectra of Si NW forests. 146

Figure 96 HMM for wideband spectral-selective absorption/emission. 148

Figure 97 Optical setup of plasmonic laser.. 150

ABSTRACT

The rapid development of the semiconductor industry in the past decades has driven advances in nano-manufacturing technologies towards higher resolution, higher throughput, better large-area uniformity, and lower manufacturing cost. Along with these advancements, as the size of the devices approaches tens of nanometers, challenges in patterning technology due to limitations in physics, equipment and cost have quickly arisen. To solve these problems, unconventional lithography systems have attracted considerable interest as promising candidates to overcome the diffraction limit. One recently evolved technology, plasmonic lithography, can generate subwavelength features utilizing surface plasmon polaritons (SPPs). Evanescent waves generated by the subwavelength features can be transmitted to the photoresist (PR) using plasmonic materials. Another approach of plasmonic lithography involves the use of hyperbolic metamaterial (HMM) structures, which have been studied intensively because of their unique electromagnetic properties. Specifically, epsilon near zero (ENZ) HMMs offer the potential to produce extremely small features due to their high optical anisotropy.

Despite the advancements in plasmonic lithography, several key issues impede progress towards more practical application, which includes shallow pattern depth (due to the evanescent nature of SPPs), non-uniformity over a large area (due to the interference of multiple diffraction orders) and high sensitivity of the roughness on the films and defects on the mask. The light intensity in the PR is very weak which results in an extremely long exposure time. To this end, this dissertation is dedicated to plasmonic lithography systems based on SPP waveguides and ENZ HMMs for patterning nanostructures with high aspect-ratio and large-area uniformity.

New schemes are exploited in this thesis to address these challenges. Lithography systems based on a specially designed waveguide and an ENZ HMM are demonstrated. By employing the spatial filtering properties of the waveguide and the ENZ HMM, the period, linewidth and height of the patterns can be well controlled according to various design purposes. Periodic structures were achieved in both systems with a half-pitch of approximately 50 ~ 60 nm, which is 1/6 of the exposure wavelength of 405 nm. The thickness of the PR layer is around 100 ~ 250 nm, which gives an aspect-ratio higher than 2:1. The subwavelength patterns are uniform in cm^2 areas.

In addition to the design principle, various numerical simulations, fabrication conditions and corresponding results are discussed. The design principle can be generalized to other materials, structures and wavelengths. The real-world performance of the lithography system considering non-idealities such as line edge roughness and single point defect is analyzed. Comparisons between the plasmonic systems based on different design rules are also carried out, and the advantages of the spatial frequency selection principle is verified.

The plasmonic waveguide lithography systems developed in this dissertation provide a technique to make deep subwavelength features with high aspect-ratio, large-area uniformity, high light intensity distribution, and low line-edge-roughness for practical applications. Compared with the previously reported results, the performance of plasmonic lithography is drastically improved. A plasmonic roller system combining the photo-roller system and plasmonic lithography is also developed. This plasmonic roller system can support a continuous patterning with a high throughput for cost sensitive applications. Several potential applications of the plasmonic materials including near field spin Hall effects and a particle based Lidar design are explored. Other advances towards plasmonic functional devices including silicon (Si) nanowire (NW) arrays, light-thermal converters and plasmonic lasers are also reported.

CHAPTER 1

Principle of Plasmonic Lithography

1.1 Introduction to lithography and resolution limit

To keep up with the rapidly growing market in display, photovoltaic and biological applications, there has been a surging demand for cost effective patterning technologies capable of printing on a large area with high precision and large throughput. Developing a suitable patterning technology is critical for applications that depend heavily on surface properties, such as wire grid polarizers and structural color filters to improve the brightness and power efficiency of liquid crystal displays (LCDs), self-cleaning and anti-reflective surfaces for photovoltaic devices, as well as patterned surfaces to suppress the bacteria growth. Despite recent progress on various fronts, patterning process that can meet all the necessary requirements for next-generation nano-manufacturing technologies are still lacking. Ideally, this process should exhibit the features such as high resolution, low process time, cost effectiveness and large area capability, all at the same time. Therefore, the new lithography technology is still critically needed and remains to be an important research topic in both academic and industrial world.

Photolithography is the most widely used patterning technology globally. As a state-of-art microfabrication technique in the semiconductor industry, it is a parallel, cost effective, high throughput process. A practical lithography system usually consists of three key components [1,2]: a set of masks, an energy source and a photoresist (PR) to record the patterns, as shown in Figure 1 (a). For the photomask, we usually consider either an isolated object (a point source) for arbitrary

patterns or a periodic structure. The radiation of a point source can be expanded in Fourier space. In this k space, only a portion of the expanded waves can pass through the projection system and finally reach the PR layer. For this reason, some spatial information from the mask is lost during the lithography process. Thus, we can calculate the smallest feature size obtainable from certain lithography using inverse Fourier transformation, which is essentially the Raleigh criterion.

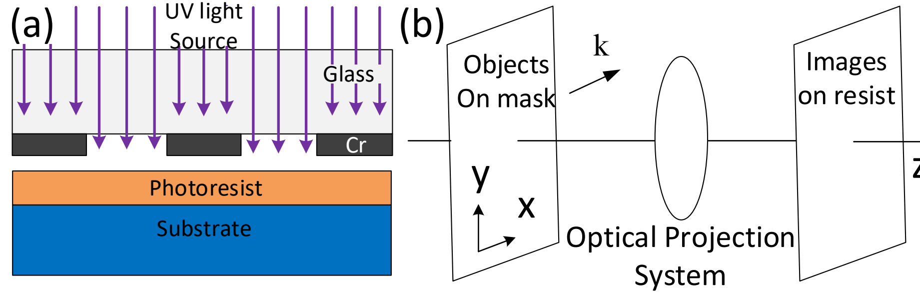

Figure 1 Schematic of a typical lithography system.
(a) Schematic of a typical lithography system including a mask, a light source and photoresist, (b) Schematic of an optical system in a Cartesian coordinate.

In a typical lithography optical system, as shown in Figure 1 (b), incoming light carrying the information of the mask goes through an optical projection system and forms images on the PR. With a point source, if the optical axis of the projection system is along the z-axis and the field is propagating in full space, the electric component of the field can be expressed with 2D Fourier expansion [3],

$$E(\bar{r}) = \iint_{-\infty}^{\infty} A(k_x, k_y) \exp\left[i\left(k_x x + k_y y + k_z z\right)\right] dk_x dk_y \quad (1)$$

Where $A(k_x, k_y)$ stands for the field amplitude of each component in spatial frequency k space. This is also called the angular spectrum representation of light propagation. The electric field must satisfy the Helmholtz equation, which is given by the following:

$$(\nabla^2 + k^2)E(\bar{r}) = 0 \tag{2}$$

Hence, we can obtain the dispersion relation of k_x, k_y and k_z as $k_x^2 + k_y^2 + k_z^2 = k^2 = \omega^2/c^2$. The wavevector of the propagating wave in the k_z direction can be expressed as

$$k_z = \sqrt{\frac{\omega^2}{c^2} - k_x^2 - k_y^2}, \quad \frac{\omega^2}{c^2} > k_x^2 + k_y^2 \tag{3}$$

Accordingly, the electric field for propagating waves is $E(\bar{r}) = A(x,y)\exp(-ik_z z)$ along z direction. In contrast, for evanescent waves, the wavevector is imaginary

$$k_z = i\sqrt{k_x^2 + k_y^2 - \frac{\omega^2}{c^2}}, \quad \frac{\omega^2}{c^2} < k_x^2 + k_y^2 \tag{4}$$

The corresponding field $E(\bar{r}) = A(x,y)\exp(-|k_z|z)$ shows a decaying amplitude of evanescent waves along z-axis. Since the waves that can be captured by the optical system and exposed on the PR in the far field limit are usually restricted to propagating waves with $k_x^2 + k_y^2 < \omega^2/c^2$, the maximum resolution in the image cannot be better than:

$$\Delta = \frac{2\pi}{k_{\max}} \approx \frac{2\pi}{\omega/c} = \lambda \tag{5}$$

For a photomask with periodic structures (gratings), a series of diffraction orders are generated with both propagating and evanescent waves. In the extreme case, the first order should be transmitted to reconstruct an image and higher orders can be lost. Under this assumption, a similar conclusion can be obtained, *i.e.* the resolution of the system is still close to the effective wavelength. If we use the angular spectrum representation of a grating, the reflected field and transmitted field can be given as the following [4–6]:

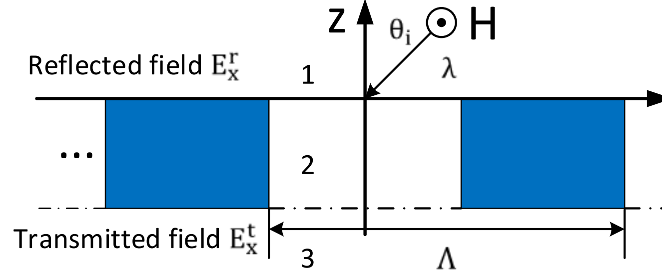

Figure 2 Schematic of a subwavelength grating.

$$E_x^r = \sum_{m=-\infty}^{\infty} \{\delta_{m,0} \exp\left[-ik_0(n_1^2 - \gamma_m^2)^{\frac{1}{2}}z\right] + r_m \exp[ik_0(n_1^2 - \gamma_m^2)^{\frac{1}{2}}z]\}\exp(ik_0\gamma_m x) \tag{6}$$

$$E_x^t = \sum_{m=-\infty}^{\infty} t_m \exp\left[-ik_0(n_3^2 - \gamma_m^2)^{\frac{1}{2}}z\right] \exp(ik_0\gamma_m x) \tag{7}$$

As illustrated in Figure 2, E_x^r is the reflected electric field along x-axis and E_x^t is the associated transmitted field. $k_0 = 2\pi/\lambda$ is the free space wavevector. n_1 and n_3 are the refractive indices of the superstrate (region 1) and substrate (region 3). r_m and t_m are the amplitudes of the mth reflected and transmitted diffracted orders, respectively, and γ_m is normalized tangential wavevector, defined as $\gamma_m = n_1 \sin\theta_i + m\lambda/\Lambda$, where Λ is the period of the grating and θ_i is the incident angle. In the angular spectrum representation, a propagating wave has a wavevector smaller than the refractive index $\gamma_m < n_1$. Based on Fourier transform theory, the zeroth order does not contain any useful spatial information. At least the first order component should be transmitted through for lithographic purposes, thus the resolution of a grating for normal incidence $\theta_i = 0$ can be calculated as:

$$\Delta = \Lambda = \frac{\lambda}{n_1} \tag{8}$$

In the extreme case of an off-axis illumination with $\theta_i \sim \pi/2$, the resolution can be calculated as $\Lambda = \lambda/2n_1$. Therefore, for both isolated objects and periodic structures, the resolution of photolithography is proportional to the light wavelength and inversely proportional to the numerical aperture $\Delta \sim \lambda/NA$.

1.2 Plasmonic lithography

As discussed in last section, the resolution of a conventional photolithography system [2,3,7] is restricted by the wavelength of the exposure light and the numerical aperture of the projection system. Naturally, one approach for resolution enhancement is to simply scale the exposure wavelength, and extreme ultraviolet (EUV) lithography [8] is one such example. However, there are still some significant technological challenges of the EUV lithography due to poor readiness of the light sources, photomasks, resists, tools and optics, since all materials in nature absorb EUV light. In addition, nanoimprint lithography [9–11] offers an alternative way to achieve smaller patterns without the need of a light source, but it is still far from ideal. Nanoimprint lithography, as its name suggests, is based on mechanical deformation to transfer patterns from mask to resist. Consequently, they are prone to defect generation due to the forced contact and the stress created during the demolding in the nanoimprint process.

Meanwhile, there are other lithography techniques that can bypass the Raleigh criterion and achieve subwavelength pattern sizes using regular UV sources, such as near field optical lithography, [2,12] phase shift lithography, [1] and plasmonic lithography. Among them, plasmonic lithography is particularly interesting and intensively studied because it has been demonstrated to improve the resolution by utilizing surface plasmonic polaritons (SPPs) excited at the interface between the metal and the dielectric. Plasmonic lithography is a type of contact

lithography using UV light and plasmonic materials. Plasmonic materials usually refer to noble metals including silver (Ag), aluminum (Al) and gold (Au) *etc*. The noble metals have many free electrons, and induced oscillations in noble metals exhibit retardation with regards to the incident light. Therefore, the SPP excited at the metal surface has a wavelength much smaller than that of the excitation light (can be 10 times smaller depending on the permittivity of metals), which can be applied in the lithography systems and naturally leads to better resolution.

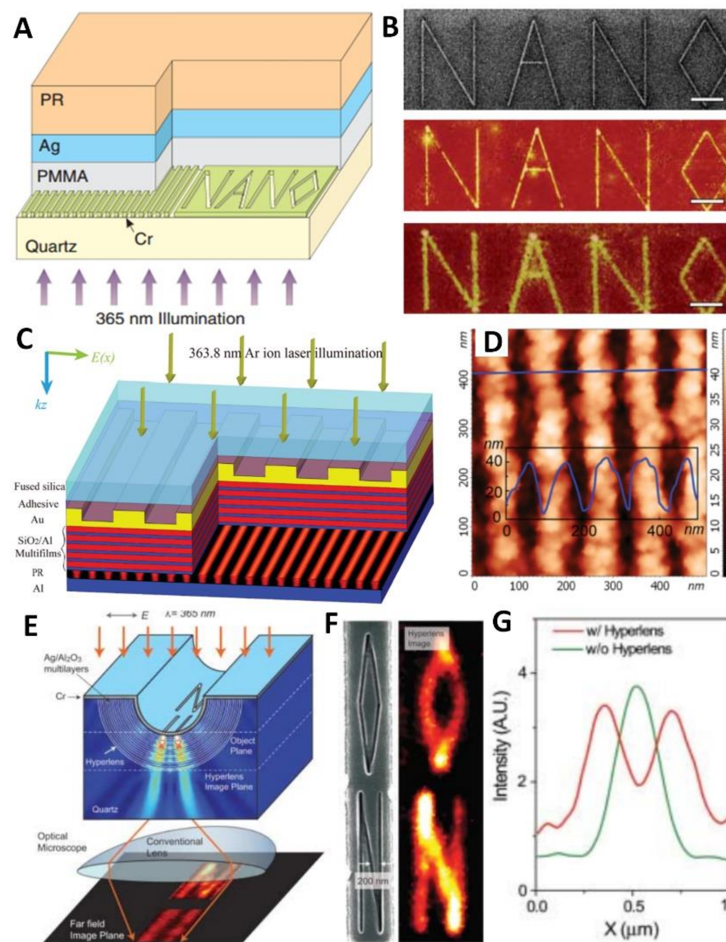

Figure 3 Typical plasmonic lithography/imaging systems and their results.
(A) Superlens scheme. (B) Patterns with a linwidth of 40 nm produced by superlens system. [25] (C) An Al/SiO_2 HMM lithography system. (D) AFM of the patterns with a half-pitch of 45 nm produced in the HMM system. [13] (E) Schematic of an Ag/Al_2O_3 hyperlens and numerical simulation of the imaging system. (F) An arbitrary object imaged with subdiffraction resolution. (G) Averaged cross section of hyperlens image of the line pair object with 150-nm spacing (red), and a diffraction-limited image obtained in the control experiment (green). [14]

Over the past decades, many promising simulated and experimental results using plasmonic lithography and imaging techniques have been reported. Systems using thin metal layers, [15–18] lamellar alternating metal/ dielectric metamaterials, [19–23] subwavelength gratings, [24,25] and nanowire based metamaterials, [26,27] *etc.* were demonstrated to make subwavelength objects. There are several major plasmonic lithography systems: superlens made of simple metallic films and hyperbolic metamaterials (HMMs) made of alternating metal and dielectric films. Hyperlens can also image subwavelength patterns. Here we discuss the typical design of these approaches and focus on their principle and performance. As the shown in Figure 3A, [28] the superlens is made of a thin Ag layer with a thickness of 35 nm. The Ag film can transmit evanescent waves and therefore print subwavelength patterns. The scanning electron microscope (SEM) and atomic force microscope (AFM) images show that the letters of "NANO" with the feature width of 40 nm as in Figure 3B. In comparison, the HMM lithography system [13] as shown in Figure 3C is made of 5 pairs of stacked alternating silicon dioxide (SiO_2) films with a thickness of 30 nm and Al films with thickness of 15 nm. By using the interference of second order diffraction, period 1D patterns were obtained with a half pitch of 45 nm, about a 4 times reduction from the patterns on the photomask (Figure 3D). In addition, a curved hyperlens made of 16 layers of Ag and aluminum oxide (Al_2O_3) stacks was used in imaging systems to resolve subwavelength patterns, as shown in Figure 3E-G. [14] Diffraction-limited objects with a separation of 150 nm and a linewidth of 40 nm can be imaged to the far field by the high-k waves supported by the curved hyperlens.

Despite the innovative concept of plasmonic lithography taking advantage of intrinsically shorter SPP wavelength, there are still several key issues impeding its progress towards more practical applications, which includes (1) shallow pattern depth (2) non-uniformity over a large area (3) high sensitivity of the roughness on the films and defects on the mask (4) extremely weak intensity

in the photoresist and (5) necessity of a direct contact of the mask and resist made on two separate substrates. The shallow depth and non-uniformity of the image render the PR impractical for use as an etch mask or a structural material for subsequent processing steps. Furthermore, producing ultrathin and smooth metal layers needed for masks used in plasmonic lithography can be quite challenging. The size of the patterned area is small because most of the masks for plasmonic lithography are made by electron beam lithography, which only has limited throughput. Moreover, because multiple metal layers are used in an HMM system, the light intensity in the PR is several orders of magnitude weaker than that of the incident light, which results in an extremely long exposure time (up to a few hours). [13] Last but not least, in most of the plasmonic lithography systems, the PR is directly spin coated on to the projection system, which is far from ideal for practical applications. To compare the quality of the patterns created in various approaches, Figure 4 shows SEM/ AFM images of the corresponding PR with 100 nm grating patterns made by (A) EUV lithography, [8] (B) nanoimprint lithography [10] and (C) plasmonic lithography. [28] Obviously, though the patterns have almost the same linewidth, the PR exposed by plasmonic lithography have a small patterned area, shallow pattern depth, irregular shapes and more severe roughness. The patterns shown in Figure 4C have a thickness of only around 10 nm, and are not uniform even over a few microns. However, there is no inevitable barrier if the systems can be further optimized and the pattern profile *via* plasmonic lithography can be greatly improved.

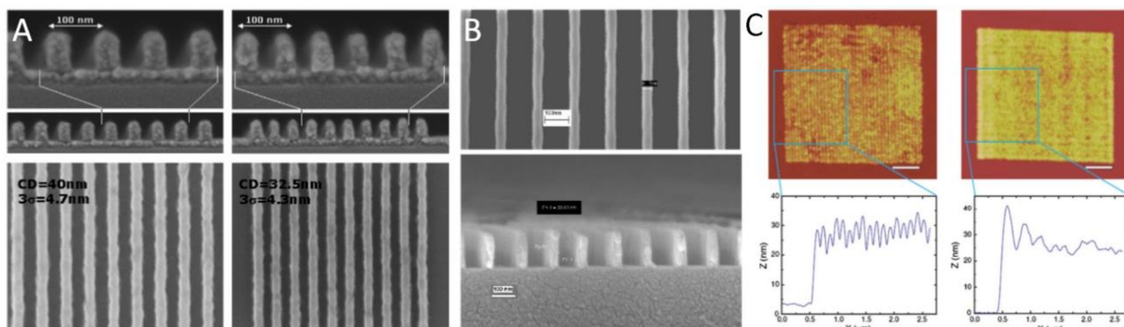

Figure 4 Previous experimental results using different techniques.
The comparison of around 100 nm period grating patterns generated in (A) EUV lithography [8] (B) nanoimprint lithography [10] and (C) plasmonic lithography. [25]

1.2.1 Superlens system

A superlens system represents one major category of plasmonic lithography. As shown in Figure 5A, the SPP wavelength excited by a transverse magnet (TM) polarized light is much smaller than the wavelength of the incident light in vacuum, which can be employed to expose PR in a plasmonic lithography system. The wavelength of SPP $\lambda_{spp} = 2\pi/k_{spp}$ is given by

$$\lambda_{spp} = \lambda_0 \sqrt{\frac{\epsilon_m + \epsilon_d}{\epsilon_m \epsilon_d}} \ll \lambda_0 \tag{9}$$

Where ϵ_m and ϵ_d are the relative permittivities of the metal and dielectric, respectively. To understand the limitations of the approaches reported in the previous literature, we consider a well-known plasmonic lithography scheme, [29–32] as displayed in Figure 5B. In this scheme, the photomask is a subwavelength metallic grating, usually made by chromium (Cr). A thin metal film, separated from the mask by a spacer layer, serves as a superlens to transfer the grating pattern into the PR. In this work, subwavelength metal patterns on the substrate are permitted to transmit through the superlens made of Ag and reach the PR layer. Since this technique is based on the surface waves, which propagate along the horizontal direction and decays exponentially in the normal (depth) direction, the produced patterns are naturally shallow. Under the angular spectrum representation (*i.e.,* Fourier transformation), as illustrated in Figure 5C, the grating generates a series of diffracted light when excited by the incident light, including both propagating and evanescent waves. In spatial frequency domain (*i.e., k*-space), the diffracted waves can be expressed as $\gamma_m = m\lambda/\Lambda$ [4,6,33] for normal incident light, where m stands for the mth

diffraction order, λ the exposure wavelength and Λ the period of the grating, respectively. The metal superlens supports symmetric and antisymmetric TM modes, hence a range of evanescent waves can transmit through. Therefore, subwavelength objects can be captured by the PR. Considering the transmission of Ag at the illumination wavelength of 365 nm, the passband in the evanesce regime is broad. Therefore, in the k space, the subwavelength grating generates a series of diffraction orders. With the broad transmission of the superlens for evanescent waves, multiple orders are allowed to pass. According to Fourier theory, a single spatial frequency leads to sinusoidal oscillations, whereas, the inference of multiple diffractions results in a distorted wave front, which looks similar to the morphology of the AFM of the patterned PR. Hence in a superlens system, due to the near field nature of the evanescent field, the associated methodologies of PR patterns were created when interfacing with the superlens, contributing to non-uniformity over a large exposure area. An appropriate design discussed in Chapter 2 of the dissertation can potentially address these issues and produce subwavelength light by an interference lithography system incorporating the PR layer in an optical waveguide to improve the aspect-ratio and uniformity of the patterns. [34]

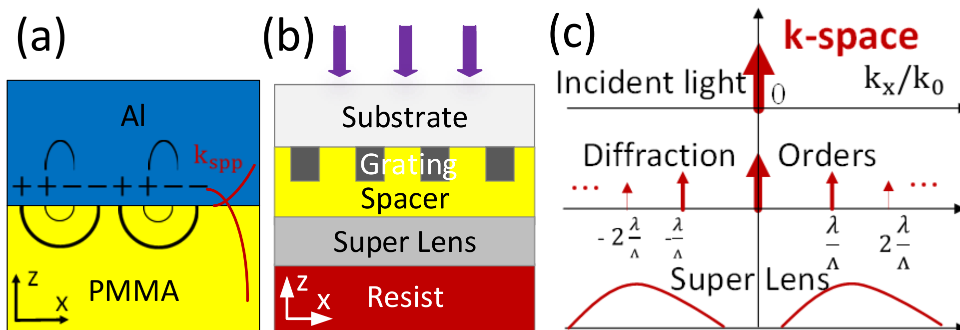

Figure 5 Illustration of SPP and subwavelength grating.
(a) SPP wave Cartesian coordinates (b) A typical plasmonic lithography system including a subwavelength grating on a fused silica substrate, followed by a polymer spacer, a metal super lens, and photoresist. Coordinates x and z refer to the horizontal and vertical directions, respectively. (c) Spatial frequency distribution in terms of normalized tangential wavevector.

1.2.2 HMM system

Another major category of the plasmonic lithography is the HMM based systems. First, we need to familiarize ourselves with some special properties of HMM materials before we can fully utilize them for lithographic purposes. In recent years, the focus of metamaterial research has shifted towards active and tunable metamaterials, as well as simplifying structures while preserving many of their unique properties and functionalities. One class of metamaterials is highly anisotropic which have a hyperbolic dispersion, [14,19,35–39] as determined by their effective electric and/or magnetic tensors. Such HMMs represent the ultra-anisotropic limit of traditional uniaxial crystals, in which one of the principal components of either their permittivity (ε) or permeability (μ) tensors is opposite in sign to the other two principal components. The dielectric permittivity can be expressed in tensor form with only principal components as the following:

$$\bar{\bar{\epsilon}} = \begin{pmatrix} \epsilon_{xx} & 0 & 0 \\ 0 & \epsilon_{yy} & 0 \\ 0 & 0 & \epsilon_{zz} \end{pmatrix} \tag{10}$$

The signs of the tangential permittivity of HMMs are the same $\epsilon_{\parallel} = \epsilon_{xx} = \epsilon_{yy}$ while the signs of its tangential and vertical permittivity are opposite $\epsilon_{\parallel} \cdot \epsilon_{\perp} = \epsilon_{xx} \cdot \epsilon_{zz} < 0$, where both $\epsilon_{\parallel}$ and $\epsilon_{\perp}$ are complex values. Various forms of the metamaterials have been proposed to construct such HMM, including multilayer structures, [40] nanorod based structures [41] and metamaterials composed of metallic nanowire in dielectric hosts. [42] Among these structures, the HMM composed of alternating metal and dielectric stacked layers is most often seen in planar plasmonic nanolithography systems. Following the effective medium theory for HMM [43–46], the effective permittivity of the stacked structure can be calculated as:

$$\epsilon_{xx} = \epsilon_{yy} = f\epsilon_m + (1-f)\epsilon_d \quad (11)$$

$$\epsilon_{zz} = \frac{\epsilon_m\epsilon_d}{(1-f)\epsilon_m + f\epsilon_d} \quad (12)$$

where f stands for the fill ratio of the metal $f = t_m/(t_m + t_d)$, and ϵ_m (ϵ_d) is the relative permittivity for the metal (dielectric), and t_m (t_d) are their thicknesses. The signs of ϵ_{xx} and ϵ_{zz} determine the type of the metamaterials. [36,37,44] Type I HMM ($\epsilon_{xx} < 0$ and $\epsilon_{zz} > 0$), effective metal ($\epsilon_{xx} < 0$ and $\epsilon_{zz} < 0$), effective dielectric ($\epsilon_{xx} > 0$ and $\epsilon_{zz} > 0$), and type II HMM ($\epsilon_{xx} > 0$ and $\epsilon_{zz} < 0$) can all be achieved by proper tuning of the light wavelength and the metal ratio.

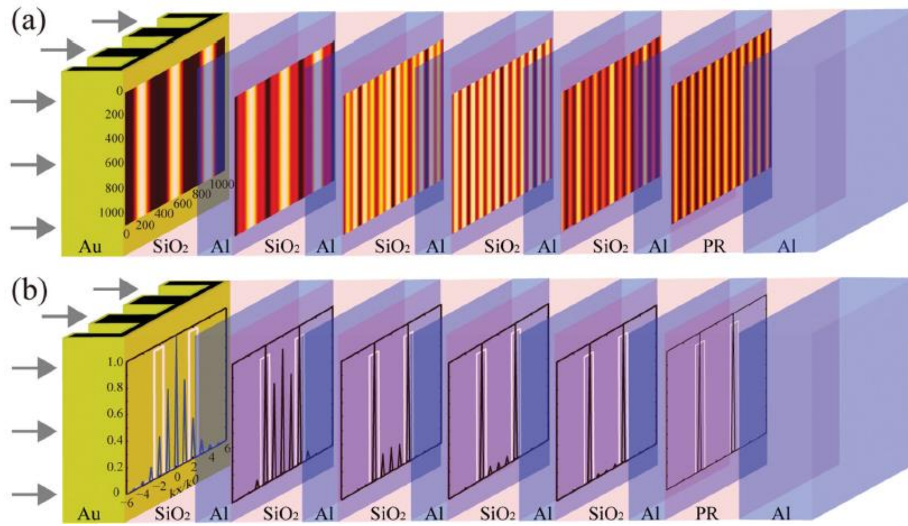

Figure 6 Principle of a HMM system
(a) Light intensity distributions inside each SiO_2 film of Al/SiO_2 multilayers. (b) Spatial frequency spectra normalized to their own maximum value and corresponding to the light distributions. [13]

HMMs have been used to improve the resolution as a hyperlens in imaging [13,19,22,34,47,48] and filters in UV lithography. [13,22,34,47–49] Using the hyperlens (a type I HMM capable of transmitting high-k modes because of a specific dispersion), patterns can be replicated with the same feature size as that of the mask by a flat structure, while a curved hyperlens can produce patterns which are even smaller than the mask. [50] The 1:1 patterning approach is challenging

because the same patterns (usually in nano-scale) should be made on the mask in fabrication. Figure 6 demonstrates the basic working principle of a typical HMM system made of Al/SiO_2 multilayers, which uses the HMM as a filter [13,38] to produce patterns based on interference effects of light. Figure 6A and B visualize the light propagation in real space and k-space, respectively. [13] The spatial frequency is generated by the subwavelength grating. As the incident light transmits through the metal and dielectric films, only the second order diffraction is selected. Therefore, uniform interference pattern can be formed in the light-sensitive PR layer. However, due to the strong attenuation of the light propagating in the HMMs, the field intensity in the PR layer is several orders of magnitude weaker than that of the incident light, which increases the exposure time significantly (up to several hours), thus severely limiting the throughput of lithography. [13,21] To overcome these obstacles, a system which can create interference patterns while maintaining high light transmission is highly desired. To mitigate these problems, we propose the use of a special type of HMM in plasmonic lithography in Chapter 3, which can make period reduction patterns as well as enhance the light intensity in the PR. [51] The epsilon near zero (ENZ) HMM greatly alleviates the difficulty of making the mask, and significantly reduces the exposure time (down to a few seconds).

1.3 Dissertation overview

This dissertation attempts to address the aforementioned challenges and aims to design a nanolithography technique to pattern periodic structures with (1) subwavelength features, (2) high height-width aspect ratio, (3) large area uniformity (4) high light intensity in the PR (4) period reduced patterns and (5) low line edge roughness for practical applications. Our proposed design is also integrated to a roll-based system for continuous patterning over large areas to improve the throughput. Plasmonic lithography process is essentially a contact photolithography technique,

thus it is immune to pattern defects occurring in nanoimprint during the demolding process when imprinting high density and high aspect ratio structures, especially in high speed processing. It is also much more durable as it only has contact with the resist layer, unlike in nanoimprint process where the mold undergoes high mechanical stress during imprinting and demolding steps. Compared with EUV lithography, our proposed approaches have proved to be cost effective with high throughput, and hence are especially attractive for applications that require printing patterns with a high aspect ratio over a large area. In addition, other potential applications of the proposed systems and functional plasmonic devices are discussed.

This dissertation discusses principle, experiments, analyses and applications about plasmonic lithography for patterning high aspect-ratio nanostructures. **Chapter 1** introduces the basic principles of the resolution limit and plasmonic lithography. **Chapter 2** presents the design of a plasmonic lithography system using an Al optical waveguide [34] to make large-area uniform patterns with high aspect ratio. A plasmonic roller lithography system to print nano-patterns continuously is also developed. **Chapter 3** discusses the plasmonic lithography system using epsilon-near-zero (ENZ) HMM, [22,51] which is able to make period reduced patterns while maintaining high light intensity in the PR. **Chapter 4** compares the performance of several plasmonic lithography systems. [52,53] The impact of line-edge roughness and uniformity is analyzed and the advantages of spatial frequency selection is confirmed. **Chapter 5** focuses on Mie scattering of dielectric particles, including photonic spin Hall effects, as well as its application in lithography system (near field) and Lidar design (far field). Some other works relevant to plasmonic materials including silicon (Si) nanowire (NW), light-thermal converter, [39] and plasmonic laser are also presented. **Chapter 6** summarizes the current achievements and proposes some potential directions for future work.

CHAPTER 2

Waveguide Lithography Utilizing Single High-k Mode

2.1 Spatial frequency selection

Lithography lays the foundation for the semiconductor industry, and photolithography is the most widely used patterning technology nowadays. The resolution of photolithography [2,3,7] is limited by the light diffraction $\Delta = k_1\lambda/NA$, where Δ is the minimum feature size, λ is the wavelength of the exposure light and NA is the numerical aperture of the projection system, and k_1 is a coefficient that accounts for various process-related factors and resolution enhancement. In order to obtain smaller features, various techniques have been developed, such as extreme ultraviolet (UV) lithography [8] by using much shorter wavelengths and nanoimprint lithography [9–11] by mechanically deforming the resist. Meanwhile, to break the diffraction limit and achieve subwavelength patterns, other techniques, such as near field optical lithography [2,12] and phase shift lithography [1] have been explored. Plasmonic lithography, [29–32,37,54] which was recently studied, has been demonstrated to improve the resolution by utilizing SPP wave excited at the interface between metal and dielectric. The surface wave is induced by free electron oscillations at metal surface and has the wavelength much smaller than that of the excitation light. Over the past decades, several promising simulated and experimental results have been reported, by using thin metal layers, [15–18] alternating metal/dielectric stacked metamaterials, [13,14,19,21,22,50] subwavelength gratings, [24,25] and nanowire based metamaterials [26,27] to image subwavelength objects onto light-sensitive photoresist (PR). However, almost all the experimental efforts were only able to show very shallow patterns due to

the evanescent nature of the SPP wave; and the periodic patterns could only be achieved in a localized region experimentally. [24,54,55] Achieving high aspect ratio patterns and maintaining pattern uniformity over large area are basic requirements for practical applications. Therefore, in this chapter, [34] we propose a new design principle to address these problems, which is supported by experimental demonstrations of $\sim\lambda/6$ wide gratings with height up to 200 nm in square centimeter areas. To understand the limitations of approaches reported in the previous literatures, we consider a well-known plasmonic lithography scheme as discussed in Chapter 1, the metal superlens supports symmetric and antisymmetric transverse magnetic (TM) modes, and a range of evanescent waves are allowed to transmit through. Therefore, the subwavelength objects can be captured by the PR.

Silver (Ag) is usually employed as the superlens material at 365 nm wavelength, [29–32,37,54] because of the strong SPP resonance near its plasma frequency. When ϵ_{Ag} ~ -1.5, the wavevector of the SPP $k_{spp} = \sqrt{\epsilon_{Ag}\epsilon_d/(\epsilon_{Ag} + \epsilon_d)}$ at the interface of Ag and the surrounding dietetic with ϵ_d = 1.5 can be very high. The transmission band $|E_t/E_i|^2$ of silver at 365 nm is broad, where E_i stands for the incident electric field and E_t refers to the transmitted electric field. This requirement on the passband of Ag with certain permittivity limits the applications of the superlens. Figure 7A shows the transmitted field amplitude as a function of normalized tangential wavevector k_x/k_0. If 365 nm wavelength light is used for the exposure, a wide band of high-k evanescent waves, amplified by the SPP, can transmit through the thin metal (this is indicated by the white dash-dot line at 365 nm extending from ~$2k_0$ to $8k_0$). The term high-k refers to the fact that the SPP evanescent wave has a tangential wavevector larger than that of the free space k_0. As a result, multiple diffraction orders of the subwavelength grating can penetrate the thin Ag film and reach the PR. The transmitted light of different diffraction orders interferes with each other, resulting in

modulated patterns in the resist with varied spatial frequencies, inevitably resulting in pattern non-uniformity. In addition, the diffracted evanescent waves propagate along the interface and decay rapidly in the normal direction, seriously limiting the pattern depth.

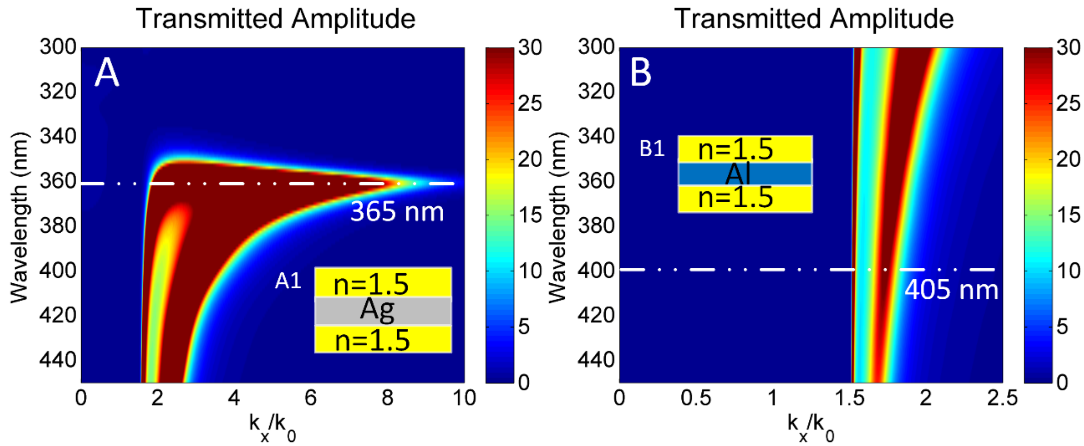

Figure 7 OTF of Ag and Al films.
Transmitted amplitudes $|E_t/E_i|^2$ as a function of normalized tangential wavevector k_x/k_0 and wavelength, through (A) a 30 nm Ag layer and (B) a 15 nm Al layer with background refractive index of 1.5. The insets show the schematics of the corresponding (A1) dielectric/Ag/dielectric and (B1) dielectric/Al/dielectric system.

To avoid shadow surface waves, the incident light is coupled into an optical waveguide to improve the propagation depth of the pattern. The optical waveguide has thin aluminum (Al) layer and low index materials as its cladding and it supports evanescent waves. To make large area uniform subwavelength patterns with high aspect ratio, a single high k mode should be selected. As marked by the white dash line in Figure 7B, a thinner Al still gives narrower transmission band because of higher loss at 405 nm. This can be utilized to filter out the irrelevant diffracted light and select one diffraction order to achieve uniform periodic patterns. Utilizing this feature, spatial frequency selection of the single k mode can be achieved by using a thin Al layer to block the 0th order direct transmitted light, as well as incorporating the PR in a waveguide structure to only couple to a single high-order diffraction from the grating mask. It should be noted that the same metal can function diversely at different wavelengths. Ag films can function as a filter at longer wavelengths

while Al films can be used as a superlens in the deep UV regime. [52] Furthermore, the mask and substrate are prepared separately, thus can be optimized individually.

2.2 Waveguide lithography

2.2.1 Design of waveguide lithography

The diagram of the proposed lithography system is shown in Figure 8, which consists of the mask and the substrate to be exposed. The photomask and substrate are prepared separately, which is more convenient and can be implemented to practical contact lithography systems. The mask is on a silica substrate, composed of a one-dimensional (1-D) 22-nm-thick Al grating, 245 nm period and 50% duty cycle, followed by a 40-nm-thick poly methyl methacrylate (PMMA) spacer and a 10 nm Al layer underneath. The substrate is a polyethylene terephthalate (PET) sheet coated with 15 nm Al, 44 nm SiO_2 and 100 nm PR layer. During exposure, the mask is in conformal contact with the PR layer to ensure the wave coupling. Compared with the previous design, the mask containing the thin Al layer can be reused, while the thin SiO_2 and Al layer underneath the PR can be used as hard mask to help transfer the pattern into the substrate or a thicker polymer resist layer.

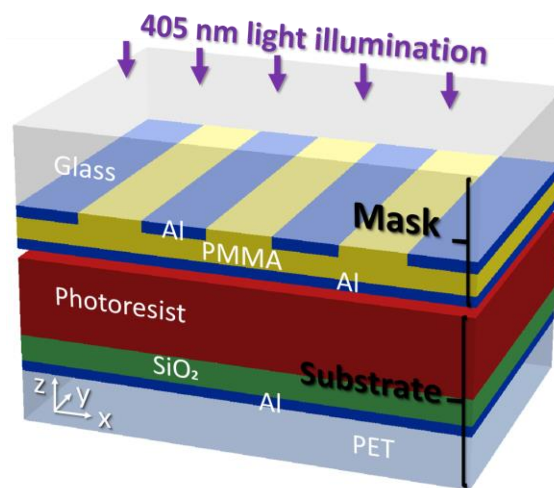

Figure 8 Schematics of the design in a Cartesian coordinate.
The electric field of the incident light is along *x*-axis. The light has a wavelength of 405 nm with normal incident angle.

When the grating mask is irradiated by a 405 nm (h-line) wavelength TM polarized light, a series of harmonic modes are excited with the extra momenta provided by the Al grating, as discussed in Chapter 1. In the Fourier space, the SPP wave at the Al and PMMA interface has a wavevector of $k_{\mathrm{spp}} \sim 1.62 k_0$ at 405 nm wavelength. When the 1st order diffraction of the grating $\gamma_1 = \lambda/\Lambda$ couples to the surface wave, *i.e.,* $\gamma_1 \sim k_{\mathrm{spp}}/k_0$, it forms a strong high-k resonance. The Al layer filters out the unwanted diffraction light due to its narrow pass-band (Figure 1B), as illustrated in Figure 9A. To achieve high aspect ratio features by increasing the penetration depth of the surface wave, an optical waveguide with an effective mode index of n_{eff} [56–58] is formed to extract the SPP mode. The optical waveguide consists of the PR as its core, sandwiched between thin Al layer and low index materials as claddings. The effective index n_{eff} can be adjusted to satisfy the phase matching condition *i.e.,* tangential momentum conservation, by optimizing the thickness of PR, SiO_2, and bottom Al. When the phase matching condition is reached, *i.e.,* $\gamma_1 \sim k_{\mathrm{spp}}/k_0 \sim n_{\mathrm{eff}}$, the high-k resonance is further enhanced while effectively rejecting other diffraction orders from reaching the PR layer. The interference of $\pm 1^{st}$ order light, or two counter-propagating waveguide modes form a standing wave with a sufficient intensity contrast and a large pattern depth. The period of the pattern can be calculated by $\lambda/2n_{\mathrm{eff}}$, where the effective index n_{eff} can be regarded as the effective numerical aperture of the system. The refractive index of the PR used is 1.69055 + 0.034625i at 405 nm. The value of n_{eff} is around 1.653 in case of 245 nm period grating, leading to deep subwavelength patterns with a period of 122.5 nm, 1/2 the mask period because of the mode interference. Next we investigate the thickness dependence of the PR pattern to achieve high aspect-ratio grating patterns. The effective index of the waveguide modes in PMMA-Al-PR-SiO_2-Al multilayer system as a function of the PR thickness is given in Figure 9B. As the PR thickness varies from 100 nm to 300 nm, the effective index almost maintains constant, which indicates that

such mask design can be used to expose PR of different thicknesses, thereby creating patterns with desired aspect-ratios. An upper limit can be determined to be ~250 nm for lithography by considering the losses in the metal and the dissipation of the waveguide mode.

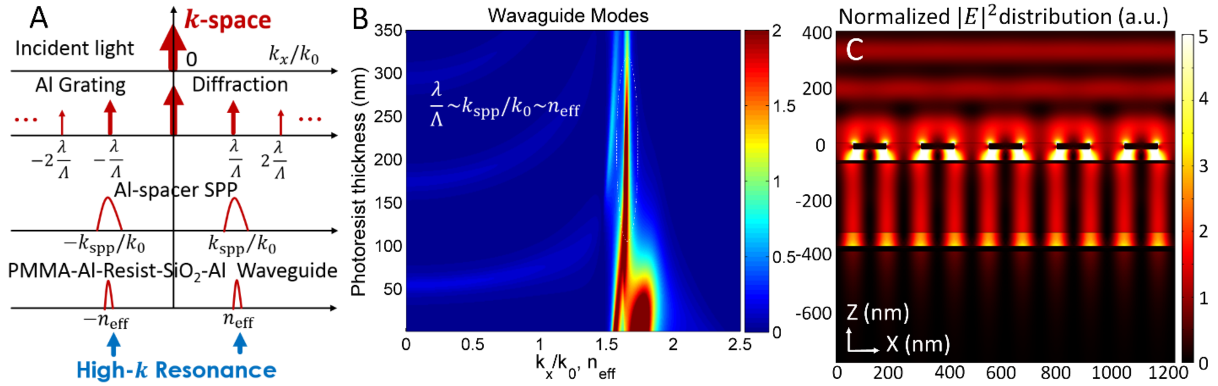

Figure 9 Spatial frequency selection principle for waveguide lithography.
(A) Phase matching condition and the spatial frequency selection principle, illustrated in normalized k-space. (B) PMMA-Al-Resist-SiO_2-Al waveguide modes. Red regions corresponds to stronger modes, and the sharper mode with mode index of ~1.65 marked by white dashed curve is selected. (C) Normalized $|E|^2$ map for 250 nm thickness PR. The electric field intensity of the incident light is set at 1 V/m, and the colors with a scalebar in arbitray unit on the right stand for the field intensity distribution in xz plane. Brighter colors indicates stronger field in the map.

The simulated normalized $|E|^2$ field distribution maps in xz plane are given both in Figure 9C for PR with 250 nm thickness and in Figure 10A for PR with 100 nm thickness. Clearly uniform patterns with high contrast can be formed at different PR thicknesses. Figure 10B gives the $|E|^2$ distribution for the case of 100 nm PR along the horizontal cut-lines as a function of positions along x-axis. The field distributions at z = -80 nm, -125 nm and -170 nm are marked by black, green and red sinusoidal curves, respectively. Three curves at different z positions have almost the same distributions with a 2.8 V^2/m^2 maximum, a 0.1 V^2/m^2 minimum and a 122.5 nm periodicity (the incident light E-field is set at 1 V/m). The fact that field distribution is nearly identical at different depths suggests that vertical sidewall should be possible using this structure and indeed observed in experiments. The maximum field intensity in the PR is higher than the incident light,

indicating that the field is enhanced by the plasmonic resonances. The contrast of the patterns in the PR can be calculated from Figure 10B as $(|E|^2_{\max} - |E|^2_{\min})/(|E|^2_{\max} + |E|^2_{\min}) = 0.931$. The high field intensity and contrast in the PR ensure the exposure stability in experiments.

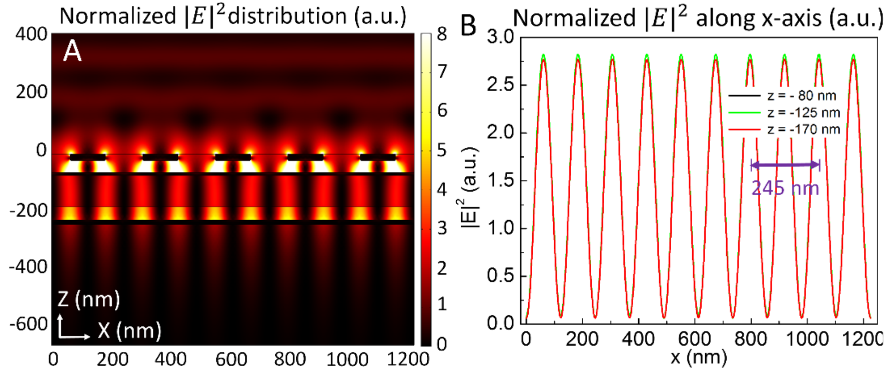

Figure 10 Simulations of the electric field distribution for 100 nm PR.
(A) Normalized $|E|^2$ map for 100 nm thickness PR. (B) Normalized $|E|^2$ distributions along horizontal lines at z = -80, -125 and -170 nm. Three sinusoidal curves are nearly identical, and have 61.25 nm half-pitch.

As a brief summary for the design criteria, the function of each layer is as follows: 1) the grating provides the needed high-k momentum; 2) the PMMA spacer layer helps form the strong resonance; 3) the Al in between serves as a high pass filter to eliminate the 0th , 2nd and higher diffracted orders while select only 1st order light for exposure; 4) the SiO_2 is a tunable layer for index matching (and can be replaced by other material, *e.g.,* a polymer layer with index lower than that of the PR); and the bottom Al layer serves as a reflector in the waveguide to improve the pattern depth. In conventional near-UV photolithography, contact photolithography [2,12] can define small patterns due to its near field nature, but the field decays along vertical direction so that the field at different depths of the PR are not uniform. In addition, off-axis illumination [1,2] design can block the 0th order light and employ the higher order propagating wave for exposure, where the PR layer has to be thin because of the light diffraction. Furthermore, the photolithography techniques that utilize interferometry to generate small features requires two or

more beam illuminations on the resist which increases process complexity. In comparison, our design uses the interference of the $\pm 1^{st}$ order evanescent wave from the subwavelength grating, which carries high spatial frequency information.

2.2.2 Waveguide mode analyses

To achieve high aspect ratio features, the PR is sandwiched between two claddings to form an optical waveguide [56–58] with the mode effective index to be n_{eff}. A more accurate and realistic analysis can be made by treating all dielectric constant to be complex numbers as the following. The wavevector is given by the dielectric-metal-dielectric (DMD) waveguide modes, and the symmetric and asymmetric mode [7,58] of the thin metal in dielectric surrounding media can be calculated as

$$\alpha_{\mathrm{m}} a = 2\mathrm{arctanh}(-\frac{\epsilon_{\mathrm{m}} \alpha_{\mathrm{d}}}{\epsilon_{\mathrm{d}} \alpha_{\mathrm{m}}}) \tag{13}$$

$$\alpha_{\mathrm{m}} a = 2\,\mathrm{arctanh}(-\frac{\epsilon_{\mathrm{d}} \alpha_{\mathrm{m}}}{\epsilon_{\mathrm{m}} \alpha_{\mathrm{d}}}) \tag{14}$$

where a is the thickness of the metal and $\alpha_{\mathrm{m}} = (k_x^2 - \epsilon_{\mathrm{m}} k_0^2)^{\frac{1}{2}}$ and $\alpha_{\mathrm{d}} = (k_x^2 - \epsilon_{\mathrm{d}} k_0^2)^{\frac{1}{2}}$ are the wavevector in z direction in the metal and dielectric, respectively. The solution of k_x to the DMD modes derived from eq. (13) and eq. (14) is $(1.565 + 0.00178i)k_0$ and $(1.788 + 0.0888i)\,k_0$, respectively. They are close to the wavevector calculated by the bulk SPP $k_{\mathrm{spp}} = (1.620 + 0.0176i)\,k_0$, at the light frequency far below the plasma frequency of the thin metal, thus we simply use $\mathrm{Re}(k_{\mathrm{spp}})$ for clearer understanding.

To illustrate the modes and coupling in the lithography system, Figure 11A shows the magnetic field distribution of the proposed design, where the resonances are highlighted by the stronger field

distributions in the spacer layer and the PR layer. As a signature feature of SPP, the resonances are enhanced at the dielectric/metal interfaces, and exponentially decay towards the both sides. The rectangle enclosed by dotted line is the optical cavity formed in the grating-spacer-Al layers, and the bottom dashed rectangle illustrates the PMMA-Al-resist-SiO_2-Al waveguide mode. The period of the two modes is the same, which indicates that the phase matching condition is satisfied. The modes of the PMMA-Al-Resist-SiO_2-Al waveguide are solved for the eigenmodes of the system using transfer matrix method [6,58]. Here, to gain a better insight of the nature of the modes, we first simplify the model by approximating metal-dielectric-metal (MDM) waveguide [56–58] composed of the PR as the core and two semi-infinite Al as claddings. Plasmonic TM_0 and TM_1 modes, oscillatory TM_m modes and TE_m modes in the MDM waveguide are given by eq. (15), eq. (16), eq. (17) and eq. (18), respectively.

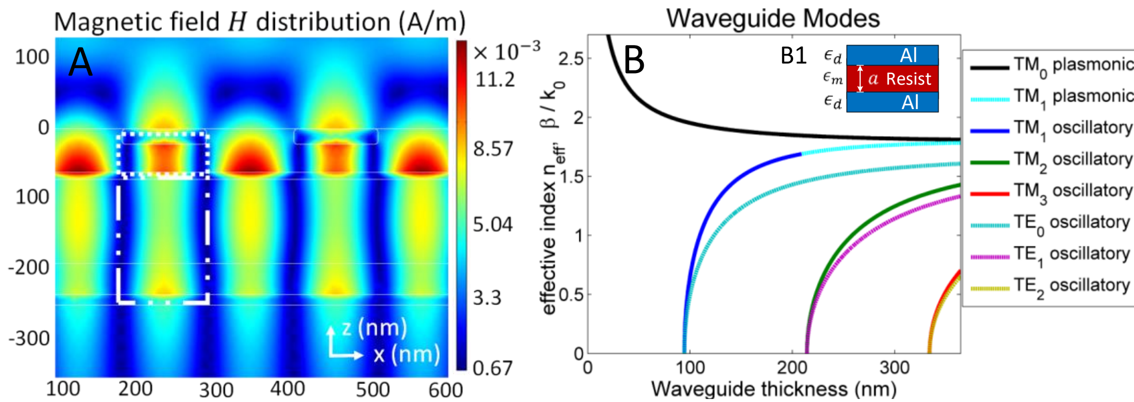

Figure 11 Mode analyses of the plasmonic lithoraphy system.
(A) Magnetic field distribution of the proposed design. The dotted line indicates an optical cavity formed in the grating-spacer-Al layers, while the dash-dot line indicates the PMMA-Al-Resist-SiO_2-Al waveguide mode. (B) The Al-resist-Al waveguide modes with the corresponding waveguide sketch on the upper right (B1).

$$\alpha_d a = 2\text{arctanh}\left(-\frac{\epsilon_d \alpha_m}{\epsilon_m \alpha_d}\right) \tag{15}$$

$$\alpha_{\mathrm{d}} a = 2\mathrm{arctanh}(-\frac{\epsilon_{\mathrm{m}}\alpha_{\mathrm{d}}}{\epsilon_{\mathrm{d}}\alpha_{\mathrm{m}}}) \quad (16)$$

$$\kappa_{\mathrm{d}} a = (m-1)\pi + 2\arctan(-\frac{\epsilon_{\mathrm{m}}\kappa_{\mathrm{d}}}{\epsilon_{\mathrm{d}}\alpha_{\mathrm{m}}}) \quad (17)$$

$$\kappa_{\mathrm{d}} a = m\pi + 2\arctan(\frac{\alpha_{\mathrm{m}}}{\kappa_{\mathrm{d}}}) \quad (18)$$

where $\alpha_{\mathrm{d}} = (\beta^2 k_0^2 - \epsilon_{\mathrm{d}} k_0^2)^{\frac{1}{2}}$ for plasmonic mode, $\kappa_{\mathrm{d}} = (k_0^2\epsilon_{\mathrm{d}} - \beta^2 k_0^2)^{\frac{1}{2}}$ for oscillatory mode, and $\alpha_{\mathrm{m}} = (\beta^2 k_0^2 - \epsilon_{\mathrm{m}} k_0^2)^{\frac{1}{2}}$, a is the thickness of the waveguide and β is the propagation constant of the waveguide mode. The propagation constant β is defined as the ratio between the propagating wavevector and normal wavevector $\beta = k_x/k_0$, which characterize the effective mode index n_{eff} of the waveguide. ϵ_{d}, ϵ_{m} are the dielectric constants of PR ($\epsilon_{\mathrm{d}} = \epsilon_{\mathrm{PR}}$ =2.8568) and Al ($\epsilon_{\mathrm{m}} = \epsilon_{\mathrm{Al}}$ = -24), respectively. No loss is considered in the dispersion relation shown in Figure 11B where the illustration of the first six modes of Al-Resist-Al system at the wavelength of λ = 405 nm is displayed. The number of modes supported by the waveguide increases with the waveguide thickness a and the effective index variation as the waveguide thickness changes is displayed in Figure 11B. The plasmonic modes have imaginary k_z and hyperbolic sine or hyperbolic cosine field distributions in the PR core while the oscillatory modes have real k_z and sine or cosine distributions. The hybrid TM_0 and TM_1 mode in the PMMA-Al-Resist-SiO_2-Al waveguide system forms a strong resonance since the lossy metal layers are very thin.

2.3 Fabrication and experimental setup

2.3.1 Nanofabrication of mask and substrate

The fabrication procedures of the glass mask and PET substrate are illustrated in Figure 12. An 1-

D Si grating with a period of 245 nm was prepared as a mold to generate mr-I resist patterns by thermal nanoimprint [11,22,59] lithography (NX-2000 Nanonex). Nanoimprinting lithography is used to make the photomask because it can create desired patterns over a large area with low cost. The residual layer of the imprinted mr-I resist was removed by subsequent reactive-ion etching (RIE) followed by angled evaporation of 10 nm titanium (Ti) and e-beam evaporation of 22 nm Al. After lift-off in acetone, Al grating with 245 nm period (around 50% duty cycle) and height of 22 was obtained on glass. A thin 40 nm PMMA layer was spin-coated on top of Al grating as a spacer, which was flattened by the imprinter to so that a thin and flat 10 nm Al could be sputtered. After the sputtering, mask fabrication was completed. For the preparation of the substrate, regular PET films were planarized by spin coating of a 10 μm thickness SU-8 resist, and followed by 15 nm Al sputtering and 44 nm SiO_2 evaporation. The PR used in the experiment is 1:1 diluted AR-N 7500 positive resist at 405 nm wavelength illumination. The diluted PR layer with 100 nm thickness was spin-coated on the SiO_2 layer, and soft baked on a hot plate at 85 °C for 1 minute.

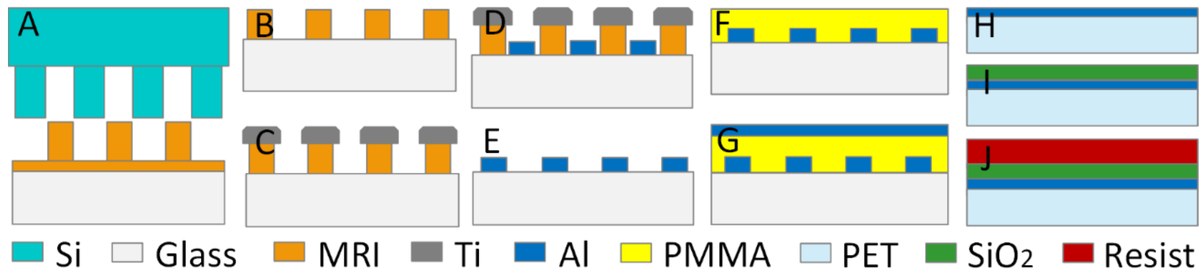

Figure 12 Fabrication process flow of masks on transparent glass substrate.
(A-G) and PR on SU-8 planarized PET flexible substrate (H-J). (A) Transfer of patterns from a Si mold to mr-I resist by nanoimprint lithography (B) mr-I patterns after RIE (C) Ti by shadow evaporation (D) Al by evaporation (E) Lift-off. (F) PMMA spin coating and planarization (G) Al by sputtering (H) Al sputtered on planarized PET (I) SiO_2 by evaporation (J) PR by spin-coating.

2.3.2 Exposure system

Once the mask and the substrate were prepared, they were put in conformal contact to ensure the near field exposure, as shown in Figure 13A and B. Since the Al grating is protected by the PMMA

spacer and the Al layer, it suffers much less damages and is expected to have a longer life time as compared with typical contact photolithography approaches such as conventional near field lithography [2,12] and nanoimprint lithography. The optical setup built to ensure the conformal contact is shown in Figure 13B. The mask and PET substrate coated with a PR layer were placed between a clean glass slice and a thick polydimethylsiloxane (PDMS) cushion on a flat stage. Conformal contact can be realized since both mask and substrate have flat surface while PET film and PDMS cushion are flexible. Two screws were used to provide pressure when tightened to ensure conformal contact during the light exposure. Collimated 405nm TM polarized diode laser (ONDAX x6474) light with its electric field perpendicular to the grating direction was incident to the mask through a circular aperture with diameter of ~1 cm. The laser intensity was set at 3 $mW \cdot cm^{-2}$ and the exposure last for 15~20 seconds. Finally, the resist on PET was taken out and immersed in 1:1 diluted AR 300-35 developer for 45~50 seconds, followed by 30 seconds deionized (DI) water rinse. Once the mask and the substrate were prepared, they were put in conformal contact to ensure the near field exposure, as shown in Figure 13A and B. Since the Al grating is protected by the PMMA spacer and the Al layer, it suffers much less damage and is expected to have a longer life time as compared with typical contact photolithography approaches such as conventional near field lithography and nanoimprint lithography.

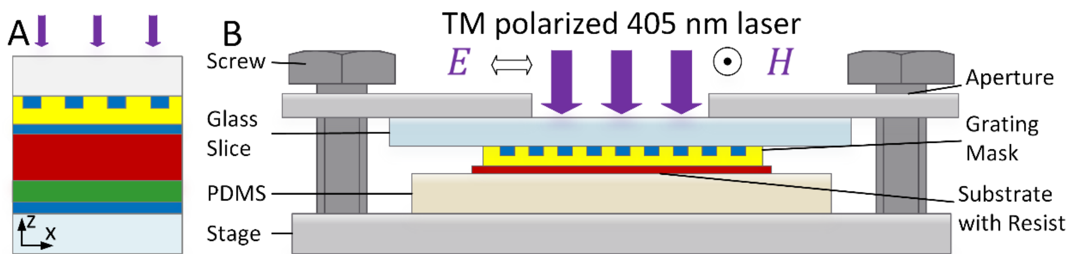

Figure 13 Exposure setup of the plasmonic lithography system.
(A) Conformal contact of mask and substrate (B) schematic of the optical setup with electric field of the laser light polarized across the grating.

2.4 Results and discussions

2.4.1 Experimental conditions

Figure 14 shows the scanning electron microscopy (SEM) image of the resulting patterns obtained on the PR with thickness of 100 nm. Large-area subwavelength periodic structures were obtained with approximately 55 nm linewidth, which is less than 1/6 of the light wavelength. The period of the pattern is 122.5 nm, which is 1/2 of the grating mask, and the aspect ratio is around 2:1, significantly improved over previously reported results. Multiple samples were prepared with the same experimental conditions and good large-area uniformity was achieved consistently. Each sample is 1.5 cm×1.5 cm in size while the patterned area has a diameter of ∼1 cm determined by the laser beam size used in the optical setup, and the uniformity is confirmed by SEM and optical microscopy characterizations.

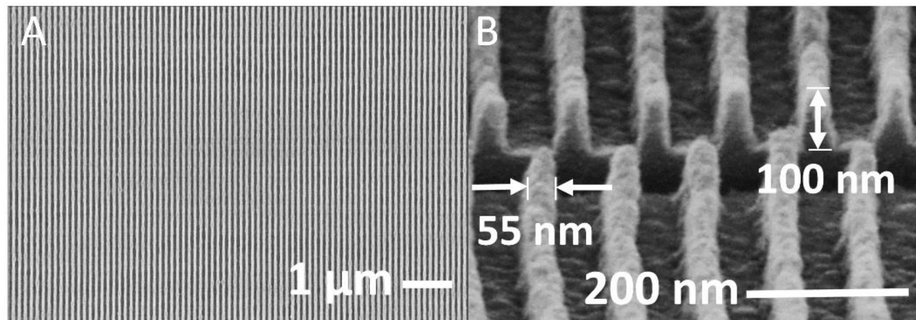

Figure 14 SEM images of 100 nm thickness PR.
(A) Top view which shows large area uniformity. (B) Cross section. The image was taken at 30° angle and the marked dimensions have been converted into that at the normal view.

Figure 14B is the corresponding cross section view of the pattern, and the approximately rectangular profiles were observed which verified our design principle. The labeled height of the PR pattern was obtained by considering the viewing angle of the SEM to avoid confusion. The SiO_2 and Al layer underneath the PR can function as a hard mask if subsequent etching process is needed to transfer the pattern into features with even higher aspect ratio on the substrate. The

flexible substrate was cleaved by a sharp razor blade to ensure a clean cut across the resist patterns as the resist was spontaneously broken by the pressure of the cutting. Along the lines there is tiny roughness, which can be attributed to the defects on the mask including the roughness along the grating and the deposited thin films (*e.g.,* the thin Al film), as well as the limitation of the sensitivity, resolution and contrast of the chosen PR at the exposure wavelength. In comparison, due to the low intensity contrast, the interference of multiple modes and the exposure of the shallow surface wave, the previously reported [13,15,24,29,54,55] patterns made experimentally by plasmonic lithography could only obtain localized uniformity in micron-scale and the patterns were much shallower (*e.g.,* periodic subwavelength patterns usually ~ 50 nm height at 365 nm light illumination) than the ones achieved in this work.

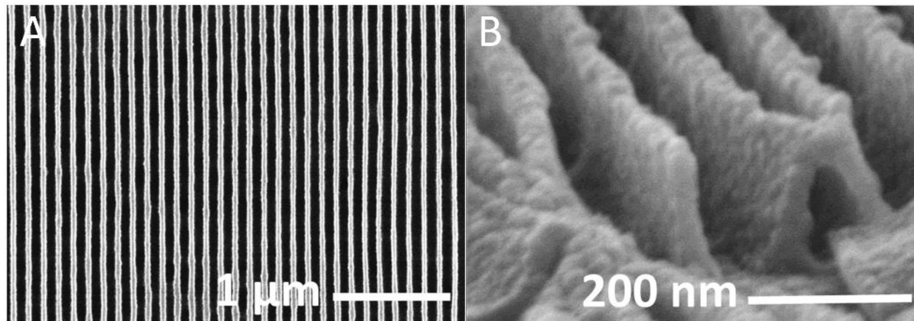

Figure 15 SEM images of the 200 nm thick patterned PR.
(A) Top view of the uniform PR patterns. (B) Corresponding cross section view of the patterns from 30° angle. The profile and thickness of the resist are shown.

To study the impact of the resist thickness, PR with thickness of 200 nm was also tested aiming for even higher aspect ratio patterns. Figure 15 shows the SEM images of the resulting pattern on such PR. To accommodate the increased thickness, longer exposure time of 40~50 seconds and develop time of 90~105 seconds were used while other experimental conditions remained unchanged. The exposure laser had 30 mA current and 30 mA current and 3 $mW \cdot cm^{-2}$ power. As shown in Figure 15A, uniform patterns with the same half-pitch of 61.25 nm were achieved. Figure

15B is the cross section of the patterns taken at 30° angle, showing higher aspect ratio patterns. However, the patterns collapsed due to reasons, such as the surface tension of the liquid during the develop and rinsing, the weak mechanical strength of the thicker resist used during cutting or damaged by the electron beam while performing SEM characterization.

2.4.2 Partially polarized light

We also explored the effects of light polarization on the proposed plasmonic lithography system. When the polarization varies, the shape of the pattern also changes accordingly. Figure 16 A and B show the top view and the cross-section view SEM images of the resulting patterns illuminated by the light which is 30° partially TM polarized at 405 nm wavelength. The partially TM polarized light can be decomposed into TM and transverse electric (TE) *i.e.* electric field along the grating lines, which excites both TM and TE modes in the PR. Because of the momentum mismatching, the TE mode is much weaker, which results in double period patterns with tapered profiles. In Figure 16B, some of the patterns are shallower than the other, which confirms that the field distribution along the vertical direction is not uniform throughout the PR. Whereas, for totally TM polarized light, the periodic patterns are uniform. This experiment confirm the polarization dependence of SPP.

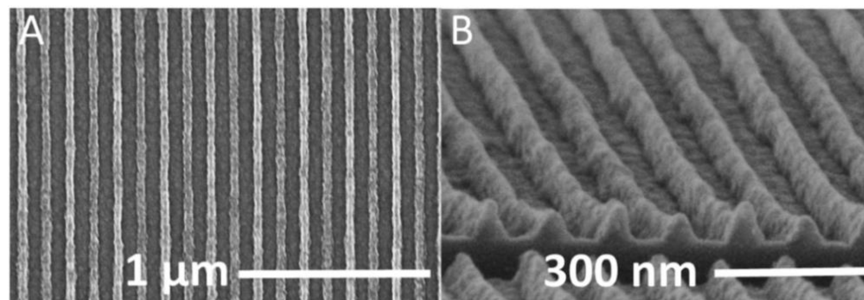

Figure 16 Experiment for partially polarized light.
(A) Top view and (B) Cross section view of SEM images of 100 nm PR under 30° partially TM polarized light illumination. The patterns show double periods with tapered profile.

2.4.3 Double exposure

Two dimensional patterns can be obtained by exposing PR twice with TM polarized light along two perpendicular directions, *e.g.* x-axis and z-axis. As shown in Figure 17C, the patterns have the same period as the single exposed ones but with a slightly smaller duty cycle and shallower depth. Under such conditions, the edge roughness is more severe due to the accumulated effects and defects in the double exposure. It can be expected that more complicated two-dimensional patterns can be achieved by multiple exposures or multiple beam interference with the electric field polarized along different orientations. Double patterning technique [60,61] with alignment can be exploited to further reduce the half-pitch of patterns. The design criteria such as frequency selection and back reflector can also be applied in the non-contact waveguide lithography systems [62–64] to improve its pattern depth, pattern profile and uniformity.

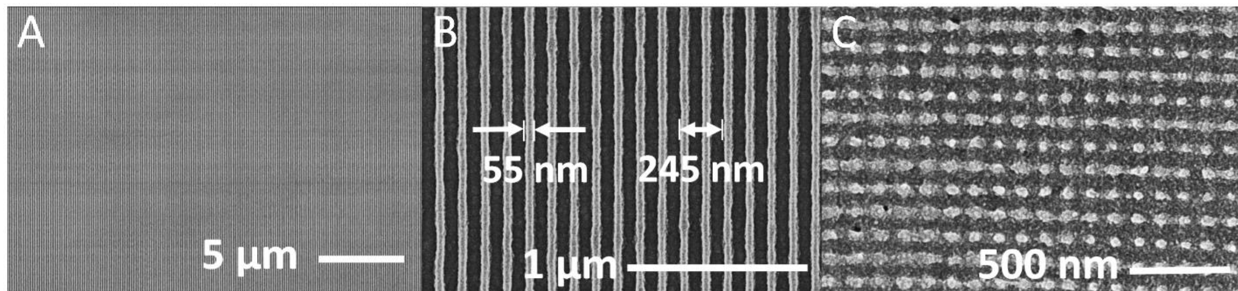

Figure 17 Experimenatal 2D patterns by double exposure.
SEM images of PR with 100 nm thickness. Top views of the single exposure patterns (A) over an area of ~24×18 μm^2 and (B) over a small area showing details, and (C) double exposure pattern. The defects accumulated and the patterns are rougher in double exposure.

2.4.4 Applications

If we expose the PR with TM polarized light twice in two perpendicular directions, for example, on along x-axis and the other one along z-axis, we can obtain the 2-D patterns, as shown in Figure 18 (a) and (b). The resulting patterns keep the same period as the 1-D patterns, with slightly larger duty cycles and shorter depth. The effects of the roughness are more severe in this case, since the

same PR film was exposed twice. Our samples appear dark grey color, so it can potentially find its application as anti-reflective films. Glass usually reflects about 4% of visible light from its surface. This reflection is not desirable when viewing images on displays (TVs, computers, tablets, cell phones, *etc*.), especially when doing so outdoors under bright sunlight. The reflection also serves as a disturbing factor in buildings, when sun, street lights and car lights are reflected from glass office buildings or storefront windows. [9,65,66] By double exposure in orthogonal directions, two-dimensional (2-D) subwavelength cone-shape nanostructure with acceptable height can be achieved. The 2-D cone nanostructures can eliminate the reflection since the light sees the surface as having a continuous refractive index gradient between air and the substrate [9,65]. The present approach has the potential in replacing the anti-reflection coatings of multi-layers.

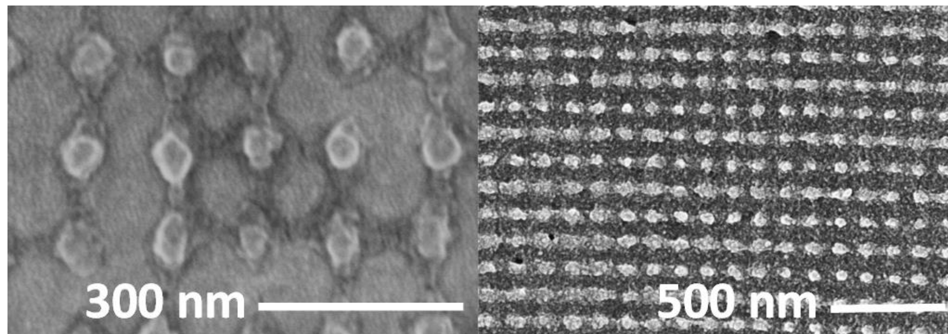

Figure 18 SEM images of 100 nm thick patterned photoresist after double exposure.
(a) top view of the photoresist showing the effects of the roughness on the mask. (b) top view of a relative large area.

Figure 19 (a) is a schematic of such anti-reflective coating. We exposed the resist twice in orthogonal directions in order to get the cone shape structure. The field distribution is optimized *via* simulation while the exposure and development processes are carefully controlled to reach desired experimental results. Figure 19 (b) is the SEM image of the tapered PR on the PET substrate from the experiment. The pattern consists of a series of bumps, each roughly 80~100 nm in height and period of approximately 122 nm, which are all subwavelength. The pattern can be

transferred onto glass surface by UV curable nanoimprint. Figure 19 (c) is a reflection-type optical microscope image of the photoresist pattern. The dark region with width of 50 microns corresponds to the patterned photoresist and the relative brighter background is the unexposed photoresist. Figure 19 (d) shows the reflection spectrum of the 2D periodic structure from simulation. The periodic bumps with 200 nm height can reduce the average reflection from 4% to 0.29%. The resist patterns can also serve as the mask for the fabrication of wire grid polarizer [33] and other nanoscale colored panels [67]. Furthermore, similar to roll to roll lithography [68–71], the proposed plasmonic lithography essentially a contact lithography technique suitable for flexible mask system. By using Al grating on a flexible mask to replace the glass mask, the roller based plasmonic interference nanolithography can be realized to enhance the throughput.

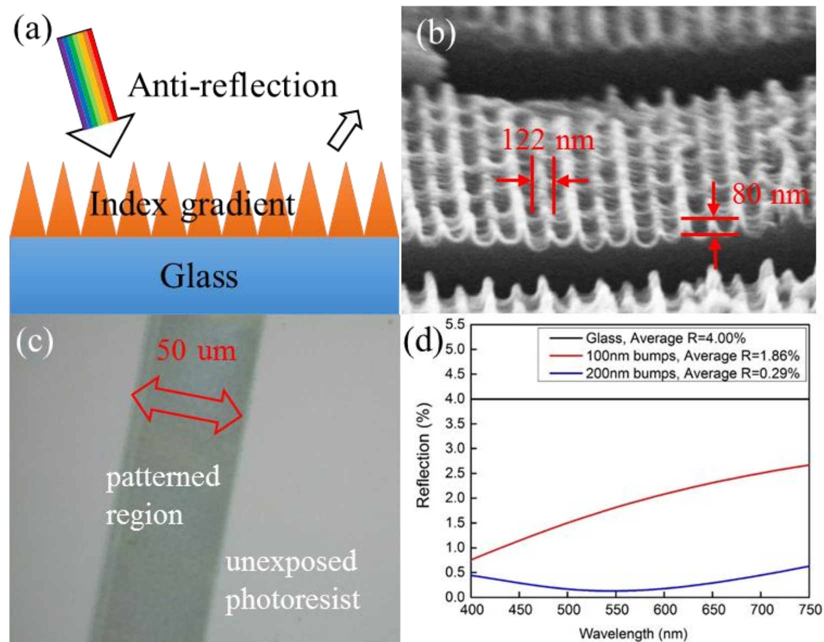

Figure 19 Applications of the pattern as an anti-reflective film.
(a) The schematic of the anti-reflection coating. (b) A SEM image of the photoresist on the PET substrate. (c) An optical microscope image of the photoresist pattern. The dark region corresponds to the patterned area.(d) The reflection spectrum of the 2D periodic structure in simulation.

2.5 Other cases

2.5.1 Effects of film roughness

In reality, planar films are not atomically flat due to the deposition process and the roughness of the underlying layers, which effect the line edge roughness of the pattern of the PR. Figure 20 A, B and C show the atomic force microscopy (AFM) height images of 15 nm thickness Al on Si substrate, PMMA layer and thick SU-8 layer, respectively. The root mean squared (RMS) roughness R_{rms} of the three films are 0.880 nm, 0.936 nm and 1.89 nm. By including the surface roughness of the Al and PR films in three-dimensional (3-D) simulation, it is possible to analyze its effect on pattern qualities, especially the line edge roughness in our experimental results.

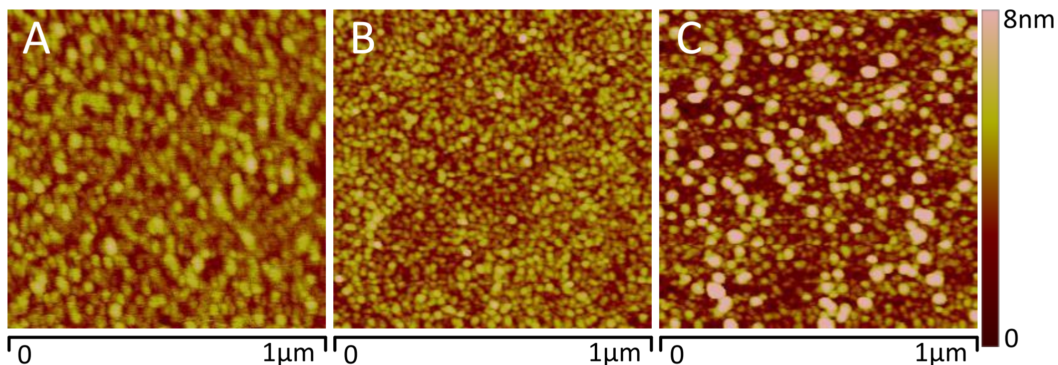

Figure 20 Roughness of 15 nm Al films.
AFM images scanning over 1 μm^2 region showing the roughness of 15 nm Al on (A) Si substrate (B) PMMA layer (C) SU-8 layer. Colored scale bar is on the right.

Figure 21 shows the simulated (COMSOL 4.4) electric field distribution in the PR (cut a horizontal plane in the middle of the PR) for the planar films in the design with different surface roughness. As shown in Figure 21A, for perfectly smooth planar films, the periodic lines are parallel with each other and straight with no line edge roughness. For films with maximum ~ 2 nm R_{rms} according to the AFM data, as shown in Figure 21B, the line edge roughness starts to affect the pattern uniformity and the pattern looks similar to the experimental results. For the films with 4 nm R_{rms} as shown in Figure 21C, line edge roughness becomes more severe (up to 1 nm),

degrading the uniformity, field contrast and the parallelism of the patterns. With improved instruments and tighter process control, film roughness issue can be addressed, which can ensure the uniform linewidth in the patterned PR.

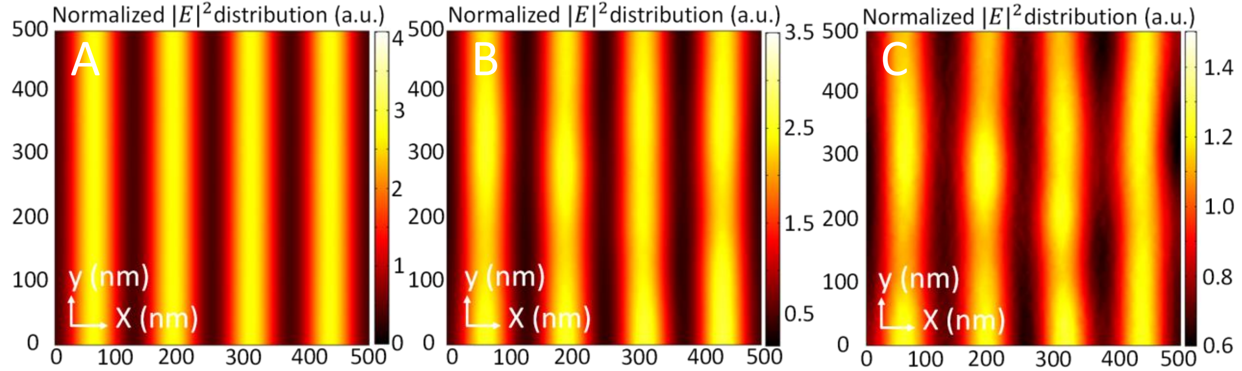

Figure 21 Simulated electric field distribution in xy plane.
Distribution with (A) smooth planar films (B) films with maximum ~2 nm R_{rms} set according to the AFM data (C) films with 4 nm R_{rms}.

2.5.2 Waveguide lithography at 365 nm and 436 nm

The approach described above is general and can be applied to other UV wavelengths. Here we provide designs for i-line and g-line light sources. Similar to 405 nm (h-line) case, at 365 nm (i-line) and 436 nm (g-line), periodic patterns can be generated in the PR with single high-k modes and the waveguide coupling strategy. For 365 nm, the mask consists of Al grating with 220 nm period and other parameters are the same as those in 405 nm design. The substrate is composed of 215 nm PR, 50 nm SiO_2 and 15 nm Al layer stacked on PET sheet. Whereas, for 436 nm, the optimal period for the grating is 264 nm and the PR thickness can be as high as 275 nm. Their simulated field distributions in xz plane are shown in Figure 22A and B. The aspect-ratios of the patterns working at 365 nm, 405 nm and 436 nm are close to 4:1 and nearly identical. The effective indices n_{eff} in the three cases are 1.659, 1.653 and 1.6515, respectively, consistent with the dispersion relation of the SPP wave.

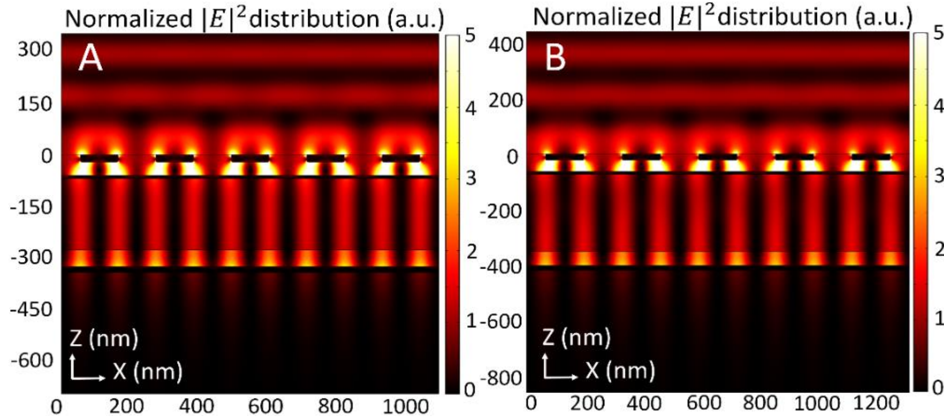

Figure 22 Field patterns at other wavelengths.
Normalized $|E|^2$ maps in xz plane at wavelengths of (A) 365 nm and (B) 436 nm. Thickness of the PR are 215 nm and 275 nm, respectively and incident electric field is 1 $\mathrm{V/m}$.

2.5.3 Extremely small patterns using 193 nm and 248 nm light

Besides making high aspect-ratio patterns, by using plasmonic waveguide coupling strategy, even smaller patterns can be achieved by modifying the thickness of metal, dielectric and PR layers. Such examples are demonstrated by simulations with shorter wavelength including 193 nm (ArF) and 248 nm (KrF) light illuminations and thicker Al layer, as illustrated in Figure 23A, B and C (COMSOL 4.4). The geometric parameters that are used in common by the three cases are as follows: grating thickness is 22 nm, grating duty cycle 50%, PMMA spacer thickness 20 nm, top Al 20 nm, and bottom Al 30 nm. For 193 nm wavelength as in Figure 23A, grating period is 52 nm and PR thickness 20 nm; for 248 nm as in Figure 23B, grating period is 110 nm and PR thickness 60 nm; for 405 nm lithography as in Figure 23C, grating period is 205 nm and PR thickness 100 nm. In each case, grating period and PR thickness differs, leading to different half-pitches 13 nm, 27.5 nm and 51.25 nm, and all of these patterns are deep subwavelength. The effective indices n_{eff} of the three are 3.71, 2.25 and 1.98, following the trend of SPP dispersion. The effective indices are much larger than the index of PR, therefore, the wave decays along z direction in the resist, scarifying the depth of the pattern.

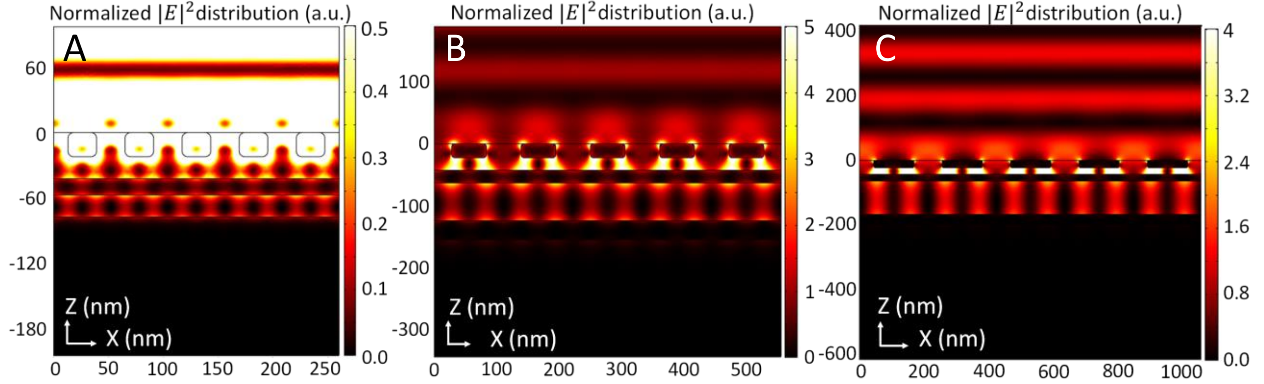

Figure 23 Simulated electric field distribution for extremely small patterns.
Electric field distribution at a wavelength of (A) 193 nm (B) 248 nm and (C) 405 nm.

2.5.4 Using high-index dielectrics for lithography

The waveguide design implements the basic idea of spatial frequency selection, and these principles can be applied to designs with various materials. Other than metals as plasmonic components, high index dielectrics can also be used to realize subwavelength confinement [72]. Dielectric materials have been reported to have nanoscale light confinement [72]. Therefore, the materials used for the waveguide can be substituted by high index dielectrics, such as TiO_2. One such design (Figure 24 (a) inset) is composed of 40 nm thick chromium (Cr) grating with 0.7 duty cycle on a glass substrate, followed by 50 nm thick PMMA spacer, 50 nm TiO_2, 100 nm photoresist, and 50 nm TiO_2 on glass substrate. By treating the TiO_2 which has the highest index as the core, and other low index materials as claddings, two coupled waveguides are formed, with photoresist as the claddings and coupler of the waveguides. The effective index n_{eff} of the waveguide is 1.89 in this case, which is smaller than the index of TiO_2 and larger than that of other materials. Figure 24 (a) illustrates the wave supported by this lithography system, at 405 nm, where n_{eff} is around 1.7~2. Figure 24 (b) shows the simulated field distribution (COMSOL 4.3), with a subwavelength standing wave propagating throughout the photoresist. To satisfy the phase matching condition, $\lambda/\Lambda \sim n_{eff}$, first we need to calculate the modes of the multilayer system to get an approximate

spatial frequency range. Then numerical simulations are employed to sweep the parameters including the grating period and the thickness of the multilayer stacks to achieve an optimal condition. In this case, the optimal period of the Cr grating is found to be 214 nm, generating patterns with period equal to 107 nm.

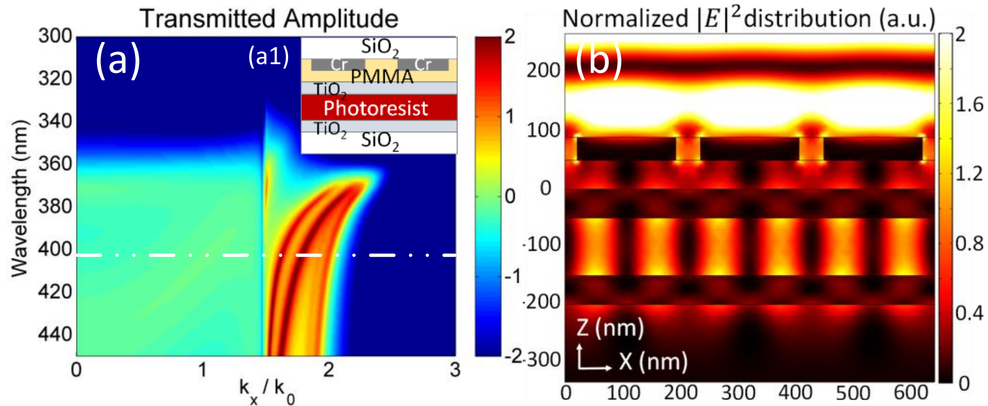

Figure 24 Lithography system using dielectrics.
(a) Transmitted amplitude of PMMA-TiO_2-resist-TiO_2 multilayer system in terms of k_x/k_0 and wavelength. The inset shows the schematic of the proposed design. (b) The corresponding simulated results of TiO_2 based interference lithography system. The bright periodic patterns are supported throughout the PR.

The principle can be applied in other high index materials such as gallium phosphide (GaP), as well as other wavelengths. Compared with Al-based lithography system, the evanescent wave transmitted band is broader, so that required period tolerance is larger. However, the pattern uniformity, contrast, and depth are worse. Furthermore, the spatial frequency selection principle can also be applied in the waveguide lithography [62–64] to improve the uniformity.

2.5.5 Comparison with direct contact lithography

Other than plasmonic interference lithography, patterns can be made by direct contact lithography exploiting near field. One such design is shown in Figure 25, which is composed of 22 nm thickness Al grating with 50% duty cycle directly in contact with 250 nm PR. Figure 25 A gives the simulated field distribution (COMSOL 4.4) with a wave propagating in the PR, showing the

excitation of SPP wave of the Al grating. Compared with Al based plasmonic waveguide lithography system with waveguide coupling, while the size of the patterns generated by this method is the same, both the field contrast and uniformity along the vertical direction are degraded, as shown in Figure 25B. As a result, it is not suitable for use in realistic application that requires features with high aspect-ratios.

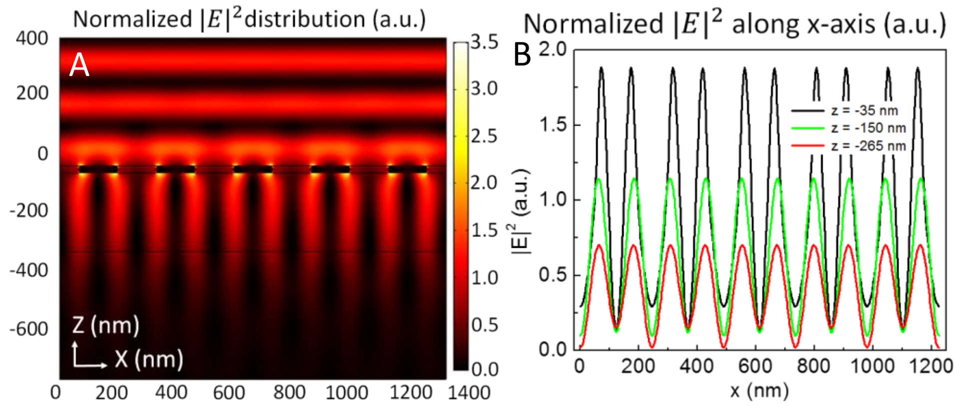

Figure 25 Field distribution of direct contact lithography for the PR with 250 nm thickness. Electric field distribution (A) in xz plane (B) along horizontal lines at z = -35, -150 and -265 nm.

2.6 Plasmonic roller system

There is growing interest in novel lithography technologies capable of generating patterns continuously with high yield, such as roll-to-roll nanoimprint lithography (R2RNIL) [68,69] and photo roller lithography (PRL) [70,71,73], which allow us to produce patterns continuously with high yields. Between these two approaches, PRL has relatively higher reproducibility, reliability than imprint-based lithography and the pre- and post-processes of photolithography are more mature. [73] In addition, PRL allows a continuous process with a linear UV light source and a flexible photomask, which can create large-area flexible electronic and photonic devices. Despite recent advancements in PRL [70,71,73], the photo-roller systems is still limited to making micron scale pattern by using regular UV light. To meet the increasing demand in flexible devices, PRL system needs to be extended to become a continuous process for large-area patterning while

maintaining high resolution. In this work, we demonstrated that the resolution of PRL can be enhanced to nano-scale by combing it with plasmonic waveguide lithography that was developed in Chapter 2. Meanwhile, by using flexible substrates and rolling the mask, the subwavelength patterns can be printed continuously in large area, which greatly improves the throughput of the planar plasmonic lithography systems.

2.6.1 Design principle of plasmonic roller system

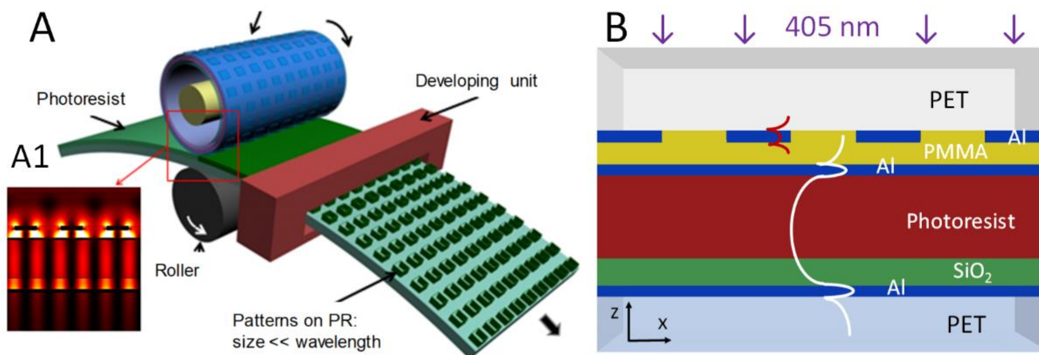

Figure 26 Schematic of plasmonic roller system.
(A) The schematic of the plasmonic roller system (A1) The light distribution of the plasmonic system. (B) Design of the waveguide plasmonic lithography system and PR film on the flexible PET substrates illuminated by 405 nm laser light.

In the planar plasmonic lithography system, substrate is made of glass, and the patterns are uniform in large scale with high aspect ratio. By using flexible substrates for both the photomask and PR, the nano-scale patterns can be formed in plasmonic roller system using the same principle. As shown in Figure 26, a flexible PET photomask is mounted on the roller system with exposure and developing unit. We use the same design as the waveguide lithography based on Al, where the plasmonic photomask based on Al grating has a period of 245 nm (details can be found in Chapter 2). The electric field distribution of the plasmonic waveguide lithography system is shown in Figure 26A1 and principle of the coupling is shown in Figure 26B. Different from the planar system, the photomask is made on a flexible PET substrate to be implemented on transparent quartz

cylinder. Upon illumination of TM polarized 405 nm UV light, when the mask and the resist are in conformal contact, the patterns on the mask can be imaged onto the PR. By rolling the mask and moving the substrate on the stage, the patterns generated in the optical waveguide can be printed continuously in large area with high speed.

2.6.2 Fabrication of the flexible mask and experimental setup

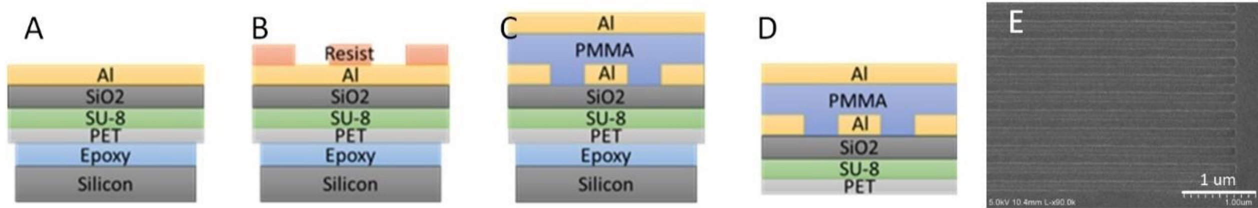

Figure 27 Fabrication of the flexible Al photomask.
(A) Deposition of Al on a flat PET substrate glued on a Si piece. A few additional layers are used to make the PET flat and smooth. (B) EBL to fabricate the resist pattern. (C) Fabrication of Al grating by RIE, spin coating of the spacer and deposition of an additional Al layer. (D) Peel the PET substrate off the Si wafer. (E) SEM image of the periodic Al grating on PET. The grating has period of 245 nm and 0.5 duty cycle.

To fabricate the flexible photomask with subwavelength features, we developed a special process as shown in Figure 27. The mask needs to be flat and smooth in order to create Al grating with period of 245nm. 3cm × 3cm PET and Si pieces were cleaned by acetone and IPA in ultrasonication bath for over 10 mins, followed by DI water rinse and dry. Then the PET piece was glued onto Si substrate by NOA 73 epoxy. In this step, a small amount of NOA 73 epoxy was carefully drop on top of clean Si substrate, and slowly covered by the PET piece to avoid air bubbles. The epoxy glue was cured for over 5 mins by UV light source, and the residue on the bottom side of the Si was cleaned by acetone and IPA. To make the top surface of the PET piece flat, a SU-8 2010 film was spin coated with 3000 RPM for 30s. The SU-8 layer was soft baked at 65C for 1 minute, and exposed by UV light for around 5 mins, followed by a hard bake at 95C for another 5 mins. The piece was further cured at 180C for 5mins before deposition of 100 nm SiO_2

and 22 nm Al. PMMA A4 was spin coated on the Al and patterned by electron beam lithography (EBL). RIE (LAM 9400) was used to etch Al patterns. PMMA spacer with thickness of 45 nm was spin coated and another layer of Al of 10 nm thickness was deposited on the planar spacer. The PET piece was peeled off the Si substrate to be used the photomask. The SEM image of the Al grating on PET is shown in Figure 27E, with 245 nm period and 0.5 duty cycle.

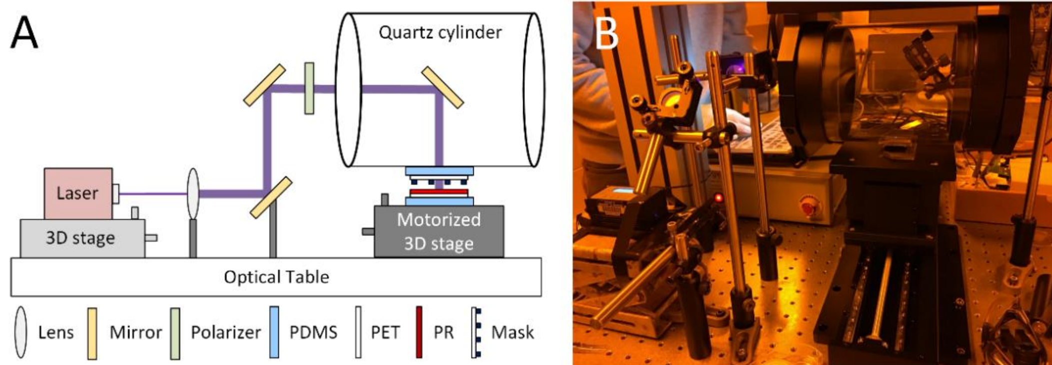

Figure 28 Optical setup of the roller system in the lab.
(A) Roller system of a transparent quartz cylinder and motorized stage (B) a photo of the setup.

We built an optical setup in the lab, as shown in Figure 28A and B. The setup of the plasmonic roller equipment consists of three parts: a substrate translation stage, a UV light exposure unit, and a developing unit. A 150 mm-diameter quartz cylinder with a thickness of 3 mm is supported by an aluminum profile in the UV light exposure unit. The edge of the quartz cylinder was installed with a ball bearing to facilitate rolling. The 405 nm polarized diode laser (ONDAX x6474) is mounted on a 3D stage. The light incident from the laser is collimated by a lens and reflected by several mirrors and directed to the quartz cylinder. Before the light entering the cylinder, a linear polarizer is used with the polarization orientated along the horizontal direction. The polarized light is reflected by a mirror mounted inside the cylinder. The photomask is made of 245 nm periodic Al grating and coated PMMA spacer and another 10 nm Al. The PR coated on a PET substrate is mounted on a linear motorized stage. The height-adjustable stage was assembled on a motor-driven

moving stage to obtain three degrees of freedom. This assembly moved at the speed of 1–24 mm/s and was controlled by a step motor system. The photomask and PR coated substrate are supported by thin adhesive polydimethylsiloxane (PDMS) films for conformal contact when the photomask was attached to the quartz cylinder. Contact between the stage and the quartz cylinder occurred when the PR-coated substrate passed through the UV light exposure unit. AR 7500 positive resist is used for exposure, and then developed in 1:1 diluted AR 300-35 developer for 60s.

2.6.3 Stress on the roller system

When the substrate and the mask in the roller system are moving, constant stress is being applied on the substrate, which might affect the light distribution in the PR layer. In this section, we evaluated this stress and the associated photoelastic properties of the PR film. As shown in Figure 29A, the transparent quartz cylinder has a diameter D of 150 mm with a thickness of 3 mm. The photomask and photoresist on the PET films are mounted on PDMS cushions with the thickness T of ~ 5 mm. The PET film has a thickness of 100 ~ 200 µm and the PR layer has a thickness t of 100 nm. The thickness of the PET mask and PR layer is negligible compared to that of PDMS cushions. Therefore, only the deformation of the PDMS cushions are taken into consideration in estimating the stress on the PR layer. Based on the experimental setup, the area of PDMS cushions in contact is $A = W \times L$ = 5 mm × 40 mm. The angle of the contact region is $\theta = W/\pi D$ ~ 3.82°, which is quite small. Thus, we can treat the PDMS cushions as flat surfaces during the contact exposure. The PDMS cushions have a Young's modulus E of ~ 1.8 MPa, [70,74] and the deformation in thickness δT of the PDMS cushions during the movement of the stage and the cylinder can be estimated to be ~ 1 mm. The strain on the PDMS cushion is $\mathcal{E} = \delta T/T$, and the corresponding stress is $\sigma = F/A$, where F is the force and A is the contact area. According to the

definition of elastic modulus $E = \sigma/\mathcal{E}$. The force on the PR layer can be calculate as $F = EA\delta T/T$ ~ 72 N and the stress on the sample is $\sigma = E\delta T/T$ ~ 3.6×10^5 Pa.

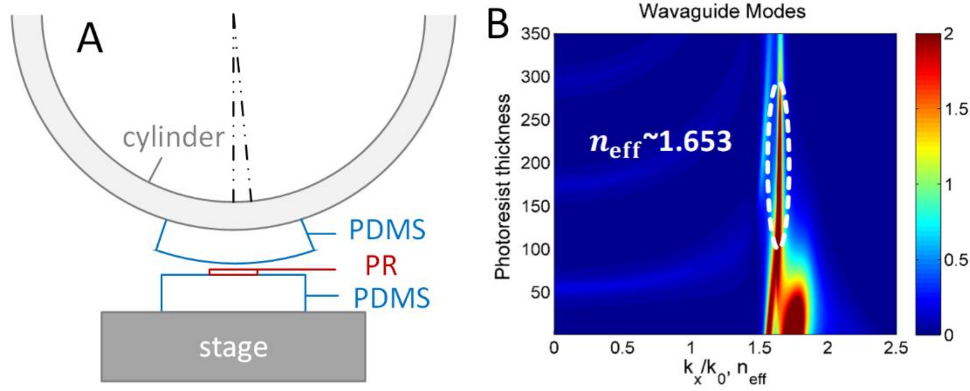

Figure 29 Stress analyses and photoelasticity of the PR film.
(A) Schematics of the quartz cylinder (B) Thickness independence of the PR layer.

By treating the thin PR layer as an isotropic medium, two-dimensional photoelasticity is applicable and the magnitude of its relative retardation is given by the stress-optic law [75]

$$\Delta = \frac{2\pi t}{\lambda} C(\sigma_1 - \sigma_2) \tag{19}$$

where Δ is the induced retardation, C is the stress-optic coefficient, t is the PR thickness, λ is the vacuum wavelength, and σ_1 and σ_2 are the first and second principal stresses, respectively. The exact value of the stress-optic coefficient of the PR film used in the experiment is not reported to the best of our knowledge, thus the typical value of polystyrene (PS) C ~ 1×10^{-10} Pa^{-1} [76] is used for the estimation of the photoelasticity. In fact, the stress-optic coefficients of polymer films including PS, polycarbonate (PC) and cyclo olefin copolymer (COC) are quite similar. Hence the index change of the film due to the stress can be estimated as $\delta n = C \cdot \sigma$ ~ 3.6×10^{-5}, which is negligible compared to the refractive index of PR n_{PR} ~ 1.69. As shown in Figure 29B, when the thickness of the PR varies from 100 nm to 300 nm, the effective mode index n_{eff} remains the same.

Since the Al film in the lithography system has losses, the quality factor (Q-factor) of the waveguide mode is low, therefore providing higher tolerance for the index change. The induced retardation due to the stress can be calculated as $\Delta = 2\pi t C\sigma/\lambda \sim 5.6\times10^{-5}$ rad across the whole resist layer, which is far less than $\pi/2$. Because of the weak PR thickness dependence, this tiny phase retardation should not affect the interference of light. Therefore, we conclude that despite of the constant stress from the roller during the exposure, the light distribution in the PR remains unchanged and uniform.

2.6.4 Results and discussions

Continuous nano-scale patterns are successfully produced using our plasmonic roller system, as shown in Figure 30. The photomask mounted on PDMS in the PRL is illustrated in Figure 30A, and the SEM image of the pattern is shown in Figure 30C. The patterns are composed of parallel lines with the linewidth around 50 nm on PR with thickness of 100 nm, which is comparable to the result of waveguide lithography system discussed in Chapter 2. Since the mask is currently made by EBL, the scale of the patterns is 2 mm ×1 mm, the corresponding photo of the mask and resist under microscope is shown Figure 30B and D, respectively. If larger pattern is desired, the width can be readily extended by increasing the size of the mask and laser beam. However, the length of the final pattern is determined by the motion of the motorized stage.

In this preliminary work, we used the photomask on PET made by EBL; however, the mask can also be made by nanoimprint lithography or photolithography to achieve an Al grating over a larger area. Plasmonic photo roll lithography is possible with custom-built equipment to print large-scale patterns continuously with high-speed. Larger pattern size is possible as hardware upgrades. If larger pattern is desired, the width can be readily extended (might up to several meters) by

increasing the size of the mask and laser beam. The length of the pattern is can be controlled determined by the motion of the motorized stage (might up to kilometer). With further optimization, such systems can find their have practical applications in the large-scale production of electronics and photonics, such as integrated circuits, solar panels as well as LCDs, *etc*.

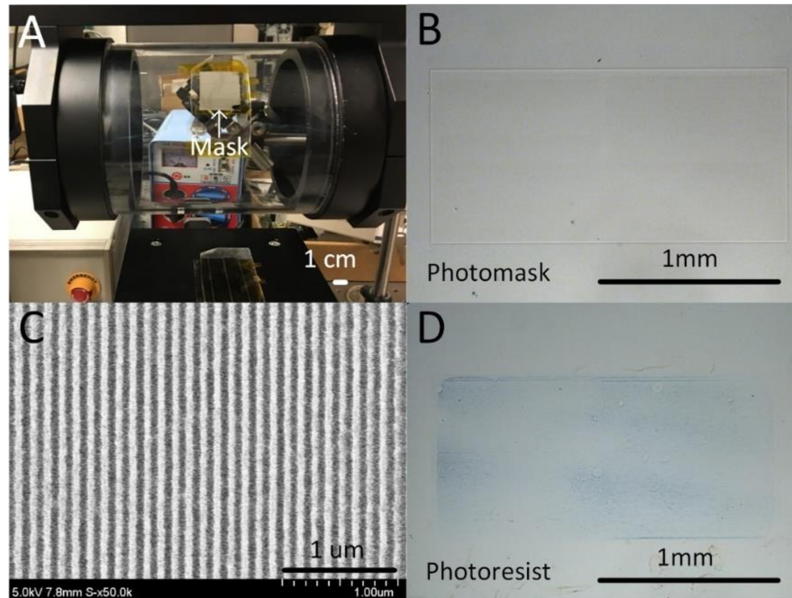

Figure 30 Experimental results made by the plasmonic roller system.
(A) Photo of the PET mask mounted on the quartz cylinder (B) Periodic pattern on the PET mask under microscope. The scale of the mask is 2 mm × 1 mm. (C) SEM images of the nanoscale pattern in PR with thickness of 100 nm. (D) Photo of the resist pattern under microscope.

2.7 Summary

In this chapter, a plasmonic interference lithography system by utilizing Al grating on glass as a mask and PR film on stacked metal/dielectric on PET substrate is demonstrated. This design is based on spatial frequency selection of evanescent waves, so that a single high-k mode is maintained and imaged in the PR, which results in a uniform deep subwavelength periodic pattern. The proposed lithographic approach can be applied to fabricate 61.25 nm half-pitch lines with large area pattern uniformity and depth exceeding 100 nm. This plasmonic waveguide approach overcomes two major drawbacks (poor uniformity and limited depth) in previous plasmonic

lithography and broadens its applications in nanoscale patterning. In addition to the experimental progress towards large-scale applications of plasmonic interference lithography, the general criteria of designing such exposure system is also discussed, which can be used for nanoscale fabrication in this fashion to various applications with different requirements for wavelength, pitch, aspect-ratio and structure. Furthermore, other than simple 1-D grating, 2-D structures can be generated by multiple exposures in experiment, which can serve as anti-reflective films. It is also worth noting that the proposed plasmonic lithography system can adopt a flexible mask system. By replacing the glass mask with Al grating on a flexible substrate, one can envision a roll-based plasmonic interference nanolithography for improved throughput. The plasmonic roller system combines the concepts of the photo roller lithography and the planar plasmonic waveguide lithography, and thus it can produce large-area subwavelength patterns with high throughput on a moving substrate in a continuous fashion. Since current immersion lithography at 193 nm and extreme ultraviolet (EUV) lithography tools usually cost several hundreds of millions, the plasmonic roller system using a regular UV light source has the potential to be used for cost-effective applications.

CHAPTER 3

Interference Lithography Based on ENZ HMM

3.1 Lithography system using HMM

Hyperbolic metamaterials (HMMs) have been used to improve the resolution, which are described by an effective electric permittivity [14,19,35–39] in the tensor form: $\bar{\bar{\epsilon}} = \begin{pmatrix} \epsilon_{xx} & 0 & 0 \\ 0 & \epsilon_{yy} & 0 \\ 0 & 0 & \epsilon_{zz} \end{pmatrix}$ with only principal components. The sign of the tangential permittivity of HMMs is the same $\epsilon_{\parallel} = \epsilon_{xx} = \epsilon_{yy}$ but the signs of its tangential and vertical permittivity are opposite $\epsilon_{\parallel} \cdot \epsilon_{\perp} = \epsilon_{xx} \cdot \epsilon_{zz} < 0$, where both $\epsilon_{\parallel}$ and $\epsilon_{\perp}$ are complex values. HMMs have been widely exploited for various proposes, particularly as a hyperlens in imaging [13,19,22,34,47,48] and filters in ultraviolet (UV) lithography. [13,22,34,47–49] Using the hyperlens, subwavelength patterns can be replicated with the same size as that of the mask by flat structure (illustrated in Figure 31C1). As a type I HMM, hyperlens can allow high-k modes to pass through because of its special dispersion. While a curved hyperlens can produce patterns smaller than the mask, [50] the 1:1 patterning approach is challenging because of the complexity in making the mask. The approaches using HMMs as filters [13,38] produce patterns based on interference effect (Figure 31C3). However, due to the strong attenuation of the light propagating in the HMMs, the field intensity in the light-sensitive photoresist (PR) layer is several orders of magnitude weaker than that of the incident light. [13,21] These two characteristics have seriously restricted the practicality of a nanolithography system based on HMMs. To overcome these issues, a system which can create interference patterns while maintaining high light transmission is needed. We proposed to utilize a special epsilon-near-zero

(ENZ) HMM to produce subwavelength patterns. ENZ metamaterials [41,42,77–85] have been reported in many applications, such as tailoring propagation and radiation patterns, [42,77,79,80] waveguide coupling, [78,79,81] and coherent perfect absorption. [82] Among those various structures, a special type of HMM whose tangential component of permittivity almost reaching zero $\epsilon_{xx} \rightarrow 0$ is studied in this work. The ENZ HMM consists of alternating metal and dielectric films which provides a planar structure necessary for constructing a plasmonic lithography system. The effective permittivity of the stacked structure can be calculated by the effective medium theory [14,19,35–37] as $\epsilon_{xx} = \epsilon_{yy} = f\epsilon_m + (1-f)\epsilon_d$ and $\epsilon_{zz} = \epsilon_m\epsilon_d/[(1-f)\epsilon_m + f\epsilon_d]$, where f stands for the fill ratio of the metal $f = t_m/(t_m + t_d)$, and ϵ_m (ϵ_d) is the relative permittivity for the metal (dielectric), and t_m (t_d) are their thicknesses. We use aluminum (Al) and aluminum oxide (Al_2O_3) to construct a type II ENZ HMM ($\epsilon_{||} \rightarrow 0$ and $\epsilon_{\perp} > 0$) for nanolithography at a wavelength of 405 nm, *i.e.,* the h-line in UV lithography. It is worth noting that similar ENZ HMMs can be utilized to realize lithography at other wavelengths including 365 nm (i-line) as well as DUV 248 nm and 193 nm. In addition, the plasmonic material is not limited to Al. A sliver Ag based ENZ HMM at wavelength of 405 nm with appropriate fill ratio has the same property as that of Al based ENZ system. Although a plasmonic lithography system usually relies on the spatial frequency selection principle, [13,22,34] in this design we analyzed the HMMs in terms of mode expansion and wave propagation. In this chapter, [51] by investigating these optical properties of the type II ENZ HMM, we take advantage of the special field distribution inside the HMM to create deep subwavelength patterns in PR layer, with a half-pitch 1/6 of the photomask. The design of period reduced patterns can greatly alleviate the difficulty of making the mask. Furthermore, the light intensity in the PR is comparable with the incident light, which can significantly reduce the exposure time and thus improve the throughput of lithography.

3.1.1 ENZ HMM lithography system using Al

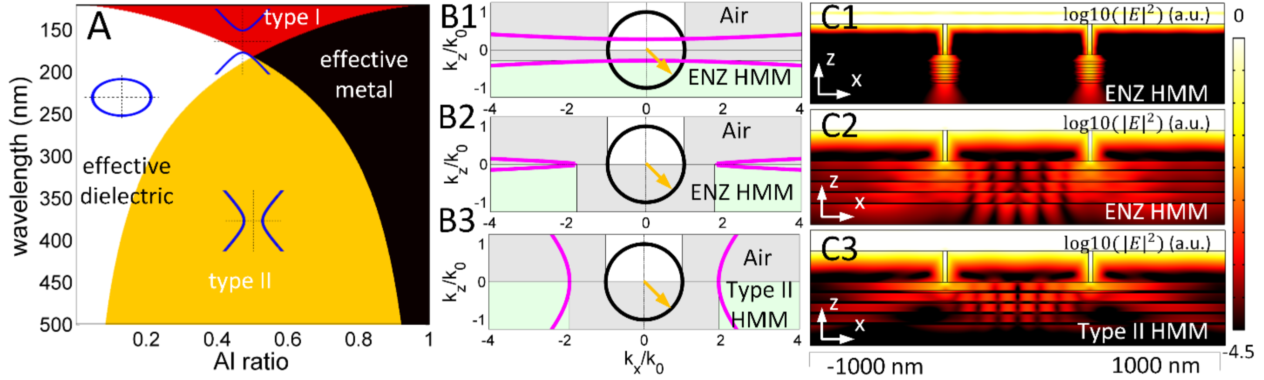

Figure 31 Different HMMs and their applications in lithography systems.
(A) Types of the Al/Al_2O_3 HMM as a function of Al fill ratio and wavelength. (B1) Iso-frequency curve of air indicated by black circle and the HMM indicated by magenta hyperbola at the wavelength 175 nm with fill ratio of f=16/30. (B2-B3) Iso-frequency curves of air indicated by black circles and the HMMs indicated by magenta hyperbolas at the wavelength 405 nm with fill ratio of (B2) f=6/51 and (B3) f=12/51. The yellow arrows refer to the wavevector, the grey regions represent the forbidden zones in air/HMM, and the green regions correspond to the allowed zones in air/HMM. (C1) Normalized electric field distribution $\log10(|E|^2)$ in the xz plane of double slits through Al/Al_2O_3 HMM made of 7 layers of 16 nm Al and 14 nm Al_2O_3 films at wavelength 175 nm. (C2-C3) Normalized electric field distribution $\log10(|E|^2)$ in the xz plane of double slits through Al/Al_2O_3 HMM made of (C2) 7 layers of 6 nm Al and 47 nm Al_2O_3 films and (C3) 7 layers of 12 nm Al and 39 nm Al_2O_3. The TM polarized 405 light travels downwards from PMMA to PR.

For the Al/Al_2O_3 stacked HMM, both ϵ_{xx} and ϵ_{zz} are frequency dependent, and the signs of ϵ_{xx} and ϵ_{zz} determine the type of the HMMs. [36,37,44] As shown in Figure 31 A, different types of the metamaterials depends on wavelength and the metal ratio. [36,37,44] The multilayer structure made of Al and Al_2O_3 is a type I HMM ($\epsilon_{xx} > 0$ and $\epsilon_{zz} < 0$) for shorter wavelength, while a type II HMM ($\epsilon_{xx} < 0$ and $\epsilon_{zz} > 0$) at longer wavelength; an effective dielectric ($\epsilon_{xx} > 0$ and $\epsilon_{zz} > 0$) when Al fill ratio is small while an effective metal ($\epsilon_{xx} < 0$ and $\epsilon_{zz} < 0$) when Al fill ratio is large. The transverse magnetic ™ wave propagating in a HMM is described by equation $k_x^2/\epsilon_{zz} + k_z^2/\epsilon_{xx} = k_0^2$. Based on Figure 31 A, with the Al fill ratio is 6/51, ENZ occurs around the wavelength of 405 nm, which is the h-line in UV lithography. To illustrate the typical light propagation in ENZ HMMs, incident light the wavelengths of 405 nm with different fill ratios are

selected. The HMM is a type II HMM ENZ ($\epsilon_{xx} \rightarrow 0$) with ϵ_{xx} = -0.04974 + 0.5014i and ϵ_{zz} = 3.2219+ 0.009919i for f = 6/51 (Figure 31B2), while a type II HMM with ϵ_{xx} = -3.1372 + 1.0422i and ϵ_{zz} = 3.8202 + 0.02898i for f = 12/51 (Figure 31B3). In Figure 31B, the black circle shows the index ellipsoid of air, and magenta hyperbola depicts the iso-frequency curve of HMM as a function of the normalized wavevector k_x/k_0 and k_z/k_0. The light is incident from air and goes into the HMM, as shown by the yellow arrows of the incident wavevector. For the indication of the forbidden zones and allowed zones, the upper panels with $k_z > 0$ indicates the air, while the lower panels with $k_z < 0$ shows the HMM, where the white and green regions correspond to the allowed zones for propagating waves, while the grey regions represent the forbidden zones for evanescent waves in air and the HMMs, respectively. Because of the forbidden region between $n_{air} < k_x/k_0 < \sqrt{\epsilon_{zz}}$ in the type II HMM (Figure 31B2 and B3), the wave becomes evanescent as it enters the HMM, with an imaginary $k_z = i\sqrt{\epsilon_{xx}\, k_x^2/\epsilon_{zz} - \epsilon_{xx} k_0^2}$. Double-silt interference simulation is performed to demonstrate the strong dependence on the ϵ_{xx} and ϵ_{zz}, and the corresponding electric field distributions $|E|^2$ are shown in Figure 31C1-C2. The TM plane wave travels from the positive z-axis in air with zero angle of incidence, and transmits through a 150-nm-thick chrome (Cr) photomask with two slits of 20 nm width and 700 nm separation d. A PMMA layer with a thickness of 50 nm as an index matching PMMA layer is placed underneath the photomask, followed by HMM consisting of the seven layers of alternating stacked Al and Al_2O_3. When separation $d \ll \lambda$, $|k_x| \gg k_0$, evanescent waves is generated because of the subwavelength nano-slits located in the near-field proximity of the HMM. Therefore, the high-k eigenmodes of the HMM is efficiently excited. When the HMM becomes the ENZ with 7 layers of 6 nm Al and 47 nm Al_2O_3 films (Figure 31 C2), the electric field is straight along the vertical direction with periodic distribution in the horizontal direction. For regular type II HMM with 7

layers of 12 nm Al and 39 nm Al_2O_3 (Figure 31 C2), the field diverges from the slit with a large angle, which follows the normal direction of the hyperbolic iso-frequency curve (Figure 31 B2) [37]. For different types of HMM, type I HMM has been reported as a hyper-lens [14,19,36,37,44] to obtain subwavelength patterns. In this work, we will mainly work on ENZ metamaterial towards the applications in lithography system utilizing the mode propagation.

3.1.2 ENZ HMM lithography system using Ag

To demonstrate the generality of the design, the ENZ slab composed of other metals for example silver (Ag) is discussed as well. The type dependence of the HMM based on Ag and Al_2O_3 on the wavelength and the fill ratio of Ag is shown in Figure 32A. The HMM is a type I HMM ($\epsilon_{xx} > 0$ and $\epsilon_{zz} < 0$) in the wavelength regime 329 - 348 nm, while a type II HMM ($\epsilon_{xx} < 0$ and $\epsilon_{zz} > 0$) at the wavelength longer than 405 nm. From Figure 32A, around the wavelength of 405 nm, type II ENZ HMM occurs at the Ag fill ratio of 10/26. The lithography design at 405 nm for Ag based HMM is plotted in Figure 32B, where the scheme is the same as that given in Figure 32A. 7 layers of 10 nm Ag and 16 nm Al_2O_3 is illuminated by 405 nm wavelength TM polarized light. The Ag grating has thickness of 40 nm, period of 530 nm, and the duty cycle of 75%. The PMMA spacer is 40 nm in thickness, the PR is 30 nm in thickness, and he bottom Ag layer is 22 nm in thickness. Within one period, six periodic patterns are created, corresponding to the interference of 3rd order diffraction of the grating. To illustrate the typical light propagation in different types of Ag based HMMs, incident light with the wavelengths of 340 nm, 365 nm, 405 nm and 550 nm are demonstrated, as shown in Figure 32C. The metamaterial is a type I HMM ($\epsilon_{xx} > 0$ and $\epsilon_{zz} < 0$) at 340 nm wavelength with ϵ_{xx} = 1.329 + 0.249i and ϵ_{zz}= -1.785 + 6.147i with fill ratio of $f = 10/26$ (Figure 32C1), a type I ENZ HMM ($\epsilon_{xx} \rightarrow 0$ and $\epsilon_{zz} < 0$) at 365 nm with ϵ_{xx}= 0.00749 + 0.24876i and ϵ_{zz}= -12.655 + 11.237i with fill ratio of f = 16/30 (Figure 32C2), a type II ENZ

HMM ($\epsilon_{xx} \rightarrow 0$ and $\epsilon_{zz} > 0$) at 405 nm with ϵ_{xx} = -0.00135 + 0.134i and ϵ_{zz} = 7.479 + 0.369i (Figure 32C3), and a type II HMM at 550 nm with ϵ_{xx} = -3.113 + 0.113i and ϵ_{zz} = 5.218 + 0.0197i (Figure 32C4). Light propagating in the type I HMM is allowed with $k_z = \sqrt{\epsilon_{xx}k_0^2 - \epsilon_{xx}\,k_x^2/\epsilon_{zz}}$ as shown in Figure 32C1, C2. In contrast, incident from air to the type II HMM, as in Figure 32C3 and C4, the wave becomes evanescent with an imaginary $k_z = i\sqrt{\epsilon_{xx}\,k_x^2/\epsilon_{zz} - \epsilon_{xx}k_0^2}$.

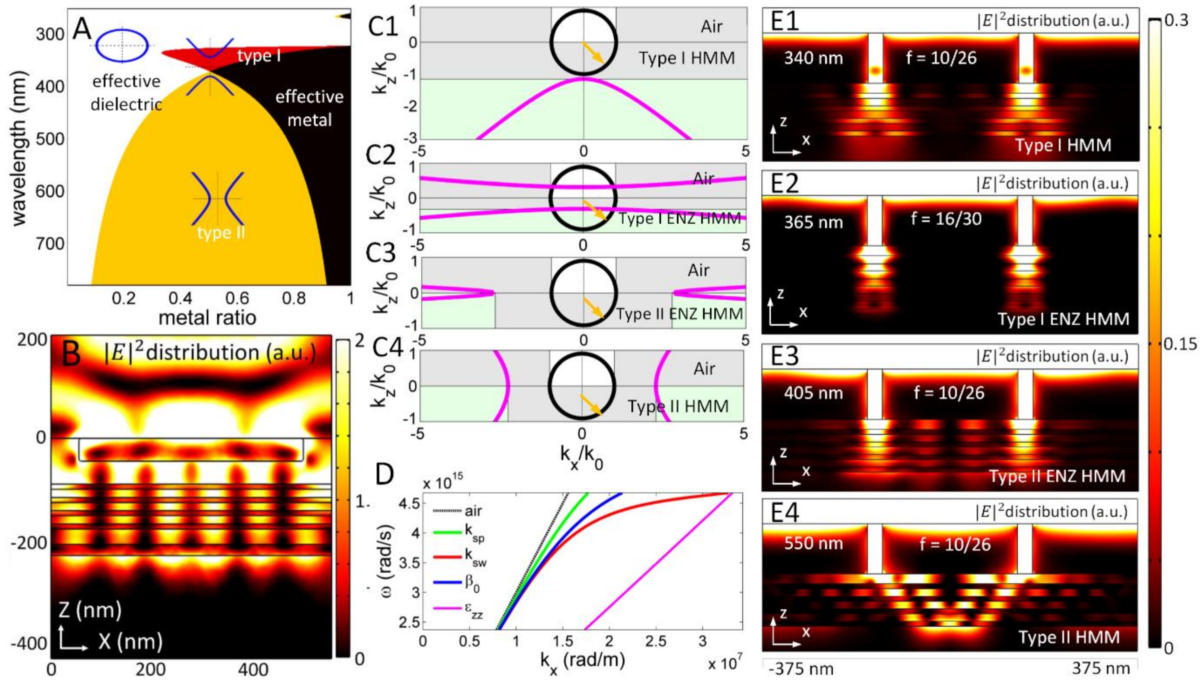

Figure 32 ENZ lithography design based on Ag.
(A) Types of metamaterial as a function of Ag fill ratio and wavelength. (B) Normalized $|E|^2$ distribution of the ENZ lithography in the xz plane at 405 nm wavelength illumination. The ENZ HMM is made of 7 layers of 10 nm Ag and 16 nm Al_2O_3. (C2) Iso-frequency curve of air (black circle) and the HMM (magenta hyperbola) at the wavelength 365 nm with fill ratio of f=16/30. (C1, C3, C4) Iso-frequency curves of air (black circles) and the HMMs (magenta hyperbolas) with fill ratio of f=10/26 at a wavelength of (C1) 340 nm (C3) 405 nm and (C4) 550 nm. The yellow arrows refer to the incident wavevectors, the grey regions represent the forbidden zones, and the white/green regions correspond to the allowed wave zones in air/HMM. (D) Dispersion relation of air, the SPP at air/Ag interface, the surface wave at air/type II HMM interface as well as $\sqrt{\epsilon_{zz}}$ as a function of tangential wavevector k_x and angular frequency ω. (E1, E3, E4) Normalized electric field distribution $|E|^2$ in the xz plane of double-slit interference into Ag/Al_2O_3 HMM at a wavelength of (E1) 340 nm (E3) 405 nm and (E4) 550 nm. The HMM is made of 7 layers of 10 nm Ag and 16 nm Al_2O_3. (C2, E2) The dispersion relation and field distribution of 7 layers of 16 nm Ag and 14 nm Al_2O_3 ENZ HMM at 365 nm wavelength.

In the double-silt interference as shown in Figure 32E1-E3, the TM plane wave travels from the positive z-axis in air with zero angle of incidence. Light transmits through a 100-nm-thick chromium (Cr) photomask with two slits which has width of 30 nm and separation of 300 nm. The PMMA spacer has thickness of 20 nm, followed by HMM consisting of the 7 layers of 10 nm Ag and 16 nm Al_2O_3 (Figure 32E1, E3, E4) and 16 nm Ag and 14 nm Al_2O_3 (Figure 32E2). At wavelength of 340 nm, the field propagates and diffracts in the type I HMM as if it is a normal dielectric (Figure 32E1); while at 365 nm, the light propagation becomes directional (Figure 32E2). At 405 nm (Figure 32E3), the electric field is straight along the vertical direction with periodic distributions. At 550 nm (Figure 32E4), the field diverges from the slits with a large angle, which follows the normal direction of the hyperbolic iso-frequency curve. [48,86]

3.2 Principle of ENZ HMM

3.2.1 Surface wave

To study the light propagation inside the HMM, the transverse electric (TE) and TM waves propagating in the two media can be expresses in eq. (20) and (21),

$$k_x^2 + k_{sz}^2 = \epsilon_{xx} k_0^2, \qquad \mathrm{Im}(k_{sz} \geq 0) \tag{20}$$

$$\frac{k_x^2}{\epsilon_{zz}} + \frac{k_{pz}^2}{\epsilon_{xx}} = k_0^2, \qquad \mathrm{Im}(k_{pz} \geq 0) \tag{21}$$

Similar to the surface SPP, a surface wave (SW) can be excited at the interface between an isotropic medium and a uniaxial medium, which propagates along the interface and decays in normal direction towards both sides. Surface waves can be supported by a few types of materials and geometries including SPP [7,87], modes confined at the edge of photonic crystals [88,89], media with both negative permittivity and permeability [90], as well as Dyakonov surface wave [91]

excited at certain angles of two transparent anisotropic optical crystals. Using ϵ_1 for the isotropic medium and $\bar{\bar{\epsilon}}$ for HMM, as shown in Figure 33. The magnetic field of the surface wave is:

$$\begin{cases} H_{1y}(z) = H_0 \exp(ik_x x) \exp(-\alpha_{1z} z), z > 0 \\ H_{2y}(z) = H_0 \exp(ik_x x) \exp(\gamma_{2z} z), z < 0 \end{cases} \tag{22}$$

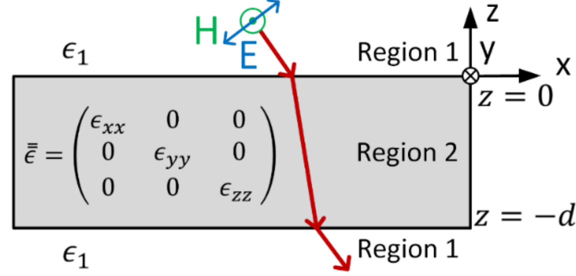

Figure 33 Schematic for the symmetric slab waveguide.
A HMM with relative permittivity $\bar{\bar{\epsilon}}$ as its core and isotropic media ϵ_1 as claddings.

where $\alpha_{1z} = \sqrt{k_x^2 - \epsilon_1 k_0^2}$ is the decaying wavevector in the isotropic medium with relative permittivity ϵ_1 and $\gamma_{2z} = \sqrt{\epsilon_{xx} k_x^2/\epsilon_{zz} - \epsilon_{xx} k_0^2}$ in the uniaxial medium for TM polarized light. The corresponding tangential electric field is $E_x = -\frac{i}{\omega\epsilon_0\epsilon}\frac{\partial H_y}{\partial z}$, *i.e.*,

$$\begin{cases} E_{1x}(z) = \dfrac{iH_0\alpha_{1z}}{\omega\epsilon_0\epsilon_1} \exp(ik_x x) \exp(-\alpha_{1z} z), z > 0 \\ E_{2x}(z) = -\dfrac{iH_0\gamma_{2z}}{\omega\epsilon_0\epsilon_{xx}} \exp(ik_x x) \exp(\gamma_{2z} z), z < 0 \end{cases} \tag{23}$$

By matching the boundary conditions for the tangential electromagnetic field H_y and E_x at $z = 0$, the surface wave should satisfy the following relationship,

$$\frac{\alpha_{1z}}{\epsilon_1} = -\frac{\gamma_{2z}}{\epsilon_{xx}} \tag{24}$$

Therefore, to form the surface wave, $\epsilon_{xx} \cdot \epsilon_1 < 0$ should be met. The corresponding k_x of the SW with resonance can be solved as,

$$k_{sw} = k_0 \sqrt{\frac{\epsilon_1 - \epsilon_{xx}}{\frac{\epsilon_1}{\epsilon_{zz}} - \frac{\epsilon_{xx}}{\epsilon_1}}} \tag{25}$$

The required condition $\epsilon_{xx} \cdot \epsilon_1 < 0$ indicates that only the type II HMM and the effective metal support the surface wave. It can be inferred that when $\epsilon_1 = \sqrt{\epsilon_{xx}\epsilon_{zz}}$, the resonance reaches its the maximum. Moreover, if $\epsilon_{xx} = \epsilon_{zz} = \epsilon_m$, k_{sw} becomes the same as that of the SPP $k_{spp} = k_0\sqrt{\epsilon_1\epsilon_m/(\epsilon_1 + \epsilon_m)}$. The dispersion relation of air, the SPP at the interface of Ag and air $k_{sp} = \sqrt{\epsilon_{Ag}\epsilon_{air}/(\epsilon_{Ag} + \epsilon_{air})}$, and the surface wave at the interface of air and Ag based HMM k_{sw} as well as β_0 and $\sqrt{\epsilon_{zz}}$ are given in Figure 32D. It can also be seen that $\sqrt{\epsilon_{zz}}k_0 > k_{sw} > k_0 > k_{sp} > k_{air}$, where the surface wave locates at between the air line and the allowed zone of the HMM. When it becomes a type II ENZ HMM at the wavelength of 405 nm, $k_{sw} \rightarrow \sqrt{\epsilon_{zz}}k_0$, and the HMM becomes highly anisotropic as indicated by the flat iso-frequency curve in Figure 32B, and the behavior to the ENZ slab is restricted by the dispersion relation.

3.2.2 Waveguide modes

A symmetric slab waveguide with type II HMM as its core and isotropic media as claddings is shown in Figure 33. The relative permittivity of the cladding is ϵ_1, and the relative permittivity of the core (region 2) is a tensor $\bar{\bar{\epsilon}}$ with $\epsilon_{xx} < 0$ and $\epsilon_{zz} > 0$. The type II NHM slab supports both plasmonic and oscillatory modes. [58] The plasmonic mode propagates along the x-axis, and decays in z direction (Figure 35A1 and A2, C1 and C2). The magnetic field of TM wave can be expressed as the following group of equations in different regions.

$$\begin{cases} H_{1y}(z) = H_0 \cosh\left(\frac{\gamma_{2z}d}{2} + \psi\right) \exp\left[-\alpha_{1z}\left(z - \frac{d}{2}\right)\right] & z > \frac{d}{2} \\ H_{2y}(z) = H_0 \cosh(\gamma_{2z}z + \psi) & -\frac{d}{2} \leq z \leq \frac{d}{2} \\ H_{3y}(z) = H_0 \cosh\left(\frac{\gamma_{2z}d}{2} - \psi\right) \exp\left[\alpha_{1z}\left(z + \frac{d}{2}\right)\right] & z < -\frac{d}{2} \end{cases} \quad (26)$$

where d denotes the thickness of the HMM slab, $k_z = i\gamma_{2z} = i\sqrt{\epsilon_{xx}\beta^2/\epsilon_{zz} - \epsilon_{xx}k_0^2}$ in the HMM core $\alpha_{1z} = \sqrt{\beta^2 - \epsilon_1 k_0^2}$ in the isotropic claddings, and tangential wavevector β denotes the mode with $\beta = n_{\text{eff}}k_0$. Plasmonic modes mean that the wavevector along z direction $k_z = i\gamma_{2z}$ is an imaginary number. The magnetic field in the uniaxial medium region 2 is the superposition of two waves decaying in opposite directions, thus it can be represented by cosh functions. The associated tangential electric field $E_x = -\frac{i}{\omega\epsilon_0\epsilon}\frac{\partial H_y}{\partial z}$ is: $E_z = -\frac{i}{\omega\epsilon_0\epsilon}\frac{\partial H_y}{\partial x}$

$$\begin{cases} E_{1x}(z) = \frac{iH_0\alpha_{1z}}{\omega\epsilon_0\epsilon_1} \cosh\left(\frac{\gamma_{2z}d}{2} + \psi\right) \exp\left[-\alpha_{1z}\left(z - \frac{d}{2}\right)\right] & z > \frac{d}{2} \\ E_{2x}(z) = -\frac{iH_0\gamma_{2z}}{\omega\epsilon_0\epsilon_{xx}} \sinh(\gamma_{2z}z + \psi) & -\frac{d}{2} \leq z \leq \frac{d}{2} \\ E_{3x}(z) = -\frac{iH_0\alpha_{1z}}{\omega\epsilon_0\epsilon_1} \cosh\left(\frac{\gamma_{2z}d}{2} - \psi\right) \exp\left[\alpha_{1z}\left(z + \frac{d}{2}\right)\right] & z < -\frac{d}{2} \end{cases} \quad (27)$$

By matching the boundary conditions at $z = d/2$ and $z = -d/2$, the continuity of E_x and H_y,$\tanh(\gamma_{2z}d/2 + \psi) = -\epsilon_{xx}\alpha_{1z}/(\epsilon_1\gamma_{2z})$ and $\tanh(\gamma_{2z}d/2 - \psi) = -\epsilon_{xx}\alpha_{1z}/(\epsilon_1\gamma_{2z})$ should be met. Solving for γ_{2z} and ψ, the following relations can be obtained.

$$\gamma_{2z}d = 2\,\text{arctanh}(-\frac{\gamma_{2z}\epsilon_1}{\alpha_{1z}\epsilon_{xx}}) - i(m-1)\pi \quad (28)$$

$$\psi = \frac{im\pi}{2} \quad (29)$$

The TM_0 mode and TM_{1p} mode have zero and $\pi/2$ phase shift across the core, respectively. The mode equations for TM_0 mode in eq. (30) and TM_{1p} mode in eq. (31) can be simplified from eq. (28) with $m = 0$ and $m = 1$, to the following form,

$$\gamma_{2z} d = 2\,\text{arctanh}\left(-\frac{\alpha_{1z}\epsilon_{xx}}{\gamma_{2z}\epsilon_1}\right) \tag{30}$$

$$\gamma_{2z} d = 2\,\text{arctanh}\left(-\frac{\gamma_{2z}\epsilon_1}{\alpha_{1z}\epsilon_{xx}}\right) \tag{31}$$

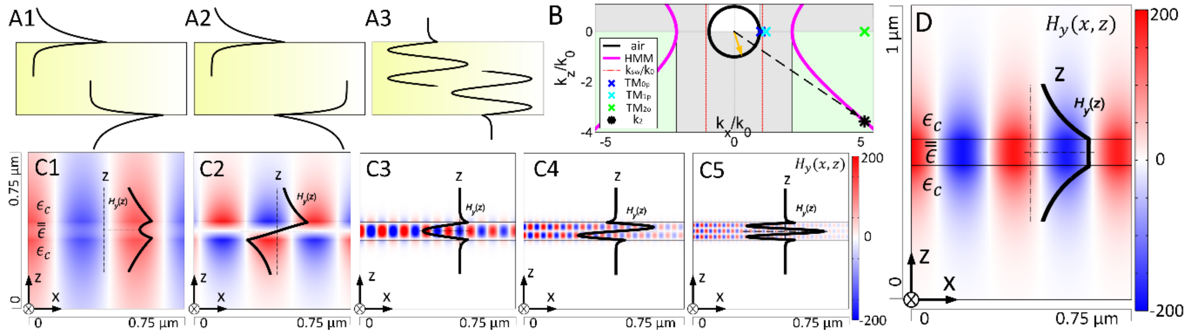

Figure 34 Field sketches at the top and the bottom interface of the waveguide.
(A1) TM_{0p} (A2) TM_{1p} plasmonic modes and (A3) TM_{mo} oscillatory modes. (B) Iso-frequency curves of air and the type II HMM made of 7 layers of 16 nm Ag and 14 nm Al_2O_3 at a wavelength of 550 nm. The red dashed lines indicate where $k_x = \pm k_{sw}$, the cross points correspond to β/k_0 for different orders of modes, where $\beta_{2o} > \sqrt{\epsilon_{zz}} k_0 > \beta_{1o} > k_{sw} > \beta_{0o}$. The yellow arrow refers to the incident wavevector in air, and the black star and arrow indicate the wavevector in HMM for the TM_{2o} mode. (C1-C5) Magnetic field distributions $H_y(x,z)$ in the xz plane (color) and $H_y(z)$ along the z axis (black curve) of the (C1) TM_{op}, (C2) TM_{1p} (C3) TM_{2o} (C4) TM_{3o} and (C5) TM_{4o} modes, at a wavelength of 550 nm and the HMM core has thickness of 88 nm. (D) Magnetic field distribution of the TM_0 mode supported in the type II ENZ HMM at wavelength of 405 nm, where the field in the core is uniform. The claddings are air.

The system also supports oscillatory modes due to the allowed zones in the high-k regime (Figure 35A2, C3-5), whose wavevector along the z direction $k_z = \kappa_{2z} = \sqrt{\epsilon_{xx} k_0^2 - \epsilon_{xx}\beta^2/\epsilon_{zz}}$ is a real number. The magnetic field of the oscillatory modes can be expressed by superposition of cosine functions instead of hyperbolic functions, as the following:

$$\begin{cases} H_{1y}(z) = H_0 \cos\left(\frac{\kappa_{2z} d}{2} + \phi\right) \exp\left[-\alpha_{1z}\left(z - \frac{d}{2}\right)\right] & z > \frac{d}{2} \\ H_{2y}(z) = H_0 \cos(\kappa_{2z} z + \phi) & -\frac{d}{2} \le z \le \frac{d}{2} \\ H_{3y}(z) = H_0 \cos\left(\frac{\kappa_{2z} d}{2} - \phi\right) \exp\left[\alpha_{1z}\left(z + \frac{d}{2}\right)\right] & z < -\frac{d}{2} \end{cases} \tag{32}$$

where $\alpha_{1z} = \sqrt{\beta^2 - \epsilon_1 k_0^2}$ and $\kappa_{2z} = \sqrt{\epsilon_{xx} k_0^2 - \epsilon_{xx}\beta^2/\epsilon_{zz}}$ for the propagating modes. The field in the core (region 2) is the superposition of two oscillatory waves propagating in opposite directions. The corresponding electric field $E_x = -\frac{i}{\omega\epsilon_0\epsilon}\frac{\partial H_y}{\partial z}$ is given in eq. (33),

$$\begin{cases} E_{1x}(z) = \frac{iH_0\alpha_{1z}}{\omega\epsilon_0\epsilon_1} \cos\left(\frac{\gamma_{2z} d}{2} + \phi\right) \exp\left[-\alpha_{1z}\left(z - \frac{d}{2}\right)\right] & z > \frac{d}{2} \\ E_{2x}(z) = \frac{iH_0\kappa_{2z}}{\omega\epsilon_0\epsilon_{xx}} \sin(\gamma_{2z} z + \phi) & -\frac{d}{2} \le z \le \frac{d}{2} \\ E_{3x}(z) = -\frac{iH_0\alpha_{1z}}{\omega\epsilon_0\epsilon_1} \cos\left(\frac{\gamma_{2z} d}{2} - \phi\right) \exp\left[\alpha_{1z}\left(z + \frac{d}{2}\right)\right] & z < -\frac{d}{2} \end{cases} \tag{33}$$

The boundary conditions at $z = d/2$ and $-d/2$ require the tangential electromagnetic field to be continuous, so the conditions for the waves $\tan(\kappa_{2z} d/2 + \phi) = -\epsilon_{xx}\alpha_{1z}/(\epsilon_1\kappa_{2z})$ and $\tan(\kappa_{2z} d/2 - \phi) = -\epsilon_{xx}\alpha_{1z}/(\epsilon_1\kappa_{2z})$ can be obtained. Solving for κ_{2z} and ϕ, for the mth order propagating mode for TM light, the mode equation and phase condition are the following.

$$\kappa_{2z} d = 2\arctan\left(-\frac{\kappa_{2z}\epsilon_1}{\alpha_{1z}\epsilon_{xx}}\right) + (m-1)\pi \tag{34}$$

$$\phi = \frac{m\pi}{2} \tag{35}$$

A symmetric waveguide with the type II HMM as core with thickness of 88 nm at wavelength of 550 nm is given in Figure 34 A, B and C. The performance of the field distribution and the light propagation can be explained by modes analyses, where the HMM is a regular type II HMM. The

magnetic field $H_y(x,z)$ in the xz plane is shown in the colored map, and the magnetic field distribution $H_y(z)$ along the z-axis is illustrated by the black curves shown in Figure 34 C1-C5. The tangential wavevectors of the TM_{0p}, TM_{1p} and TM_{2o} mode and the wavevector in the HMM of the TM_{2o} mode are given in Figure 34B, where the solution of the modes $\beta_{2o} > \sqrt{\epsilon_{zz}}k_0 > \beta_{1o} > k_{sw} > \beta_{0o} > k_0$. Higher order oscillatory modes have even larger tangential wavevectors.

The zeroth order plasmonic mode TM_{0p} [57,58] (Figure 35A1 and C1) has no node across the core. The surface modes at the two interfaces couple together while the corresponding waveguide mode decays in the core. The surface waves at the top and the bottom interface of the waveguide are given in Figure 35A1 and its coupled magnetic field distribution of TM_{0p} mode is shown in Figure 35C1. The magnetic field flips its sign across the interface because the electric field is also continuous and $\epsilon_1 \cdot \epsilon_{xx} < 0$. The plasmonic mode is in the forbidden zone of HMM, whereas the oscillatory modes are in the propagating zone of the HMM. When the HMM becomes type II ENZ HMM, as shown in Figure 34D, the mode propagation becomes uniform in the core. The type II HMM as a core at 550 nm is a multi-mode waveguide system, and the number of nodes indicates the mth order. Therefore, the field excited by the double slits is the superposition of the several modes. Since the core is lossy, the higher the mode is, the more it decays while propagating. The nano-scale slits can excite high-k modes in the HMM, and the main propagation angle of the field in the HMM depends on the resonance cone. [48,86] As ϵ_{xx} reaches zero at 405 nm, the HMM becomes highly anisotropic. The waveguide can only support a single mode determined by eq. (30), (31) and (34) with d = 88 nm. For the TM_0 mode, [58] $\gamma_{2z} = \sqrt{\epsilon_{xx}\beta_0^2/\epsilon_{zz} - \epsilon_{xx}k_0^2} \rightarrow 0$ when $\epsilon_{xx} \rightarrow 0$, hence the magnetic field in the core is uniform, resembling a mode propagating horizontally because $H_{2y}(z) = H_0 \cosh(\gamma_{2z}z) \rightarrow H_0$. The period of the patterns in each case by numerical simulation and experiment can be predicted tangential wavevector of the surface wave

β_0. The effective index in the simulation is close to the value of $n_{\text{eff}} = \beta_0/k_0$, and the spatial frequency determines the resolution limit $\Delta \approx 2\,\lambda/n_{\text{eff}}$. In an optimized system, the pitch of the patterns can be calculated by $P = \Lambda/6$, which ~ 88 nm for Ag based lithography, or 117 nm for Al based lithography system at 405 nm wavelength, where P is the period of the grating mask. The calculated n_{eff} = 2.30 and for Ag and 1.73 for Al, respectively.

3.2.3 Type I and II ENZ HMM

For a type I HMM, following the same method used in 3.2.2, when the boundary condition is matched, the mode equation in case of type I HMM ($\epsilon_{xx} > 0$ and $\epsilon_{zz} < 0$) can be solved as,

$$\kappa_{2z} d = 2\arctan\left(\frac{\alpha_{1z}\epsilon_{xx}}{\kappa_{2z}\epsilon_1}\right) + m\pi \tag{36}$$

where $\kappa_{2z} = \sqrt{\epsilon_{xx}k_0^2 - \epsilon_{xx}\beta^2/\epsilon_{zz}}$ and $\alpha_{1z} = \sqrt{\beta^2 - \epsilon_1 k_0^2}$. In addition, for the TM_{0o} mode which exists in type I ENZ HMM is

$$\kappa_{2z} d = 2\arctan\left(\frac{\alpha_{1z}\epsilon_{xx}}{\kappa_{2z}\epsilon_1}\right) \tag{37}$$

By using eq. (30) and (37), the solution to the tangential wavevector β and normal wavevector κ_{2z} as well as γ_{2z} as a function of the waveguide thickness d can be easily solved for type I and II ENZ HMM, respectively. From eq. (28), (34) and (36), it can be concluded that for type I ENZ HMM, β have several solutions when the core of the waveguide is thin; whereas, for type II ENZ HMM, only one solution exists for a certain thickness of waveguide, which is the fundamental TM_{0p} mode. The conclusions are based on effective medium theory (EMT) with the consideration of ϵ_{xx} and ϵ_{zz}. Therefore, the validity of the effective medium theory to explain the behaviors of the multilayer structures is also confirmed by comparing the results using different methods.

Figure 35A1 and B1 give the optical transfer function (OTF) as function of k_x/k_0 and wavelength, which is defined as the ratio between the transmitted and incident magnetic field $|H_t/H_i|^2$.

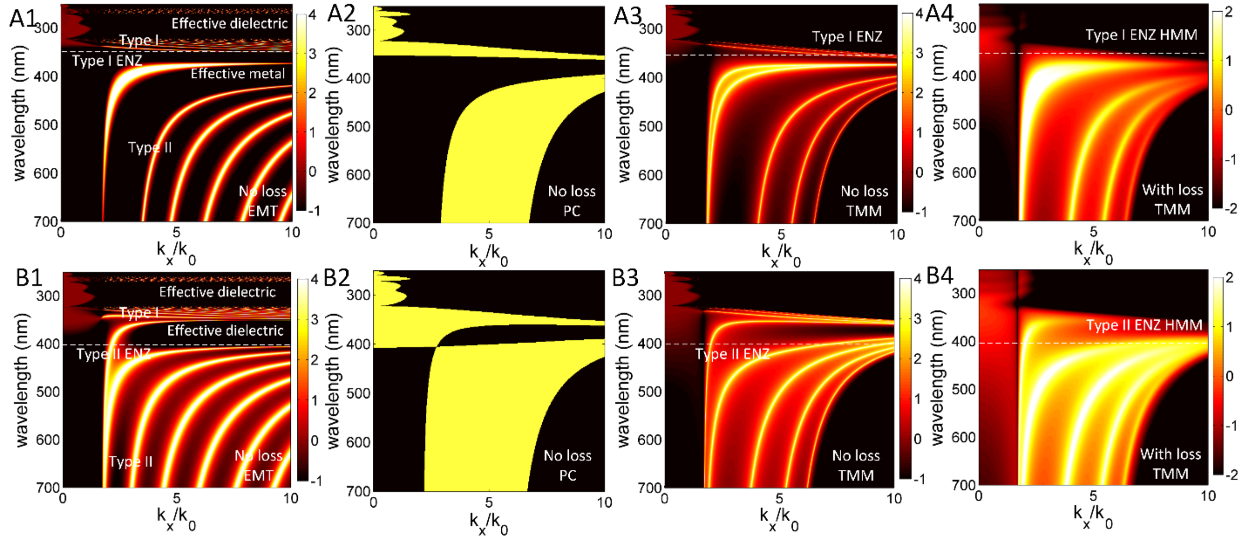

Figure 35 Comparison among different methods of the HMM.
HMM made of (A) 16 nm Ag and 10 nm Al_2O_3 and (B) 10 nm Ag and 16 nm Al_2O_3. (A1, B1) OTF as function of k_x/k_0 and wavelength, calculated by EMT with thickness 88 nm and fill ratio (A1) f =16/26 and (B1) f =10/26. HMM becomes (A1) type I ENZ at 352 nm and (B1) type II ENZ HMM at 405 nm. (A2, B2) The band structure of the HMM calculated by mode analyses of 1D PC for infinite layers of periodic structures made of (A2) 16 nm Ag and 10 nm Al_2O_3 and (B3) 10 nm Ag and 16 nm Al_2O_3. No loss is considered. (A3, B3) OTF as function of k_x/k_0 and wavelength, calculated by TMM with no loss involved for HMM made of (A3) 7 layers of 16 nm Ag and 10 nm Al_2O_3 and (B3) 7 layers of 10 nm Ag and 16 nm Al_2O_3. (A4, B4) OTF as function of k_x/k_0 and wavelength calculated by TMM with loss. All the surrounding media are PR.

In two figures, EMT is used to study the HMM (no loss) with a thickness of the core 88 nm. The surrounding media or the claddings of the waveguide structure are PR. To illustrate the property of the HMM, the bright curves indicate the eigenmode of the HMM. The types of the HMM: type I HMM, type II HMM, effective dielectric and effective metal are marked in Figure 35A1 and B1, where the type I ENZ and type II ENZ points are indicated by the white dashed lines. Photonic band structure [92] of the one-dimensional (1D) photonic crystal (PC) made of periodic 16 nm Ag and 10 nm Al_2O_3 (Figure 35A2) and 10 nm Ag and 16 nm Al_2O_3 (Figure 35B2) is calculated assuming the periodic structure is infinite. [92,93] Furthermore, accurate transfer matrix method

(TMM) is used to study the same system, with no loss (A3 and B3) and with loss (A4 and B4). The multilayer structure calculated by TMM is composed of 7 layers of 16 nm Ag and 10 nm Al_2O_3 (A3 and A4) and 7 layers of 10 nm Ag and 16 nm Al_2O_3 (A4 and B4), respectively. The dashed lines indicate the type I ENZ point at a wavelength of 352 nm (A1, A3 and A4) and type II ENZ HMM at 405 nm (B1, B3 and B4). When considering loss in the HMM system, the higher order eigenmodes have higher loss; meanwhile, several modes merge into one and cannot be distinguished one another. Comparing EMT and TMM, the high-k modes appear in EMT, but not in the TMM due to the finite thickness of unit cell 26 nm. Whereas, photonic crystal analyses show the cutoff of photonic band in the high-k regime clearly, but the surface mode is in the forbidden zone of the type II HMM. Therefore, the unusual surface mode can be seen in case of effective medium, but it cannot be predicted in the case of infinite photonic crystal.

3.2.4 Direction of the light propagation

This section discusses how light propagates in different HMMs. Assuming a plane wave propagating in zx plane $i.e. k_y = 0$, by solving the Maxwell equations, for TM waves, $\nabla \times \bar{E} = -\partial \bar{B}/\partial t$ and $\nabla \times \bar{H} = \partial \bar{D}/\partial t = \partial(\bar{\bar{\epsilon}} \cdot \bar{E})/\partial t$, the corresponding electric field and magnetic fields [37] can be expressed by:

$$\bar{H} = \hat{y} H_0 \exp[i(k_x x + k_z z) - i\omega t] \tag{38}$$

$$\bar{E} = \frac{H_0}{\omega \epsilon_0} (\frac{k_z}{\epsilon_{xx}} \hat{x} - \frac{k_x}{\epsilon_{zz}} \hat{z}) \exp[i(k_x x + k_z z) - i\omega t] \tag{39}$$

The Poynting vector can be calculated as:

$$< \bar{S} >= \frac{1}{2}\bar{E} \times \bar{H}^* = \frac{\epsilon k}{2\omega\epsilon_0\epsilon_{xx}\epsilon_{zz}} H_0^2 \tag{40}$$

Thus, the Poynting vector in x and z directions have the following components.

$$S_z = \frac{k_z}{\epsilon_{xx}} \frac{H_0^2}{2\omega\epsilon_0} \tag{41}$$

$$S_x = \frac{k_x}{\epsilon_{zz}} \frac{H_0^2}{2\omega\epsilon_0} \tag{42}$$

The refraction angles for the wave vector and Poynting vector can be determined as

$$\theta_{ph} = \tan^{-1}(\frac{k_x}{k_z}) \tag{43}$$

$$\theta_S = \tan^{-1}\left(\frac{S_x}{S_z}\right) = \tan^{-1}(\frac{k_x/\epsilon_{zz}}{k_z/\epsilon_{xx}}) \tag{44}$$

where $k_x^2/\epsilon_{zz} + k_x^2/\epsilon_{xx} = k_0^2$. In addition, the angle between the wavevector and pointing vectorϕ can be determined by

$$\phi = \cos^{-1}(\frac{\bar{k} \cdot \bar{S}}{|\bar{k}||\bar{S}|}) = \cos^{-1}(\frac{\omega^2/c^2}{\sqrt{k_x^2 + k_z^2}\sqrt{(k_x/\epsilon_{zz})^2 + (k_z/\epsilon_{xx})^2}}) \tag{45}$$

When $k_x \gg k_0$,$k_z/k_x = \pm\sqrt{|\epsilon_{zz}/\epsilon_{xx}|}$as well as$\phi = \pi/2$, the main propagation angle of the electric field is determined by the resonance cone [48,86] for $k_x \gg k_0$. The phase angle $\theta_{ph} = \arctan(\sqrt{|\epsilon_{zz}/\epsilon_{xx}|})$ is indicate by the asymptote of the hyperbola and the Poynting vector direction is expressed as $\theta_s = \pi/2 - \arctan(\sqrt{|\epsilon_{zz}/\epsilon_{xx}|})$.

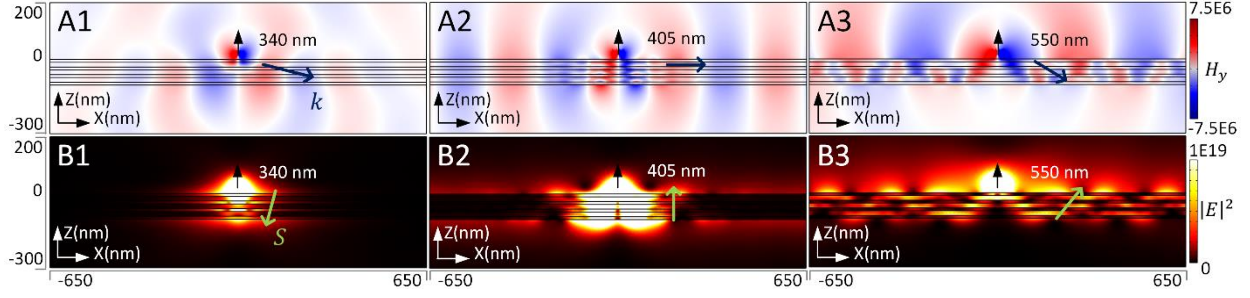

Figure 36 Light propagation in different types of HMMs.
(A1-A3) The magnetic field $H_y(x,z)$distribution of vertically oriented electric dipoles 20 nm above 7 layers of 10 nm Ag and 16 nm Al_2O_3, radiating at (A1) 340 nm (A2) 405 nm and (A3) 550 nm wavelength. (B1-B3)The electric field $|E|^2$distribution of the dipolesradiatingat (B1) 340 nm (B2) 405 nm and (B3) at 550 nm. The small black arrows indicate the dipole positions at $z = 0$ in each map, the dark blue arrows correspond to the direction of the wavevector inside the HMM and the light green arrows correspond to the direction of the field in the HMM. Scale bars are given in the right.

When the tangential permittivity is reaching zero $\epsilon_{xx} \to 0$, the metamaterial becomes highly anisotropic. Figure 36 gives the electromagnetic field distribution of an electric dipole [40] above 7 layers of 10 nm Ag and 16 nm Al_2O_3 at 340 nm, 405 nm and 550 nm wavelength, respectively. The magnetic field of a vertical dipole source can be expressed in Fourier space, [3,87] $H(\bar{r}) = \iint_{-\infty}^{\infty} A(k_x, k_y) \exp[i(k_x x + k_y y \pm k_z z)]\, dk_x dk_y$, where the coefficient $A(k_x, k_y)$ stands for the field amplitude of each component in spatial frequency k space for the angular spectrum representation. The dipole is vertically oriented with 20 nm distance away from the top surface, oscillating with single frequency. Figure 36A1-A3 gives the magnetic field H_y and Figure 36B1-B3 gives the electric field $|E|^2$ distribution. The slab is a type I HMM at 340 nm, reaches the ENZ point of the HMM at 405 nm while becomes is a type II HMM at 550 nm. Therefore, the field in Figure 36A1 and B1 is similar to the field distribution above an anisotropic dielectric. In addition, the dipole excites surface wave as shown in Figure 36B2 and B3. Because of the ENZ point, single mode with one $k_x$is excited in Figure 36B2 and the magnetic field is periodic. However, for a normal type II HMM, due to the multi-mode system, the field excited in the HMM is quite complex,

as illustrated in Figure 36B3. For type I HMM, and for type II HMM, the direction of wavevector and the pointing vector can be derived from eq. (43) and (44), and they are indicated by the dark blue and light green arrows in each figure.

The waveguide (WG) analyses are also provided to study the characteristics of type I ENZ HMM at 352 nm and type II ENZ HMM at 405 nm with fill ratio f =16/26 and f =10/26, respectively. For TM wave, the coefficients are

$$r^p = \frac{r_{12}^p + r_{23}^p \exp(i2k_{pz}d)}{\alpha} \tag{46}$$

$$t^p = \frac{k_1}{k_3} \frac{(1 + r_{12}^p)(1 + r_{23}^p)\exp(ik_{pz}d)}{\alpha} \tag{47}$$

$$r_{12}^p = \frac{\epsilon_x k_{1z} - \epsilon_1 k_{pz}}{\epsilon_x\, k_{1z} + \epsilon_1 k_{pz}} \tag{48}$$

$$r_{23}^p = \frac{\epsilon_3 k_{pz} - \epsilon_x k_{3z}}{\epsilon_3 k_{pz} + \epsilon_x k_{3z}} \tag{49}$$

$$\alpha = 1 + r_{12}^p r_{23}^{\mathrm{p}} \exp(i2k_{pz}d) \tag{50}$$

The transmitted amplitudes of the TM polarized as a function of k_x/k_0 and thickness of the ENZ core is plotted in Figure 37A and B. At type I ENZ point, the resonant curve is flat in a wide range of wavevector for the waveguide with thin core; in comparison, at type II ENZ point, a single mode is supported for certain thickness of waveguide. If we can calculate the cutoff frequency $\mathrm{k_{cutoff}}$ of the type II ENZ HMM, which depends on the slab thickness and the slab optical properties, the resolution limit of the new system can be derived as the following.

$$\Delta \approx \frac{2\pi}{k_{\max}} = \lambda \frac{k_0}{k_{\text{cutoff}}} \tag{51}$$

When the cutoff frequency is in evanescent region, $k_{\text{cutoff}} > k_0$, the resolution of the system is improved compared with conventional projection system.

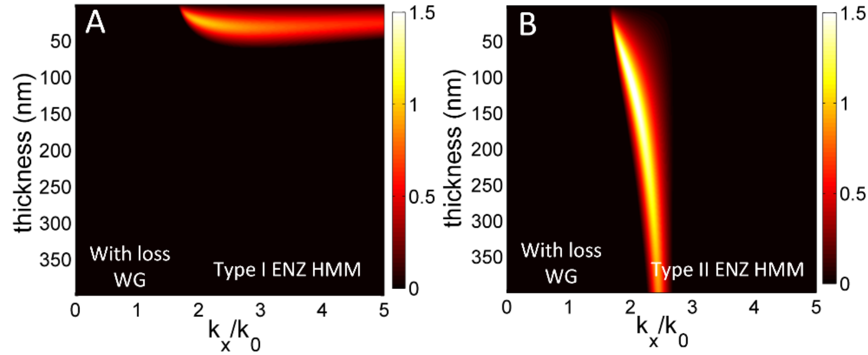

Figure 37 WG mode as a function of k_x/k_0 and thickness of the ENZ core.
Calculated by TMM for (A) type I ENZ at 352 nm and (B) type II ENZ HMM at 405 nm. No loss is considered and surrounding media/ claddings are PR.

3.2.5 Mode coupling in the HMM

The TM modes in multilayer structure can be treated as the results of the coupling between the symmetric and asymmetric modes supported by individual Al_2O_3-Ag-Al_2O_3 waveguide. [21] Figure 38 is the field in the alternating stacked Ag and Al_2O_3 system corresponding to the case shown in Figure 38 at a wavelength of 550 nm, only that the claddings in this case are PR. Figure 38 A gives the OTF of the TM mode at 550 nm with 10 nm Ag (no loss) and 16 nm Al_2O_3, where the peaks in the transmission correspond to different orders of modes. If the loss of the metal is considered, the peak broadens and the peak intensity reduces. According to the peaks given in Figure 38 A, the effective index of each mode $n_{\text{eff}} = \beta/k_0$ can be calculated, and the corresponding magnetic field can be derived by the transfer matrix method. [87,92] Figure 38 B shows the magnetic field $H_y(z)$ along the z axis across the Ag/Al_2O_3 layers for (B1) the zeroth plasmonic waveguide mode (B2) the first order plasmonic mode (B3) the second order oscillatory

mode (B4) the third order oscillatory mode and (B5) the fourth order oscillatory modes. In the actual multilayer structure, the propagation of the magnetic field results from the coupling of the plasmonic modes in each unit cell. Compared with the mode analyses presented in Figure 38, all the modes show almost identical trend, which verify that the effective medium approximation can describe the field behaviors in the HMM. In the extreme case of type II ENZ HMM, only TM_0 mode exist because $\epsilon_{xx} \rightarrow 0$, and the wave front shown in Figure 38 B1 becomes flat. The mode can be treated as the coupling between the long-range-surface-plasmon (LRSP) of each Al_2O_3-Al-Al_2O_3 waveguide, which certainly has the lowest loss as compared with other higher order mode.

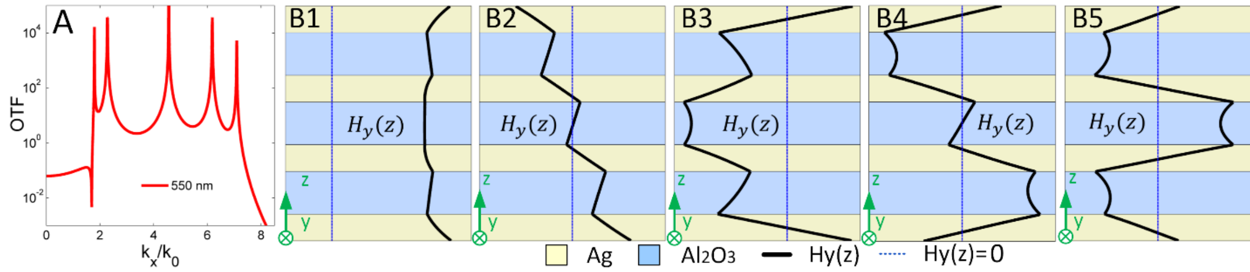

Figure 38 Coupled mode analyses of ENZ HMM.
(A) OTF of the TM light for multilayer made of 7 layers of10 nm Ag and 16 nm Al_2O_3 at 550 nm wavelength incident from PR to PR. (B1-B5) Magnetic field distribution $H_y(z)$ across the Ag (yellow) and Al_2O_3 (blue) of the HMM (B1) for the first transmission peak corresponding to TM_{0p} mode (B2) the second peak, i.e., TM_{1p} mode (B3) the third peak, i.e., TM_{2o} mode (B4) the fourth peak, i.e., TM_{3o} mode (B5) the fifth peak, i.e., TM_{4o} mode.

3.2.6 Loss of the ENZ waveguide mode

To illustrate the loss of the waveguide made of the Al based type II ENZ at 405 nm, we also studied the propagation length L_p along x-axis and decay length L_d along z-aixs for the waveguide with core thickness 165 nm. The propagation length and decay length are defined as the following for the TM_0 mode, which are related to the imaginary part of β_0 and γ_0, respectively, where $\beta_0^2/\epsilon_{zz} - \gamma_0^2/\epsilon_{xx} = k_0^2$.

$$L_p = \frac{1}{2\text{Im}(\beta_0)} \tag{52}$$

$$L_d = \frac{1}{2\text{Im}(\gamma_0)} \tag{53}$$

The normalized propagation length is shown in Figure 39 as L_p/λ and L_d/λ, respectively. The core of the waveguide is the HMM made of 7 layers of 6 nm Al and 47 nm Al_2O_3, which is treated equivalently as an effective homogenous media. In both cases, the loss of the TM_0 mode is lower than that of surface plasmon and surface wave. The coupling of the LRSP leads to lower loss of TM_0 mode; moreover, the loss of the TM_0 mode is the lowest at the ENZ point near 405 nm.

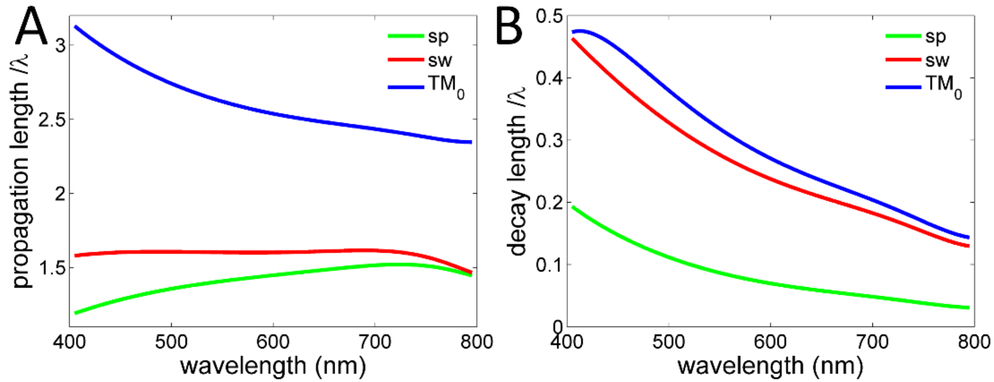

Figure 39 Loss of the waveguide mode.
(A) Propagation length $/\lambda$ and (B) decay length $/\lambda$ as a function of wavelength. The waveguide has effective HMM with thickness of 165 nm as the core and PR as claddings.

3.3 Lithography design using ENZ HMM

To understand the unusual field distribution the HMM and utilize it properly in lithography, we considered a waveguide structure with HMM as its core and PR as claddings. Using ϵ_1 for PR and $\bar{\bar{\epsilon}}$ for HMM as an effective medium, by matching the boundary conditions for H_y and E_x at the interface $z = 0$ with $\epsilon_{xx} \cdot \epsilon_1 < 0$, the corresponding k_x with surface wave resonance point k_{sw} can be solved as, $k_{sw} = k_0\sqrt{(\epsilon_1 - \epsilon_{xx})/(\epsilon_1/\epsilon_{zz} - \epsilon_{xx}/\epsilon_1)}$. The two surface waves at each

interface can couple with each other and form a waveguide mode. For the waveguide with type II HMM as core and PR as claddings, the solution to TM_0 mode is $\gamma_0 d = 2\,\text{arctanh}(-\alpha_0\epsilon_{xx}/\gamma_0\epsilon_1)$, where the decay wavevector is $\alpha_0 = \sqrt{\beta_0^2 - \epsilon_1 k_0^2}$ in the cladding and $\gamma_0 = \sqrt{\epsilon_{xx}\beta_0^2/\epsilon_{zz} - \epsilon_{xx}k_0^2}$ in the core made of HMM, β_0 is the tangential wavevector and d is the thickness of the waveguide. Although $\epsilon_{xx} \to 0$ for both type I and II ENZ HMM, the behaviors are completely different. Specifically, the magnetic field $H_y(z)$ and $H_y(x,z)$ in the Al based type II ENZ HMM are shown in Figure 40A. The field in core of the waveguide are uniform, resembling a mode propagating horizontally because $H_y(z) = H_0\cosh(\gamma_0 z) \to H_0$, which is independent of z when $\gamma_0 \to 0$. Since the waveguide mode is in the forbidden zone for both HMM and PR, it is a plasmonic mode resonating at the interface of HMM and PR. The uniform wave front observed in the HMM (Figure 40A) when treated as an effective medium corresponds to the coupling of LRSP of individual Al_2O_3-Al-Al_2O_3 waveguide in the actual multilayer structure.

Moreover, the loss of the TM_0 in the type II ENZ HMM is also much lower. As a result, the propagation length and decay length becomes also much longer. The reduced loss in this case, as compared with typical type II HMM based lithography, greatly improves the process by significantly reducing the PR exposure time. Furthermore, the high k of mode improves the resolution of the lithography. When the cutoff frequency is in the evanescent region *i.e.* $k_{\text{cutoff}} > k_0$, much smaller features can be generated. The resolution limit can be expressed as a function of the cutoff frequency $\Delta \approx 4\pi/k_{\text{cutoff}} \approx 2\lambda/n_{\text{eff}}$, where n_{eff} is the effective mode index determined by β_0/k_0. In addition, the type II ENZ HMM can also benefit from filter effects [34] as illustrated in Figure 40B. In the k space, the diffraction orders of the grating with period of 700 nm are given by the red arrows. The OTF, *i.e.,* $|H_t/H_i|^2$ shows a narrow band transmission, where the H_t and H_i are the transmitted and incident magnetic field, respectively. In this design, only the 3rd

diffraction of the grating is selected with its diffracted wavevector coinciding with the resonant peak of the OTF, while the other orders are blocked and cannot reach PR layer. With these characteristics, type II ENZ HMM is an excellent candidate in nanolithography for subwavelength patterns with high field contrast and uniformity.

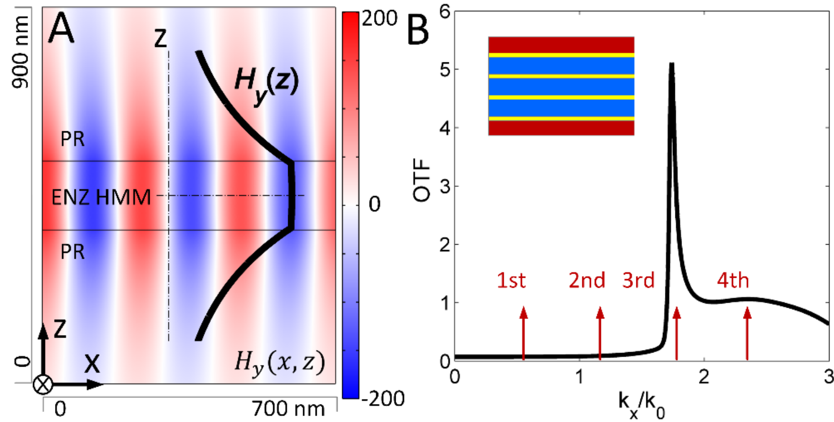

Figure 40 Surface wave in a waveguide made of ENZ HMM.
(A) Magnetic field distributions $H_y(x,z)$ in the xz plane (color) and $H_y(z)$ along the z axis (black curve) of distribution of the mode in the waveguide with Al based type II ENZ metamaterial as core and PR as claddings. The thickness of core is 165 nm. (B) Transmitted intensity $|H_t/H_i|^2$ of 7 layers of 6 nm Al and 47 nm Al_2O_3 with the TM light illumination at 405 nm wavelength, where the H_t is the transmitted magnetic field and H_i is the incident magnetic field. The diffraction orders of the 700-nm grating are marked by the red arrows.

A scheme of the ENZ UV lithography is shown in Figure 41A. One-dimensional (1-D) periodic Al grating is used as the photomask, and the type II ENZ HMM is placed in contact with a PMMA spacer as an index-matching layer, followed by the PR layer to record the imaged patterns. Additional Al and Al_2O_3 layers are placed beneath the PR layer to enhance the field inside the PR by reflection and cavity resonance. [21,34,94] The Al grating is used in the mask to increase the field contrast because of the light coupling, and similar results can be obtained experimentally by Cr mask with Al based ENZ HMM as well. [13] In addition, the system is placed on a flexible polymer substrate to ensure intimate contact between the HMM lens and the PR layer. [22,34] To make a robust design, we also studied the effects of the geometric parameters in the design

including the thickness of each layer, duty cycle and period of the grating *etc. via* simulation. Using the optimized design, the normalized electric field intensity distribution $|E|^2$ of the latent image in the PR layer is shown in Figure 41B for one mask period, illuminated by TM polarized light with a wavelength of 405 nm. The Al grating has thickness of 25 nm, duty cycle of 75%, and period of 700 nm. The PMMA spacer has thickness of 50 nm, which is on top of the HMM made of 7 stacks of 6 nm Al and 47 nm Al_2O_3 layers. The PR has thickness of 100 nm, the bottom Al layer has a thickness of 20 nm, and the two Al_2O_3 films have a thickness of 47 nm. Within one period, six periodic patterns are created, because the 3rd diffraction of the grating was employed for exposure. [34] An additional reduction factor of two comes from the interference of two counter-propagating waveguide modes. Comparing the normalized field distribution, the field intensity in the PR is strong, and the aspect ratio of the patterns is high. Moreover, the additional Al and Al_2O_3 layers underneath the PR not only further improve the contrast and uniformity of the patterns in the simulations, but also reduce the film roughness in the fabrication. The field contrast shown in the simulation can be calculated as $(|E_{max}|^2 - |E_{min}|^2)/(|E_{max}|^2 + |E_{min}|^2)$ ~ 0.915, which is sufficiently high for exposure and to obtain high contrast ratio in images. The average field distribution $|E|^2$ is around 0.225, which is near a quarter of the incident light set a 1V/m. The $|E|^2$ distribution along horizontal lines in the PR is illustrated in Figure 41C, where the amplitude of the periodic distributions at the top, middle and bottom positions are comparable, which means that the field distribution is uniform along the vertical position. It should be note that the field is several orders of magnitude stronger compared with other system using HMM, [13,21] which is due to the low loss of the specially designed waveguide mode supported by ENZ HMM in our system. Moreover, based on our simulations, the dependence of the parameters such as the thickness of each layer is acceptable for the experiments, with tolerance of a few nanometers,

which indicates that our design is quite robust. Due to the low loss and high anisotropy of type II ENZ HMM, the patterns in the PR are much smaller than the photomask while maintaining strong field intensity, high aspect ratio, and good uniformity.

Figure 41 Lithography design using ENZ HMM.
(A) Schematic of the ENZ lithography design in Cartesian coordinates. (B) Normalized $|E|^2$ distribution in the xz plane with the wavelength illumination for 7 layers of 6 nm Al and 47 nm Al_2O_3 ENZ HMM and the white dashed line indicates the middle position in the PR. (C) Normalized electric field distribution $|E|^2$ along horizontal dashed lines at the top, middle and bottom positions in the PR.

3.4 Experiment and discussion

The fabrication process of the plasmonic lithography is shown in Figure 42. 25 nm Al is e-beam evaporated on the clean glass substrate as in Figure 42A, followed by the spin coating of PMMA. A grating with 700 nm period and around 25% duty cycle was obtained by electron beam lithography (EBL), and the Al grating with the same period was achieved by reactive ion etching (RIE, LAM 9400) as shown in Figure 42C. The top view SEM image of the Al grating is shown in Figure 42C1. A thin PMMA layer with 55 nm thickness was spin-coated on top of Al grating as a spacer, which was flattened by thermal nanoimprint [11,22,59] lithography (NX-2000 Nanonex). After planarization, multilayer structure made of alternating 6 nm Al and 47 nm Al_2O_3 was deposited on the PMMA spacer by e-beam evaporation, as in Figure 42E. The cross section of the

multilayer structure on a reference Si sample is given in Figure 42E1. For the preparation of the substrate, regular PET films were planarized by spin coating of a 10 μm thickness SU-8 resist, and followed by 47 nm Al_2O_3 film, 20 nm Al sputtering and 50 nm Al_2O_3 e-beam evaporation. The PR used in the experiment is 1:1 diluted AR-N 7500.18 positive resist at 405 nm wavelength illumination. The diluted PR layer with 100 nm thickness was spin-coated on the Al_2O_3 layer, and soft baked on a hot plate at 85 °C for 1 minute.

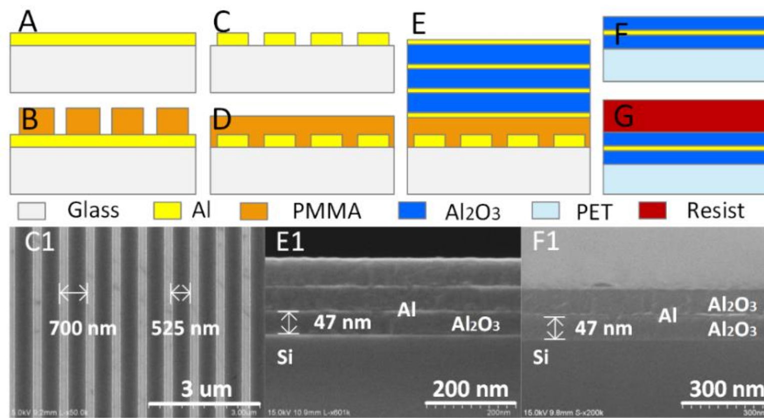

Figure 42 Fabrication process flow of ENZ mask and substrate.
(A-E) masks on glass substrate and (F-G) PR on SU-8 planarized PET substrate. (A) Al sputtered on glass substrate (B) PMMA patterns after EBL (C) Al grating after RIE (D) PMMA coating after planarization (E) e-beam evaporation of Al/Al_2O_3 multilayer films (F) Al_2O_3-Al-Al_2O_3 films sputtered on planarized PET with SU-8 (G) PR by spin-coating. (C1, E1, F1) Corresponding SEM images of the processed plotted in (C, E, F). (C1) Top view of the Al grating on glass substrate. (E1) Cross section view of the multilayer structure deposited on Si wafer and (G1) Cross section view of the Al and Al_2O_3 films deposited on Si wafer made by e-beam evaporation.

The optical setup built to ensure the conformal contact is the same as shown in the work in waveguide lithography in our previous work [22,95]. The Al/Al_2O_3 ENZ mask and the PR coated PET substrate were in conformal contact in a specially designed stage during exposure. Collimated 405nm TM polarized diode laser (ONDAX x6474) light with TM polarization was incident to the mask through a circular aperture with diameter of ~1 cm. The laser intensity was set at 3 $mW\cdot cm^{-2}$ and the exposure last for ~4 mins. Finally, the resist on PET was immersed in 1:1 diluted AR 300-35 developer for 50~55 seconds, followed by 30 seconds deionized (DI) water rinse.

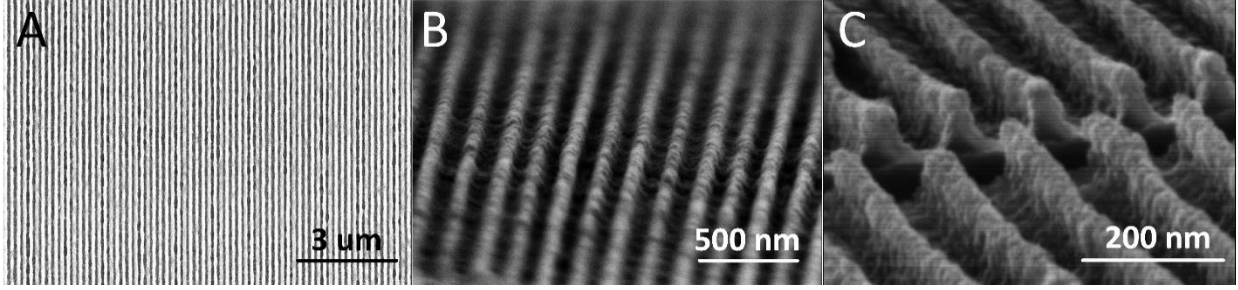

Figure 43 The SEM of the patterns made by the Al/Al_2O_3 ENZ HMM.
(A) top view, (B) angled view and (C) Cross-section view of the patterns with period around 117 nm and height of 100 nm.

To verify the theoretical and numerical calculations in various cases, we did the experiment using the Al-based ENZ metamaterial at 405 nm wavelength, made of 6 nm Al and 47 nm Al_2O_3. Furthermore, from the OTF functions, when the cutoff frequency is in the evanescent region *i.e.* $k_{\text{cutoff}} > k_0$, the resolution of the system can be improved compared to a conventional projection system. In Figure 40B, $k_{\text{cutoff}} > 2k_0$, the minimum feature size that can be patterned is beyond the diffraction limit. The resolution limit can be expressed as a function of the cutoff frequency k_{cutoff}, $\Delta \approx 2\pi/k_{\max} = \lambda k_0/k_{\text{cutoff}}$. The SEM images of the resulting patterns are shown in Figure 43. The period of the grating mask is 700 nm; however, the patterns made by interference have the period of $\Lambda/6$, which is around 117 nm. Subwavelength patterns with half-pitch of 58.5 nm were achieved, which is 1/7 of the light wavelength. The angled and cross-section view of the pattern is illustrated in Figure 43B and C. The height of the PR is 100 nm, which leads to an aspect ratio of the pattern is around 2:1. Note that the aspect ratio of the feature is lower than our previous results of waveguide lithography where the PR layer functions as the core of a waveguide. [34] The pitch of the patterns can be calculated by the $P = \Lambda/6 \approx 2\lambda/n_{\text{eff}}$ at 405 nm wavelength, where P is the period of the grating mask. To see the cross-section view, the resist on the substrate was cut manually by a razor blade and deposited with gold/platinum (Au/Pt) alloy before SEM characterization. Along the periodic lines there is tiny roughness, which might result from the

deposited metal and cutting during SEM characterization. The roughness can also be attributed to the defects on the mask, *e.g.,* the deposited thin Al film, as well as the limitation of the sensitivity, resolution and contrast of the chosen PR at the exposure wavelength. [53]

3.5 Analyses of the design

3.5.1 Optical constants

The permittivity of Ag is frequency dependent and can be expressed using Drude-Lorentz model [96] with five oscillators. All the other optical constants are extracted from come from either the ellipsometry measurement, data from books, [96] or the product information. The refractive index of the PR is n_{PR} = 1.691 + 0.0346i at 405 nm, 1.702 + 0.44i at 248 nm and 1.709 + 0.055i at 193 nm. The flexible polymer substrate is a polyethylene terephthalate (PET) sheet, and the index of the PET substrate n_{PET} = 1.65 + 0.03i at 405 nm, 1.69 + 0.04i at 248 nm and 1.70 + 0.06i at 193 nm. The relative permittivity of the index matching layer PMMA is n_{PMMA}= 1.505 at 405 nm, 1.562 at 248 nm and 1.6302 at 193 nm wavelength. The refractive index of aluminum oxide (Al_2O_3) is n_{Al2O3} = 1.68 at the wavelength of 405 nm, 1.79 at 365 nm, 1.83 at 248 nm and 1.92 at 193 nm. The relative permittivity of Al used in the simulation is ϵ_{Al} = -22.476 + 4.429i at 405 nm, -19.495 + 3.616i at 365 nm, -8.098 + 1.118i at 248 nm and -4.850 + 0.494i at 193 nm. The permittivity of Al and the index of Al_2O_3 at 175 nm is -3.4680 + 0.3083i, and 1.98, respectively.

3.5.2 Parameter sweeping

The sweeping of the parameters is performed in simulation (COMSOL), and the conclusion is listed in Table 1. The duty cycle of the grating determines the intensity as well as the contrast of the patterns. The pitch of the pattern is determined by the period of the grating: $\Lambda = P/2m$, where m is the diffraction order. The resist thickness can be as high as 150 nm while maintaining the

intensity and uniformity. The optimization of the parameters in the design is done ahead of the experiments in order to achieve the best results.

Parameter	Description
Grating duty cycle f	To get a uniform light distribution in the PR, fill ratio of the grating should be $0.5 < f < 0.9$. The larger the ratio is, more uniform the pattern is.
Period of the grating Λ	Period of the grating should be 695 nm ~ 702 nm, and the pattern uniformity changes dramatically when the period is not in the regime.
Thickness of grating h_g	Thickness of the grating can be 25 nm ~ 60 nm. More light can be transmitted to the PR with thinner grating.
Thickness of metal h_m	The acceptable thickness of the metal layer is 5 nm ~ 11 nm. If h_m is too thin, patterns are not uniform; if h_m is too thick, the intensity gets weaker.
Thickness of dielectric h_d	Thickness of the dielectric layer can vary from 35 nm to 55 nm. The intensity of all the patterns are relatively good.
Thickness of spacer h_s	Thickness of the spacer can be around 40 nm ~ 65 nm. In terms of intensity distribution, the best case is around 53 nm.
Thickness of PR h_{pr}	Thickness of the PR around 50 nm ~ 140 nm is acceptable in the simulation, which means the aspect ratio of the patterns may vary accordingly.
Thickness of bottom oxide h_o	Thickness of the bottom dielectric layer can vary from 10 nm to 70 nm to tune the effective mode propagating in the PR.
Thickness of bottom oxide h_b	Thickness of the bottom metal layer can be 14 nm ~ 20 nm to enhance the uniformity of the light in the PR along the vertical direction.
Size variation	Each layer of the design can be off set by 8 nm.

Table 1 The parameters which affect the results in ENZ lithography.

3.5.3 Discussion on experimental conditions

The effects of the experimental conditions of the proposed ENZ plasmonic lithography system are also explored. Figure 44A illustrates the top view scanning electron microscope (SEM) images of the patterns made without the bottom reflective Al_2O_3 and Al layer. Within one period of the grating (700 nm), six lines are generated with uneven spacing. According to the previous work [22,34], the bottom layer helps to enhance the light and form uniform patterns throughout

the PR. In addition, the pattern also varies with light polarization, as shown in Figure 44B. The result is the PR illuminated by partially TM polarized light at 405 nm wavelength, which can be decomposed into TM and transverse electric (TE), *i.e.,* electric field along the grating lines. Because of the momentum mismatching, the TE mode excited in the PR is much weaker, which leads to nonuniform patterns as well.

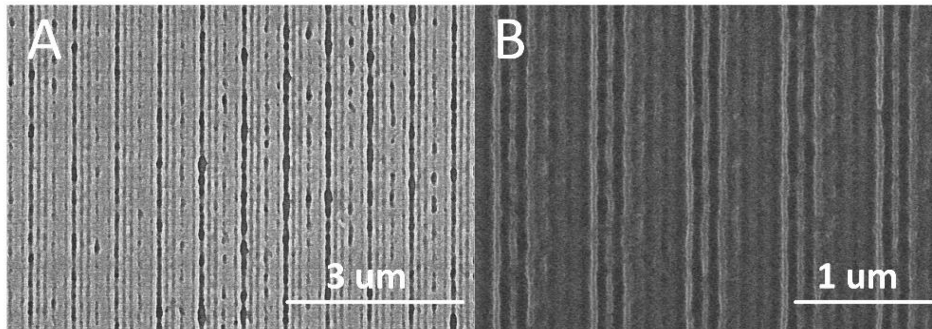

Figure 44 SEM images of the patterns on the PR.
Top view (A) without the bottom Al_2O_3 and Al layer (B) when the polarization varies.

3.5.4 Effects of film roughness

The roughness on the films of the HMM and the defects on the photomask also affect the qualities of patterns made in the experiment. Figure 45 shows the comparison of the electric field distribution $|E|^2$ between perfectly smooth film and with films root mean square (RMS) roughness equal to 2 nm at each interface of the multilayer. In the cross section xz plane (Figure 45A1 and A2) and at a horizontal plane in the middle of PR (Figure 45B1 and B2), the simulated fields are slightly different. For perfectly smooth planar films (A1 and B1), periodic lines patterns are generated with perfect straight lines. For films with a maximum ~2 nm R_{rms} (A2 and B2), the intensity of the pattern drops and tiny line roughness show up (less than 0.5 nm). Especially, as shown in Figure 45B2, the rough films induce scatters at the interface of the multilayer structure,

which might affect the performance of the system. But overall, the ENZ lithography system is quite robust in terms of film roughness.

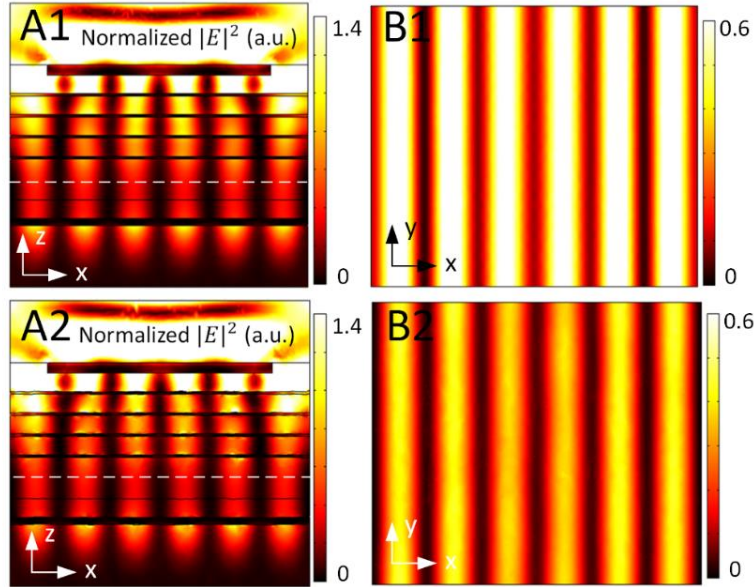

Figure 45 Normalized $|E|^2$ distribution for roughness.
(A1, A2) in the cross section xz plane and (B1, B2) in the horizontal xy plane with (A1, B1) smooth planar films (A2, B2) films with maximum ~2 nm R_{rms}. The periodic patterns in (B1, B2) are the field distribution in the middle of PR at the dash white line positions shown in (A1, A2). The corresponding scale bars are given on the right.

3.5.5 Lithography systems at a wavelength of 365 nm

In addition, though we only have a laser with wavelength of 405 nm in the lab, the similar structure designed at a wavelength of 365 nm (i-line) is also possible. Periodic patterns can be achieved in the PR layer at 365 nm wavelength, as illustrated in Figure 46. The half-pitch of the pattern can reach down to 50 nm, which is also smaller than 1/7 of the light wavelength. In this case, the period of the grating is 604 nm and the type II ENZ HMM is made of 7 layers of 6 nm Al and 36 nm Al_2O_3. The thickness of PR is 100 nm, which gives an aspect ratio of 2:1 as well. The relative permittivity of the Al and Al_2O_3 is -19.495 + 3.616i and 3.217, respectively. The ENZ HMM has the effective permittivity ϵ_{xx} = -0.0278 + 0.517i and ϵ_{zz} = 3.856 + 0.0195i.

Figure 46 ENZ design at 365 nm based on Al.
(A) Schematic of the ENZ lithography design at a wavelength of 365 nm. (B) Normalized $|E|^2$ distribution in the xz plane. The ENZ HMM is made of 7 layers of 6 nm Al and 36 nm Al_2O_3.

3.5.6 Small patterns made by light wavelength of 248 nm and 193 nm

The lithography based on ENZ HMM can also be utilized in other wavelengths as well as for other diffraction orders. Using the HMM made of Al and Al_2O_3 with different fill ratios of Al, nanolithography system capable of making extremely small patterns can be achieved, as shown in Figure 47. The normalized electric field $|E|^2$ distributions of the lithography system illuminated by light with TM polarized 248 nm and 193 nm wavelengths are illustrated in Figure 47B and C, respectively. For 248 nm (Figure 47B), the Al grating is on a fused silica substrate with period of 216 nm, duty cycle of 0.8, and thickness of 20 nm. The poly (methyl methacrylate) (PMMA) spacer has a thickness of 20 nm, and the 7 layers alternating stacked Al and Al_2O_3 films are 8 nm and 20 nm in thickness. The photoresist (PR) has a thickness of 25 nm and the bottom reflective Al layer has a thickness of 25 nm. The corresponding electric field has four periodicities within one period of the grating on the mask, indicating the usage of the 2nd diffraction in exposure. The half-pitch of the patterns in the PR is 27 nm, which is much smaller than the light wavelength of incident. For 193 nm (Figure 47C), the period of the Al grating is 224 nm, and the thickness of the Al grating is 20 nm, and the thickness of the PMMA spacer is 20 nm. The HMM is made of 7

layers of 11 nm Al and 9 nm Al_2O_3 in this case. Within one period of the grating, 8 patterns are generated, meaning the 4th order diffraction is used. The half-pitch of the pattern is 14 nm, which is even difficult in EUV lithography using double patterning.

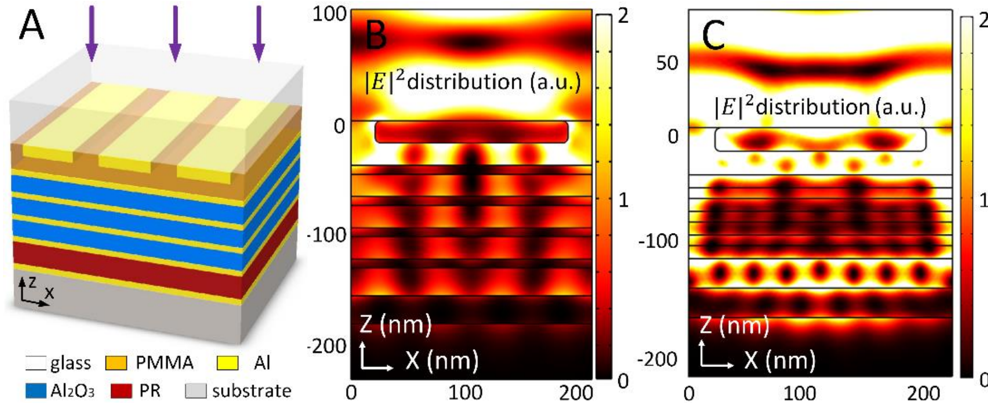

Figure 47 ENZ systems at other wavelengths.
(A) Schematic of the ENZ lithography design in Cartesian coordinates. Normalized $|E|^2$ distribution in the xz plane for (B) 7 layers of 8 nm Al and 10 nm Al_2O_3 ENZ HMM at 248 nm wavelength illumination (B) 7 layers of 11 nm Al and 9 nm Al_2O_3 ENZ HMM at 193 nm wavelength.

3.5.7 2-D patterns using circularly polarized light

Two-dimensional (2-D) periodic patterns can be achieved by either double exposure in perpendicular directions [34], as well as directly from a 2D mask with single exposure [13]. Figure 48A and B show the schematic of the lithography system and the 2D square mask, with illumination of circularly polarized light. The period of the photomask is 420 nm, and the HMM is made of 7 layers of 25 nm Al and 85 nm Al_2O_3 films. PR layer has a thickness of 100 nm, the bottom oxide layers have a thickness of 45 nm and the bottom reflective Al layer has thickness of 25 nm. A type II HMM is used as a filter to select the second order diffraction from the 2D grating, and the optical transfer function (OTF) should be very narrow to block other diffraction orders. Consequently, 16 dots with period of 105 nm can be patterned within one period, as shown in

Figure 48D. In addition, hexagonal patterns can also be achieved with the interference pattern in the PR being the Fourier transform of the photomask [13].

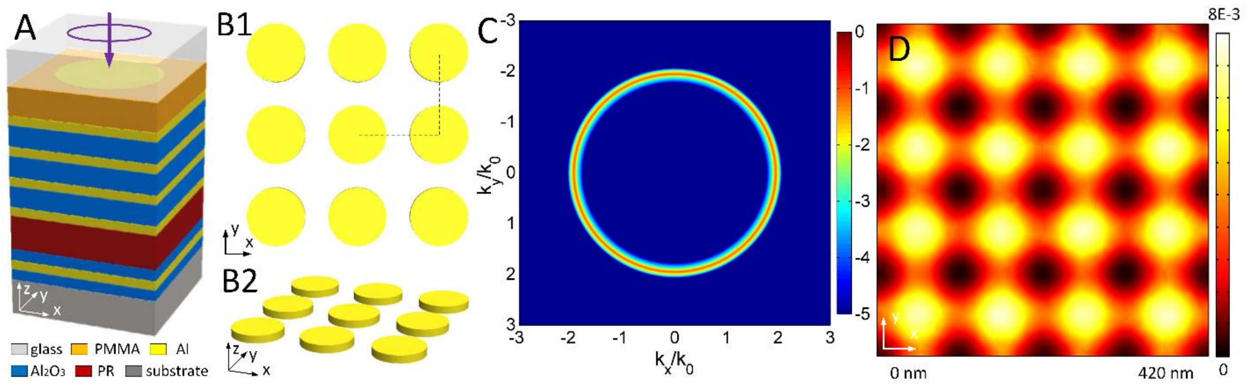

Figure 48 2-D simulation using circuarly polarized light.
(A) Schematic of the type II HMM and 2D grating with circularly polarized light. (B) a 2D square grating in (B1) xy plane and (B2) in Cartesian coordinate. (C) OTF 7 layers of 25 nm Al and 85 nm Al_2O_3 films. (D) Interference patterns in the PR layer with one period.

3.5.8 Micron-scale photomasks

The period of the grating in the ENZ HMM lithography is not limited to 700 nm. By using micron-scale photomasks, the higher order diffractions can be utilized for the exposure of the PR layer. For example, when the mask has a period of 1.16 μm or 1.39 μm, periodic patterns can also be achieved, as shown in Figure 49A and B, respectively. According to the electric field distribution, 10 and 12 lines are created in one mask period, which are due to the interference of 5th and 6th order diffraction of the photomask, respectively. The HMM is made of 7 layers of 7 nm Al and 45 nm Al_2O_3 films, and the PR layer has a thickness of 100 nm. In Figure 49A, the grating has a duty cycle of 0.65, which gives a smallest feature of 406 nm on the photomask. While in Figure 49B, the grating has a duty cycle of 0.7 with a smallest feature of 417 nm. These photomasks are compatible with regular photolithography tools using i-line. Compared with what is discussed in Chapter 2, the plasmonic roller lithography can possibly make patterns over an even larger area with micron-scale photomasks.

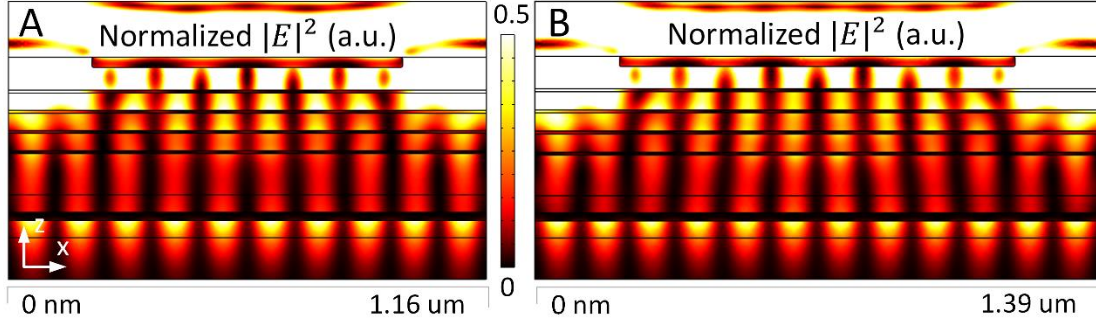

Figure 49 ENZ HMM lithography using micron-scale photomasks.
Light distribution of the photomask with the period of (A) 1.16 µm and (B) period of 1.39 µm

3.5.9 DUV Lithography system using photonic crystal

HMM can be treated as a 1D photonic crystal as discussed in Chapter 3.2.3. Similarly, in deep ultraviolet (DUV) regime, dielectric photonic crystals [92,93] can be used to make subwavelength patterns as well. As shown in Figure 50(a), 11 layers of dielectric stacks with alternating high and low refractive indices are placed underneath a subwavelength grating with the period of 119 nm and thickness of 8 nm. The grating is made of Al with the refractive index of n = 0.1135, k = 2.2029. The grating mask is illuminated by TE polarized light with wavelength of 193 nm. The photonic crystal is made of magnesium fluoride (MgF_2) films with refractive index of 1.4 and thickness of 33.74 nm as well as titanium dioxide (TiO_2) films with refractive index of 2.8 and thickness of 17.23 nm. The PMMA spacer has thickness of 20 nm and refractive index of 1.53. The PR has thickness of 140 nm. The band structure of the 1D structure can be calculated as

$$cos[k_0 dsin(\theta_i)] = cos(k_{x1}d_1)cos(k_{x2}d_2) - \frac{1}{2}(\tau k_{x2}k_{x1} + k_{x1}\tau k_{x2})sin(k_{x1}d_1)sin(k_{x2}d_2) \quad (54)$$

where $\tau = \epsilon_1/\epsilon_2$ for TM and τ =1 for TE polarization, θ_i is the incident angle, and the subscripts 1 and 2 stand for the properties in high and low index material, respectively. Using a quarter wave plate of each stack in the photonic crystal, the light with normal incident has very high reflection.

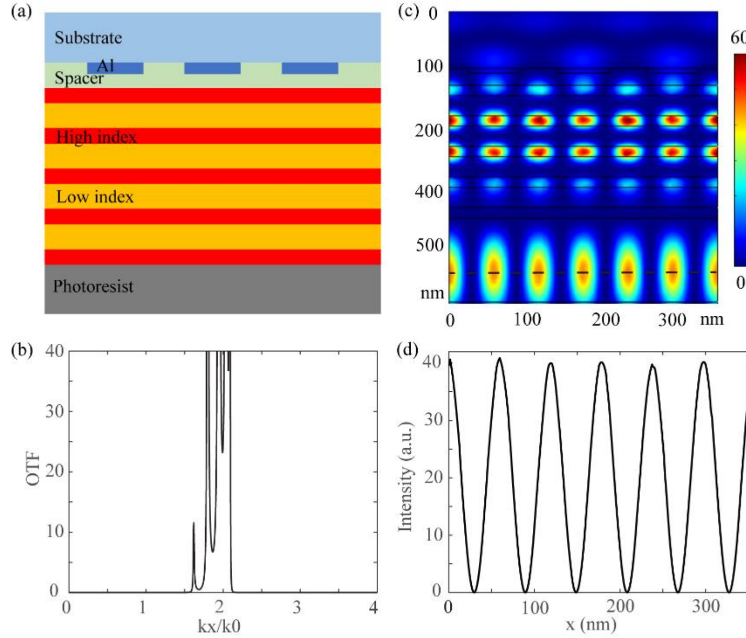

Figure 50 193 nm lithography using photonic crytals.
(a) Schematic of the design (b) OTF curve of the alternating high and low index materials with quarter wavelength thickness (c) Normalized ight intensity distribution $|E|^2$ of the the litography based on diletric photonic cyrtal within 3 period (d) Field distrubution along horiztonal cut line.

However, at high-k regime, the 1D photonic crystal has high transmission, as shown in the OTF curve in Figure 50(b). By the coupling of the Al grating, these high-k modes can be excited by the incident light and imaged onto the PR. The corresponding light distributions are shown in Figure 50(c) and (d). The light intensity in the PR is enhanced by ~25 times compared with that of the incident light. This is due to the high quality factor (Q) of the resonance, and the strong coupling. The field distribution in the PR has linewidth of 30 nm, which leadds to over 4.67:1 height-width aspect ratio. It is because the transverse wavevector coulped by the first order diffraction of the grating is $k_x = \lambda/\Lambda$, where is λ the light wavelength and Λ is period of the grating. The normal

wavevector $k_z = \sqrt{n_{PR}^2 k_0^2 - k_x^2}$. When $k_x \to n_{PR} k_0$, $k_z \to 0$. Therefore, the propagation length $L = 2\pi/k_z \sim\infty$. When the period of grating is Λ =119 nm, the effective mode index can be derived by $n_{\text{eff}} = \lambda/\Lambda$ ~ 1.622 and waveguide mode has very deep depth. This principle is similar to what is discussed in the waveguide lithography.

3.6 Analyses of natural HMM

3.6.1 Introduction to natural hyperbolic material

Apart from various types of artificial HMMs including metal/dielectric stacks, metallic nanowires in a dielectric host, natural hyperbolic material (NHM) [97–101] such as hexagonal boron nitride (h-BN) and graphene have been reported and studied intensively for different applications. NHM is a material which exhibits hyperbolic dispersion naturally $\epsilon_{xx} \cdot \epsilon_{zz} < 0$, usually in the UV and mid-IR regime. Similar to HMM, NHM has also been employed to make waveguide, realize imaging with super-resolution, detect slow light wave and make electronic heterojunctions. However, it hasn't been of particular interest that the surface wave will exist between conventional dielectric and a medium with hyperbolic dispersion, which is the long-range surface wave with extremely low loss. The TE mode distribution is not covered in other calculations either. Specially, study on the condition of existence and the behavior of the surface modes are lacking. In this section, we use h-BN as an example to analyze the wave and understand these issues.

3.6.2 Optical properties of h-BN

As many other dielectrics and metals, the relative permittivity of h-BN is frequency dependent, which can be attributed to resonances due to internal polar degrees of freedom,

$$\epsilon_l(\omega) = \epsilon_l(\infty) + \frac{f_{v,l}\omega_{v,l}^2}{\omega_{v,l}^2 - i\Gamma_{v,l}\omega - \omega^2} \tag{55}$$

where $l = x, y, z$ and other parameters can be expressed as the following, the $\omega_{v,l}$ corresponds to the plasma frequency in x, y and z directions, and $\Gamma_{v,l}$ is the damping term.

Model	l	$\epsilon_l(\infty)$	$f_{v,l}$	$\hbar\omega_{v,l}(meV)$	$\hbar\Gamma_{v,l}(eV)$
Value	x, y	4.9	2.001	168.6	0.87
	z	2.95	0.5262	94.2	0.25

Table 2 The parameters in the h-BN permittivity model.

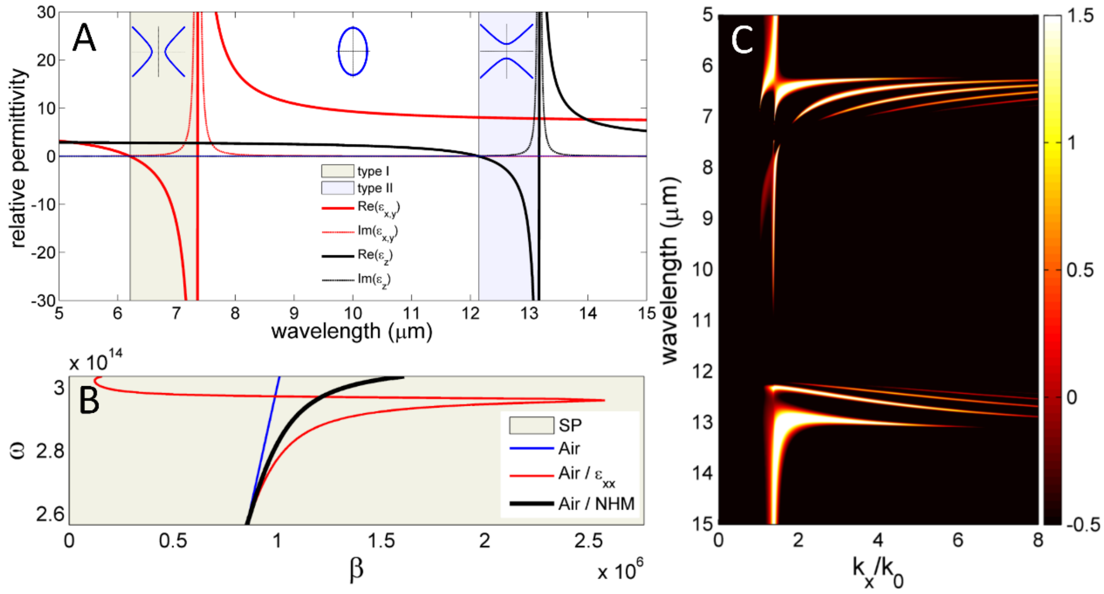

Figure 51 Dispersion of h-BN as a function of wavelength.
(A) relative permittivity of h-BN (B) dispersion relation of the surface wave (C) waveguide mode of a 1.5 μm h-BN slab as a function of wavelength.

Figure 51A gives the relative permittivity of h-BN as a function of wavelength [84,98,101–106]. The light brown region indicates the wavelength (~ 6.2 μm – 7.5 μm) where $\mathrm{Re}(\epsilon_{xx}) < 0$ and $\mathrm{Re}(\epsilon_{zz}) > 0$, and the light purple region refers to the wavelength (~ 12.1 μm – 13.1 μm) region where $\mathrm{Re}(\epsilon_{xx}) > 0$ and $\mathrm{Re}(\epsilon_{zz}) < 0$. The wavelength regions in between and outside have

ellipsoidal dispersion. Figure 51B gives the dispersion relation of the surface wave at the interface of air and h-BN. The dark curve shows the change of tangential wavevector β with the change of angular frequency ω. The wavevector of the surface wave is below the dispersive line of light in the free space (blue line), and is different from the SPP shown by the red curve, assuming the negative permittivity is ϵ_{xx}. Figure 51C is the transmitted amplitude of electric intensity $|E_t/E_i|^2$ of TM wave through a h-BN slab with 1.5 μm thickness, surrounded by air. In the region I, the mode shows positive group velocity $v_g = \partial\omega/\partial k > 0$ compared with the wavevector, while the regions II shows negative group velocity $v_g = \partial\omega/\partial k < 0$. Therefore, this region exhibits the interesting property of the slow wave with almost zero group velocity, which can find its application in imaging and detection. [101,107]

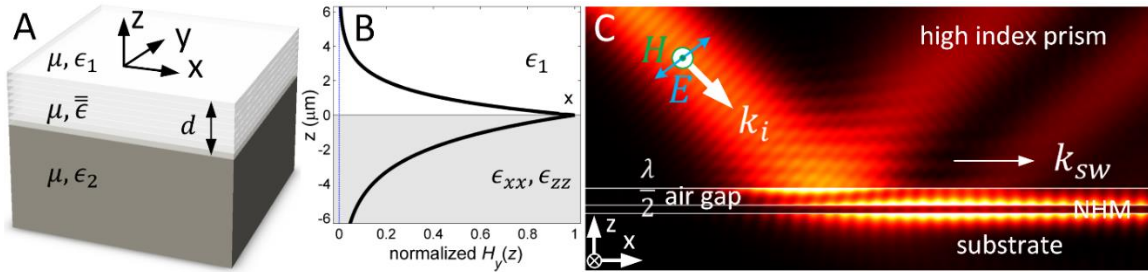

Figure 52 Excitation of the surface wave in h-BN.
(A) Schematic of a slab with hyperbolic dispersion in Cartesian coordinates (B) surface wave at the interface of h-BN and air (C) excitation of surface wave by a high index prism.

Surface waves can also be supported at the boundary of h-BN and a regular isotropic medium, as given in Figure 52A. Only TM polarized light supports a surface wave and it can only exist under the condition that the permittivity of the cladding and positive-birefringent material satisfy the relation of $\epsilon_1 \cdot \epsilon_{xx} < 0$. Here we consider the surface wave between a dielectric with $\epsilon_1 > 0$ and a NHM with $\epsilon_{xx} \cdot \epsilon_{zz} < 0$. Figure 52B plots the magnetic field at the interface of air and h-BN, where the field propagates along the interface and decays towards the normal directions. The dispersion of the surface wave between material ϵ_1 and the hyperbolic dispersive material $\bar{\bar{\epsilon}}$ is

given by eq. (25). As shown in Figure 52C, when the condition is met for h-BN at a wavelength of 6.3 μm, we can use this approach to excite the surface mode. A TM polarized Gaussian beam is incident from the z axis in a high index material, forming 45° degree angle as to the interface. Below the high index prism, there is a small air gap with thickness of $\lambda/2$. The surface wave on the h-BN is propagating long the slab and decays towards the normal directions.

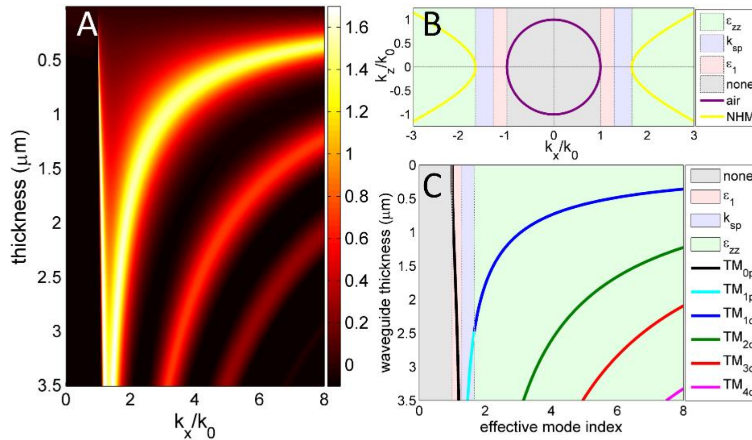

Figure 53 Waveguide modes anlyses at a wavelength of 6.3 μm
(A) Transmitted amplitude (B) dispersion (C) Dispersion of the mode as a function of thickness.

Similar to the type II ENZ HMM, the wavelength range for NHM which supports surface wave is discussed. Figure 53A shows the transmitted intensity ratio through the 1.5 μm h-BN at 6.3 μm wavelength, as functions of tangential wavevector k_x/k_0 and thickness. The mode analysis is shown in Figure 53B and C. In Figure 53B, the purple circle is the dispersion relation of light and the yellow hyperbola corresponds to the dispersion of h-BN at 6.3 μm wavelength as a function of k_x/k_0 and k_z/k_0. The wavelength of 6.3 μm is selected because h-BN is a type II HMM in this case. There are four regions indicated in Figure 53B. In the grey region, is where $k_x/k_0 < \epsilon_1$, so all the modes are forbidden in this region. Whereas, in the pink region where $k_{sp} > k_x/k_0 > \epsilon_1$, and the light purple region, $k_{sp} < k_x/k_0 < \epsilon_{zz}$, the mode decays with as $sinh$ and $cosh$ functions. They are called plasmonic mode for this reason. The light green region represents the

mode where $k_x/k_0 > \epsilon_{zz}$, and that's where the mode can propagate in the NHM (plasmonic mode). Figure 53C shows how the modes differentiate in the regions. The thicker the waveguide is, the more modes it could support. However, due to the loss of the core *i.e.* NHM, the higher mode with accumulated loss will dissipate and disappear as shown in Figure 53A.

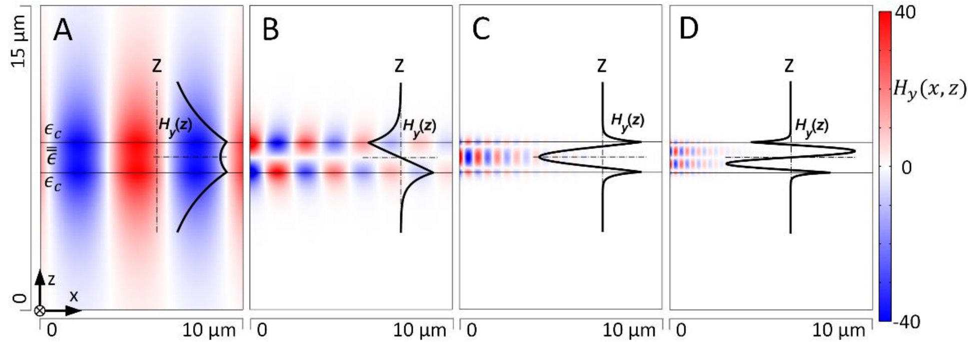

Figure 54 Magnetic field distribution at 6.3 μm.
Magnetic field distribution $H_y(z)$ and $H_y(x,z)$ of (A) TM$_{op}$, (B) TM$_{1o}$ (C) TM$_{2o}$ and (D) TM$_{3o.}$ TM_{0p}, TM_{1o}, TM_{2o} and TM_{3o} modes.

Figure 54 gives the mode distribution corresponding to the modes shown in Figure 53B. The magnetic field along y-axis as a function of x and z is shown in the colored map. In addition, $H_y(z)$ is illustrated by the black curve. The magnetic field would flip the sign across two media, since $\epsilon_1 \cdot \epsilon_{xx} < 0$. The number of nodes across the zero line indicates the mth number. The higher the mode number is, the more phase changes it has across the waveguide core, if the core material is lossy, the higher the mode is, the more it delays when propagating. According to the discussion in section 3.2.2, the plasmonic modes of the b-BN in this regime can be calculated using eq. (30), (31) and (34), and the corresponding electromagnetic mode distribution in h-BN can be plotted.

3.6.3 Waveguide modes of other regimes

Other than the type II NHM with $\epsilon_{xx} < 0$ and $\epsilon_{zz} > 0$. When $\epsilon_{xx} > 0$, the modes of type I NHM can be calculated by eq. (36) and (37). For the normal anisotropic elliptical dispersion and metallic

dispersion, the mode can also be derived accordingly using the same mode expansion method. Figure 55 shows the mode change with slab thickness for effective ellipse, type I NHM and effective metal. The cooresponding magnetic field is shown the following Figure 56 at 10 μm and at 12.3 um and Figure 57, respectively.

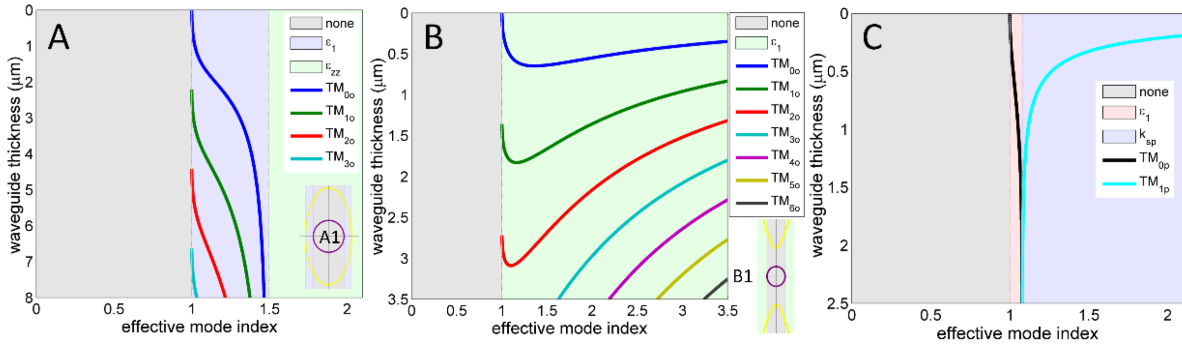

Figure 55 Waveguide mode analyses at different wavelentgths.
Modes (A) at 10 μm with elliptical dispersion and (B) 12.3 μm with type I dispersion and (C) effective metallic dispersion.

Figure 56 gives the transverse magnetic field H_y distribution in xz plane, of the TM modes at a wavelength of 10 μm, and Figure 56A, B, C and D are the TM_0, TM_1, TM_2 and TM_3 modes with h-BN slab thickness of 1.5 μm, 3 μm, 5 μm and 7.5 μm. The black curves indicate the magnetic field H_y along z-axis, where the mth order mode has m nodes across z-axis.

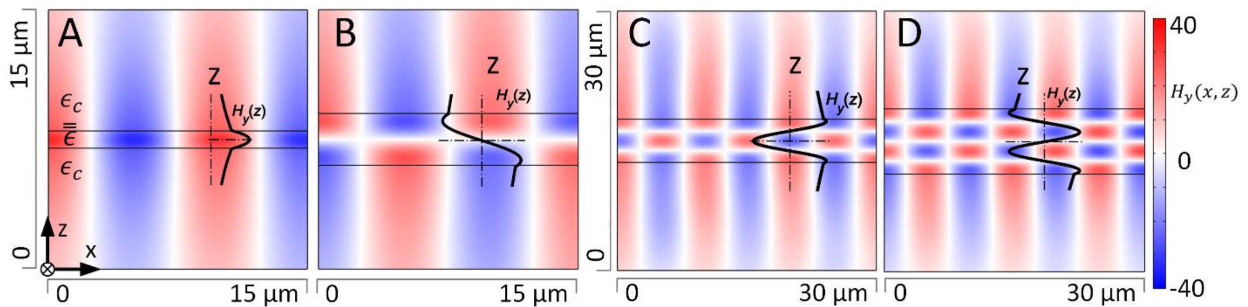

Figure 56 Waveguide mode at 10 μm.
Magnetic field H_y of (A) TM_{0o} mode for a slab with 0.5 μm thickness (B) TM_{1o} mode with 3 μm thickness (C) TM_{2o} mode 5 μm thickness and (D) TM_{3o} mode 7.5 μm thickness

Figure 57 gives the transverse magnetic field H_y distribution in xz plane, of the TM modes at a wavelength of 12.3 μm, and A, B, C and D are the plasmonic TM_0 and TM_1 with h-BN slab thickness of 0.5 μm. The black curves indicate the magnetic field H_y along z-axis, where the mth order mode has m nodes across z-axis.

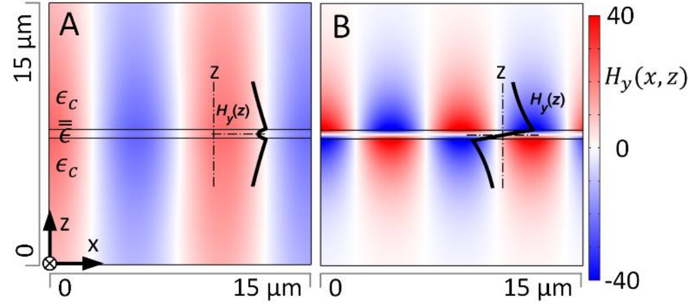

Figure 57 Modes for a slab with a thickness of 0.5 μm at a wavelength of 12.3 um. Magnetic field H_y distribution of (A) TM_{0p} mode and (B) another TM_{1p} mode

3.6.4 TE modes

In addition to TM mode, the TE mode in an anisotropic medium can also be derived, the TE mode would obey the dispersion relation of

$$k_x^2 + k_{sz}^2 = \epsilon_{xx} k_0^2, \qquad \mathrm{Im}(k_{oz} \geq 0) \tag{56}$$

Accordingly, the electric field can be written and the mode equation can be solved as the following.

$$\kappa_m d = 2\arctan(-\frac{\alpha}{\kappa_m}) + m\pi \tag{57}$$

where $k_f = \sqrt{\epsilon_{xx} k_0^2 - \beta^2}$ and $\alpha = \sqrt{\beta^2 - \epsilon_1 k_0^2}$. The mode analysis of TE mode is given at a wavelength of 12.3 μm. Figure 58A gives the transmitted field amplitude through an h-BN slab as a function of k_x/k_0 and thickness of the slab. The bright curves correspond to the modes including both TE and TM modes. It can be clearly seen that the dispersion relation for TE mode and TM mode are different. Figure 58B gives the TE mode for the same system and the ellipsoids of the

two TE modes. The light grey region indicates the forbidden k_x for the waveguide system, while the light purple region is where $\epsilon_1 < k_x/k_0 < \epsilon_{xx}$, and the light green region is where $k_x/k_0 \geq \epsilon_{xx}$. In this case, there is no modes supported by the system.

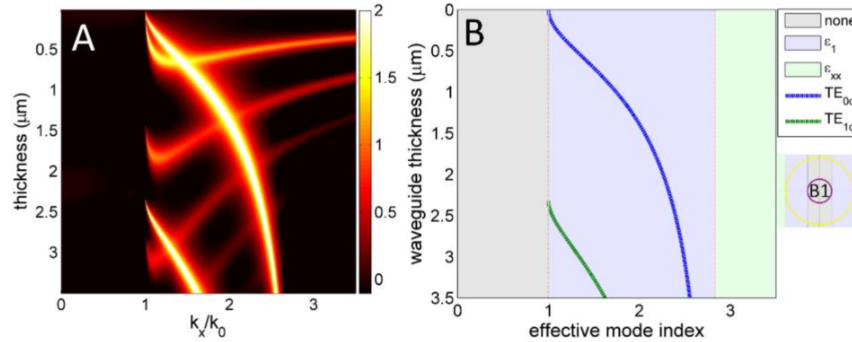

Figure 58 Wavaguide mode at a wavelength of 12.3 μm.
(A) the total transmission as a function of thickness and transverse wavevector. (B) TE mode (B1) index ellipsoid of the two media.

The electric field distribution of the TE modes is shown in Figure 58A. Figure 58B plots the TE mode at 12.3 μm. At 12.3 μm, Figure 59A-D give the transverse magnetic field H_y distribution in xz plane, of the TM modes, while A, B, C and D are the first TM_0, second TM_0, TM_1 and TM_2 modes, respectively, with h-BN slab thickness of 0.5 μm. The black curves indicate the magnetic field H_y along z-axis, where the mth order mode has m nodes across z-axis. In this case, there are two fundamental modes with two different phase shifts across the cladding and different k_f, of which the second TM_0 mode has negative group velocity. The calculations of NHM using h-BN as an example discuss the field distribution for both TE and TM waveguide mode at type I, type II, effective metal and effective dielectric regimes. These analyses provide deep understanding of the hyperbolic material and corresponding behaviors depending on the dispersions. Based on their performance, the NHM and HMM at different wavelengths can be applied in functional optical devices and quantum communications.

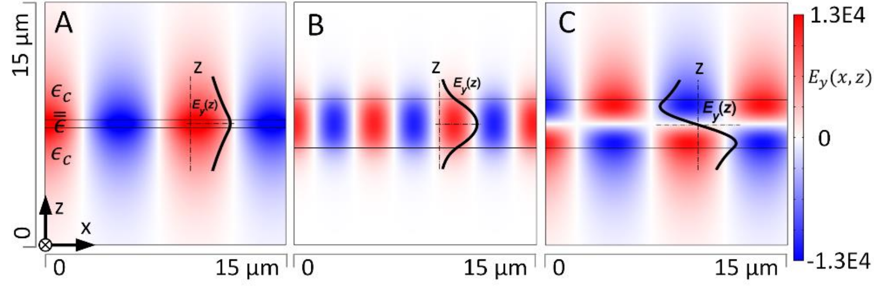

Figure 59 Waveguide mode at 12.3 µm.
Electric field $E_y(z)$ distribution and $E_y(x,z)$ map for (A) TE_{0o} mode with slab thickness of 0.5 µm (B) TE_{0o} mode with slab thickness of 3 µm (C) TE_{1o} mode with slab thickness of 3 µm.

3.7 Summary

In this chapter, a plasmonic lithography system using ENZ waveguide is studied to make period reduced patterns while maintaining high light transmission in the PR. The mode distribution in a type II HMM, and the light propagation in the ENZ HMM waveguide is investigated. Specifically, in the ENZ medium, only one single mode exists, which is suitable for the application in the UV nanolithography with the requirement of patterns with straight sidewalls and high aspect ratio. A HMM composed of Al/Al_2O_3 multilayer structure is used to demonstrate the mode distribution and the behavior of the ENZ slab by simulation. The feature size created in the ENZ lithography system is much smaller than the period of the photomask with high field contrast. Experimentally, periodic patterns with half pitch 58.3 nm at 405 nm wavelength light were achieved by Al/Al_2O_3 ENZ HMM. The principle of the design can be applied to create 2-D patterns by circularly polarized light and lithography system using dielectric photonic crystal at 193 nm. The mode analyses of NHM using h-BN in the mid-IR regime as an example are also discussed. Furthermore, the application can be extended to different metals and light wavelengths, and the ENZ metamaterials with anisotropy have the potential to be exploited in other applications to create periodic structures and directional propagation of waveguide mode with extremely low loss.

CHAPTER 4

Roughness Analyses of Plasmonic Lithography Systems

4.1 Introduction to roughness

Plasmonic photolithography can achieve features beyond the typical diffraction limit. Superlens imaging-based patterning approaches have achieved subwavelength resolution by using a thin slab of metal to amplify the transverse magnetic (TM) polarized evanescent waves, [3,108] therefore capturing the detailed evanescent components to reconstruct a faithful replica of the patterns on the mask with high resolution. In contrast, such evanescent information is mostly lost in the traditional projection-based photolithography due to the limited numerical aperture of the exposure system. [28] In addition, patterns with high degree of uniformity and aspect ratio are required for most of the real-world applications. Unlike the traditional projection lithography that uses either 4:1 or 5:1 reduction of the mask pattern [109], the superlens approach yields essentially a 1:1 imaging. This makes the fabrication of photomasks very challenging, especially when the feature size approaches 10 nm where edge and surface roughness on the mask or thin film are inevitable. It is well known that a nanoscale asperity of metals such as Ag generates localized SP resonance with intensified near-field. The roughness effect on the properties of the metal films and particles [110–113], especially Ag superlens [114–116] have been investigated in some recent works. For example, it has been shown that roughness can enhance the resolution of superlens-based approach [114]. However, one serious question to consider is whether any random roughness on mask patterns or film fundamentally limits the plasmonic-based lithography by amplifying any defects into the exposed PR. In various other works, a stacked metal/dielectric

multilayer structure was proposed to obtain super-resolution by various means including spherical hyperlens [23,50] and negative refraction [117]. Especially, hyperbolic metamaterial (HMM)-based structures can be designed as a filter to allow waves with high spatial frequency to pass through, while suppress other spatial frequencies [13]. Because thin metallic and dielectric films are required to achieve efficient coupling between the SPs at each interface between metal and dielectric, similar concerns regarding the impacts of the roughness in the mask or the thin films on the pattern quality still remain. Indeed, it has been shown in several studies that film roughness distorts the normal propagating and coupling of waves especially on nanoscale films [116,118–120], leading to non-uniform PR patterns with poor profiles [94]. All these non-ideal factors put critical restrictions on the plasmonic-based lithography for practical applications. Thus, it is important to investigate the effects of the surface roughness and line edge roughness (LER) on the performance of plasmonic lithography, which is helpful for the design and estimation of plasmonic systems. In this chapter, [52,53] non-idealities in plasmonic lithography are analyzed such as line edge roughness and single point defects. Systems with spatial frequency selection properties can achieve subwavelength patterns with better uniformity and lower LER.

4.2 The roughness of the films and validation of the simulation

4.2.1 Comparison of the rough surfaces in measurement and simulation

The roughness of the films in both systems are numerically modeled with random roughness and defects. In this model, the surface roughness is defined as the root-mean-square (RMS) *i.e.* standard deviation of the topography. First, we examined a rough metal surface with roughness RMS = 1 nm by atomic force microscope (AFM), as shown in Figure 60A. The measured image is a surface profile of 5 × 5 μm^2 area (256 × 256 pixels) scanned from a Ag film with a thickness

of 20 nm. A random function with 1 nm roughness is generated in COMSOL to mimic the surface topography. The rough surface in Figure 60B is generated by the numerical software (COMSOL Multiphysics© 4.4) with random functions to mimic the real case. The standard deviation for this rough surface is set to be 1 nm, and the average height is set to be 0 nm. Two lines with the length of 2 μm shown in Figure 60C are extracted from the measurement and simulation images, showing similar zero-mean Gaussian contour and spatial spectrum frequency distribution (Figure 60D, E). The number of mesh elements in the simulation is related to the density of knots, which are connected together to form the roughness distributions. The spacing between the two adjacent knots in a rough surface is set to be 6 nm. It is possible to create finer meshes with higher density in the areas of interest. However, the increase in mesh density does not change the result significantly while the computing time raises dramatically. To summarize, in terms of the correlation length, height of roughness and the spatial frequency distribution, the comparable result confirms that the software is feasible to simulate the rough surface.

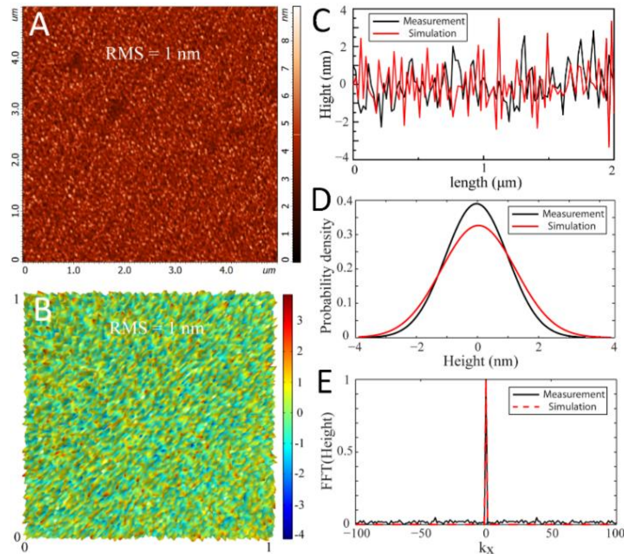

Figure 60 Image and simulation of the rough surfaces.
Rough surfaces from (A) AFM measurement and (B) COMSOL simulation. (C) Two lines abstracted from (A, B) respectively. (D, E) Distributions of height and spatial spectrum frequency corresponding to the lines in (C).

4.2.2. Calculation method of the line edge roughness

LER decribes the roughness of the PR patterns, which plays a critical role in the analyses of a lithography system. To analyze the LER, the most commonly used parameter is the RMS deviation σ (3σ values are usually reported) [121–123]:

$$\sigma = \sqrt{\frac{1}{N}\sum_{y=1}^{N}(z(y) - \bar{z})^2} \tag{58}$$

where z is the height of the point on the rough line along y direction; $\bar{z}$ is the average height of the rough line; N is the total number of the points on the line. In this Chapter, we use the average RMS deviation (σ) of the sidewalls (half peak intensity positions of the periodic field distribution) to describe the LER of the patterns in the PR film.

4.3 The comparison between the superlens and HMM

To fully capture the effects of the surface roughness on the performance of the two different lithography systems, a series of three-dimensional (3D) structures were simulated by using COMSOL. We performed comparisons between the superlens and the HMM by numerical simulations. [52,53] Superlens consists of a thin Ag, while HMM is made of 9 layers of alternating Al and SiO_2. Both systems have TM polarization with 365 nm light as illumination. The OTF curves in the k-space are used to evaluate and analyze and understand the two systems, which is calculated by rigorous coupled wave analysis (RCWA) theory [93,124] for smooth films and simulated by COMSOL for rough films. The theoretical and numerical results for the smooth Ag films agree very well, represented by $|H_t / H_i|$, where H_i and H_t are the incident and transmitted magnetic field of the TM light, respectively.

4.3.1 Performance of the superlens system

Superlens system usually uses a single Ag film to achieve sub-diffraction limited imaging [3,108,125]. In our study, an Ag film with a thickness of 20 nm is analyzed with different surface roughness. A chromium (Cr) mask with a thickness of 50 nm and the period of 90 nm on glass substrate is placed above the superlens with a PMMA spacer. A 40-nm-thick PR film is used to record the image of the mask. To enhance the contrast of the field intensity, a reflective Ag film with a thickness of 50 nm is added to the bottom of the PR film [126], as shown in Figure 61A. The corresponding permittivities of Cr and Ag at the 365 nm wavelength are ε_{Cr} = -8.55+8.96i [127] and ε_{Ag} = -2.4+0.25i [96]; the permittivities of the PMMA, substrate and PR are 2.25, 2.13 and 2.56, respectively. For superlens system with perfectly smooth films, all the evanescent components of the object are captured by the PR to reconstruct a faithful image [3]. Any loss or distortion of the high-k components inevitably affects the quality of the pattern in the PR film [118,119,128]. The cross section and top view of the electric field intensity distribution are shown in Figure 61B, C. The profile, taken from the middle position of PR film, shows a uniform pattern with straight profiles and high intensity contrast. As given in Figure 61D, such a broad OTF enables the evanescent waves of wide wave vector range to pass through the superlens. Therefore, patterns with high fidelity can be produced in PR film. However, when the roughness is introduced to the two surfaces of the Ag film, the amplitude of the OTF curves drops in case of 2 nm RMS; hence the field distribution is severely distorted. Figure 61E shows the intensity distribution of the light passing through the Ag film with surface roughness of RMS = 2 nm, where the intensity at the rough surfaces are locally enhanced significantly and the overall field intensity drops. More importantly, the field distribution in the PR film (Figure 61F) is distorted with obvious LER (RMS ~ 0.65 nm).

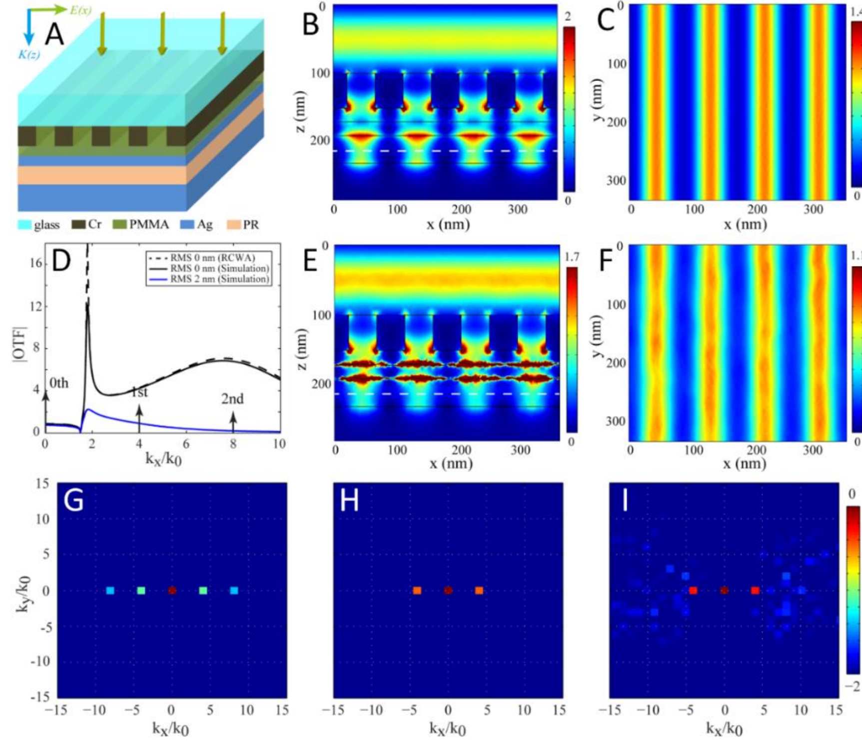

Figure 61 Performance of superlens lithography system.
(A) Schematics (B) Side view and (C) top view of the normalized electric field intensity distribution with smooth Ag film (RMS=0 nm); (D) OTF of a single Ag film with smooth and rough surfaces calculated by RCWA and COMSOL simulation. Arrows give the k-space positions of wave orders diffracted from the grating mask. (E, F) Corresponding simulation results with rough Ag film (RMS=2 nm); (G) A series of diffraction orders in the k-space generated from the grating with period of 90 nm. The distribution of diffraction orders in PR film after transmitted through a single Ag film with roughness (H) 0 nm and (I) 2 nm respectively. The logarithm scale is used in (G-I).

The 2D Fourier spectra of the optical field distribution provides further insight for these phenomena. A series of diffraction orders distributed along k_x direction is gernerated by the diffraction of grating (Figure 61G), where the spatial frequency spectrum is transformed from the magetic field $|H_y|$ component at the collection planes. After passing through a smooth Ag film, only the 0th and a pair of 1st diffracton orders are left in the PR film (Figure 61H). The 0th order is the predominent component. The interference of the $\pm 1^{st}$ orders produces uniform intensity distribution in the PR film. However, if the surface of Ag film is rough with RMS of 2 nm, many chaotic diffraction orders are generated and distributed randomly in the wave vector $k_x k_y$ space

(Figure 61I). Because the superlens can transmit these unwanted diffracted orders, the pattern in PR film is formed with poor profiles due to the complex intereference of these numerous of diffraction orders. One strategy to improve the performance of the system is to use smoother films. Our group developed a technique by introducing Al dopants to Ag by co-sputtering of Al and Ag targets. [120,129,130] Compared with pure Ag films, the SEM and AFM show that the morphology of the Al doped Ag film is much better.

4.3.2 Performance of the HMM system

In the other configuration, HMM composed of alternating metal/dielectric multilayer is designed as illustrated in Figure 62A. As an example, we use a similar stack at the reported work in reference [13] and design the corresponding stacked HMM to pass the $\pm 2^{nd}$ order diffracted waves of the grating. The transmitted diffraction orders interfere and produce uniform periodic patterns in the PR film [13] with the HMM featuring a distinctive filter behavior. To produce similar pattern size as in the superlens case, a grating type Cr mask is used with the period of 360 nm (*i.e.* four times that of the mask period in the Ag superlens case). The mask has much larger period than the actual patterns, so the mask can be fabricated by conventional UV lithography or laser interference lithography [131–133]. The HMM is composed with 9 layers of Al (15 nm) and SiO_2 (30 nm) films, which makes the spatial frequency of the desired diffraction orders coincide with the peak of transmission in the OTF. The reflective film is an Al film with a thickness of 50 nm. The permittivity of Al at 365 nm is ε_{Al} = -19.4+3.6i [127]. Other parameters are kept the same as that of the superlens lithography system. In the HMM lithography system, the calculated OTF for the Al/SiO_2 multilayer features a distinctive transmission window as shown in Figure 62D, which serves as a filter that only allows waves with wave vector $1.5k_0 < k_x < 2.5k_0$ to pass through. It is

noted that only few resonant peaks appear in the OTF curve for the 9 layer SiO_2/Al HMM due to the light absorption in the Al films [37,44,134].

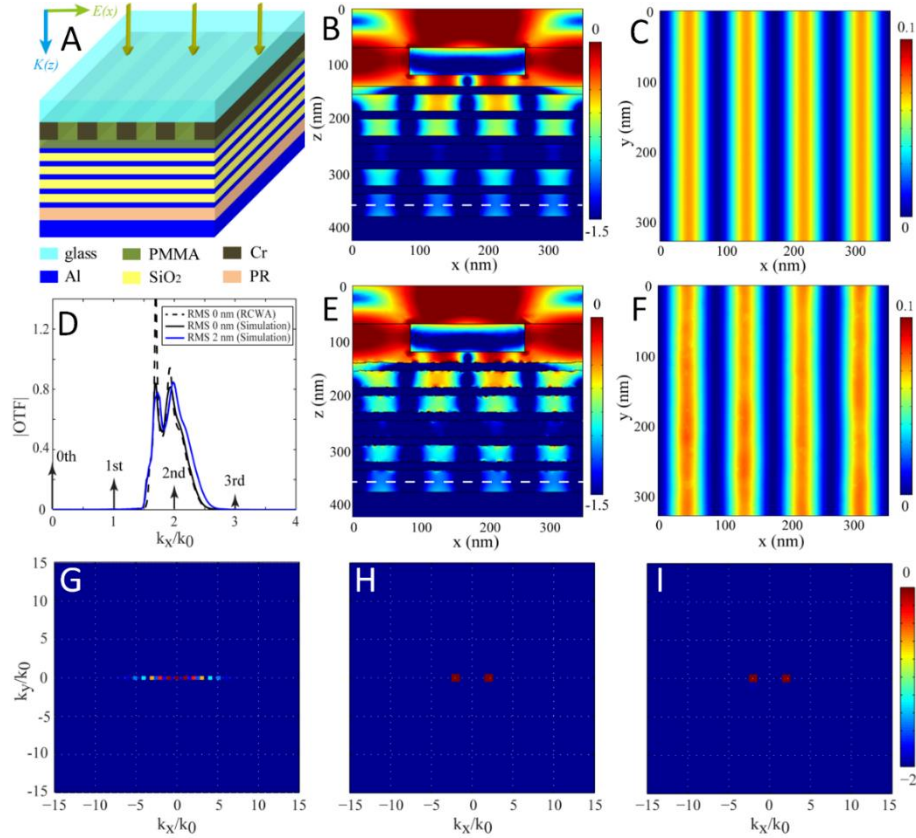

Figure 62 Performance of HMM lithography system.
(A) Schematics (B) Side view and (C) top view of the normalized electric field intensity distribution with smooth multilayer films (RMS=0 nm); (D) OTF of alternating 9 films of Al (15 nm)/ SiO2 (30 nm) with smooth and rough surfaces calculated by RCWA and simulation. Arrows show the k-space positions of wave orders diffracted by grating mask. (E, F) Corresponding simulation results with rough multilayer (RMS=2 nm); (G) A series of diffraction orders in the k-space generated from grating with period of 360 nm. The distribution of diffraction orders in PR film after transmitted through multilayer with roughness (H) 0 nm and (I) 2 nm respectively. The logarithm scale is used in (B, E, G-I).

Light can be coupled by grating equation $k_x = nk_0 sin\theta + 2\pi m/\Lambda$, where n is the refractive index of substrate, k_0 is wave vector in free space, θ is the angle of incidence, m is the order of diffraction wave, and Λ is the period of grating. When the 365-nm light normally is incident onto the grating mask, only $\pm 2^{nd}$ order diffraction waves with the wave vector about $2k_0$ can pass

through the multilayer, while other diffraction orders are strongly suppressed. The period of the interference pattern can be calculated by: $P = \Lambda/(2m)$, which is shown in Figure 62B, C. Form Figure 62D, the amplitude of the OTF curve stays about the same for the rough multilayers, and the peak shift slightly to higher-k. Therefore, even with RMS = 2 nm roughness on each surface of the multilayer structure, the transmission performance remains comparable to the RMS = 0 nm case. The field distribution in the middle of PR film confirms that the interference patterns are intact without obvious distortions, and the maximum intensity maintains about the same level. A comparison of 2D Fourier spectra can been seen in Figure 62G-I. Because of the larger period of grating on the mask, there are more diffraction orders distributing along k_x than that in the superlens case. After transmitting through the multilayer with RMS roughness 0 nm or 2 nm, only ±2nd diffraction orders with equal amplitude remain, whose intereference still produces uniform patterns in the PR film, with minimal dependence on the rough films.

The LER, field intensity, and field components for both systems with different surface roughness are compared in Figure 63a-b. The intensity is defined as the average peak intensity and the LER is calculated as the average RMS deviation at the positions along the sidewall of the patterns. For the superlens system, as the RMS roughness of the Ag film increases from 0 nm to 3.5 nm with 0.5 nm increments, the LER of the pattern in PR film increases from about 0 nm to 1.4 nm, which is denoted by the black squares. Meanwhile, the peak intensity decreases drastically from ~1.1 to ~0.67 V^2 / m^2 (denoted by the blue dots). For the HMM system, the corresponding LER increases from about 0 nm to 1.0 nm, which is lower than that in the superlens system. Because the loss in Al is higher than that of Ag at 365 nm wavelength, the intensity of the pattern transmitted through the HMM diminishes by more than one order of magnitude compared to that through a single Ag

film. However, the intensity is stable as the surface roughness increases, which is different from the decreasing trend in the superlens system.

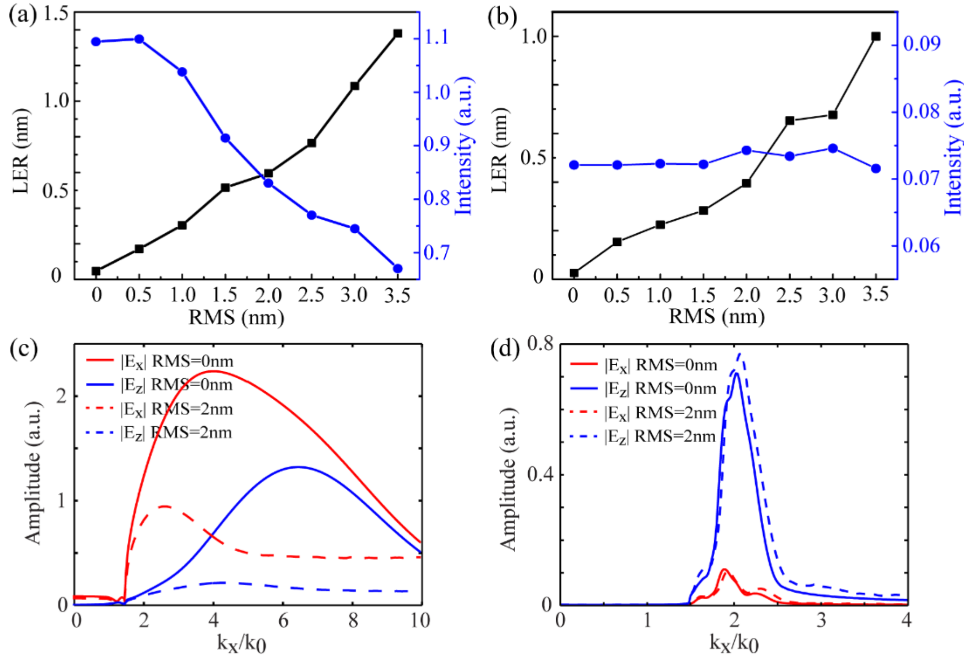

Figure 63 LER and electric field intensity variation of the patterns in the PR film.
As the RMS roughness increases in (a) superlens and (b) HMM, respectively. Normalized transmission amplitude of electric field components at the middle position of PR film corresponding to the (c) superlens and (d) HMM with smooth and rough surfaces. All these data are extracted from the COMSOL simulation with the reflective layers involved in the two systems.

To further understand the impacts of the roughness in real lithography systems, the electric field is also analyzed in the simulations with the reflective layers considered. Figure 63c-d show the electric components of the field as a function of normalized wavevector in the two systems with and without roughness, respectively. The distributions of E_x and E_z in the superlens system and HMM system verify their corresponding broadband evanescent transmission and filtering performance. Meanwhile, the total electric field intensity of the patterns can be calculated by $|\bar{E}_x + \bar{E}_z|^2$ for a TM polarized wave, where $\bar{E}_x$ and $\bar{E}_z$ are the transmission amplitudes of the electric field components extracted from the PR film. In the high-k limit, the phase difference between $|E_x|$ and $|E_z|$ components are about π/2, which will cause a half-pitch shift in the

distribution of $|\bar{E}_x|^2$ and $|\bar{E}_z|^2$ [135,136]. Additionally, the ratio between the electric field components $|E_x|$ and $|E_z|$ plays a crucial role in obtaining an image with high fidelity. But the main conclusion is that the high ratio of $|E_x|^2/|E_z|^2$ is desired to form an image with good fidelity. When taken the entire film system including the reflective layer into consideration, for the superlens structure, both $|E_x|$ and $|E_z|$ components drop drastically when the Ag layer changes from a smooth film to a rough one with RMS roughness 2 nm (Figure 63c), and the ratio of $|E_x|/|E_z|$ for the 1st order clearly decreases. While for the HMM structure, both $|E_x|$ and $|E_z|$ components hold well as the roughness increases (Figure 63d), showing its immunity to surface roughness introduced in patterning process.

4.3.3 Comparison of the electric field components

To compare the electric field distribution, we start from a simple analytic prediction. The distribution of the electric field components is analyzed *via* simulations with the reflective layers involved. For a TM wave, the electric field components in PR can be written as [7,137]:

$$\begin{cases} E_x(z) = \dfrac{k_z}{\omega\varepsilon_0\varepsilon_{pr}} H_y(z) \\ E_z(z) = \dfrac{-k_x}{\omega\varepsilon_0\varepsilon_{pr}} H_y(z) \end{cases} \tag{59}$$

where $H_y(z)$ is the y component of the magnetic field; $E_x(z)$ and $E_z(z)$ are the x and z components of the electric field, respectively; k_x and k_z are the wavevectors with $k_x^2 + k_z^2 = \varepsilon_{pr}k_0^2$. If the feature size Λ_p of the mask in the transverse direction is much smaller than the wavelength, $k_x \sim 2\pi/\Lambda_p \gg k_0$, the wavevector along the z direction can be simplified as a function of the parallel wavevector k_x

$$k_z = i\sqrt{k_x^2 - \varepsilon_{pr} k_0^2} \approx i k_x \tag{60}$$

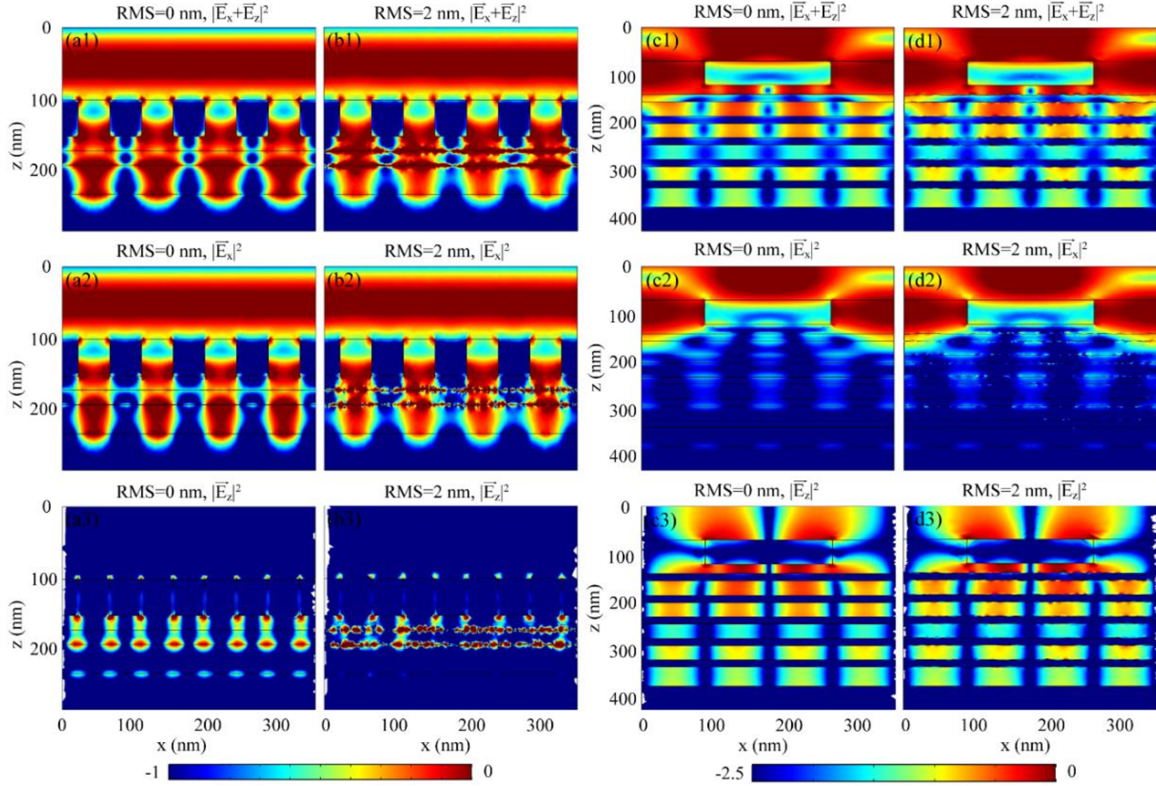

Figure 64 Electric field distribution to analyze the mode.
Normalized distributions of $|\bar{E}_x + \bar{E}_z|^2$ (top panel), $|\bar{E}_x|^2$ (middle panel), and $|\bar{E}_z|^2$ (bottom panel) in the lithography systems with (a) smooth superlens, (b) rough superlens, (c) smooth HMM, and (d) rough HMM. The logarithm scale is used in this figure.

In this high-k limit, the phase difference between $\bar{E}_x$ and $\bar{E}_z$ components is about $\pi/2$, which will cause a half-pitch shift between the distribution of $|\bar{E}_x|^2$ and $|\bar{E}_z|^2$ [135,138]. Generally the total electric field intensity of the pattern can be calculated by $|\bar{E}_x + \bar{E}_z|^2$ for a TM polarized wave. Due to the natural shift between the two electric components for the high-k evanescent waves, if $|\bar{E}_x|$ and $|\bar{E}_z|$ have equal amplitude of transmission, blurred pattern will be formed in the PR film. Therefore, high ratio of $|\bar{E}_x/\bar{E}_z|^2$ is desired to form an image with good fidelity. For this reason, the distribution and ratio of the field components can be used to evaluate the performance of the two systems.

The phase difference and the associated intensity shift can be confirmed by the simulation in both superlens and HMM lithography systems, as shown in Figure 64. The dominance and distribution of $|\bar{E}_x|^2$ and $|\bar{E}_z|^2$ components are different in the two systems. For the superlens system, the component $|\bar{E}_x|^2$ dominates the imaging area; while the component $|\bar{E}_z|^2$ is much weaker and is not located at the imaging position, as shown in Figure 64a1-a3. In addition, when switching from a smooth Ag film to a rough one with RMS roughness of 2 nm, both $|\bar{E}_x|$ and $|\bar{E}_z|$ components drop down drastically (Figure 64b2-b3). While, the ratio of $|\bar{E}_x/\bar{E}_z|^2$ for the 1st diffraction order ($4k_0$) decreases from 11.1 to 9.9, indicating that the quality of the pattern (*e.g.* intensity and fidelity) gets worse according to the foregoing analyses. However, for the HMM system, the component $|\bar{E}_z|^2$ is dominant in the PR film; while the distribution of the component $|\bar{E}_x|^2$ shift a half period compared with that of component $|\bar{E}_z|^2$, as shown in Figure 64c1-c3. Furthermore, both $|\bar{E}_x|$ and $|\bar{E}_z|$ components hold well as the roughness increases (Figure 64d2-d3). The ratio $|\bar{E}_z/\bar{E}_x|^2$ for the 2nd diffraction order ($2k_0$) even increases a little from 76 to 80, maintaining its stable performance regardless of the surface roughness in the patterning process.

In addition, the contribution of E_x and E_z is also related to the different types of modes excited in superlens and HMM lithography systems. In the superlens lithography system, $|E_x|$ component is dominant (Figure 63c and Figure 64a-b), meaning that the waves propagate vertically along the z direction. Whereas, in the HMM lithography system, $|E_z|$ component is dominant (Figure 63d and Figure 64c-d), corresponding to the ±2nd order diffracted waves propagate laterally. This behavior makes it possible for the two high-k waves to interfere with each other, resulting in periodic patterns in the PR film beneath it.

4.3.4 Waveguide lithography using frequency selection principle

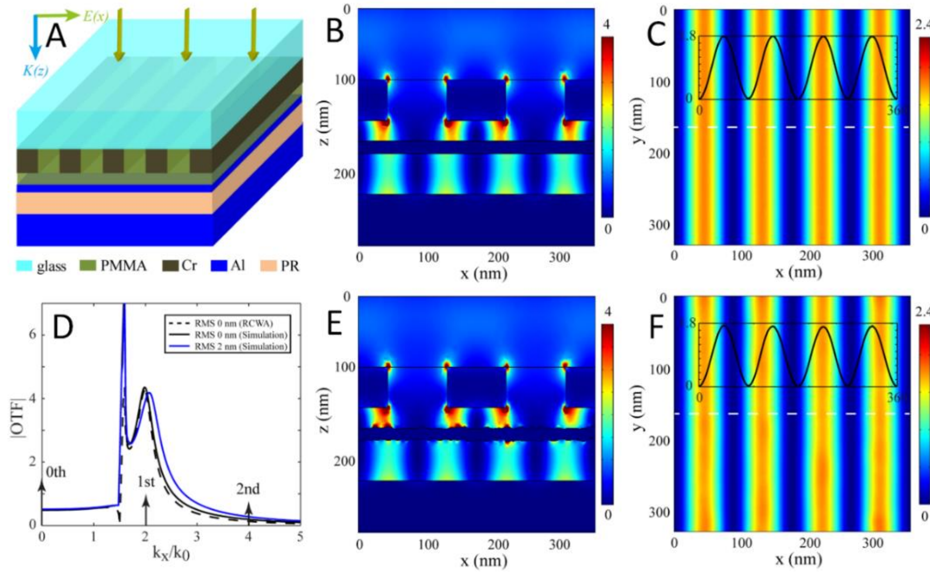

Figure 65 Roughness performance of the waveguide lithography system.
(A) Schematics (B) Side view and (C) top view of the normalized electric field intensity distribution with smooth Al film (RMS=0 nm); (D) OTF of a single Al film with smooth and rough surface calculated by RCWA and simulation. Arrows show the k-space positions of wave orders diffracted by the grating mask. (E, F) Corresponding simulation results with the rough Al film (RMS=2 nm). The inset corresponds to electric field distribution at the dashed line.

To validate the generality of the above conclusion, we carried out similar analysis in a the plasmonic lithography system based on waveguide [34], which is discussed earlier. Though the structure looks almost identical to the superlens system, the thin metal film serves as a filter. Therefore, the system has inherent spatial frequency selection property, which leads to the observed uniform and high-aspect-ratio pattern over cm^2 area. Figure 65 is a schematic of the waveguide lithography system at 365 nm light illumination and Al film thickness of 12 nm. In the roughness analysis, the period of the grating mask is 180 nm, and only the $\pm 1^{st}$ order of the diffracted waves are allowed to pass through while the 0th and other high orders are blocked. As expected, the pattern in PR film with period of 90 nm shows high contrast and straight edges, and this performance is less affected by the rough surface of Al film with RMS of 2 nm, as shown in

Figure 65. Its robust performance further confirms the analyses of spatial frequency selection principle. In addition, the same metal can function differently in different schemes and wavelength range. For example, the thin Al film functions as a spatial frequency filter in forgoing analyses, but works as a superlens in DUV range [139]. Al film based superlens system is capable of imaging at 193 nm wavelength as well.

Compared with superlens and hyperlens capable of making arbitrary patterns, one concern of the filtering approach is that it can only produce periodic pattern based on interference. The main point of this roughness study is the trade-off between the ability to image arbitrary patterns and the sensitivity to the variations on the films and masks. In fact, deep-subwavelength periodic patterns (*i.e.* dense line and spacing) are the gold standard for lithography testing and characterization. Large-area periodic patterns can find applications in many fields such as wire grid polarizers and structural color filters for liquid crystal displays (LCDs), self-cleaning and anti-reflective surfaces for photovoltaic devices, as well as patterned surfaces to suppress the bacteria growth.

4.3.5 Effect of rough surface on SP excitation

In order to analyze the the excitation of the localized surface plasmon (LSP) resonance by the randomness at the rough surfaces of the films, the grating excitation of the SP is introduced first. Because of the mismatch in the wavevector, SP cannot be excited on a metal surface directly by the light in the free space. However, it can be excited by light illuminating on a grating, since the periodic grating can provide additional momentum to match the wavevector of the SP.

$$k_{sp} = nk_0 sin\theta + m(\frac{2\pi}{P}) \quad (61)$$

where n is the index of substrate; k_0 is the free space wave vector; θ is the incident angle; m is the order of diffraction wave; P is the period of the grating.

More generally, the rough surface can be considered as the superposition of many gratings with different periodicities and orientations. For the distribution of the random roughness, the correlation function can be used to describe the spatial distance between the two points on the rough surface. Kretschmann defined a statistical correlation function for a rough surface [140,141]:

$$G(x,y) = \frac{1}{a}\int_0^a z(x',y')z(x'-x,y'-y)dx'dy' \tag{62}$$

where z is the height above the mean surface height at the (x,y) position, and a is the area of integration. Assuming that the statistical correlation function has a Gaussian form

$$G(x,y) = \delta^2 \exp(-\frac{r^2}{l^2}) \tag{63}$$

where δ is the RMS height; r is the distance from the point (x,y); and l is the correlation length. Then the Fourier transform of the correlation function G is

$$|s(k_{surf})|^2 = \frac{1}{4\pi} l^2 \delta^2 exp(-\frac{\delta^2 {k_{surf}}^2}{4}) \tag{64}$$

where the values of k_{surf} correspond to the different periods of the gratings at different directions in the wavevector space. The valuve of s is a measure of the number of each spatial freqnuency k_{surf}. If the surface has only one Fourier component of roughness (*i.e.* the surface profile is sinusoidal), then the s is discrete and exists only at $k = 2\pi/P$, resulting in a single direction for SP coupling. For a random surface, s becomes continuous, meaning that the coupling becomes

possible at multiple directions. We can conclude that the rough surface can lead to a series of exciations of the LSP.

4.3.6 Fourier transform of 2D field distribution

According to the Fourier transform theory, the electromagnetic field in the x-y space can be transformed to the wavevector k_x- k_y space.

$$(u, v) = \frac{1}{XY}\sum_{x=0}^{X}\sum_{y=0}^{Y} f(x, y)e^{-j2\pi(u\frac{x}{X}+v\frac{y}{Y})} \tag{65}$$

where f is the field component at (x, y) position; X and Y is the maximum position in x and y direction, respcetively; u and v is the horizontal and vertical cordinates in Flourier space, respectively. If define $\Delta k_x = \frac{2\pi}{X}, \Delta k_y = \frac{2\pi}{Y}$, eq. (65) can be transfered to:

$$\left(k_x, k_y\right) = \frac{1}{XY}\sum_{x=0}^{X}\sum_{y=0}^{Y} f(x, y)e^{-j(k_x x+k_y y)} \tag{66}$$

Where f is the magnetic field $|H_y|$ component in the real space.

4.4 Other systems and result

4.4.1 Impact of isolated defects on the mask

The quality of the mask also plays an important role in sub-diffraction lithography. The impact of defects on the mask layer is also evaluated in both superlens and HMM systems. The structures are kept the same as previous studies, with an isolated asperity with the radius of 10 nm on the grating masks, as given in Figure 66. In the superlens lithography system, the point defect feature

in the mask is transferred and reproduced in the PR film because of its broad passband, leading to a dip with weak intensity in the PR pattern (Figure 66B, C). However, in the HMM lithography system, the defect merely causes the phase change in the interference, rather generates severe intensity variation in the PR film Figure 66D, E). Therefore, the impact of a single defect on the mask layer in superlens system is much greater than that in HMM system. In other words, there is a tradeoff between the superlens and HMM systems for arbitrary patterns and periodic patterns. Though the superlens system offers the capability of replicating arbitrary patterns, inevitably it reacts much more sensitively to any imperfections of the thin film and the mask. On the other hand, the HMM system has the spatial frequency selection properties, is more immune to such imperfections than the superlens.

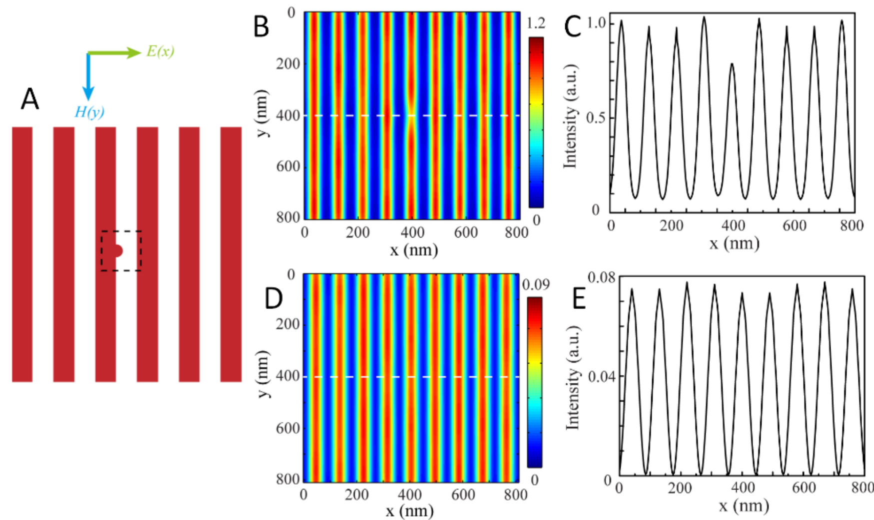

Figure 66 Performance of isolated particle on the mask.
(A) Schematic of the defective grating mask. (B, D) Normalized electric field intensity distribution in the PR film of superlens and HMM lithography systems, respectively. (C, E) Corresponding intensity distribution at the dashed lines positions in (B, D).

4.4.2 Effect of rough mask in plasmonic lithography

The grating masks with rough surfaces are simulated in both superlens and HMM lithography systems, which are shown in Figure 67. When the TM polarized light illuminates on the grating

with RMS roughness of 2 nm, the sub-diffraction limited features can be reconstructed in the PR film for both systems. In addition, as the RMS roughness increases form 0 nm to 3.5 nm, the LER increases gradually in both systems. Due to the LSP excited on the rough surface of mask, non-uniform intensity distribution is delivered to the PR film. Meanwhile, the intensity of the patterns decreases slightly, which is because of the light scattering at the rough grating cuts down the transmission. However, with the same RMS roughness, the quality of the pattern formed in superlens system is impacted more severely than that in HMM system. Additionally, comparing the simulation of rough surface on films and gratings, it is observed that the pattern in the PR film is more sensitive to rough films than to rough gratings.

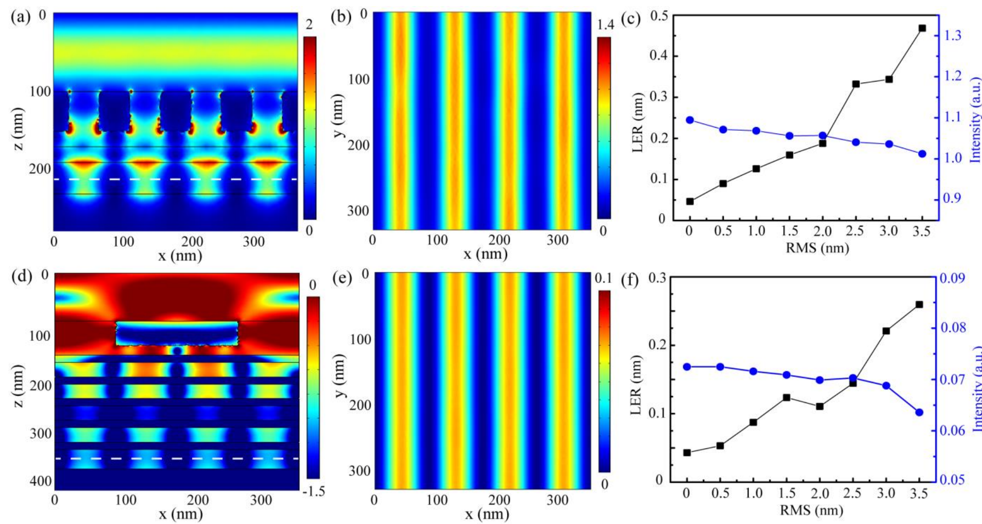

Figure 67 Effect of rough mask.
Side view (a) and top view (b) of the normalized electric field intensity distribution in superlens system with RMS =2 nm on the mask surface. (c) LER and intensity variation of the pattern in PR film as the RMS increases. (d, e, f) Corresponding simulation results in the HMM system with rough surface of mask. The logarithm scale is used in (d). The dashed lines give the positions of collection planes in the patterns.

4.4.3 Different functions of metal films at different wavelengths

Superlens is designed to provide broad transmission passband but HMM acts as a filter which has much narrower passband. However, even for the same metal, it can function diversely in different

schemes or wavelengths. Figure 68a-b shows the dispersions of Ag (20 nm-thick) film and Al (12 nm-thick) film, respectively. Here, the permitivities of Ag and Al are calculated based on the Drude model [7,142]. For the Ag film, the dispersion shows a broad passband near the wavelength of 365 nm. Therefore, it is advantigous to be used as a superlens in imaging. However, the Al film has a narrow passband at the wavelength of 365 nm, which is helpful to transmit a single k-vector mode. In addition, the thin Al film functions as a spatial frequency filter in the foregoing analyses, but works as a superlens in the deep ultraviolet (DUV) range [143]. Figure 68c shows the OTF of Al film at the working wavelength of 193 nm. It presents a broad passband range of 0~5 k_0. In this case, a grating mask with period of 90 nm can be reconstructed very well in the PR film, which is shown in below Figure 68.

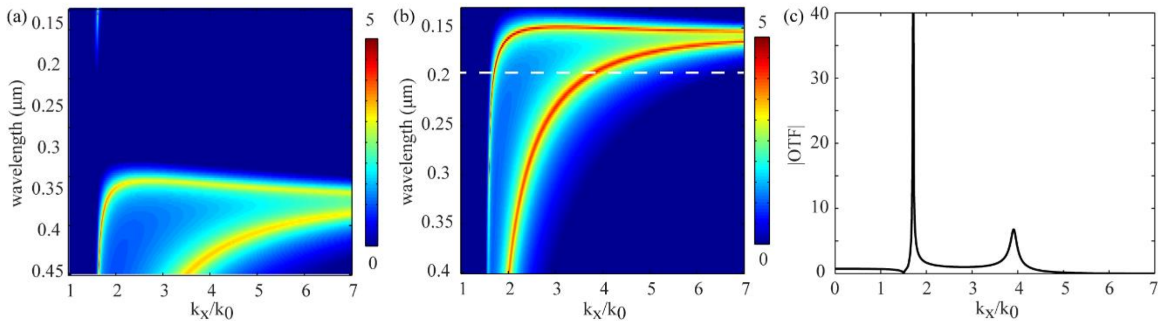

Figure 68 Superlens using Al at 193 nm.
(a, b) Dispersions of Ag film (20 nm-thick) and Al film (12 nm-thick), respectively. (c) OTF of Al film (12 nm-thick) at wavelength 193 nm (the dashed line positon in (b)).

The structure in Figure 69a is almost identical to the Ag film-based superlens system, except that the thin metal film is an Al-based film with thickness of 12 nm. In the case of smooth film, the normalized intensity distribution imaged from the 90 nm-period grating mask is shown in Figure 69b. The cross-section, taken from the middle position of PR film, shows a uniform pattern with straight profiles and high intensity contrast (Figure 69c). However, when the roughness of RMS = 2 nm is introduced to the both surfaces of the Al film, the field distributions are severely distorted

(Figure 69e-f). The pattern produced in the PR film presents sinuous profiles and large LER. Meanwhile, the intensity of the patterns is reduced dramatically (Figure 69d). These behaviors are the same as the Ag film-based superlens system. Since the broad passband of evanescent waves, the effects of roughness cannot be suppressed, which result in poor profiles on the patterns.

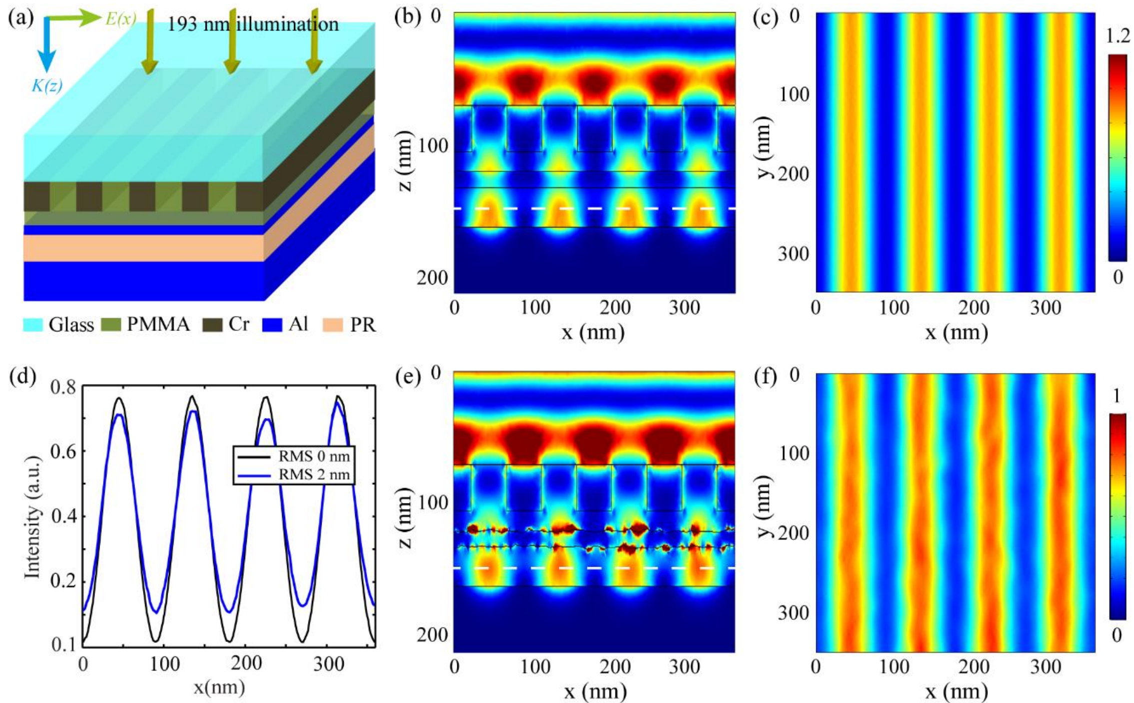

Figure 69 Roughness of plasmonic lithography with an Al film-based superlens.
(a) Schematics The working wavelength of the system is 193 nm. (b) Side view and (c) top view of the normalized intensity distributions with smooth Al film (RMS=0 nm); (e, f) Corresponding simulation results with rough Al film (RMS=2 nm); (d) Normalized intensity distributions extracted from the dashed line positions in (b, e).

4.5 Summary

In this chapter, two plasmonic lithography systems with rough films are simulated and analyzed systematically. For the superlens system, as the surface roughness of the Ag film increases, the LER of the patterned PR grows gradually, and the corresponding intensity decreases dramatically. This behavior is ascribed to the broad passband of the Ag film and the localized SP scattered by the rough surface, which result in poor profiles on the patterns. In contrast, the OTF of the HMM

system presents a function of spatial frequency selection, which naturally suppresses the impacts of rough surfaces and leads to steady interference with the selected diffracted waves. As a result, with the increasing surface roughness on the Al/SiO_2 multilayer, the LER of the pattern imaged by the HMM increases slightly while the field intensity is stable. Additionally, the HMM system is more tolerant to the isolated defects on the mask. The benefits of this filtering-based design are also verified by a waveguide lithography system. Therefore, spatial frequency selection is an optimal way to construct periodic patterns in subwavelength lithography. In addition, the same metal can function differently in different schemes and wavelength ranges. An Al film-based superlens system is capable of imaging at a wavelength of 193 nm, which also presents sensitivity to the roughness due to its broad passband of evanescent waves. These analyses give new insights into plasmonic nanopatterning, and can be a useful guideline in designing future plasmonic lithography systems.

CHAPTER 5

Applications and Other Plasmonic Works

5.1 Photonic spin Hall effect

5.1.1 Mie scattering of dielectric particles

In Chapter 4, the effects of an isolated particle on the photomask are discussed. In this chapter, Mie scattering of the dielectric particles are discussed, including its near-field and far field performance, and explored their applications in lithography. Electromagnetic scattering from dielectric nanometer-scale objects [144–151] has long been a topic of great interest. Due to their various resonances, Dielectric particles are useful in many fields including optical cloak, [152] metamaterial [150,153], unique backscattering property [146,154], non-radiative scattering [155], chiral properties [156], and hologram [157,158]. To identify the Mie resonances, both high index dielectric particles including silicon (Si) particles and low index particles such as silicon dioxide (SiO_2) are investigated. For a spherical dielectric particle, the resonance can be calculated analytically by Mie theory. The scattering cross section (SCS) and extinction cross section (ECS) of the Dielectric particles can be expressed in eq. (67) and (68), respectively [145,151,159]. The cross sections have the same unit as the effective aperture area m^2. Both SCS and ECS are functions of a_n and b_n, which are the Mie coefficients for electric field and magnetic field expanded in spherical coordinate.

$$\sigma_{sca} = \frac{2\pi}{k^2}\sum_{n=1}^{\infty}(2n+1)(|a_n|^2 + |b_n|^2) \quad (67)$$

$$\sigma_{ext} = \frac{2\pi}{k^2} \sum_{n=1}^{\infty} (2n+1) Re(a_n + b_n) \tag{68}$$

The coefficients a_1, b_1, a_2 and b_2 represent the contributions from electric dipole (ED), magnetic dipole (MD), electric quadrupole (EQ) and magnetic quadrupole (MQ), respectively. [160,161] The contribution from each individual component can also be derived using σ_{sca} and σ_{ext}. [159] The peaks of each resonance in σ_{sca} and σ_{ext} curves depend on the size and refractive index contrast between the particle and the host. For a Si particle with a radius of 50 nm, the total ECS as well as the ED and MD resonances as a function of the wavelength calculated by Mie theory are shown in Figure 70A. Therefore, the electric dipole moment of the Si particle are proportional to the incident electromagnetic field, defined as $\bar{p} = \epsilon_0 \alpha_e \bar{E}$ and $\bar{m} = \frac{1}{\mu_0} \alpha_m \bar{B}$; where the polarizability of the ED and MD are $\alpha_e = \frac{6\pi i}{k_0^3} a_1$ and $\alpha_m = \frac{6\pi i}{k_0^3} b_1$, respectively. In the Rayleigh limit, when $nk_0 r_0 \ll 1$, α_e and α_m approach the quasi-static limit, $\alpha_e|_{nk_0 r_0 \ll 1} = 4\pi r_0^3 \frac{n^2-1}{n^2+2}$ and $\alpha_m|_{nk_0 r_0 \ll 1} = 4\pi r_0^3 (n^2-1) \frac{k_0^2 r_0^2}{30}$. For a Si particle with a radius of 50 nm, the ED resonance is around 405 nm and the MD resonance is around 466 nm.

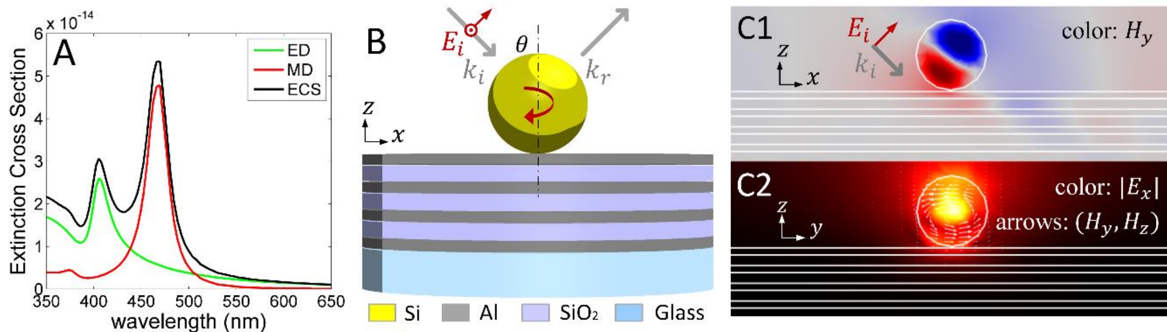

Figure 70 The ED and MD of a Si particle with radius of 50 nm.
(A)The ECS of the particle and the corresponding ED and MD contribution. (B) Schematics of the subwavelength Si particle sitting on the HMM made of Al and SiO_2. The red arrow indicates the electric field and the grey arrows refer to the incident and reflected wavevector with an angle of incidence θ. (C) The electromagnetic field for a Si particle siting on HMM with 405 nm light

illumination and 45-degree angle of incidence of TM polarized plane wave. (C1) The magnetic field H_y in xz plane and (C2) the electric field $|E_x|$ and magnetic vector (H_y, H_z) in the yz plane.

By simply putting the particle on top of a hyperbolic metamaterial (HMM) system, we can study the near field scattering of the particle in a plasmonic lithography system. We still focus our effort on the light with a wavelength of 405 nm. The scheme of the light scattering of the Si particle on the HMM is shown Figure 70B. The HMM is made of 7 layers of 10 nm aluminum (Al) and 15 nm SiO_2 deposited on a glass substrate, and it's a type II HMM with $\epsilon_{xx} < 0$ and $\epsilon_{zz} > 0$. To study the near field coupling inside the HMM, the incident light is tuned to have transverse electric (TE) and transverse magnetic (TM) polarizations, circular polarization and diagonal polarization with various angles including 0, 15, 30, 45, 60 and 75 degrees. Because of the metallic property of the HMM, the reflection of the light is also very strong. Given that the incident wavevector in xz plane has an angle of incidence θ, electric field can be decomposed as $\bar{E} = \hat{x}\bar{E}_x + \hat{y}\bar{E}_y + \hat{z}\bar{E}_z$. The corresponding induced ED moment is proportional to the incident electric field $\bar{p} = \alpha\bar{E}$. Therefore, the induced dipole is oriented as $\bar{p} = [p_x, p_y, p_z]$ accordingly. Interestingly, when the light incidents with an angle, the near field scattering of the nano-particle is asymmetric, which allows us to observe the photonic spin Hall effects. From the plots of the electromagnetic field (H_y and E_x) around the Si particle as shown in Figure 70C, the ED resonance can be clearly seen when H_y has two lobes and $|E_x|$ is confined at the center. When TM polarized incident light has an incident angle of 45°, whose normalized electric field is $\hat{E} = [1/\sqrt{2}, 0, 1/\sqrt{2}]$, the scattered light of the Si particle is coupled to the right side only.

5.1.2 Introduction to photonic spin Hall effects

Intensity, incident angle and polarization characterize the intrinsic properties of a light beam. Among them, polarization has been of particular interest, especially with regard to photonic spin

Hall effects. [162–172] Various applications based on photonic spin Hall effects have been explored, for example, directional light coupling, [163] optical-mechanical detection, [165,173–175] waveguide, [162,164,176] quantum system, [166] meta-surfaces, [177,178] and particle scattering. [169,179] When a polarized beam illuminates a nano-scatter, the scattering of the nanoparticle differs depending on the polarization states of the incident light. These particles are usually placed on a substrate, which might also cause additional background field to the scatters. If the substrate provides a strong reflection, the additional phase change and the associated interference between the incident light and reflected light can also have a significant influence on the particle scattering. This interference and superposition of light induce a circularly polarized dipole, which has polarization dependent scattering properties. [171,172] In addition, researchers have demonstrated that an active circularly polarized radio-frequency (RF) source can be excited inside and outside a HMM for polarization-controlled routing of subwavelength modes. [168] HMM can support plasmonic modes because it is a uniaxial medium with hyperbolic dispersion, as discussed in Chapter 3, leading to various scattering depending on the intrinsic properties of the HMM and the source. These works have proven the principle of photonic spin Hall effects, although the practical applications, especially in the visible range are still lacking.

5.1.3 Circularly polarized dipole

In this study, we show that the phase change in the reflected light can cause photonic spin scattering of nano-particles. When the reflected light has a comparable amplitude and a $\pi/2$ phase difference, a circularly polarized electric dipole can be induced because the components of the electric field is out of phase, *i.e.*, $E_x \sim iE_z$. We exploited the interference between the incident light and reflected light to induce the rotation of the electromagnetic field inside the particle. The circularly particle excited by complex field can be expressed as [171,172]

$$\bar{p} = \frac{p_0}{\sqrt{2}}(\hat{x} - i\hat{z}) \tag{69}$$

The spinning particle can be excited by different ways. [165,166,180] Figure 71 illustrates various ways of excitation for the rotated particle, for example, by oblique or normal incidence of circularly polarized light [169,171], by a highly focused beam [172,181,182], by an evanescent wave [180,183] or by the interference of incident and reflected beam as we proposed. Especially for evanescent wave, since $k_x \gg k_0$ and k_z is imaginary, the electric field is $[k_z, 0, -k_x]\frac{1}{\omega\epsilon_0\epsilon_r}H_y$ with a phase difference between the x and z components. The particle is excited by evanescent waves, when $k_x < k_0$ and k_z becomes imaginary. In the plasmonic lithography applications with a HMM as the reflector, the coordinate and the incident plane is defined in Figure 71. Wave interference [165,173–175,180,184,185] is a fundamental manifestation of the superposition principle when the incident and reflected waves undergoing different phase advances during propagation. Because of the photonic spin Hall effects, the patterns formed in the photoresist (PR) are highly dependent on the light polarizations and the incident angle. We show that the near field of the particle is essential for the coupling and detection of light polarizations.

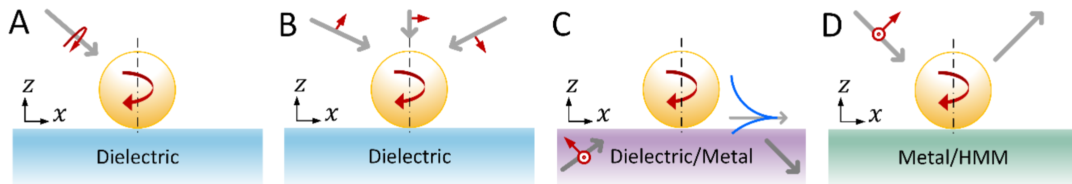

Figure 71 Several ways of excitation of rotated electromagnetic field.
(A) by oblique circularly polarized light (B) by highly focused beam (C) by evanescent waves or SPP (D) by linearly polarized plane wave.

5.1.4 Reflection phase from a reflective material

The scattering of a subwavelength particle sitting on a reflective HMM can be treated in two parts: (1) the excitation of the spinning dipole by the interference of the incident and reflected light, as

well as (2) the scattering of the dipole on top of the structure. For the first problem, the spinning dipole depends on the phase and amplitude of reflection coefficients for TE and TM polarized light r^s and r^p, respectively. The reflection coefficients are determined by the angle of incidence θ, the light wavelength λ , as well as the optical constants of the media at the interface ϵ_1 ,ϵ_{xx} ,ϵ_{zz} and the thickness of the slab d, as given in Figure 70B. For the reflection of TM light, the reflection and transmission coefficients are given in 3.2.4 and eq. (46)-(50). For TE polarized light, the corresponding transmission and reflection coefficients are [186] the following:

$$r^s = \frac{r_{12}^s + r_{23}^s \exp(i2k_{sz}d)}{\alpha} \tag{70}$$

$$t^s = \frac{(1 + r_{12}^s)(1 + r_{23}^s)\exp(ik_{sz}d)}{\alpha} \tag{71}$$

$$r_{12}^s = \frac{k_{1z} - k_{sz}}{k_{1z} + k_{sz}} \tag{72}$$

$$r_{23}^s = \frac{k_{sz} - k_{3z}}{k_{sz} + k_{3z}} \tag{73}$$

$$\alpha = 1 + r_{12}^s r_{23}^s \exp(i2k_{sz}d) \tag{74}$$

where r is the reflection coefficient and t is the transmission coefficient, and the thickness of the slab is d. To calculate the interference of the incident light and reflected light, different light polarizations need to be considered. The TE and TM polarizations are the basis for all other polarization states, which can be treated as the superposition of linear polarized light. Figure 72 shows the reflection amplitude and phase for TE and TM light. The light is incident from air to a glass substrate, and transmits through the HMM consisting of 7 layers of 10 nm Al and 15 nm

SiO2. As shown in Figure 72A1 and B1, the reflection $R_s = |r_s|^2$ and $R_p = |r_p|^2$ are very high (> 65%). The phase change across the HMM surface for both TE and TM cases is close to $-\pi/2$, as given in Figure 72A2 and B2. The reflection also shows a slight angle and wavelength dependence.

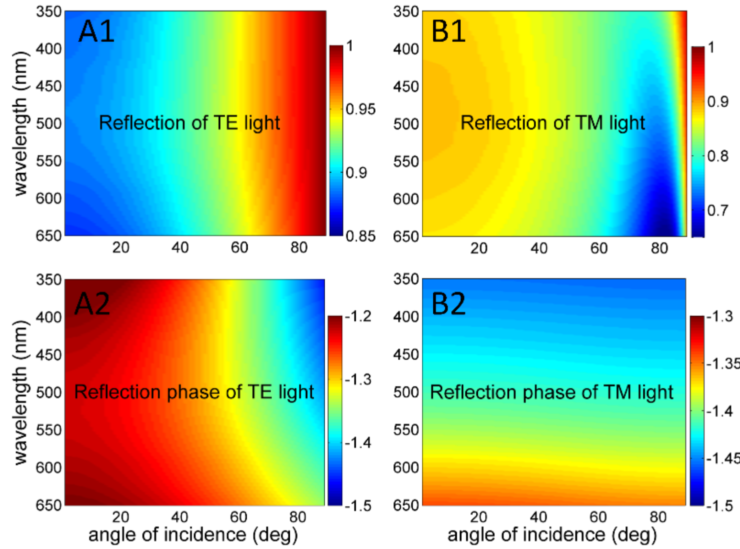

Figure 72 The reflection amplitude and phase of a HMM.
Reflection (A1) R_s of the TE polarized light (B1) R_p of the TM light. The maximum of reflection is one. Reflection phase of the (A2) σ^s TE polarized light and (B2) σ^p TM polarized light, and Note that the -π/2 equals -1.57 and the scale bar are marked in rad.

For TM light, $H_y = H_0\, exp(ik_x + ik_z)$ and the electric field components are listed in eq. (59). Thus, with an incidence angle θ and a light wavelength λ, the normalized incidence vector for the electric field of TM light can be expressed in the xz plane as $\hat{E}_i^p = [cos\,\theta,\ 0,\ sin\,\theta]$, the reflection phase acquired is $r^p(\theta,\lambda) = |r^p|e^{i\delta^p}$. In comparison, for TE polarized light, the magnetic field can be expressed in terms of electric field E_y as:

$$\begin{cases} H_x = \dfrac{-k_z}{\omega\mu_0} E_y \\ H_z = \dfrac{k_x}{\omega\mu_0} E_y \end{cases} \tag{75}$$

Therefore, for the TE polarized light with incidence angle θ and wavelength λ in the xz plane, the normalized incidence vector for the electric field can be expressed as $\hat{E}_i^s = [0,1,0]$, and the reflection phase acquired is $r^s(\theta,\lambda) = |r^s|e^{i\delta^s}$. The reflected field is $\hat{E}_r^s = [0, |r^s|e^{i\delta^s}, 0]$, and the total field resulting from the interference of the incident and reflected light is $\hat{E}_t^s = [0,1 + |r^s|e^{i\delta^s}, 0)]$. Because the induced dipole is proportional to the background light, the induced ED has a normalized dipole moment vector is $\hat{p} = [0,1,0]$. For TM light, the reflected electric field is $\hat{E}_r^p = [-|r^p|e^{i\delta^p} cos\,\theta,\ 0,\ |r^p|e^{i\delta^p}\ sin\,\theta]$, and the total background field due to the superposition is $\hat{E}_t^p = [(1 - |r^p|e^{i\delta^p}) cos\,\theta,\ 0,\ (1 + |r^p|e^{i\delta^p})\ sin\,\theta)$. Therefore, the phase difference between E_{tx}^p and E_{tz}^p $is\ D_p(\theta,\lambda) = \arg\left(1 - |r^p|e^{i\delta^p}\right) - \arg(1 + |r^p|e^{i\delta^p})$, and the amplitude difference between E_{tx}^p and E_{tz}^p $is\ D_a(\theta,\lambda) = \frac{|E_{tz}^p|}{|E_{tx}^p|} = \left|\frac{1+|r^p|e^{i\delta^p}}{1-|r^p|e^{i\delta^p}}\right| \tan\theta$. The amplitude and phase of the reflected light has an impact on the dipole orientation. If we consider the induced electric dipole by the electric field, the dipole moment can be expressed as $\bar{p} = [D_p, 0, D_a]$. If using an ideal case to simplify the problem, assuming the phase change is $-\pi/2$, and the reflectivity is a unit, the unit dipole moment can be expressed as $\hat{p} = [1/\sqrt{2}, 0, -i/\sqrt{2}]$, which is a circularly polarized dipole as we discussed before.

5.1.5 Near field scattering of a dipole on HMM

When the Si particle is placed on top of the HMM, the scattering depends on the resonance cone of the HMM, as shown in Figure 73A. The scattered light is determined by the TE or TM modes supported by the HMM waveguide defined by the following equation: [169,172,182]

$$I \propto \left|\begin{pmatrix} E_{TM} \\ E_{TE} \end{pmatrix}\right|^2 \propto \left|\frac{\sqrt{n^2k_0^2 - k_\perp^2}}{|k_z|} e^{-|k_z|d} \widehat{M} \cdot \bar{p}\right|^2 \tag{76}$$

Where I is the light intensity, and $\widehat{M}$ is the density matrix determined by the properties of the HMM. The light coupling direction is affected by the dipole orientation, and the cooreponding TE or TM enginmodes that it excites. To study the light scattering in lithography system, a simulation of a circularly polarized dipole placing on top of the HMM is carried out. The dispersion of the type II HMM is shown in Figure 73A. The dipole is 15 nm away from the top surface of the HMM and the field is at the interface between the HMM and the glass substrate. Excited by an electric dipole with moment $\bar{p} = [1,0.-i]$, the scattering is asymetric as shown in Figure 73B. The electric field distibution is observed at the interface of the HMM and glass substrate. In addition, the scattering angle and the distribution of the intensity in simulations can be calculated as discussed in Chapter 3.2.4.

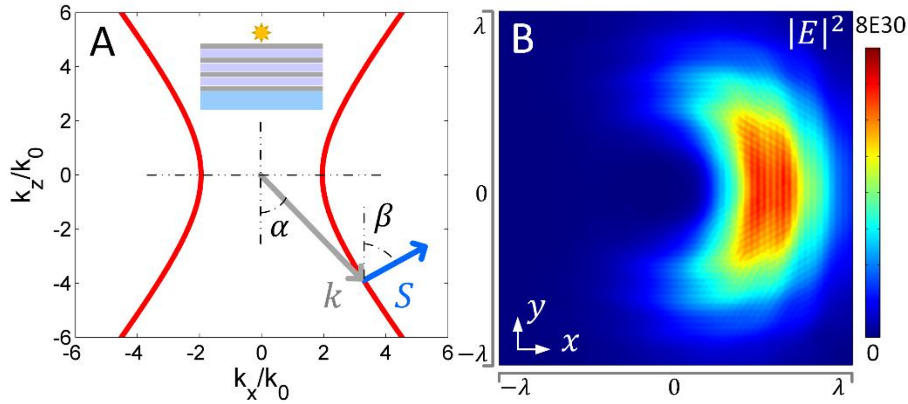

Figure 73 Resonant cone of HMM and circularly polarized dipole.
(A) Resonant cone of a type II HMM. (B) The iso-frequency curve of the HMM composed of 7 layers of 10 nm Al and 15 nm SiO_2. The wavevector $\bar{k}$, pointing vector $\bar{S}$, angle α and β are indicated. The inset shows the schematic of the dipole on the HMM on the glass substrate. (B) The electric field distribution $|E|^2$ in the xy plane.

Not only electric dipole, magnetic dipole and other higher order quadrupoles can also be excited by the interference of TE polarized light. For example, the electromagnetic field of a rotating

magnetic dipole at a wavelength of 466 nm is shown in Figure 74. The Si particle also has a radius of 50nm. Comparing with the what is illustrated Figure 70B, the corresponding electric field E_y and $|E_y|$ in the xz plane is shown to illustrate the magnetic resonance. For a type II HMM, by our study in Chapter 3.6, it allows high-k TM modes but not TE mode modes. Because both horizontal and vertical ED can excite TM wave, the near field scattered light of the particle can be coupled to and transmitted HMM to the glass. However, the MD can excite mostly TE modes, which is reflected by the HMM. The light at 466 nm is coupled, but reflected asymmetrically. For both ED and MD, the performance in the near field light is unidirectional. The symmetry of the field can be applied to other dielectric waveguide or photonic crystal, which is confirmed by our simulation as well. This work provides a new platform to generate the spinning of the particles passively and a potential application of the unidirectional scattering of a rotating emitter by putting it on top of a HMM. These analyses are also applicable to chiral quantum optics.

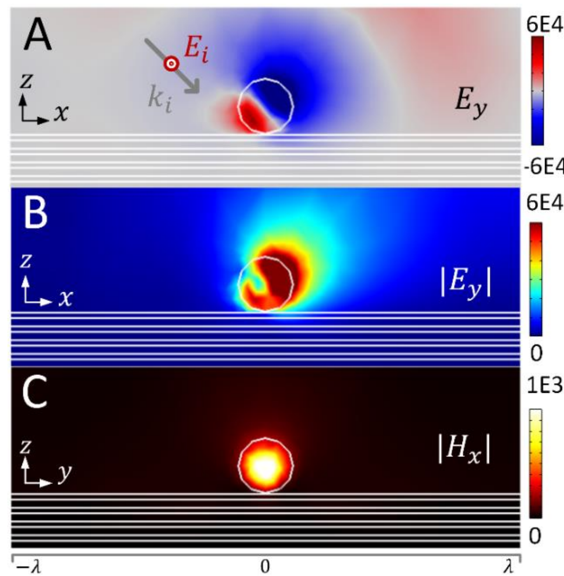

Figure 74 Electromagnetic field for a Si particle siting on HMM with 466 nm light.
Light illuminates with 45° angle of incidence of TM polarized plane wave. (C1) The magnetic field H_y in xz plane and (C2) the electric field $|E_x|$ and magnetic vector (H_y, H_z) in the yz plane.

5.1.6 Scattering by different polarizations

After understanding the general rule, we then turned our attention to several specific cases and their applications in lithography. The result of TE ($\hat{E}_i^s = [0,1,0]$), TM ($\hat{E}_i^p = [cos\,\theta,\ 0,\ sin\,\theta]$), diagonal ($\hat{E}_i^d = \left[\cos\theta/\sqrt{2}, -1, \sin\theta/\sqrt{2}\right]$ with both TE and TM components) [185] and circularly ($\hat{E}_i^c = \left[\cos\theta/\sqrt{2},\ i, \sin\theta/\sqrt{2}\right]$) polarized light with different incident angles are discussed at a wavelength of 405 nm. Figure 75 shows the electric field distribution $|E|^2$ at the interface between the bottom of the HMM and the glass substrate with the TE incidence and various angles of incidence including 0, 15, 30, 45, 60 and 75 degrees. The light scattering in the xy plane is the projection of the electric field component. Since the normalized ED moment is $\hat{p} = [0,1,0]$ for all the incident angles, the field distributions scattered along y-axis are very similar regardless of the light intensity.

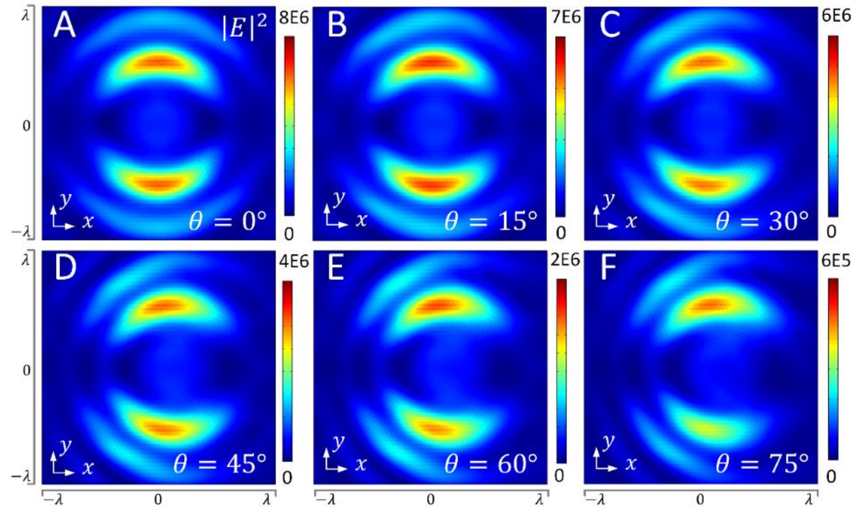

Figure 75 Anglar dependent scattering of TE polarized light.
Electric field distribution at the interface between the bottom of the HMM and the glass substrate with the (A) 0 degree, (B) 15 degree (C) 30 degree (D) 45 degree (E) 60 degree and (F) 75 degree.

Figure 75 shows the angular dependence of $|E|^2$ for the TM polarized light with angles of incidence including 0, 15, 30, 45, 60 and 75 degrees. For TM polarized wave, the dipole is $\bar{p} =$

$[D_p, 0, D_a]$, where D_p and D_a depends on the incident angle. As shown in Figure 75, when the angle is zero degree, the field is symmetric along x-axis. However, when the angle of incidence increases gradually, more of light is scattered along the $+x$ direction, especially at 45° incidence. These results are consistent with the theoretical calculation. When the diagonal polarized and circularly polarized light has $\pi/2$ phase difference, the interference becomes very complex. [185] The scattering of the particle for diagonal polarized light and circularly polarized light are shown Figure 78 and Figure 78. The phase change by planar structures is a function of the angle of incidence, the materials made of the metamaterials and the polarization of the incident light.

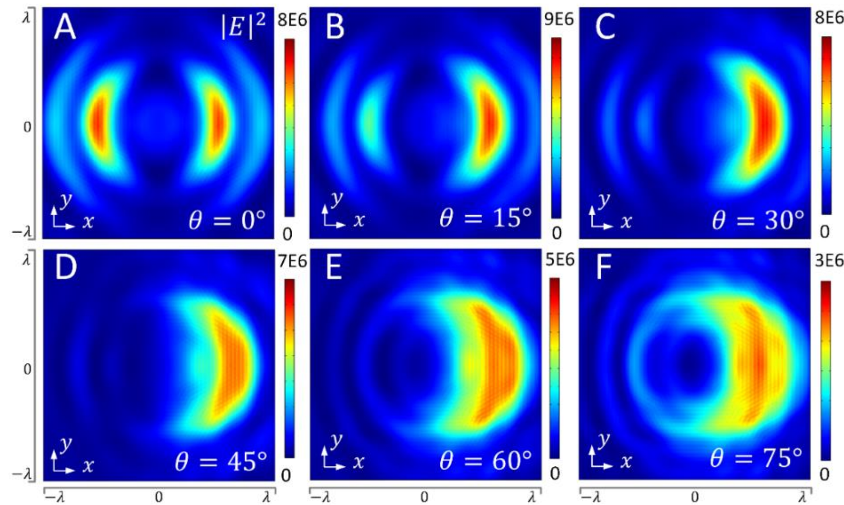

Figure 76 Anglar dependent scattering of TM polarized light.
Electric field distribution at the interface between the bottom of the HMM and the glass substrate with the (A) 0 degree, (B) 15 degree (C) 30 degree (D) 45 degree (E) 60 degree and (F) 75 degree.

We explore the unidirectional scattering of a Si particle on the HMM caused by the photonic spin Hall effects. The HMM can also be substituted by other reflected materials including other metallic and photonic crystal slabs to realize the unidirectional light scattering. Meanwhile, besides the electric dipole resonance, other resonances, for example, magnetic dipole, toroidal dipole, can be excited and examined to observe these phenomena as well. Not only the electric field and the electric field component, but also the magnetic field and the magnetic dipole resonance can

generate the rotated magnetic dipole to provide even more complicated near field and far field radiation. For the photonic spin Hall effects, using leakage radiation microscopy [163,187,188], our simulation result of spin-dependent particle scattering can be confirmed.

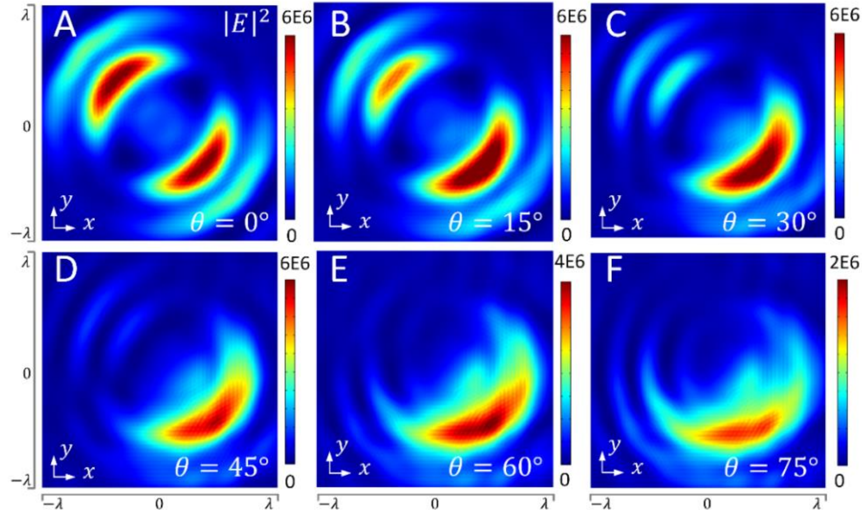

Figure 77 Anglar dependent scattering of diagonal polarized light.
Electric field distribution at the interface between the bottom of the HMM and the glass substrate with the (A) 0 degree, (B) 15 degree (C) 30 degree (D) 45 degree (E) 60 degree and (F) 75 degree.

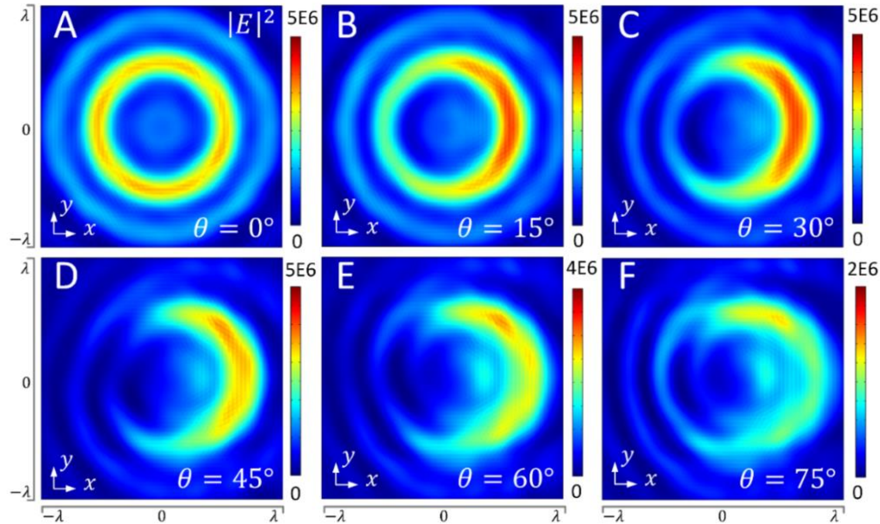

Figure 78 Anglar dependent scattering of circularly polarized light.
Electric field distribution at the interface between the bottom of the HMM and the glass substrate with the (A) 0 degree, (B) 15 degree (C) 30 degree (D) 45 degree (E) 60 degree and (F) 75 degree.

5.2.7 Chiral absorption

Circular dichroism (CD) [189–191] is dichroism involving circularly polarized light, *i.e.*, the differential absorption of left- and right-handed light, which is defined as $\Delta\varepsilon = \varepsilon_L - \varepsilon_R$. Chirality and nonzero CD effect in a molecule are present if a molecule has neither mirror-symmetry planes nor a center of symmetry. In such a case, a molecule acquires a sense of rotation (clockwise or counterclockwise) and hence it reacts on right- and left-handed circularly polarized photons differently and shows a nonzero CD signal. The chirality may appear due to (1) synthesis of nanocrystals involving a chiral adsorbate, (2) the chiral molecular adsorbate, that modifies the surface states, or (3) the chiral distortion of the surface which remains after a chiral adsorbate has been removed. [192] To confirm the conclusions obtained in last section, an optical simulation is performed with a Ag helix nano-particle to mimic the chiral material [193–195], as shown in Figure 79A. The helix has three turns, major radius R of 30 nm, minor radius r of 10 nm and axial pitch h of 50 nm. The Ag helix is placed 100 nm Al on glass substrate, with different light polarizations.

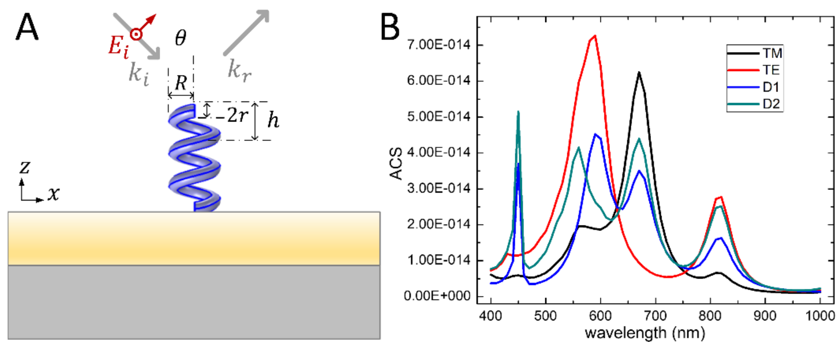

Figure 79 Absorption of a Ag helix particle.
(A) Schematic of the Ag helix on top of Al film with thickness of 100 nm deposited on glass substrate. The geometric parameters are illustrated accordingly. (B) ACS of the helix for the light with TE, TM, D1 and D2 polarization and 45° degree incidence.

For a nanoparticle, electric dipole moment p_e and electric dipole moment p_m can be induced by the incident light. The absorption rate of the particle can be calculated by

$$\sigma^{\pm} = \frac{\omega}{2} Im(\bar{E}^{*} \cdot \bar{p} + \bar{B}^{*} \cdot \bar{m}) \quad (77)$$

Where $\bar{E}$ and $\bar{B}$ are corresponding electric and magnetic field of the background light, and $\bar{p}$ and $\bar{m}$ are induced ED and MD moment. To create complex absorption difference, the helix is shined by light with TE polarized ($\hat{E} = [1/\sqrt{2}, 0, 1/\sqrt{2}]$), TM polarized ($\hat{E} = [0, 1, 0]$), diagonal 1 polarized ($\hat{E} = [1/\sqrt{2}, 1/2, 1/\sqrt{2}]$) and diagonal 2 polarized ($\hat{E} = [1/\sqrt{2}, -1/2, 1/\sqrt{2}]$) light with 45° angle of incidence. The absorption cross section (ACS) as a function of wavelength calculated by simulation in each circumstance is shown in Figure 79B. In COMSOL simulation, the ACS of the Ag nano-particle can be calculated by using the integration of optical loss inside the particle. [196]

$$\sigma_{abs} = \iiint_{V_p} Q_{loss} dV \quad (78)$$

With different polarization states, the resonant peaks in absorption spectra of the particle are distinctive. It is due to the plasmon-induced charge in the electromagnetic field inside the Ag chiral structure, which creates a change in the angle between the effective electric and magnetic dipole. This work provides a new platform to passively generate spin particles, and highlight potential applications of the unidirectional scattering of a rotating emitter by putting it on top of a HMM. In addition, the technique does not require any modification of the chiral structures or sophisticated setup, and could therefore serve as a reliable and easy-to-adopt technique for the characterization of a broad class of chiral materials, as an alternative of CD. These analyses have applications in the detection of polarization change and signal transmission in quantum communication.

5.2 Lidar design

5.2.1 Magnetic resonance for efficient size detection

Mie resonances in high-index dielectric nanoparticles have prominent mode intensities since a large index contrast benefits the field enhancement and the Q factor by high reflection at particle boundaries [144,145,197]. Typical Mie resonances in low-index nanoparticles are weak and broad due to poor light confinement caused by low reflection at particle boundaries, so that the optical properties of low-index nanoparticles do not strongly depend on wavelength. Therefore, in this work, a metal dress created by a two-step deposition process enhances the Mie resonances of low-index nanoparticles by improving the light confinement ability. The enhanced TE_{11} Mie resonance in metal-dressed SiO_2 nano-spheres is observed as a pronounced peak in forward scattering spectrum. This resonance depends on sphere size and has a reasonable line width. Since it occurs in the visible range, distinct size dependent colors of the nano-spheres are visualized.

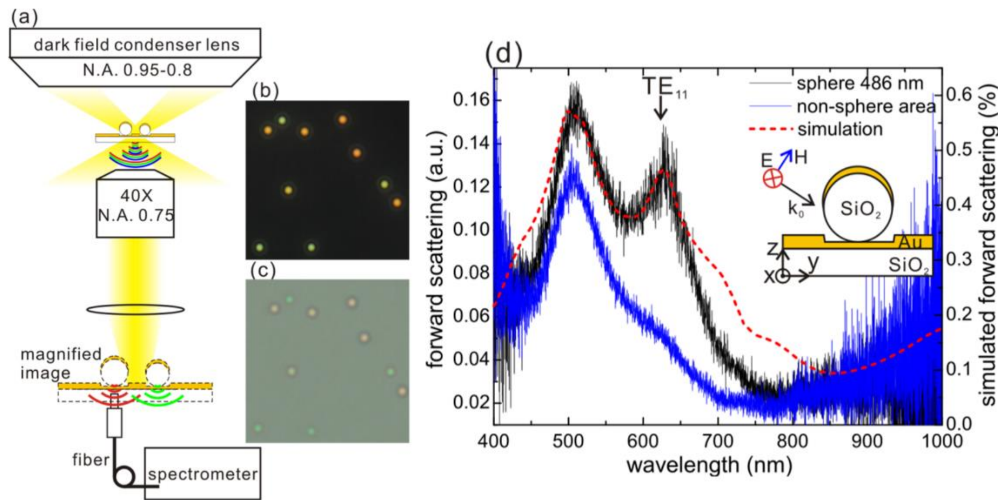

Figure 80 Demonstration of the particle sizing .
(a) Sketch of the dark field transmissive characterization set-up. (b)-(c) Photo pictures of the metal dressed SiO_2 nanospheres with dark field illumination and with bright field illumination. (d) Measured forward scattering spectrum of a 486 nm nanosphere (black) together with simulation (red), and the measured spectrum at a blank area without nanospheres. The measured spectra are normalized to light scattering from some facets at the sample edge. The simulated spectrum is

normalized to the incident power. The incident light in simulation is a TE wave (electric field along x-axis). Inset: sketch of the metal dressed nanosphere illuminated by oblique incident light.

As shown in Figure 80, the size detection of the low index particles is based on dark field transmission spectra. With a multimode fiber (core diameter ~200 nm), the dark field transmission of a single nano-sphere could be selectively collected at the magnified image plane and analyzed by a spectrometer (Figure 80a). Since the background transmission is significantly suppressed (comparison between Figure 80b and 3c), the local property of any single metal-dressed nano-sphere could be revealed by the spectrum. As an example, the dark field transmission at a nano-sphere with a diameter around 486 nm (size determined by SEM) is plotted in Figure 80d (black curve). The peak around 510 nm is due to the interband transition in Au near this wavelength. This can be confirmed by analyzing the stray light through a blank area of only the 60 nm Au film without any nano-spheres. The peak around 510 nm in the spectrum (blue curve in Figure 80d) can be attributed to the material property of Au film only. The peak around 630 nm is a resonance caused by the metal dressed SiO_2 nano-sphere and responsible for the distinctive colors. Simulations were also performed for comparison. The dark field transmission was simulated by integrating the transmitted power over a solid angle corresponding to the NA of the objective lens. The simulated spectrum as plotted by the dashed red curve in Figure 80d, agrees with the measurement (black curve) in terms of the peak positions and profiles. A size difference as small as 8 nm was resolved by peak shift or even by color change. Beyond an optical cavity, the metal dress also functions as an antenna to couple the concentrated light power to the far field, leading to scattering maxima in the spectra. At the enhanced TE_{11} Mie resonance, considerable magnetic response could be expected in low-index nanoparticles due to the strong circulating displacement currents induced by the intensified electric field instead of a high permittivity. The enhanced Mie

resonances could be used to sense minute changes in size or refractive index of low-index nanoparticles and benefit their wide range of applications.

5.2.2 Introduction to Lidar system in self-driving cars

Recently, interest in accurate object detection has been drastically increasing along with the growing need for self-driving cars. One widely used technology to detect objects is Lidar, which refers to light detection and ranging. Lidar typically resembles a remote sensor that uses light to measure distances and objects, thus enables a self-driving car to see the world. Lidar has been applied in many fields, including the design of airplanes and helicopters, which are the most commonly used platforms for the mapping of both natural and manmade environments. However, Lidar system with high accuracy, precision and flexibility in a self-driving car has not yet been fully explored. We propose a Lidar reflector embedded in a transparent windshield by employing dielectric particles with metallic caps for the enhanced signal detection. The proposed Lidar uses near infrared (IR) light near a wavelength of 900 nm to image objects. The particles coated with metallic caps provide a strong backscattering at 900 nm while maintaining high transparency in the visible range to allow drivers to see through. Because the windshield of a car is usually oblique, the particles also resonant strongly for oblique light incidence with angle of 30° and 60°, for different light polarizations. The proposed Lidar design can target a wide range of materials, including obstacles, rocks and rain, and offer accurate navigation for the cars.

5.2.3 Far field scattering of dielectric particles

In the previous sections, the near field scattering of the particle is discussed. However, the far field scattering of dielectric particles is also of great interest. For example, in Lidar design. In the far field regime, backscattering cross section (BCS) and forward scattering cross section (FCS) are

usually two important parameters. To calculate BCS and FCS, radar cross section (RCS) is used, which is defined as the ratio between the scattered power density S_s seen at a distance r away from the target and the incident power density S_i measured at the target. Using the electric field, RCS can also be expressed in terms of E_s and E_i, which are the far field scattered and incident electric field intensities, respectively. [196]

$$\sigma = \lim_{r\to\infty} 4\pi r^2 \frac{S_s}{S_i} = \lim_{r\to\infty} 4\pi r^2 \frac{|E_s|^2}{|E_i|^2} \tag{79}$$

Accordingly, the BCS can be calculated as,

$$\sigma_b = \frac{2\pi}{k^2}\left|\sum_{n=1}^{\infty}(2n+1)(-1)^n(a_n - b_n)\right|^2 \tag{80}$$

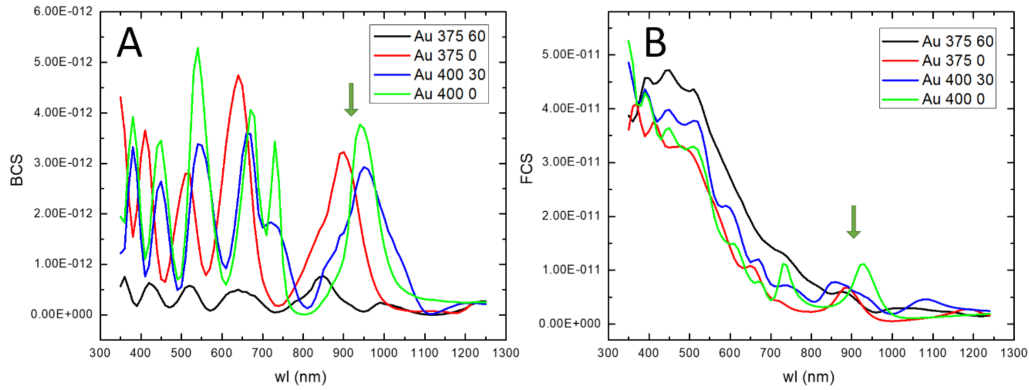

Figure 81 BCS and FCS of particles wirh different size and angle.
(A) BCS and (B) FCS of SiO_2 particle coated with 25 nm Au caps as a function of wavelength. The particles have a radius of 375 nm and 400 nm, and the angle of incidence is 60 and 0°.

In COMSOL simulation, where the far field is defined as $E_{far} = \lim_{r\to\infty} rE_{sca}$ [198], BCS and FCS can be calculated with the angle θ = 180° and 0°, respectively.

$$\sigma = 4\pi \frac{|E_{far}(\theta)|^2}{|E_i|^2} \tag{81}$$

The purpose of the Lidar is used to enhance the backscattering in near IR, while maintaining strong forward scattering in the visible. Dielectric particles with dimension close to the wavelength react with light and create Mie resonances. [151] Figure 82 shows the schematic of the Lidar design based on particle scattering in air. A SiO_2 particle is coated with two metallic caps, which enhance the Mie resonances inside the particle. Light is incident from the negative x-axis and the electric field component of the light is along the z-axis. When the angle of incidence is 0°, the caps are aligned along the x-axis. When the angle of incidence is 60°, the particle is rotated in the xz plane in 60° while the field remains the same, as shown in Figure 82B. The polarization of the incident light is defined as TE polarized in this case, and might change to TM with magnetic component oscillating along z-axis. Backward and forward scattering of the particle are collected along the negative x-axis and the positive x-axis, respectively. [159,198]

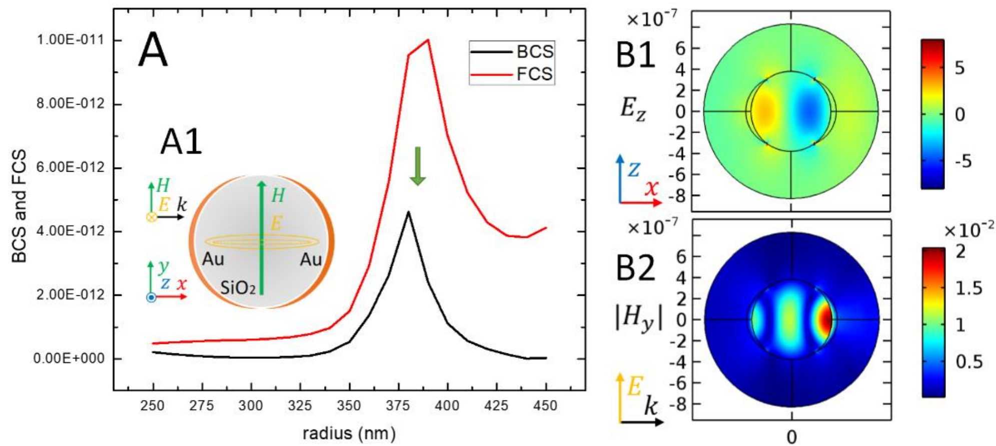

Figure 82 The resonance of electrical dipole and magnetic dipole.
(A) BCS and FCS of different SiO_2 particles as a function of radius at a wavelength of 900 nm. Inset (A1) shows the schematic of a MD resonance and the corresponding electric and magnetic field distribution. (B) Distribution of (B1) z component of the electric field E_z (B2) y component of the magnetic field $|H_y|$ for a particle with radius of 375 nm, showing the MD resonance.

Mie resonances depend on the size and the refractive index of a particle. The BCS and FCS of a SiO_2 particle coated with 25 nm Au caps as a function of the core radius are shown in Figure 82A. Both BCS and FCS have a peak resonance near the radius of 380 nm, which is due to the hybrid MD resonance. [144,147,199] The inset plot illustrated in Figure 82A1 gives the schematic of a magnetic resonance in xy plane, where the magnetic field inside the particle is polarized along the y-axis and the electric field is circulating in the sphere. To confirm the result, the electromagnetic field of the particle with a radius of 380 nm is shown in Figure 82B1 and B2, where the electric field of the incident light is 1V/m. The z component of the electric field has two lobes and the y component of the magnetic field is strongest at the center of the particle, which verifies the hybrid MD resonance. The Au caps help confine the field and create a resonance with a higher quality factor (Q-factor).

5.2.4 Size, angular, material and polarization dependence

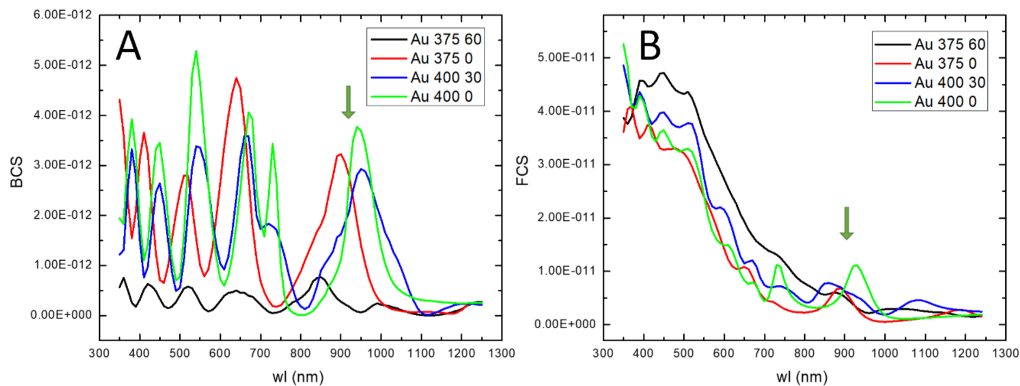

Figure 83 BCS and FCS of particles wirh different size and angle.
(A) BCS and (B) FCS of SiO_2 particle coated with 25 nm Au caps as a function of wavelength. The particles have a radius of 375 nm and 400 nm, and the angle of incidence is 60 and 0°.

More studies on size and angle dependence are performed in simulations. The curves shown in Figure 83A and B show the BCS and FCS of SiO_2 particle as a function of wavelength. The particles are coated with 25 nm Au caps with radius of 375 nm and 400 nm. The angle of incidence

for the TE polarized light is 0° and 60°, respectively. In the BCS curve as illustrated in Figure 83A, several oscillations are generated due to ED, MD, EQ, MQ, etc. All the particles show a pronounced peak in the BCS curve and a weak peak in the FCS curve near the wavelength of 900 nm, which is due to the hybrid MD. For the FCS as shown in Figure 83B, the forward scattering at shorter wavelengths is much stronger. The trend shows a $1/\lambda^2 \sim 1/\lambda^4$ relationship, which is in accordance with the prediction of Rayleigh scattering. As the radius of the SiO_2 core increases from 375 nm to 400 nm, the oscillation shows a red shift, as predicted by Mie theory. When the angle of incidence rises from 0° to 30° and 60°, the peaks shift accordingly. At the same time, the intensity of BCS reduce greatly at higher angle of 60° while the intensity of FCS slightly strengthens.

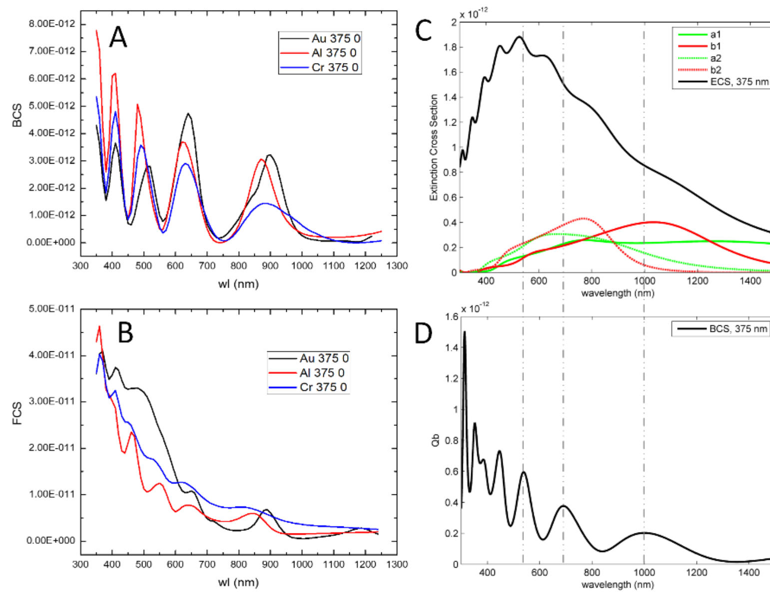

Figure 84 SiO_2 particles coated with different materials.
(A) BCS and (B) FCS of 375-nm SiO_2 particles coated with Au, Al and Cr caps for normal incident light. (C) ECS and (D) BCS of particles for a SiO_2 particle with radius of 375 nm using Mie theory.

To identify the Mie resonance, and differentiate them from the localized surface plasmon (LSP) resonance, particles coated with different materials including Au, aluminum (Al) and chromium (Cr) as well as a pure SiO_2 particle are prepared. As we know, Al shows worse LSP performance

compared with Au, and Cr does not support LSP. As shown in Figure 84A and B, although the shape of the peaks varies slightly, the positions of peaks remain the same for different coating materials. The difference in the Q-factor is due to the confinement or reflection of each material. This confirms that the oscillations are results from the intrinsic properties of the particle, not due to the metallic caps. For a SiO_2 particle with no caps, the resonance can be calculated analytically by Mie theory, as shown in Figure 84C. The back scattering BCS calculated using Mie theory is shown in Figure 84 D, where the radius of the SiO_2 particle is 375 nm. Comparing Figure 84 C and D, the peak of BCS curve is located where none of the a_1, b_1, a_2 and b_2 reaches its maximum. It's because σ_b is determined by $|a_n - b_n|^2$. For the peak in BCS near the wavelength near 900 nm, the interference of ED and MD lead to a strong backscattering. [151,161]

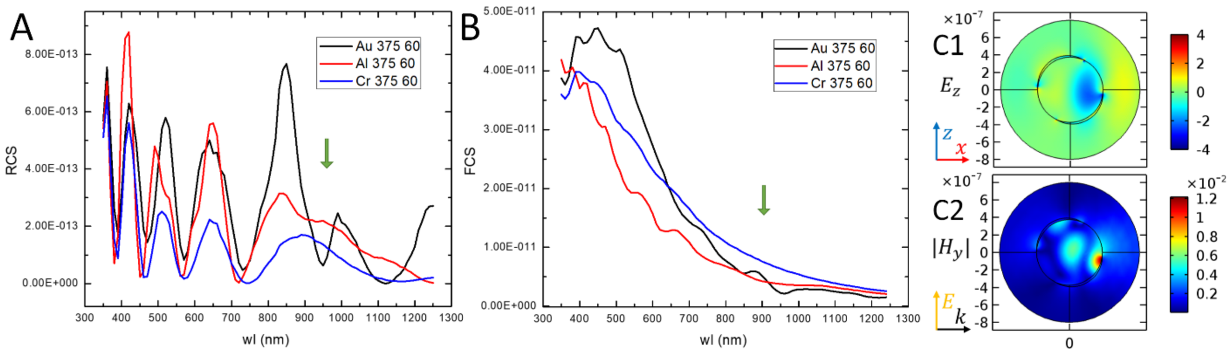

Figure 85 For light with incident angle of 60°.
(A) BCS and (B) FCS of 375-nm SiO_2 particles coated with 25 nm Au, Al and Cr caps for light with incident angle of 60° and TE polarization. (B1) z component of the electric field $|E_z|$ (B2) y component of the magnetic field $|H_y|$ for a particle with radius of 375 nm and Au caps at a wavelength of 850 nm, where the BCS curve has a resonant peak.

The performance for the particles with 60° angle of incidence for TE polarized light is shown in Figure 85A. The oscillations in BCS and the decaying trend of the FCS remains similar for the caps made of Au, Al and Cr. There is a split of the peak near the wavelength of 900 nm, which is due to the Fano resonance between the MD and LSP. Especially, the particles coated with Al and Cr give much lower intensity and broader resonances, while Au shows the highest intensity near

the wavelength of 835 nm and exhibits a dip near 950 nm. The electromagnetic field of the particle coated with Au caps is shown in Figure 85C1 and C2. The strong magnetic field can still be observed in Figure 85C2; however, the caps also create strong hot spots due to the asymmetric light illumination, which can be attributed to LSP created by Au coating.

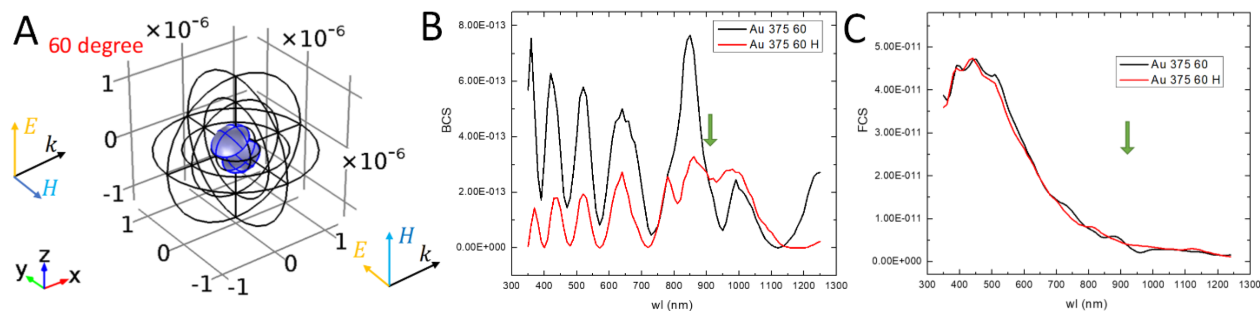

Figure 86 Different light polarizations.
(A) Schematic of 60° incident light with different polarizations. (B) BCS and (C) FCS of 375-nm SiO_2 particles coated with Au, Al and Cr caps with TE and TM polarized light inflammations.

To confirm the analyses, TM polarization is also performed with an angle of incidence of 60°. The magnetic field is polarized along z-axis and the corresponding electric field is polarized along x-axis. The two polarizations of light are shown in Figure 86A. For the same SiO_2 particle coated with Au caps placed in air, TM polarized light induces much lower peak near 900 nm, as shown in Figure 86B and C, respectively. Those results confirm that the resonance for an angled incidence is caused by the coupling between LSP and MD, because LSP is polarization dependent. Furthermore, both polarizations can give the resonance near 900 nm in BCS.

5.2.5 Particles dispersed in glass

For the Lidar design to be applied in windshield glass, the particles have to be dispersed and embedded in glass. The performance of the SiO_2 particle sitting in glass for different illumination angles with TE light is shown in Figure 87. Though the particle shows similar MD resonance, the behavior in terms of BCS (Figure 87A) and FCS (Figure 87B) is slightly worse, especially the FCS

curve. From the field plots as given in Figure 87C1 and C2, the caps just create confined resonances. Light travels inside the particle as if it is in the surrounding media because the core and host have close refractive indices.

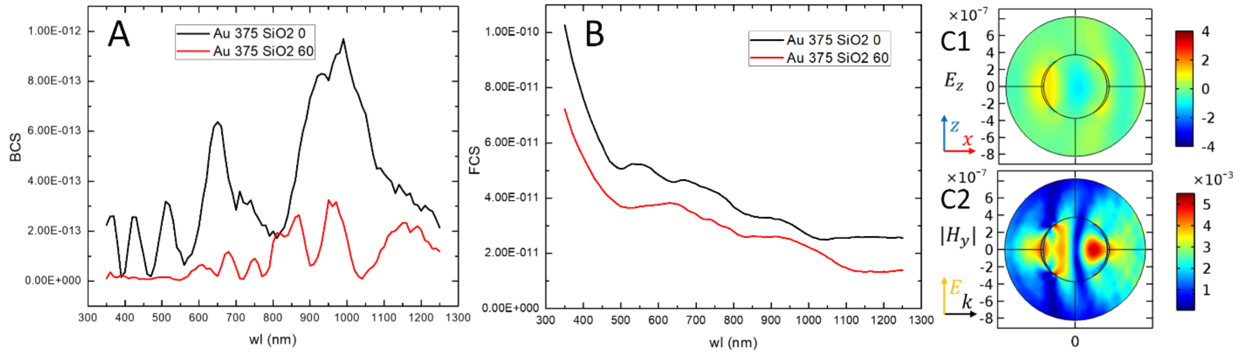

Figure 87 Scattering of SiO_2 particle in glass.
(A) BCS and (B) FCS of 375-nm SiO_2 particles with 0° and 60° incidence embedded in glass. (C1) z component of the electric field E_z (C2) y component of magnetic field $|H_y|$ for the particle at the wavelength of 900 nm, showing the MD resonance.

To maintain the same resonance and index contrast between the host and core, titanium dioxide (TiO_2) particle is used as the core. The BCS and FCS of TiO_2 particles with a radius of 375 nm and 200 nm are calculated assuming TE polarized light and angle of incidence 0 and 60°, as given in Figure 88. The particles are coated with Au caps, and embedded in glass. TiO_2 particle with a radius of 375 nm shows higher order resonance, as illustrated in Figure 88C1 and C2. TiO_2 particle with a radius of 200 nm resonates as a hybrid MD due to the localized magnetic field in the center. In both two cases, the BCS curves of the particles show a strong resonance near the wavelength of 900 nm. In addition, similar to the results using SiO_2 particle in air, the FCS of the TiO_2 particle in the visible range is much stronger than that of the near IR, although efficiencies differ slightly for those particles. This might be due to the interference of the intrinsic modes induced inside the particles. It is thus concluded that by using different materials and sizes, comparable performance can be achieved. By embedding these dielectric particles in glass, we expect to this Lidar design

to achieve detection with high accuracy. With further optimization, our design can be potentially adopted as a highly accurate Lidar in self-driving cars.

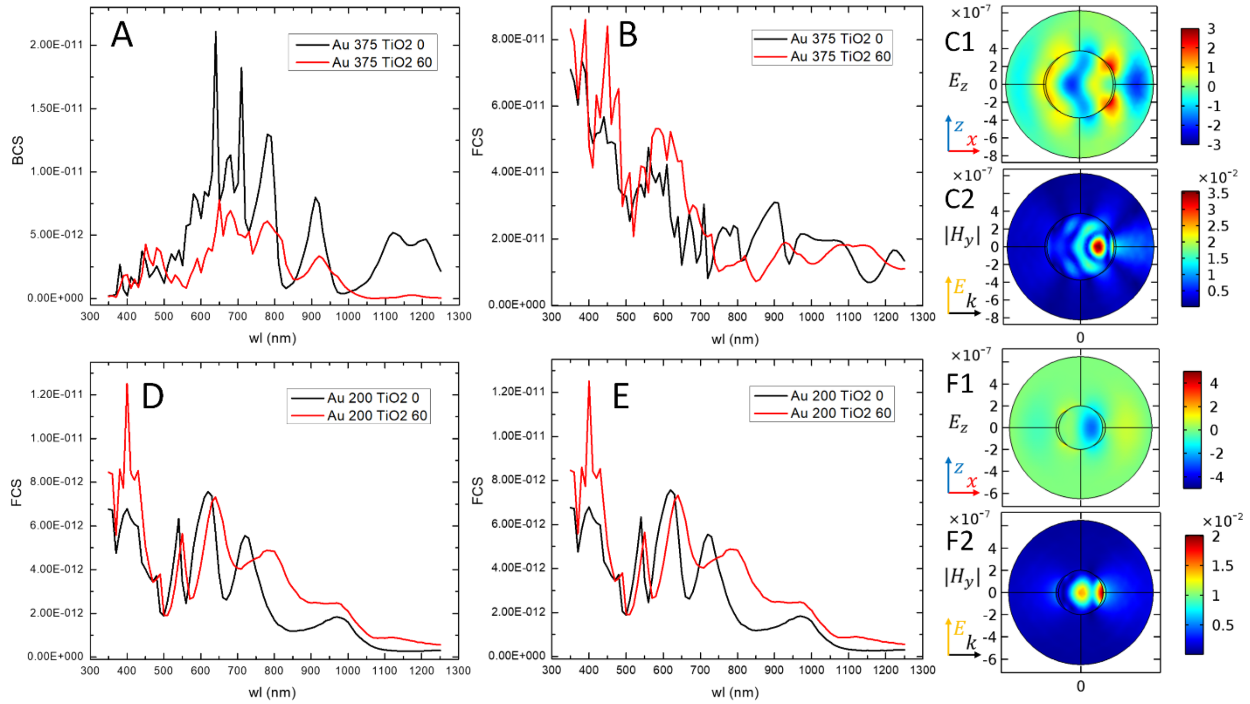

Figure 88 Light scattering of TiO_2 particle in glass.
(A) BCS and (B) FCS of 375-nm TiO_2 particles with 0° and 60° incidence embedded in glass. (C1) z component electric field E_z (C2) y component electric field $|H_y|$ for the 375-nm particle at a wavelength of 900 nm. (D) BCS and (E) FCS of 200-nm TiO_2 particles with 0° and 60° incidence embedded in glass. (F1) E_z and (F2) $|H_y|$ for the 200-nm particle.

5.3 Si nanowires in optical applications

5.3.1 Metal assisted chemical etching to fabricate Si NW

Si devices are the building blocks in the semiconductor industry. The devices consisting of nano-scale structures can be fabricated by numerous techniques. Among them, Si nanowire (NW) made by metal-assisted chemical etching [200–204] has been reported to be simple and cost effective. This technique can be tailored in a controlled fashion so that Si NWs with different morphologies can be created and employed in various applications including intense photoluminescence (PL) of molecules, antireflective films, solar energy conversions and lithium (Li^+) ion batteries. [200–203]

The Si NW was successfully achieved by metal-assisted chemical etching using the procedures shown in Figure 89. Either p or n type bare Si wafers was prepared, and cleaned by piranha solution (H_2SO_4: H_2O_2, 1:1, v: v) for 10 minutes, followed by DI water rinsing for 5 minutes. The clean Si wafer was deposited with gold and palladium (Au + Pd) alloys by sputtering with a pressure of 100 μatm, a current of 20 mA for 120 seconds. The thickness of the alloys on top of wafers was around 5 nm. The wafer with metallic islands was then soaked into etching solution (HF: H_2O_2: H_2O, 4:1:8, v: v: v) for 2 minutes. Hydrofluoric acid (HF) is the main etchant, while and hydrogen peroxide (H_2O_2) acts as an oxidative agent. Metal particle catalyzes the chemical reactions so that the area covered by it is etched much faster than the other regions. As the metallic particles sink into the substrate (due to Si underneath being etched away), porous structures or Si wires are formed. In our experiment, with optimized metal thickness and deposition rate, the Si NW arrays can be achieved. The resulting Si NWs have diameters around 20~200 nm depending on the film morphology and height of 2 μm, which can be modulated by etching time.

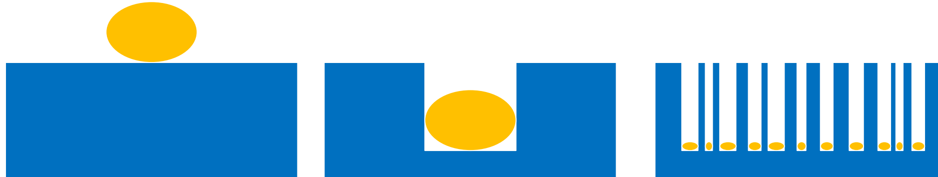

Figure 89 Schematic of the formation of Si NW by MacEtching.

5.3.2 Si NW array as surface enhanced IR sensor

Heavily doped Si has plasmonic property [205,206] with plasma frequency around 0.14 eV (8.86 μm, for heavily doped p-typed Si with carrier concentration 3–6 10^{19} cm^{-3}). [205] Figure 90(a) shows the real part and imaginary part of the permittivity of the heavily doped Si by using Drude model. For Si NW, it naturally forms an effective anisotropic material, which is a potential in the

regime where Si has plasmonic property (real part of permittivity is negative). When treated as an effective medium, the effective permittivity of the Si NW forests can be expressed as

$$\epsilon_{xx} = \epsilon_{yy} = \epsilon_h \frac{(1+f)\epsilon_i + (1-f)\epsilon_h}{(1-f)\epsilon_h + (1+f)\epsilon_h} \tag{82}$$

$$\epsilon_{zz} = f\epsilon_i + (1-f)\epsilon_h \tag{83}$$

By using the effective medium approach, the fill ratio of the Si can be obtained by Ellipsometry by comparing the phase spectra with fitting data. Figure 90(b) illustrates the effective parallel and perpendicular permittivity of Si NW hyperbolic metamaterial (HMM) in air with a Si NW filling ratio of 0.3. It's an effective type I HMM ($\epsilon_{xx} > 0$ $\epsilon_{zz} < 0$) at the wavelength larger than 10 µm, which provides a potential application in surface-enhanced infrared absorption spectroscopy (SEIRAS). [207,208] Infrared (IR) spectroscopy deals with the infrared light matter interactions, which is mostly based on absorption. SEIRAS [208–210] is a variation of conventional IR spectroscopy, which exploits the enhanced surface field usually caused by metal particles to detect monolayer chemicals.

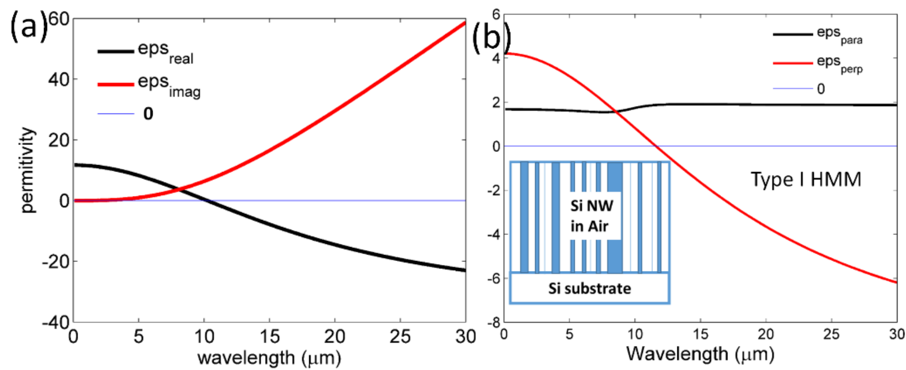

Figure 90 Optical property of Si NW.
(a) The real and imaginary part of the permittivity of heavily doped Si by using Drude model. The metallic property appears beyond 10 µm. (b) The effective parallel and perpendicular permittivity of Si NW HMM in air with Si NW filling ratio 0.3.

The absorptivity of molecules is proportional to the light intensity. When shined by mid-IR light, the strong enhanced light intensity around the Si NW can be employed to improve the absorption. Figure 91 shows the corresponding simulated results. The 10 μm thick Si NW (with diameters varying from 40 nm to 400 nm) forests on Si substrate is exposed in air, as shown in Figure 91(a). 15 μm wavelength light incidents normally onto the NW forest and couple in to it, forming a Fabry Perot (FP) strong resonance along the vertical direction around each NW. Figure 91(b) illustrates a standing wave along the z direction, where the thickness dependence of the FP resonance can be clearly seen. Figure 91(c) shows the top view of the dipole-like field distribution around a single NW, and Figure 91(d) is the coupled field of multiple NWs on the substrate plane.

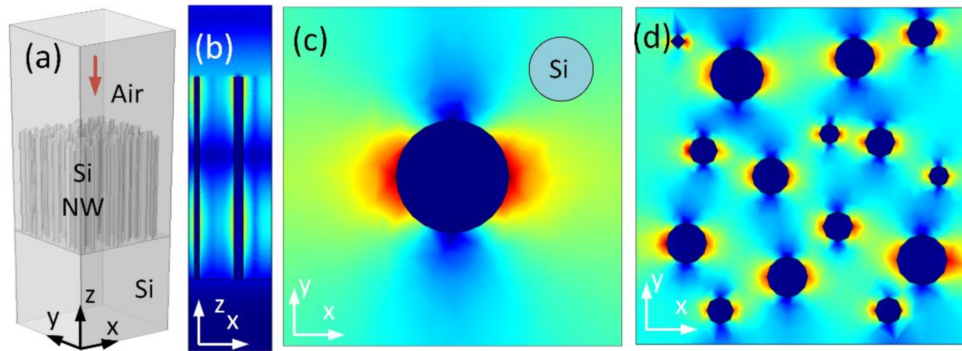

Figure 91 The simulation of Si NW with thickness 10 μm on Si substrate.
(a) Schematic os NW arrays in COMSOL 4.3. (b) The electric field distribution in xz plane, and the bottom of every NW is a node due to the strong reflection. (c) Dipole-like electric field distribution of a single nanowire in xy plane. (d) Coupled field of multiple nanowires in xy plane.

HMM have high local density of states, they can be applied in light emission devices such as light emission diodes (LEDs). [37,211] However, the high local density of states inside the HMM is difficult to be extracted out. Therefore, some groups demonstrated the HMM structure with grating on top of it for the applications using high density of states. [37,211] In this case, since Si NW array is effectively a type I HMM, the light can be coupled in and out with no extra moment required. Compared with multilayer structure HMM, NWs act as small scatters and create strong

coupled light interactions. Furthermore, it is a three-dimensional (3D) metamaterial, which means the effective working area is larger other than that of other nanoparticles including Si particles or metal particles. The detected objects are not limited to monolayer in a 3-D metamaterial.

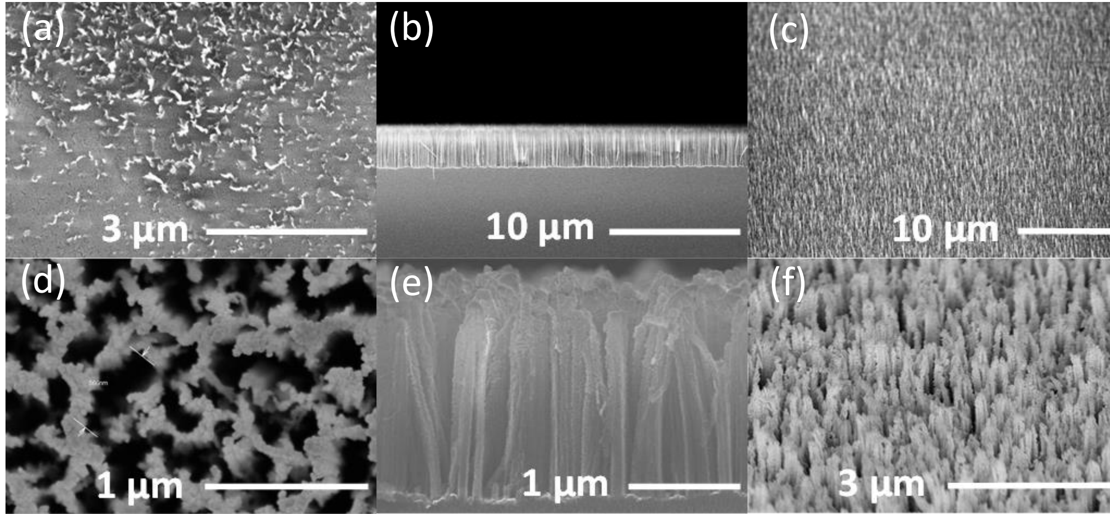

Figure 92 SEM images of Si nanowires with different conditions.
(a) top view (b) cross section (c) tiltited view of the Si NW. (a) top view (b) cross section (c) tiltited view of the Au covered Si NW. The white bar at the bottom indicates the scales.

The SEM images of the fabricated Si NW are shown in Figure 92 (a)- (c). The Si NW is vertical and straight, and the surface of the Si NW forest is flat. Figure 92 (d)- (f) shows the gold (Au) covered Si NW (physically deposited), which shows metallic properties. The Au layer was deposited by sputtering, and the set thickness of Au film is around 50 nm. The roughness on top of the Si NW shown in Figure 92 (d)-(f) corresponds to the Au grains. The deposited Au stuck on the sidewall of NW is around 10~30 nm, about less than half of the set thickness. Figure 93 shows the simulation result of the Si NW with a thickness of 1.5 µm coated with Au films with a thickness of 50 nm. Incident light with a wavelength of 440 nm travels from z^+ direction, hits the core shell wire and reaches Si substrate. A standing wave along the wire on the surface of Au is formed with the bottom of each wire as a node, and the near field around the wire is dramatically enhanced. The Si NW array coated with Au film is also able to couple the light out by itself. Therefore, we

propose to use it as an easily-fabricated candidate to enhance the light emission and fluoresce light of molecules, for example, to get enhanced Raman signals [204,212] of toluene on top of the Au covered Si NW samples.

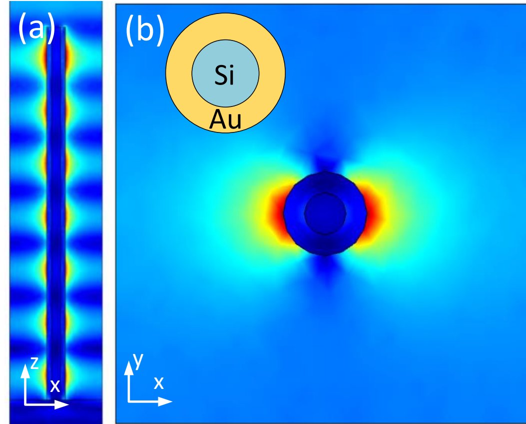

Figure 93 Simulation of the effective modes in Si NW covered by Au layer.
The NW has a diameter of 20 nm coated with 20 nm Au. Total length of the Si NW on Si substrate is 1.5 μm. Incident light has a wavelength of 440 nm. (a) The electric field distribution of the core shell in xz plane. (b) The electric field distribution of a single nanowire in xy plane.

5.3.3 Si NW array as color panel

When Si NW forests are fabricated with different experimental conditions, they appear in different colors, as demonstrated in the reflective microscope images shown in Figure 94. This phenomenon suggests that it may also find its application as color panels. [67] Compared with other structured colors, this alternative way using Si NW does not require complicated nanofabrication, and provide a straightforward way of making reflective color filters with high performance. The colors of the Si NW vary from red to purple depending on the density of Si NW versus air and the thickness of the Si NW forests, where the dependence on thickness d, effective index n and incident angle θ is described by the FP resonance:

$$2ndk_0 cos\theta = 0, 2\pi, 4\pi, ... \quad (84)$$

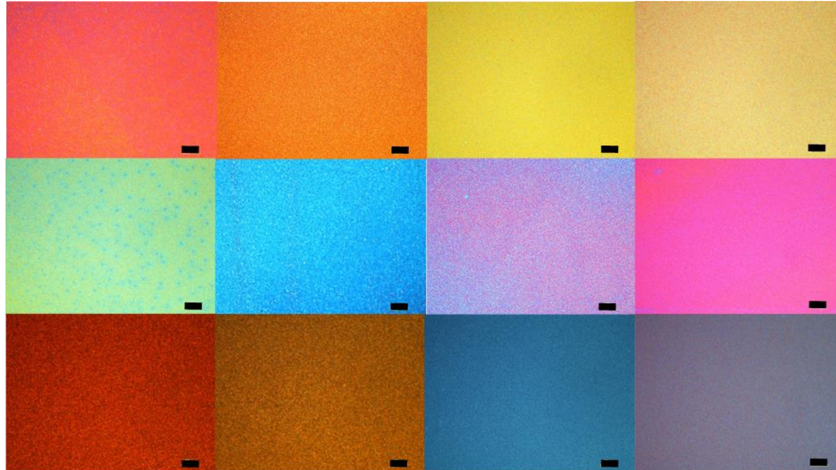

Figure 94 Reflective microscope bright field images of various Si NW forests.
The black bar indicates 20 μm length and the colors depend on the property of NW arrays.

Figure 95 shows the simulated reflection spectra of TE polarized light as a function of fill ratio of Si NW and wavelength. Figure 95 (a), (b) and (c) are the spectra of the Si NW forests with thickness of 1000 nm, 400 nm and 100 nm, respectively. The darker curves in the spectra refer to the FP resonance of the transmitted light, which is consistent with the experimental observation.

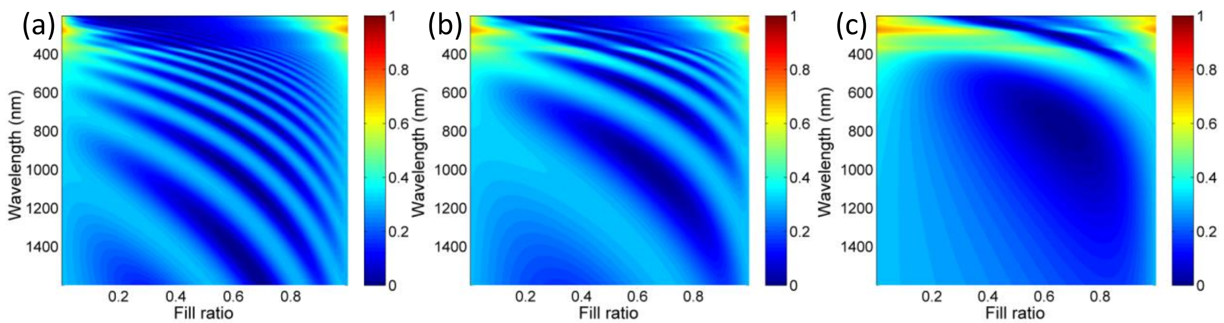

Figure 95 Reflection spectra of Si NW forests.
Reflection of Si NW forest with a thickness of (a) 1000 nm, (b) 400 nm and (c) 100 nm.

We explored an alternative way of making subwavelength structures, especially semiconductor materials, by using metal-assisted chemical etching. Si NW arrays with various thicknesses, density and morphologies can be achieved by controlling the etching conditions. These Si NW arrays can be used to enhance the IR absorption of molecules and organism as the surface agents in the mid-IR regime. With optimization, the Si NW arrays can also create various colors due to

the FP resonances of the visible light. Semiconductor materials other than Si, including germanium (Ge), silicon carbonite (SiC), gallium nitride (GaN) and gallium arsenide (GaAs) can also be etched into NW arrays by metal-assisted chemical etching. [200] In addition, metal films such as Au, platinum (Pt), titanium nitride (TiN) etc. can be coated onto the surface of the semiconducting NWs to form core shell structures by chemical or physical approaches.

5.4 Functional devices using plasmonic materials

5.4.1 Efficient thermal-light inter-conversions based on HMM

Photonic crystals [213–215] and perfect-absorber metamaterials [216] have been proposed for wideband spectral-selective emissivity or absorptivity. However, the complexity of these structures hinders their practical applications. HMM with an optical topological transition (OTT) [44,217] could serve as a spectral selective emitter/absorber. Multilayered structures with spectral-selective absorptivity/emissivity have been studied under the framework of 1D photonic crystal [218]. In our case [39] the thickness of each metal or dielectric layer is much smaller than the wavelengths so the whole structure can be effectively considered as an effective anisotropic medium.

Figure 96 (a) [39] shows the wavelength dependent $\epsilon_{||}$ and $\epsilon_{\perp}$ of a Au/Al_2O_3 multilayered structure with f = 0.15. At the wavelengths larger than the ENZ point (~710 nm), $\epsilon_{||}$ <0 and $\epsilon_{\perp}$ > 0. As shown in Figure 96(b), the isofrequency curve (IFC) at wavelength of 800 nm indicates that it is a type II HMM. Since a type II HMM only supports high k modes, the light from the free space (black circle in Figure 96 (b)) cannot transmit into the medium but mostly gets reflected, leading to high reflection (Figure 96 (c)). With the decreasing wavelength, the metamaterial undergoes an OTT at the ENZ point, where $\epsilon_{||}$ turns from negative to positive. Thus, the metamaterial becomes an effective dielectric with an elliptical IFC like the red line in Figure 96 (b) for the wavelength of 600 nm. As a result, light can penetrate into the multilayered

structure and gets absorbed, leading to high absorption (Figure 96 (c)). Therefore, a metal-dielectric multilayered structure undergoes a transition from a good absorber to a good reflector with the increasing wavelength. For thermophotovoltaics, the wideband emission/absorption above the ENZ point is not ideal [219]. But for thermal-light inter-conversions, the OTT induced wideband spectral-selective emission/absorption is desired. Since the ENZ point can be shifted by tuning the fill ratio as shown in Figure 96 (d), if it is set at the border between the visible and the IR range, a desired wideband spectral-selective emitter/absorber for efficient thermal-light inter-conversions is realized.

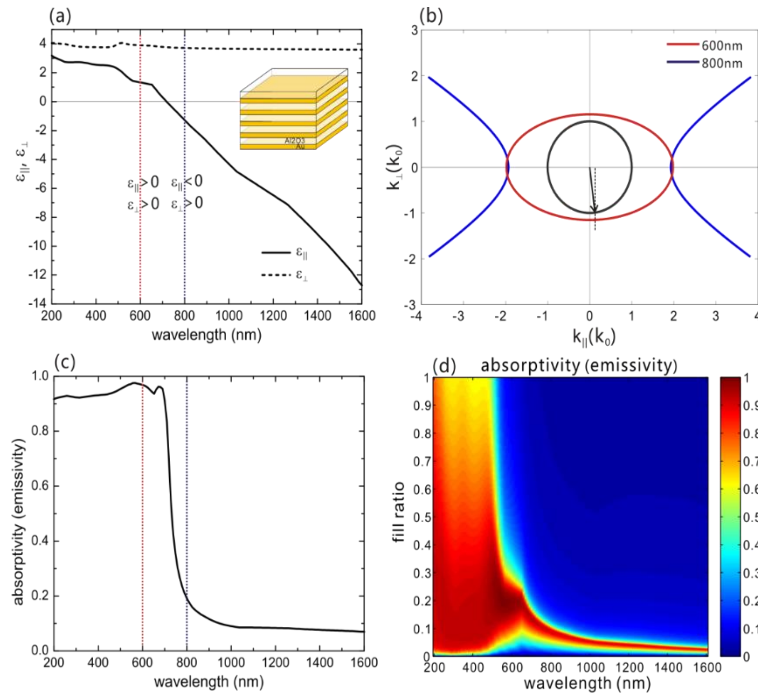

Figure 96 HMM for wideband spectral-selective absorption/emission.
(a) Wavelength dependent anisotropic permittivity of a Au/Al_2O_3 multilayered structure (f=0.15). (b) IFC of light in the Au/Al_2O_3 multilayered structure at a wavelength of 600 nm and 800nm and IFC of light in free space. (c) Wavelength dependent absorptivity/emissivity of the Au/Al_2O_3 multilayered structure. (d) Wavelength and fill ratio dependent absorptivity/emissivity of the Au/Al_2O_3 multilayered structure. [39]

For efficient thermal-light inter-conversions, we propose to utilize HMM as wideband spectral-selective emitters/absorbers [39], whose emissivity/absorptivity is high in the visible range and low in the IR range. With the decreasing wavelength, it turns from an effective metal, which is a good reflector, to an effective

dielectric, which is a good absorber. By setting the ENZ point at the border between the visible and the IR range with a proper fill ratio, a wideband spectral-selective emitter/absorber is achieved. Alternating stacks composed of titanium nitride (TiN) and SiO_2 films were made for the demonstration. The emissivity/absorptivity was measured as 1-reflectivity at variant temperatures from 23°C to 750°C. The performance agrees with our expectation and shows temperature dependence. The concept of metamaterials with optical topological transitions is generalized beyond the multilayered structures to other forms for various applications. Estimation based our measurements shows that the TiN/SiO_2 multilayered structure as a filament coating could enhance the visible/IR emission ratio by 2 to 3 folds during incandescent lighting. As a concentrating solar power (CSP) receiver at 1000°C, the TiN/SiO_2 multilayered structure could suppress the thermal radiation to 19% while still absorbs 65% of the solar power.

5.4.2 Plasmonic lasing using dye molecules and 2D materials

Plasmonic systems are widely used to enhance light emission from active materials. [220–224] By using periodic plasmonic resonances, the stimulated emission of the dye molecules can be excited. As shown in Figure 97A, we implemented an inverse microscope for the detection of lasing. The dye molecule LDS821 as the gain material, which is dissolved in dimethylsulfoxide (DMSO) solution as the device under test (DUT). The period of the periodic metallic structure is 530 nm. PL measurements were performed using a florescent microscope equipped with an excitation laser operated at a wavelength of 532 nm as shown in Figure 97B. A laser power of 30uW with a focus spot of 10um (focused by a 40X objective lens) was used to illuminate on the sample. A spectrometer (Andor 550i) were used to detect the PL signal with integration time of 20s. Two-dimensional (2D) materials, such as groups of transition metal dichalcogenides (TMDCs) are crystalline materials comprised of multiple monolayers of atoms. They are direct bandgap two-dimensional (2D) material semiconductors and have properties dramatically different from the

bulk materials, making them promising light active materials for optoelectronic applications [225]. Recently, TMDCs have shown great potential in ultrafast and ultrasensitive photodetectors as ultrathin light absorbers and emitters [226,227]. However, their application in photonic devices is limited by their low absolute PL due to low quantum efficiency and weak absorption. A lot of efforts have been dedicated towards obtaining enhanced light emission from TMDCs. [228–231] However, several intrinsic issues are still present when integrating 2D materials with plasmonic nanostructures. The most severe one among them is the unavoidable damage with the direct deposition of metallic nanostructures on 2D materials [232].

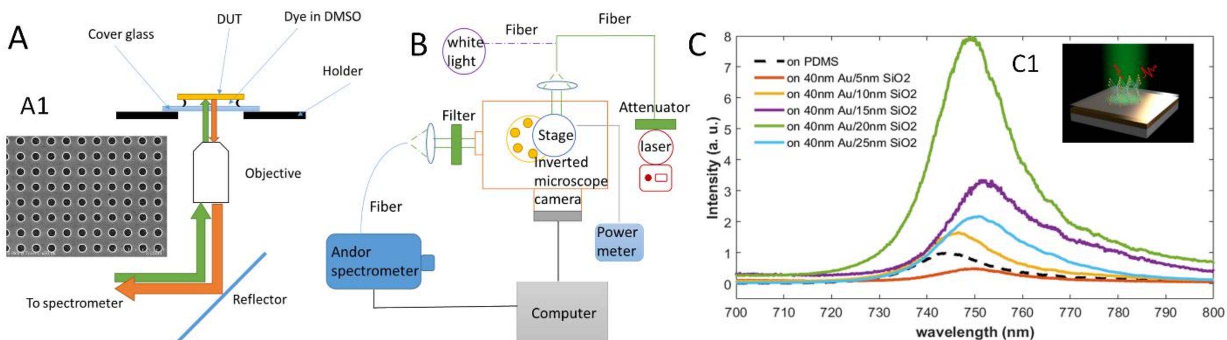

Figure 97 Optical setup of plasmonic laser.
(A) Inverse microscope setup for device under test. Dye molecules are dissolved in DMSO and covered by a glass slide. (A1) The SEM image of the periodic metal hole array. (B) Optical path for laser pumping and detection. (C) Measured PL spectra of exfoliated monolayer WSe_2 flakes on SiO_2/Au/Glass DMD structures with the SiO_2 spacer layer range from 5 nm to 25 nm. The spectra are normalized to the peak value of the case of WSe_2 directly on PDMS. (C1) Schematic of enhanced signal observed of WSe_2.

We also performed the PL enhancement for a 2D semiconductor tungsten diselenide (WSe_2). Our planar dielectrics/metal/dielectrics (DMD) structure consists of a glass substrate, 40nm Au film and one SiO_2 spacer (5nm-25nm) layer separating the metal film and the WSe_2 monolayer as in shown in Figure 97C1. In this test, all the conditions were kept the same for all those samples in order to investigate the role of the spacer thickness. Figure 97C shows the measured PL spectra of

WSe_2 monolayers on SiO2/Au/Glass DMD structures with the SiO_2 spacer layers ranging from 5 nm to 25 nm. The dependence of the separation between the metal and WSe_2 are apparent from the plot, as either enhancement or inhibition can be achieved when the 2D materials interact with the DMD structures. Considerable shifts of the spectra peak were also observed. Both the enhancement and shift show highly sensitive dependence on the thickness of the spacer layer for changes as small as only 5 nm. Investigation of the underlying physical processes such as non-radiative exciton-plasmon energy transfer and group coherency can be conducted. [233,234] This plasmonic laser setup not only provides a general method to enhance light emission from active materials but also offers a good platform to study the fundamental physics of plasmon interacted exciton dynamics.

5.5 Summary

In this chapter, several applications of plasmonic materials are discussed in simulations and experiments. A Si nanoparticle is placed on top of the HMM, which can be treated as a localized dipolar emitter. Depending on the polarization of the incident light, the scattering of the particle can be unidirectional when the dipole is circularly polarized. When a plane wave is incident onto the HMM, the reflected light acquires a large phase change and forms interference patterns. This phenomenon can be utilized for a lithography system, and the detection of polarization states. It provides a new platform to passively generate spin particles, inspire potential applications of the unidirectional scattering and study of chiral molecules and structures. In addition, a Lidar design based on dielectric particles coated with metallic caps is proposed for object detection suitable for self-driving cars. For both normal and angled incidences, the particles provide a strong backscattering near a wavelength of 900 nm to detect obstacles in IR range. The strong resonance is based on intrinsic hybrid MD resonance induced by the core, while the metal caps improves the

confinement of light. Those particles also produce strong forward scattering in the visible range, which does not comprise the transparency of the windshield. Both SiO_2 and TiO_2 particles with different dimensions and capping materials are studied and they showed comparable behaviors, which proves the flexibility and robustness of the Lidar design. In addition, Si NW forests were fabricated by metal assisted chemical etching. The size, density and height of the NW array can be controlled, to generate different colors. Due to the plasmonic properties of Si in IR range, the NW arrays can also find their application as IR sensors to enhance the surface absorption. Other progresses towards plasmonic functional devices including thermal-light converters and plasmonic lasers are studied as well.

CHAPTER 6

Conclusions and Future Work

In this dissertation, we mainly discussed the design principle, experimental implementation, analyses of results and potential applications of the plasmonic lithography systems. First, we introduced the basic principle of different types of plasmonic waveguide lithography systems reported in earlier work. The resolution limits for individual systems are derived here and the major drawbacks in previous demonstrations of plasmonic lithography systems are also discussed.

Second, two plasmonic interference lithography systems based on Al waveguide and type II epsilon-near-zero (ENZ) hyperbolic metamaterial (HMM) are proposed. Mode distribution and light propagation in the waveguide and HMM composed of aluminum (Al) and aluminum oxide (Al_2O_3) films are investigated. Our designs are based on spatial frequency selection of the evanescent waves. Based on this principle, only one single high-k mode is maintained and imaged in the PR, which results in a uniform and deep periodic pattern smaller than the wavelength of the light source. Experimentally, using the Al waveguide system, we showed that periodic patterns with high aspect-ratio, and a half-pitch about 1/6 of the wavelength can be achieved with good uniformity over cm^2 areas. In the ENZ HMM system, periodic patterns with a half pitch of 58.3 nm were achieved utilizing the interference of 3rd order diffracted light of the grating. These patterns represented about a 6 times reduction from the mask and were $1/7$ smaller than the wavelength of the incident light. Both systems overcome several major drawbacks (including shallow depth, non-uniformity, extremely weak intensity and direct contact, *etc.*) in previously reported plasmonic lithography and broaden its applications in nanoscale patterning. In addition

to the experimental progress towards large-scale applications of plasmonic interference lithography, the general criteria of designing such exposure system is also discussed, which can be used as a guideline for nanoscale fabrication in various applications with different requirements for pitch, aspect-ratio and structure. The theoretical analyses performed in this work are also widely applicable to structures made of different materials such as silver (Ag), as well as the systems working at deep ultra-violet wavelengths including 193 nm, 248 nm, 365 nm and 436 nm. Furthermore, a plasmonic roller system was developed to produce large-area, subwavelength patterns on a moving substrate on a continuous basis. This roller system combines the concepts of the photo-roller lithography and plasmonic lithography, and it is suitable for continuous patterning nanoscale features over a large area with high throughput for cost-sensitive applications.

Third, the effects of surface roughness of thin films and defects on photomasks are investigated in two representative plasmonic lithography systems: a thin Ag film-based superlens and an Al based HMM. Superlens can replicate arbitrary patterns because of its broad evanescent wave passband, which also makes it inherently vulnerable to roughness on a thin film and imperfections on a photomask. On the other hand, the HMM system has spatial frequency filtering characteristics and its pattern formation is based on interference. Based on our simulation results, we show that the HMM system is more immune to such imperfections due to its spatial frequency selection so that uniform and stable periodic patterns can be maintained. The analyses are verified by a waveguide interference lithography system. The results suggest that the HMM and waveguide system built on spatial frequency selection principle can serve as a powerful tool to produce deep-subwavelength periodic patterns with high degree of uniformity and fidelity.

Lastly, several other applications related to plasmonic lithography are proposed and demonstrated experimentally. Due to photonic spin Hall effects of a rotating emitter, the patterns formed in the

PR underneath the HMM are highly dependent on light polarizations and the incident angle. The patterns provide a new platform to passively generate spin particles, and inspires potential application of unidirectional scattering. A Lidar design based on dielectric particles coated with metallic caps is proposed for object detection suitable for self-driving cars. Silicon (Si) nanowire (NW) arrays were achieved by metal assisted chemical etching. The NW forest can be treated as a metamaterial and can serve as infrared (IR) sensors or color panels in the visible range. Many developments of plasmonic materials in electronic and optical devices are also discussed.

To summarize, we have achieved some progress towards optimizing plasmonic waveguide lithography to meet the evolving demands of future patterning technologies in various applications. Plasmonic waveguide lithography process is a contact photolithography technique, thus more immune to defects especially in high speed processing. It is durable because the photomask is flat and only has contact with the PR layer. Our proposed approaches especially the roller systems are cost effective with high throughput, and hence are attractive for applications that require printing patterns with a high aspect ratio over a large area.

Here we will also discuss some of the possible directions we can follow to further extend the progress. From the experimental point of view, plasmonic roller system with even larger exposure area is possible. The system we demonstrated in a waveguide lithography system currently uses a photomask with a period of 245 nm, which was rather limited since it is written using electron beam lithography (EBL). By using the ENZ HMM lithography, a grating mask can have a much larger period such as 700 nm or even in micron scale. This grating can be achieved by nanoimprint lithography and conventional photolithography with cm^2 scale or an even larger area, which will potentially improve the capability of the plasmonic roller system. For the photonic spin Hall effects, our simulation result of spin-dependent particle scattering can be confirmed by using leakage

radiation microscopy to detect various polarization states. Far-field scattering of particles can also be accomplished by experiment and further optimized for self-driving cars. The absorption of chiral structures and the enhanced signals by Si NW arrays in IR regime can be performed to verify the distinctive simulation results. Furthermore, with the understanding of the plasmonic materials and spatial frequency selection principle, more plasmonic functional devices can be inspired.

REFERENCES

[1] T. Ito and S. Okazaki, Nature **406**, 1027 (2000).

[2] S. J. McNab and C. Hans, Evanescent near-Field Optical Lithography: Overcoming the Diffraction Limit., University of Canterbury, 2001.

[3] J. B. Pendry, Phys. Rev. Lett. **85**, 3966 (2000).

[4] F. J. Garcia-Vidal, L. Martin-Moreno, T. W. Ebbesen, and L. Kuipers, Rev. Mod. Phys. **82**, 729 (2010).

[5] J. Zhou and L. J. Guo, 2013 IEEE Photonics Conf. IPC 2013 180 (2013).

[6] J. a. Porto, F. J. Garcia-Vidal, and J. B. Pendry, 4 (1999).

[7] S. a. Maier, *Plasmonics: Fundamentals and Applications* (Springer Science & Business Media, 2007).

[8] K. Kemp and S. Wurm, Comptes Rendus Phys. **7**, 875 (2006).

[9] Z. Yu, H. Gao, W. Wu, H. Ge, and S. Y. Chou, J. Vac. Sci. Technol. B Microelectron. Nanom. Struct. **21**, 2874 (2003).

[10] J. J. Wang, L. Chen, X. Liu, P. Sciortino, F. Liu, F. Walters, and X. Deng, Appl. Phys. Lett. **89**, (2006).

[11] C. Zhang, S. Chen, T. Ling, L. J. Guo, and S. Member, **15**, 3241 (2015).

[12] J. G. Goodberlet and H. Kavak, Appl. Phys. Lett. **81**, 1315 (2002).

[13] G. Liang, C. Wang, Z. Zhao, Y. Wang, N. Yao, P. Gao, Y. Luo, G. Gao, Q. Zhao, and X. Luo, Adv. Opt. Mater. **3**, 1248 (2015).

[14] Z. Liu, H. Lee, Y. Xiong, C. Sun, and X. Zhang, Science **315**, 1686 (2007).

[15] X. Luo and T. Ishihara, Appl. Phys. Lett. **84**, 4780 (2004).

[16] D. B. Shao and S. C. Chen, Appl. Phys. Lett. **86**, 1 (2005).

[17] D. B. Shao and S. C. Chen, Opt. Express **13**, 6964 (2005).

[18] C. Wang, P. Gao, Z. Zhao, N. Yao, Y. Wang, L. Liu, K. Liu, and X. Luo, Opt. Express **21**, 20683 (2013).

[19] Z. Jacob, L. V Alekseyev, and E. Narimanov, Opt. Express **14**, 8247 (2006).

[20] M. Maenhoudt, J. Versluijs, H. Struyf, J. Van Olmen, and M. Van Hove, **5754**, 1508 (2005).

[21] P. Zhu, H. Shi, and L. J. Guo, Opt. Express **20**, 12521 (2012).

[22] F. Y. and X. C. and E.-H. C. and C. S. L. and P. J. and L. J. Guo, Appl. Phys. Express **8**, 62004 (2015).

[23] J. Rho, Z. Ye, Y. Xiong, X. Yin, Z. Liu, H. Choi, G. Bartal, and X. Zhang, Nat. Commun. **1**, 143 (2010).

[24] Z. Liu, S. Durant, H. Lee, Y. Pikus, Y. Xiong, C. Sun, and X. Zhang, Opt. Express **15**, 6947 (2007).

[25] Y. Xiong, Z. Liu, C. Sun, and X. Zhang, Nano Lett. **7**, 3360 (2007).

[26] J. Yao, Z. Liu, Y. Liu, Y. Wang, C. Sun, G. Bartal, A. M. Stacy, and X. Zhang, Science **321**, 930 (2008).

[27] B. D. F. Casse, W. T. Lu, Y. J. Huang, E. Gultepe, L. Menon, and S. Sridhar, Appl. Phys. Lett. **96**, 2008 (2010).

[28] N. Fang, H. Lee, C. Sun, and X. Zhang, Science (80-.). **308**, 534 (2005).

[29] R. J. Blaikie, D. O. S. Melville, and M. M. Alkaisi, Microelectron. Eng. **83**, 723 (2006).

[30] X. Zhang and Z. Liu, Nat. Mater. **7**, 435 (2008).

[31] Z. Xie, W. Yu, T. Wang, H. Zhang, Y. Fu, H. Liu, F. Li, Z. Lu, and Q. Sun, Plasmonics **6**, 565 (2011).

[32] H. Liu and J. Teng, J. Mol. Eng. Mater. **1**, 1250005 (2012).

[33] J. Zhou and L. J. Guo, Sci. Rep. 180 (2013).

[34] X. Chen, F. Yang, C. Zhang, J. Zhou, and L. J. Guo, ACS Nano **10**, acsnano.5b06137 (2016).

[35] C. L. Cortes, W. Newman, S. Molesky, and Z. Jacob, arXiv Prepr. arXiv1204.5529 (2012).

[36] A. Poddubny, I. Iorsh, P. Belov, and Y. Kivshar, Nat. Photonics **7**, 948 (2013).

[37] L. Ferrari, C. Wu, D. Lepage, X. Zhang, and Z. Liu, Prog. Quantum Electron. **40**, 1 (2014).

[38] L. Liu, P. Gao, K. Liu, W. Kong, Z. Zhao, M. Pu, C. Wang, and X. Luo, Mater. Horiz. **4**, 290 (2017).

[39] J. Zhou, X. Chen, and L. J. Guo, Adv. Mater. 1 (2016).

[40] C. L. Cortes and Z. Jacob, (n.d.).

[41] R. J. Pollard, a. Murphy, W. R. Hendren, P. R. Evans, R. Atkinson, G. a. Wurtz, a. V. Zayats, and V. a. Podolskiy, Phys. Rev. Lett. **102**, 1 (2009).

[42] L. V. Alekseyev, E. E. Narimanov, T. Tumkur, H. Li, Y. a. Barnakov, and M. a. Noginov, Appl. Phys. Lett. **97**, 0 (2010).

[43] Z. Jacob, L. V Alekseyev, and E. Narimanov, Opt. Express **14**, 8247 (2006).

[44] C. L. Cortes, W. Newman, S. Molesky, Z. Jacob, and a B. Tg, 1 (n.d.).

[45] V. P. Drachev, V. A. Podolskiy, and A. V Kildishev, Opt. Express **21**, 15048 (2013).

[46] A. Poddubny, I. Iorsh, P. Belov, and Y. Kivshar, Nat. Photonics **7**, 948 (2013).

[47] P. Zhu, P. Jin, and L. Jay Guo, Opt. Commun. **305**, 8 (2013).

[48] S. Ishii, A. V. Kildishev, E. Narimanov, V. M. Shalaev, and V. P. Drachev, Laser Photonics Rev. **7**, 265 (2013).

[49] X. G. Luo, Sci. China Physics, Mech. Astron. **58**, 1 (2015).

[50] G. Liang, Z. Zhao, N. Yao, C. Wang, B. Jiang, Q. Zhao, and X. Luo, J. Nanophotonics **8**, 83080 (2014).

[51] X. Chen, C. Zhang, F. Yang, G. Liang, Q. Li, and L. J. Guo, ACS Nano (2017).

[52] G. Liang, X. Chen, Q. Zhao, and L. J. Guo, Nanophotonics **7**, 277 (2018).

[53] X. Chen, G. Liang, and L. J. Guo, in *SPIE Adv. Lithogr.* (International Society for Optics and Photonics, 2017), p. 101470U–101470U.

[54] W. Srituravanich, N. Fang, C. Sun, Q. Luo, and X. Zhang, Nano Lett. **4**, 1085 (2004).

[55] X. Luo and T. Ishihara, Opt. Express **12**, 3055 (2004).

[56] I. P. Kaminow, W. L. Mammel, and H. P. Weber, Appl. Opt. **13**, 396 (1974).

[57] Y. Kou and X. Chen, Opt. Express **19**, 6042 (2011).

[58] S. J. Orfanidis, *Electromagnetic Waves and Antennas* (2004).

[59] C. Zhang, T. Ling, S. Chen, and L. J. Guo, (2014).

[60] M. Maenhoudt, J. Versluijs, H. Struyf, J. Van Olmen, and M. Van Hove, in (2005), pp. 1508–1518.

[61] C. Bencher, Y. Chen, H. Dai, W. Montgomery, and L. Huli, in (2008), p. 69244E–69244E–7.

[62] B. Wang, A. Bian Chew, J. Teng, G. Si, and A. J. Danner, Appl. Phys. Lett. **99**, 15 (2011).

[63] X. Wang, D. Zhang, Y. Chen, L. Zhu, W. Yu, P. Wang, P. Yao, H. Ming, W. Wu, and Q. Zhang, Appl. Phys. Lett. **102**, 6 (2013).

[64] K. Kusaka, H. Kurosawa, S. Ohno, Y. Sakaki, K. Nakayama, Y. Moritake, and T. Ishihara, Opt. Express **22**, 18748 (2014).

[65] Y. M. Song, H. J. Choi, J. S. Yu, and Y. T. Lee, Opt. Express **18**, 13063 (2010).

[66] P. Spinelli, M. a. Verschuuren, and a. Polman, Nat. Commun. **3**, 692 (2012).

[67] Y.-K. R. Wu, A. E. Hollowell, C. Zhang, and L. J. Guo, Sci. Rep. **3**, 1194 (2013).

[68] S. H. Ahn and L. J. Guo, Adv. Mater. **20**, 2044 (2008).

[69] S. H. Ahn and L. J. Guo, ACS Nano **3**, 2304 (2009).

[70] M. K. Kwak, J. G. Ok, J. Y. Lee, and L. J. Guo, Nanotechnology **23**, 344008 (2012).

[71] J. G. Ok, M. K. Kwak, C. M. Huard, H. S. Youn, and L. J. Guo, Adv. Mater. **25**, 6554 (2013).

[72] S. Jahani and Z. Jacob, Optica **1**, 96 (2014).

[73] S. H. Lee, J. H. Lee, C. Park, and M. K. Kwak, J. Micromechanics Microengineering **26**, (2016).

[74] P. J. Yoo, S.-J. Choi, J. H. Kim, D. Suh, S. J. Baek, T. W. Kim, and H. H. Lee, Chem. Mater. **16**, 5000 (2004).

[75] J. W. Dally and W. F. Riley, Exp. Stress Anal. 3rd Ed. McGraw-Hill Inc., New York **184**, (1991).

[76] I. Min and K. Yoon, Korea-Australia Rheol. J. **24**, 73 (2012).

[77] A. Alù, M. G. Silveirinha, A. Salandrino, and N. Engheta, Phys. Rev. B - Condens. Matter Mater. Phys. **75**, 1 (2007).

[78] B. Edwards, A. Alù, M. E. Young, M. Silveirinha, and N. Engheta, Phys. Rev. Lett. **100**, 1

(2008).

[79] B. Edwards, a. Al, M. G. Silveirinha, and N. Engheta, J. Appl. Phys. **105**, (2009).

[80] Y. Xu and H. Chen, Appl. Phys. Lett. **98**, (2011).

[81] J. Luo, P. Xu, H. Chen, B. Hou, L. Gao, and Y. Lai, Appl. Phys. Lett. **100**, 0 (2012).

[82] S. Feng and K. Halterman, Phys. Rev. B - Condens. Matter Mater. Phys. **86**, 10 (2012).

[83] S. Molesky, C. J. Dewalt, and Z. Jacob, Opt. Express **21 Suppl 1**, A96 (2013).

[84] R. Maas, J. Parsons, N. Engheta, and A. Polman, Nat. Photonics **7**, 907 (2013).

[85] M. Yu, Y. Wang, W. Zhong, R. Guo, and X. Zhou, Appl. Phys. A Mater. Sci. Process. **108**, 65 (2012).

[86] X. Yang, J. Yao, J. Rho, X. Yin, and X. Zhang, Nat. Photonics **6**, 450 (2012).

[87] L. Novotny and B. Hecht, *Principles of Nano-Optics* (Cambridge university press, 2012).

[88] A. Yariv and P. Yeh, *Optical Waves in Crystals* (Wiley, New York, 1984).

[89] J. D. Joannopoulos, P. R. Villeneuve, and S. Fan, Solid State Commun. **102**, 165 (1997).

[90] I. V Shadrivov, A. a Sukhorukov, Y. S. Kivshar, A. a Zharov, A. D. Boardman, and P. Egan, Phys. Rev. E 1 (2004).

[91] O. Takayama, L.-C. Crasovan, S. K. Johansen, D. Mihalache, D. Artigas, and L. Torner, Electromagnetics **28**, 126 (2008).

[92] J. Schilling, Phys. Rev. E - Stat. Nonlinear, Soft Matter Phys. **74**, 1 (2006).

[93] B. Wood, J. B. Pendry, and D. P. Tsai, Phys. Rev. B - Condens. Matter Mater. Phys. **74**, 1 (2006).

[94] P. Gao, N. Yao, C. Wang, Z. Zhao, Y. Luo, Y. Wang, G. Gao, K. Liu, C. Zhao, and X. Luo, Appl. Phys. Lett. **106**, (2015).

[95] X. Chen, F. Yang, C. Zhang, J. Zhou, and L. J. Guo, ACS Nano **10**, 4039 (2016).

[96] P. B. Johnson and R. W. Christry, Phys. Rev. B **6**, 4370 (1972).

[97] L. Ferrari, C. Wu, D. Lepage, X. Zhang, and Z. Liu, Prog. Quantum Electron. **40**, 1 (2015).

[98] S. Dai, Q. Ma, T. Andersen, a S. Mcleod, Z. Fei, M. K. Liu, M. Wagner, K. Watanabe, T. Taniguchi, M. Thiemens, F. Keilmann, P. Jarillo-Herrero, M. M. Fogler, and D. N. Basov, Nat. Commun. **6**, 6963 (2015).

[99] J. Sun, J. Zhou, B. Li, and F. Kang, Appl. Phys. Lett. **98**, 1 (2011).

[100] H. Chen, B. Zheng, L. Shen, H. Wang, X. Zhang, N. I. Zheludev, and B. Zhang, Nat. Commun. **4**, 2652 (2013).

[101] J. D. Caldwell, A. Kretinin, Y. Chen, V. Giannini, M. M. Fogler, Y. Francescato, C. T. Ellis, J. G. Tischler, C. R. Woods, A. J. Giles, M. Hong, K. Watanabe, T. Taniguchi, S. a. Maier, and K. S. Novoselov, arXiv **5**, 1 (2014).

[102] K. Korzeb, M. Gajc, and D. A. Pawlak, Opt. Express **23**, 25406 (2015).

[103] S. Dai, Z. Fei, Q. Ma, a S. Rodin, M. Wagner, a S. McLeod, M. K. Liu, W. Gannett, W. Regan, K. Watanabe, T. Taniguchi, M. Thiemens, G. Dominguez, a. H. C. Neto, a Zettl,

F. Keilmann, P. Jarillo-Herrero, M. M. Fogler, and D. N. Basov, Science (80-.). **343**, 1125 (2014).

[104] A. Woessner, M. B. Lundeberg, Y. Gao, A. Principi, P. Alonso-González, M. Carrega, K. Watanabe, T. Taniguchi, G. Vignale, M. Polini, J. Hone, R. Hillenbrand, and F. H. L. Koppens, Nat. Mater. **14**, 421 (2014).

[105] R. Geick, C. Perry, and G. Rupprecht, Phys. Rev. **146**, 543 (1966).

[106] E. Yoxall, M. Schnell, A. Y. Nikitin, O. Txoperena, A. Woessner, M. B. Lundeberg, F. Casanova, L. E. Hueso, F. H. L. Koppens, and R. Hillenbrand, Nat. Photonics **9**, 674 (2015).

[107] A. Woessner, M. B. Lundeberg, Y. Gao, A. Principi, P. Alonso-González, M. Carrega, K. Watanabe, T. Taniguchi, G. Vignale, M. Polini, J. Hone, R. Hillenbrand, and F. H. L. Koppens, Nat. Mater. **14**, 421 (2014).

[108] Y. Fu and X. Zhou, Plasmonics **5**, 287 (2010).

[109] S. D. Berger, J. M. Gibson, R. M. Camarda, R. C. Farrow, H. A. Huggins, J. S. Kraus, and J. A. Liddle, J. Vac. Sci. Technol. B Microelectron. Nanom. Struct. Process. Meas. Phenom. **9**, 2996 (1991).

[110] V. P. Drachev, U. K. Chettiar, A. V Kildishev, H.-K. Yuan, W. Cai, and V. M. Shalaev, Opt. Express **16**, 1186 (2008).

[111] A. V Kildishev, J. D. Borneman, K.-P. Chen, and V. P. Drachev, Sensors **11**, 7178 (2011).

[112] A. Trügler, J.-C. Tinguely, J. R. Krenn, A. Hohenau, and U. Hohenester, Phys. Rev. B **83**, 81412 (2011).

[113] M. Gómez-Gómez, J. Calderón, R. Abargues, P. J. Rodríguez-Cantó, I. Suárez, J. P. M. Pastor, and D. Hill, Mater. Today Proc. **3**, 294 (2016).

[114] S. Huang, H. Wang, K.-H. Ding, and L. Tsang, Opt. Lett. **37**, 1295 (2012).

[115] H. Wang, J. Q. Bagley, L. Tsang, S. Huang, K.-H. Ding, and A. Ishimaru, J. Opt. Soc. Am. B **28**, 2499 (2011).

[116] Z. Guo, Q. Huang, C. Wang, P. Gao, W. Zhang, Z. Zhao, L. Yan, and X. Luo, Plasmonics **9**, 103 (2014).

[117] T. Xu, A. Agrawal, M. Abashin, K. J. Chau, and H. J. Lezec, Nature **497**, 470 (2013).

[118] M. Schøler and R. J. Blaikie, J. Opt. A Pure Appl. Opt. **11**, 105503 (2009).

[119] Shivanand, a Ludwig, and K. J. Webb, Opt. Lett. **37**, 4317 (2012).

[120] C. Zhang, D. Zhao, D. Gu, H. Kim, T. Ling, Y. K. R. Wu, and L. J. Guo, Adv. Mater. **26**, 5696 (2014).

[121] V. Constantoudis, E. Gogolides, G. P. Patsis, A. Tserepi, and E. S. Valamontes, J. Vac. Sci. Technol. B Microelectron. Nanom. Struct. Process. Meas. Phenom. **19**, 2694 (2001).

[122] G. P. Patsis, V. Constantoudis, A. Tserepi, E. Gogolides, and G. Grozev, J. Vac. Sci. Technol. B Microelectron. Nanom. Struct. Process. Meas. Phenom. **21**, 1008 (2003).

[123] N. Li, X. Zhaoa, W. Wanga, and H. Lia, in *SPIE 31st Int. Symp. Adv. Lithogr.* (International Society for Optics and Photonics, 2006), p. 615246.

[124] M. G. Moharam and T. K. Gaylord, **71**, (1981).

[125] V. a Podolskiy and E. E. Narimanov, **30**, 75 (2005).

[126] M. D. Arnold and R. J. Blaikie, Opt. Express **15**, 11542 (2007).

[127] J. Barth, R. L. Johnson, M. Cardona, and E. D. Palik, Acad. Press. New York (1991).

[128] E. S. P. Leong, Y. J. Liu, B. Wang, and J. Teng, ACS Appl. Mater. Interfaces **3**, 1148 (2011).

[129] D. Gu, C. Zhang, Y. K. Wu, and L. J. Guo, ACS Nano **8**, 10343 (2014).

[130] D. Zhao, C. Zhang, H. Kim, and L. J. Guo, Adv. Energy Mater. **5**, 2 (2015).

[131] a. J. Turberfield, Nature **404**, 53 (2000).

[132] Y. Yang, Q. Li, and G. P. Wang, Opt. Express **16**, 11275 (2008).

[133] X. Zhang, X. Ma, F. Dou, P. Zhao, and H. Liu, Adv. Funct. Mater. **21**, 4219 (2011).

[134] V. Drachev, V. Podolskiy, and A. Kildishev, Opt. Express **21**, 1699 (2013).

[135] Z. Zhao, Y. Luo, W. Zhang, C. Wang, P. Gao, Y. Wang, M. Pu, N. Yao, C. Zhao, and X. Luo, Sci. Rep. **5**, (2015).

[136] W. Zhang, H. Wang, C. Wang, N. Yao, Z. Zhao, Y. Wang, P. Gao, Y. Luo, W. Du, and B. Jiang, Plasmonics **10**, 51 (2015).

[137] W. Zhang, N. Yao, C. Wang, Z. Zhao, Y. Wang, P. Gao, and X. Luo, Plasmonics **9**, 1333 (2014).

[138] Q. Huang, C. Wang, N. Yao, Z. Zhao, Y. Wang, P. Gao, Y. Luo, W. Zhang, H. Wang, and X. Luo, Plasmonics **9**, 699 (2014).

[139] A. Schilling, J. Schilling, C. Reinhardt, and B. Chichkov, Appl. Phys. Lett. **95**, (2009).

[140] E. Kretschmann, Opt. Commun. **5**, 331 (1972).

[141] E. Kretschmann, Opt. Commun. **10**, 353 (1974).

[142] D. B. Sirdeshmukh, L. Sirdeshmukh, K. G. Subhadra, and C. S. Sunandana, in *Electr. Electron. Magn. Prop. Solids* (Springer, 2014), pp. 33–48.

[143] A. Schilling, J. Schilling, C. Reinhardt, and B. Chichkov, Appl. Phys. Lett. **95**, 121909 (2009).

[144] a. García-Etxarri, R. Gómez-Medina, L. S. Froufe-Pérez, C. López, L. Chantada, F. Scheffold, J. Aizpurua, M. Nieto-Vesperinas, and J. J. Sáenz, Opt. Express **19**, 4815 (2011).

[145] A. I. Kuznetsov, A. E. Miroshnichenko, Y. H. Fu, J. Zhang, and B. Luk'yanchuk, Sci. Rep. **2**, 492 (2012).

[146] S. Person, M. Jain, Z. Lapin, J. J. Sáenz, G. Wicks, and L. Novotny, Nano Lett. **13**, 1806 (2013).

[147] A. B. Evlyukhin, S. M. Novikov, U. Zywietz, R. L. Eriksen, C. Reinhardt, S. I. Bozhevolnyi, and B. N. Chichkov, Nano Lett. **12**, 3749 (2012).

[148] A. B. Evlyukhin, C. Reinhardt, A. Seidel, B. S. Luk'Yanchuk, and B. N. Chichkov, Phys. Rev. B - Condens. Matter Mater. Phys. **82**, 1 (2010).

[149] M. S. Wheeler, J. S. Aitchison, and M. Mojahedi, Phys. Rev. B - Condens. Matter Mater. Phys. **73**, 1 (2006).

[150] P. Moitra, B. a. Slovick, W. Li, I. I. Kravchencko, D. P. Briggs, S. Krishnamurthy, and J. Valentine, ACS Photonics **2**, 692 (2015).

[151] Y. Kivshar and A. E. Miroshnichenko, Opt. Photonics News **January**, 24 (2017).

[152] J. Valentine, J. Li, T. Zentgraf, G. Bartal, and X. Zhang, Nat. Mater. **8**, 568 (2009).

[153] S. Liu, M. B. Sinclair, T. S. Mahony, Y. C. Jun, S. Campione, J. Ginn, D. a. Bender, J. R. Wendt, J. F. Ihlefeld, P. G. Clem, J. B. Wright, and I. Brener, Optica **1**, 250 (2014).

[154] X. Li, Z. Chen, A. Taflove, and V. Backman, Opt. Express **13**, 526 (2005).

[155] A. E. Miroshnichenko, A. B. Evlyukhin, Y. F. Yu, R. M. Bakker, A. Chipouline, A. I. Kuznetsov, B. Luk'yanchuk, B. N. Chichkov, and Y. S. Kivshar, Nat. Commun. **6**, 8069 (2015).

[156] S. Yoo and Q.-H. Park, Sci. Rep. **5**, 14463 (2015).

[157] J. Scheuer and Y. Yifat, Nat. Nanotechnol. **10**, 296 (2015).

[158] L. Wang, S. Kruk, H. Tang, T. Li, I. Kravchenko, D. N. Neshev, and Y. S. Kivshar, Optica **3**, 1504 (2016).

[159] C. Mätzler, IAP Res. Rep **8**, 1 (2002).

[160] I. Staude, A. E. Miroshnichenko, M. Decker, N. T. Fofang, S. Liu, E. Gonzales, J. Dominguez, T. S. Luk, D. N. Neshev, I. Brener, and Y. Kivshar, ACS Nano **7**, 7824 (2013).

[161] M. Decker, I. Staude, M. Falkner, J. Dominguez, D. N. Neshev, I. Brener, T. Pertsch, and Y. S. Kivshar, Adv. Opt. Mater. **3**, 813 (2015).

[162] J. Petersen, J. Volz, and A. Rauschenbeutel, Science (80-.). **346**, 67 (2014).

[163] J. Lin, J. P. B. Mueller, Q. Wang, G. Yuan, N. Antoniou, X.-C. Yuan, and F. Capasso, Science (80-.). **340**, 331 (2013).

[164] S. Zhang, H. Wei, K. Bao, U. Håkanson, N. J. Halas, P. Nordlander, and H. Xu, Phys. Rev. Lett. **107**, 1 (2011).

[165] D. Gao, W. Ding, M. Nieto-Vesperinas, X. Ding, M. Rahman, T. Zhang, C. Lim, and C.-W. Qiu, Light Sci. Appl. **6**, e17039 (2017).

[166] P. Lodahl, S. Mahmoodian, S. Stobbe, A. Rauschenbeutel, P. Schneeweiss, J. Volz, H. Pichler, and P. Zoller, Nature **541**, 473 (2017).

[167] A. Aiello, P. Banzer, M. Neugebauer, and G. Leuchs, Nat. Photonics **9**, 789 (2015).

[168] P. V. Kapitanova, P. Ginzburg, F. J. Rodríguez-Fortuño, D. S. Filonov, P. M. Voroshilov, P. a. Belov, A. N. Poddubny, Y. S. Kivshar, G. a. Wurtz, and A. V. Zayats, Nat. Commun. **5**, (2014).

[169] D. O'Connor, P. Ginzburg, F. J. Rodríguez-Fortuño, G. a. Wurtz, and a. V. Zayats, Nat. Commun. **5**, 1 (2014).

[170] K. Y. Bliokh, F. J. Rodríguez-Fortuño, F. Nori, and a. V. Zayats, Nat. Photonics **9**, 796 (2015).

[171] F. J. Rodríguez-Fortũno, G. Marino, P. Ginzburg, D. O'Connor, A. Martínez, G. a. Wurtz, and A. V. Zayats, Science (80-.). **340**, 328 (2013).

[172] M. Neugebauer, T. Bauer, P. Banzer, and G. Leuchs, Nano Lett. **14**, 2546 (2014).

[173] L. He, H. Li, and M. Li, Sci. Adv. **2**, e1600485 (2016).

[174] T. Zhang, M. R. C. Mahdy, Y. Liu, J. H. Teng, C. T. Lim, Z. Wang, and C. W. Qiu, ACS Nano **11**, 4292 (2017).

[175] M. Antognozzi, C. R. Bermingham, R. L. Harniman, S. Simpson, J. Senior, R. Hayward, H. Hoerber, M. R. Dennis, a. Y. Bekshaev, K. Y. Bliokh, and F. Nori, Nat. Phys. **12**, 731 (2016).

[176] D. Pan, H. Wei, L. Gao, and H. Xu, Phys. Rev. Lett. **117**, 1 (2016).

[177] N. Shitrit, I. Bretner, Y. Gorodetski, V. Kleiner, and E. Hasman, Nano Lett. **11**, 2038 (2011).

[178] C. Pfeiffer, C. Zhang, V. Ray, L. Jay Guo, and A. Grbic, Optica **3**, 427 (2016).

[179] A. Y. Bekshaev, K. Y. Bliokh, and F. Nori, Opt. Express **21**, 7082 (2013).

[180] K. Y. Bliokh, A. Y. Bekshaev, and F. Nori, Nat. Commun. **5**, 1 (2014).

[181] Y. Gorodetski, K. Y. Bliokh, B. Stein, C. Genet, N. Shitrit, V. Kleiner, E. Hasman, and T. W. Ebbesen, Phys. Rev. Lett. **109**, 1 (2012).

[182] M. Neugebauer, T. Bauer, A. Aiello, and P. Banzer, Phys. Rev. Lett. **114**, 1 (2015).

[183] K. Y. Bliokh and F. Nori, Phys. Rev. A - At. Mol. Opt. Phys. **85**, 1 (2012).

[184] K. Y. Bliokh and Y. P. Bliokh, Phys. Rev. E - Stat. Nonlinear, Soft Matter Phys. **75**, 1 (2007).

[185] A. Y. Bekshaev, K. Y. Bliokh, and F. Nori, Phys. Rev. X **5**, 1 (2015).

[186] A. Eroglu, *Wave Propagation and Radiation in Gyrotropic and Anisotropic Media* (Springer Science & Business Media, 2010).

[187] Z. Lei and T. Yang, IEEE Photonics Technol. Lett. **29**, 615 (2017).

[188] Z. Lei and T. Yang, Appl. Phys. Lett. **108**, (2016).

[189] S. Yoo and Q. H. Park, Phys. Rev. Lett. **114**, 1 (2015).

[190] K. Y. Bliokh and F. Nori, Phys. Rev. A - At. Mol. Opt. Phys. **83**, 1 (2011).

[191] Y. Tang and A. E. Cohen, Phys. Rev. Lett. **104**, 1 (2010).

[192] Y. Kim, B. Yeom, O. Arteaga, S. J. Yoo, S. G. Lee, J. G. Kim, and N. a. Kotov, Nat. Mater. **15**, 461 (2016).

[193] Z. Y. Zhang and Y. P. Zhao, J. Appl. Phys. **104**, (2008).

[194] J. G. Gibbs, a. G. Mark, S. Eslami, and P. Fischer, Appl. Phys. Lett. **103**, (2013).

[195] L. Hu, Y. Huang, L. Pan, and Y. Fang, Sci. Rep. **7**, (2017).

[196] S. Yushanov, J. S. Crompton, and K. C. Koppenhoefer, COMSOL Conf. Bost. (2013).

[197] S. Liu, M. B. Sinclair, T. S. Mahony, Y. C. Jun, S. Campione, J. Ginn, D. a. Bender, J. R. Wendt, J. F. Ihlefeld, P. G. Clem, J. B. Wright, and I. Brener, Optica **1**, 250 (2014).

[198] S. Yushanov, J. S. Crompton, and K. C. Koppenhoefer, in *Proc. COMSOL Conf.* (2013), pp. 1–7.

[199] Y. H. Fu, A. I. Kuznetsov, A. E. Miroshnichenko, Y. F. Yu, and B. Luk'yanchuk, Nat.

Commun. **4**, 1527 (2013).

[200] Z. Huang, N. Geyer, P. Werner, J. De Boor, and U. Gösele, Adv. Mater. **23**, 285 (2011).

[201] X. Li, Curr. Opin. Solid State Mater. Sci. **16**, 71 (2012).

[202] H. J. Kim, S. E. Lee, J. Lee, J. Y. Jung, E. S. Lee, J. H. Choi, J. H. Jung, M. Oh, S. Hyun, and D. G. Choi, Phys. E Low-Dimensional Syst. Nanostructures **61**, 204 (2014).

[203] H. J. Kim, J. Lee, S. E. Lee, W. Kim, H. J. Kim, D. G. Choi, and J. H. Park, ChemSusChem **6**, 2144 (2013).

[204] S. M. Prokes, O. J. Glembocki, J. E. Livenere, T. U. Tumkur, J. K. Kitur, G. Zhu, B. Wells, V. a. Podolskiy, and M. a. Noginov, Opt. Express **21**, 14962 (2013).

[205] J. W. Cleary, R. E. Peale, D. J. Shelton, G. D. Boreman, C. W. Smith, M. Ishigami, R. Soref, a. Drehman, and W. R. Buchwald, J. Opt. Soc. Am. B **27**, 730 (2010).

[206] M. Shahzad, G. Medhi, R. E. Peale, W. R. Buchwald, J. W. Cleary, R. Soref, G. D. Boreman, and O. Edwards, J. Appl. Phys. **110**, (2011).

[207] K. Ataka, S. T. Stripp, and J. Heberle, Biochim. Biophys. Acta - Biomembr. **1828**, 2283 (2013).

[208] M. Osawa, Bull. Chem. Soc. Jpn. **70**, 2861 (1997).

[209] M. Osawa, K. I. Ataka, K. Yoshii, and Y. Nishikawa, Appl. Spectrosc. **47**, 1497 (1993).

[210] F. Le, D. W. Brandl, Y. a. Urzhumov, H. Wang, J. Kundu, N. J. Halas, J. Aizpurua, and P. Nordlander, ACS Nano **2**, 707 (2008).

[211] T. G. Alfsky, H. N. S. K. Rishnamoorthy, W. N. Ewman, E. E. N. Arimanov, Z. J. Acob, and V. M. M. Enon, **2**, 62 (2015).

[212] L. Gu, J. E. Livenere, G. Zhu, T. U. Tumkur, H. Hu, C. L. Cortes, Z. Jacob, S. M. Prokes, and M. a. Noginov, Sci. Rep. **4**, 7327 (2014).

[213] G. Veronis, R. W. Dutton, and S. Fan, J. Appl. Phys. **97**, 93104 (2005).

[214] I. Celanovic, N. Jovanovic, and J. Kassakian, Appl. Phys. Lett. **92**, 193101 (2008).

[215] E. Rephaeli, A. Raman, and S. Fan, Nano Lett. **13**, 1457 (2013).

[216] X. Liu, T. Tyler, T. Starr, A. F. Starr, N. M. Jokerst, and W. J. Padilla, Phys. Rev. Lett. **107**, 45901 (2011).

[217] Y. Guo, W. Newman, C. L. Cortes, Z. Jacob, W. Newman, S. Molesky, Z. Jacob, and a B. Tg, Adv. Optoelectron. **14**, 1 (2012).

[218] W.-X. Zhou, Y. Shen, E.-T. Hu, Y. Zhao, M.-Y. Sheng, Y.-X. Zheng, S.-Y. Wang, Y.-P. Lee, C.-Z. Wang, and D. W. Lynch, Opt. Express **20**, 28953 (2012).

[219] S. Molesky, C. J. Dewalt, and Z. Jacob, Opt. Express **21**, A96 (2013).

[220] B. Luk'yanchuk, N. I. Zheludev, S. a. Maier, N. J. Halas, P. Nordlander, H. Giessen, and C. T. Chong, Nat. Mater. **9**, 707 (2010).

[221] W. Zhou, M. Dridi, J. Y. Suh, C. H. Kim, D. T. Co, M. R. Wasielewski, G. C. Schatz, and T. W. Odom, Nat. Nanotechnol. **8**, 506 (2013).

[222] J. Cuerda, F. R??ting, F. J. Garc??a-Vidal, and J. Bravo-Abad, Phys. Rev. B - Condens.

Matter Mater. Phys. **91**, 1 (2015).

[223] W. Zhu, T. Xu, H. Wang, C. Zhang, P. B. Deotare, A. Agrawal, and H. J. Lezec, Sci. Adv. **3**, e1700909 (2017).

[224] Z. Yu, Y. Wu, L. Xiao, J. Chen, Q. Liao, J. Yao, and H. Fu, J. Am. Chem. Soc. **139**, 6376 (2017).

[225] J. S. Ross, P. Klement, A. M. Jones, N. J. Ghimire, J. Yan, D. G. Mandrus, T. Taniguchi, K. Watanabe, K. Kitamura, W. Yao, D. H. Cobden, and X. Xu, Nat. Nanotechnol. **9**, 268 (2014).

[226] B. Radisavljevic, a. Radenovic, J. Brivio, V. Giacometti, and a. Kis, Nat. Nanotechnol. **6**, 147 (2011).

[227] M.-H. Chiu, C. Zhang, H.-W. Shiu, C.-P. Chuu, C.-H. Chen, C.-Y. S. Chang, C.-H. Chen, M.-Y. Chou, C.-K. Shih, and L.-J. Li, Nat. Commun. **6**, 7666 (2015).

[228] Z. Wang, Z. Dong, Y. Gu, Y. H. Chang, L. Zhang, L. J. Li, W. Zhao, G. Eda, W. Zhang, G. Grinblat, S. a. Maier, J. K. W. Yang, C. W. Qiu, and A. T. S. Wee, Nat. Commun. **7**, 1 (2016).

[229] K. C. J. Lee, Y. H. Chen, H. Y. Lin, C. C. Cheng, P. Y. Chen, T. Y. Wu, M. H. Shih, K. H. Wei, L. J. Li, and C. W. Chang, Sci. Rep. **5**, 1 (2015).

[230] B. Lee, J. Park, G. H. Han, H. S. Ee, C. H. Naylor, W. Liu, a. T. C. Johnson, and R. Agarwal, Nano Lett. **15**, 3646 (2015).

[231] S. Najmaei, A. Mlayah, A. Arbouet, C. Girard, J. Léotin, and J. Lou, ACS Nano **8**, 12682 (2014).

[232] A. N. Sidorov, G. W. Sławiński, a. H. Jayatissa, F. P. Zamborini, and G. U. Sumanasekera, Carbon N. Y. **50**, 699 (2012).

[233] J. Li, S. K. Cushing, F. Meng, T. R. Senty, A. D. Bristow, and N. Wu, Nat. Photonics **9**, 601 (2015).

[234] T. Shin, K. S. Cho, D. J. Yun, J. Kim, X. S. Li, E. S. Moon, C. W. Baik, S. Il Kim, M. Kim, J. H. Choi, G. S. Park, J. K. Shin, S. Hwang, and T. S. Jung, Sci. Rep. **6**, 1 (2016).